

LEABHARLANN CHOLÁISTE NA TRÍONÓIDE, BAILE ÁTHA CLIATH | TRINITY COLLEGE LIBRARY DUBLIN
Ollscoil Átha Cliath | The University of Dublin

Terms and Conditions of Use of Digitised Theses from Trinity College Library Dublin

Copyright statement

All material supplied by Trinity College Library is protected by copyright (under the Copyright and Related Rights Act, 2000 as amended) and other relevant Intellectual Property Rights. By accessing and using a Digitised Thesis from Trinity College Library you acknowledge that all Intellectual Property Rights in any Works supplied are the sole and exclusive property of the copyright and/or other IPR holder. Specific copyright holders may not be explicitly identified. Use of materials from other sources within a thesis should not be construed as a claim over them.

A non-exclusive, non-transferable licence is hereby granted to those using or reproducing, in whole or in part, the material for valid purposes, providing the copyright owners are acknowledged using the normal conventions. Where specific permission to use material is required, this is identified and such permission must be sought from the copyright holder or agency cited.

Liability statement

By using a Digitised Thesis, I accept that Trinity College Dublin bears no legal responsibility for the accuracy, legality or comprehensiveness of materials contained within the thesis, and that Trinity College Dublin accepts no liability for indirect, consequential, or incidental, damages or losses arising from use of the thesis for whatever reason. Information located in a thesis may be subject to specific use constraints, details of which may not be explicitly described. It is the responsibility of potential and actual users to be aware of such constraints and to abide by them. By making use of material from a digitised thesis, you accept these copyright and disclaimer provisions. Where it is brought to the attention of Trinity College Library that there may be a breach of copyright or other restraint, it is the policy to withdraw or take down access to a thesis while the issue is being resolved.

Access Agreement

By using a Digitised Thesis from Trinity College Library you are bound by the following Terms & Conditions. Please read them carefully.

I have read and I understand the following statement: All material supplied via a Digitised Thesis from Trinity College Library is protected by copyright and other intellectual property rights, and duplication or sale of all or part of any of a thesis is not permitted, except that material may be duplicated by you for your research use or for educational purposes in electronic or print form providing the copyright owners are acknowledged using the normal conventions. You must obtain permission for any other use. Electronic or print copies may not be offered, whether for sale or otherwise to anyone. This copy has been supplied on the understanding that it is copyright material and that no quotation from the thesis may be published without proper acknowledgement.

An investigation into the causes of higher rates of restenosis in peripheral arteries compared with coronary arteries following stenting

A thesis submitted to the University of Dublin in partial fulfilment of the requirements for the degree of

Doctor in Philosophy

Trinity College Dublin

April, 2010

Michael Early, BA, BAI

Supervisor

Dr. Daniel J. Kelly

External Examiner
Prof. Francesco Migliavacca
(Politecnico di Milano)

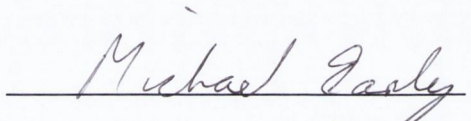
Internal Examiner
Dr. Ciaran Simms

TRINITY COLLEGE
27 AUG 2010
LIBRARY DUBLIN
THESIS
8924

Declaration

I declare that I am the sole author of this thesis and that the work presented in it, unless otherwise referenced, is my own. I also declare that the work has not been submitted, in whole or in part, to any other university or college for a degree or other qualification.

I authorise the library of Trinity College Dublin to lend or copy this thesis on request.



Michael Early

April, 2010

Summary

The use of stenting in peripheral arteries has been limited by rates of in-stent restenosis and stent fracture considerably higher than seen in coronary arteries. Traditional balloon expandable stainless steel stents were found to be incompatible in femoral and popliteal arteries. The change to more flexible nitinol stents saw an improvement in restenosis rates, but outcomes were still poor compared with coronary stents. The advent of drug eluting stents, which decreased restenosis rates in coronary arteries, has yet to result in significant improvement in peripheral arteries. Artery movement, caused by joint flexion, has long been thought of as a major contributory factor of the high restenosis rates seen in peripheral arteries. However, this hypothesis has not been adequately assessed, and there are other factors which could contribute to the poor performance of peripheral stents. The material properties and geometries of the coronary and peripheral arteries are different, and the stent types are now different too. This could affect outcomes by inducing higher stresses in peripheral arteries, or by raising the probability of fatigue failure of the stent.

The principal hypothesis of this thesis is that the artery deformation caused by the mechanical environment of peripheral arteries causes (i) higher stresses and thus more injury and restenosis in the artery and (ii) stent fatigue fracture. To rigorously test this hypothesis, a number of studies were required. To fully understand the differences between coronary and peripheral arteries, mechanical and biochemical analyses were undertaken on the two artery types. As human arteries were not available, porcine arteries were used instead. As expected, it was found that the composition of the arteries influences the material behaviour. While relative differences in mechanical behaviour of coronary and peripheral arteries were similar in porcine tests compared with published human data, important differences do exist. As porcine arteries are used as a substitute for human arteries in many studies, including pre-clinical trials, the consequences of this were investigated in relation to stenting. Finite element models were created of stent deployment in porcine and coronary arteries. The less stiff porcine arteries were predicted to have lower stresses induced, and to cause less recoil of the stent than human arteries. The influence of stent design, in terms of the differences in predicted arterial stresses following implantation, was more evident in human arteries. This may explain why some animal trials fail to differentiate between stents in the same way that randomised human trials do.

Finite element models were also used to investigate the differences between coronary and peripheral stenting, other than the mechanical environment, which could cause higher rates of restenosis. It was found that using a nitinol stent in a peripheral artery induced lower arterial stresses than using a stainless steel stent in a coronary artery. However, the more distensible peripheral artery and stent lead to a greater change in diameter caused by the pulse of blood pressure. For the models considered, fatigue failure was not predicted. However, in oversized stents, this factor becomes more significant, and could be important in conjunction with other influences, such as the mechanical environment.

Bending and compression of the artery were modelled using data obtained from angiographic studies. Appropriate boundary conditions were applied to the artery and the arterial stresses and stent strains were measured. Bending was predicted to cause higher stresses in the artery, in particular the intima. The probability of stent fatigue also became significant. Compression of the artery also raised the strain amplitude, and thus likelihood of fatigue failure, in the stents.

The work presented here corroborates the hypothesis that it is the mechanical environment caused by joint flexion that is the primary cause of high rates of restenosis and stent fracture seen in peripheral arteries. It is demonstrated that stent design is an important factor in this, and further work in this area could lead to improved results in peripheral stenting. Furthermore, the finite element models presented are suggested as a valuable pre-clinical tool for testing and comparing stent designs when used in conjunction with mechanical testing and pre-clinical animal trials.

Acknowledgements

Like my supervisor before me, I aspired to a job and a shiny car on finishing my undergraduate degree. For giving me the opportunity (and convincing me to take it) to pursue postgraduate research, I am most grateful to Dr. Daniel Kelly. As well as providing the encouragement, guidance and, perhaps most of all, patience which enabled me to complete this research, he allowed me the freedom to explore my own ideas while providing the restraint that ensured a minimum of time was wasted on the more outlandish ones.

This thesis could not have been undertaken without the assistance of many other people. Dr. Alex Lennon and Dr. Catriona Lally provided invaluable assistance on the computational side of the research; likewise, Dr. Conor Buckley guided me through the unfamiliar world of biochemical experimentation, and Peter O'Reilly, Mick Reilly, Paul Normoyle, and J.J., Sean and Gabriel helped me setting up the experimental rigs. Thanks also to Joan, Sheena and Nicole for helping with, well, everything, and to Peter, Anne, and Tom in the BRU.

Doing research would be a lot less fun without the tea breaks, nights out, conferences and witty banter provided by my fellow biomechanical engineers both here in TCD and in RCSI; Jen, Shane, Damo, Thomas, Steve, Alanna, Colin, Tanya, Grá, Orlaith, Matt, Niamh, Laura, Mike, Brianne, Eoghan, Peter, Eamon, Karen, Geraldine, Pavel, Kevin, Saied, Brianne, Dave, Tat, and Ruth. Special thanks too to Dave for all the tea, Christmases and awful puns.

Most of all, I'd like to thank my family (Mum, Dad, Diarmuid, Cormac and Connie) for supporting me as I resided in the ivory tower when I could have been out doing something useful (and more interesting and profitable) with my life. Finally, I'd like to thank Jim, who gave me a first glimpse of what engineers can achieve, and inspired me towards a career in biomechanics and designing and developing medical devices.

This project was funded in part by a grant from Enterprise Ireland (CFTD/07/129).

Publications and presentations arising from this study

Journal articles

Michael Early, Catriona Lally, Patrick J. Prendergast, and Daniel J. Kelly

Stresses in peripheral arteries following stent placement: a finite element analysis

Computer Methods in Biomechanics and Biomedical Engineering, 12(1), 25-33; 2009

Michael Early and Daniel J. Kelly

The role of vessel geometry and material properties on the mechanics of stenting in the coronary and peripheral arteries.

Proceedings of the Institution of Mechanical Engineers, Part H, Journal of Engineering in Medicine, 224(3), 465-476; 2010

Presentations at national and international conferences

Michael Early and Daniel J. Kelly

Finite element modelling of stent expansion.

In *Proceedings of the 12th Annual Conference of the section of Bioengineering of the Royal Academy of Medicine in Ireland*, Galway, 2006.

Michael Early and Daniel J. Kelly

An analysis of the stresses in peripheral arteries following stenting using the finite element method.

In *Proceedings of the 5th World Congress of Biomechanics*, Munich, 2006.

Michael Early and Daniel J. Kelly

A study of the factors affecting stresses in peripheral arteries following stenting

In *Proceedings of the 13th Annual Conference of the section of Bioengineering of the Royal Academy of Medicine in Ireland*, Fermanagh, 2007.

Michael Early and Daniel J. Kelly

A study of the factors affecting stresses in peripheral arteries following stent placement

In *Proceedings of the European Society of Biomechanics Workshop*, Dublin, 2007.

Michael Early and Daniel J. Kelly

Can differences in vessel geometry, material properties, or stent type explain higher rates of restenosis in peripheral arteries

In *Proceedings of the 14th Annual Conference of the section of Bioengineering of the Royal Academy of Medicine in Ireland*, Sligo, 2008.

Michael Early and Daniel J. Kelly

Influence of stent type and arterial properties and geometry on stent-artery interactions

In *Proceedings of the 16th Congress of the European Society of Biomechanics*, Lucerne, 2008.

Michael Early and Daniel J. Kelly

Differences between porcine and human arteries in stenting: implications for pre-clinical trials.

In *Proceedings of the 15th Annual Conference of the section of Bioengineering of the Royal Academy of Medicine in Ireland*, Limerick, 2009.

Michael Early and Daniel J. Kelly

Why are rates of restenosis higher in peripheral arteries than coronary arteries? A computational study.

In *Proceedings of the ASME Bioengineering Division 2009 Summer Bioengineering Conference*, Lake Tahoe, 2009.

Nomenclature

B	Left Cauchy-Green strain tensor
C_{ij}	Components of right Cauchy-Green deformation tensor
E	Young's modulus
E_{ij}	Components of Green-Lagrangian strain tensor
I_i	Stretch invariants
S_{ij}	Components of second Piola-Kirchhoff stress tensor
T	Temperature
u	Displacement vector
W	Strain-energy

m	Metres
cm	Centimetre
mm	Millimetre
µm	Micrometres
l/L	Litres
ml	Millilitres
µl	Mircrolitres
g	Grams
mg	Milligrams
µl	Micrograms
Pa	Pascals
kPa	Kilopascals
MPa	Megapascals

σ_s^{AS+}	starting tensile stress in austentite to martensite transformation
σ_f^{AS+}	finishing tensile stress in austentite to martensite transformation
σ_s^{SA+}	starting tensile stress in martensite to austentite transformation
σ_f^{SA+}	finishing tensile stress in martensite to austentite transformation
σ_s^{AS-}	starting compressive stress in austentite to martensite transformation
SIM	Stress induced martensite
A_s	Auestentite start temperature
A_f	Auestentite finish temperature
M_s	Martensite start temperature
M_f	Martensite finish temperature

σ_{ij}	Component of Cauchy stress
λ	Stretch
ε	Linearised strain

°	Degrees

List of Figures

2.1 Composition of healthy artery showing three distinct layers (intima, media and adventitia) and fiber directions. Taken from [Gasser et al., 2006]. 12

2.2 The musculo-elastic fascicle, as proposed by Clark and Glagov. A varying number of repeating layers of this unit make up the media in arteries. E = elastin, Ce = smooth muscle cells and F = collagen fiber bundles that exist between the elastin sheets. [Clark et al., 1985] 13

2.3 Cross sections of typical (top) elastic artery and (bottom) muscular artery [Berne et al., 1979]. 15

2.4 (a) Classification of injury scores at different points on cross-section of a stented artery (b) Correlation between injury score and neointimal growth for stented porcine arteries. [Schwartz et al., 1994] 19

2.5 Balloon angioplasty. http://www.nhlbi.nih.gov/health/dci/images/angio_lowres.gif 21

2.6 Palmaz-Schatz Coronary Stent. [Bonsignore, 2004]. 22

2.7 Different ways of constructing a stent from expandable rings and connecting elements. (a) closed cell, peak to peak, flex connector. (b) open cell, non-flex connector, peak to peak. (c) open cell, non-flex connector, peak to peak. (d) open cell, flex connector, peak to peak. (e) open cell, non-flex connector, peak to valley. (f) open cell, non-flex connector, midstrut. [Bonsignore, 2004] 23

2.8 (a) Nitinol Smart stent, a typical peripheral stent design. (b) Smart stent showing high flexibility www.clevelandclinic.org/heartcenter/images/guide/disease/vascular/stent_smart.jpg http://www.abbottvascular.com/en_US/content/image/absolute7_lg.jpg 24

2.9 Angiographies of (A) knee extension and (B) knee flexion. Point 1 is a hinge point, points 2, 3 and 4 are accessory flexions. The artery is divided into (a) pre-hinge point segment, (b) hinge point zone, and (c) post-hinge point segment. [Diaz et al., 2004] 27

2.10 Bending of femoropopliteal arterial segment at knee/hip flexion angles of (a) 0°/0°, (b) 70°/20° and (c) 90°/90°. Taken from [Smouse et al., 2005]. 28

2.11 Shape memory properties of Nitinol. Above A_f (point a), the material is fully austentite (cubic structure). As the temperature is reduced to below M_f, a phase transformation to twinned martensite (monoclinic B19 structure) occurs. When the material is stressed, detwinning begins (c) until full detwinning (d). When the material is unloaded, elastic recovery begins, but phase transformation is not complete until temperature is raised to A_f again.[Robertson, 2006] 31

2.12 Representative stress-strain behaviour of nitinol in loading and unloading under uniaxial tension. 33

2.13 Material behaviour of nitinol under uniaxial tension. Blue line shows experimental data on Ti-50.8at%Ni thin wall tubes [Favier et al., 2006], red line shows simulation model used for finite element analysis. [Wu et al., 2007a] 35

2.14 Mechanical and thermal behaviour of nitinol showing parameters used to describe constitutive behaviour. (Note: $\sigma_s = \sigma_s^{AS+}$). [Migliavacca et al., 2004] 36

2.15 Goodman diagram for 316L stainless steel microsamples. 37

2.16 Graph showing samples passing (empty squares) and failing (black squares) stent samples at various levels of strain amplitude and mean strain [Pelton et al. 2008]. Dotted line shows strain amplitude value of 0.4%. 38

2.17 Mechanical behaviour of elastin, collagen, and whole artery artery. Elastin is tested on its own by digesting the collagen with formic acid, while collagen is isolated by digesting the artery in trypsin. [Roach et al., 1957] 40

2.18 The SEF for a single fiber (with $\varepsilon \geq 0$) folded with a probability distribution function (PDF) gives an overall SEF for the collagen. 51

2.19 Single cell representative of stent expansion. (a) Pressure controlled boundary conditions using 3-d model. (b) Displacement controlled boundary conditions using 2-d model. [Dumoulin et al., 2000] 53

2.20 Shape of expanded stent at maximum diameter (a) in vitro and (b) using finite element model. [Migliavacca et al., 2005] 54

2.21 Relationship of areas of plastic deformation in (b) finite element model with (c)&(d) Luders lines seen using scanning electron microscope. [Migliavacca et al., 2005] 55

2.22 A comparison of stent expansion using realistic balloon models. The balloon can be modelled by (a) deflating a cylindrical balloon with a negative pressure and then inflating the balloon or (b) modelling the balloon folding. [Gervaso et al., 2008] [De Beule et al., 2008] 57

2.23 Final stent shape, stent von Mises stresses and Artery von Mises stresses for (a) cylindrical balloon expanded with displacement control, (b) pressure applied directly to stent and (c) realistic pressure controlled balloon model. [Gervaso et al., 2008] 57

2.24 Modelling a folded balloon, showing (a) folding the balloon and (b) deployment of the balloon using free expansion. [Laroche et al., 2006] 58

2.25 Finite element model of stent deployment in carotid artery showing (a) artery displacement, (b) artery stresses and (c) stent stresses following stenting. [Wu et al., 2007a] 61

3.1 Typical slip verification study showing strain measured using gauge length and visual technique. 74

3.2 Thickness (mean ± standard deviation) of three different artery types. Statistical difference ($P<0.05$) is indicated with an asterisk (*). 75

3.3 Typical pre-conditioning cycles for porcine arteries. 76

3.4 Stress-stretch curve for tensile tests on coronary arteries in the longitudinal direction. 77

3.5 Stress-stretch curve for circumferential ring tests on coronary arteries. 77

3.6 Stress-stretch curve for tensile tests on femoral arteries in the longitudinal direction. 78

3.7 Stress-stretch curve for compressive tests on femoral arteries. 78

3.8 Stress-stretch curve for tensile tests on aorta in the longitudinal direction. 79

3.9 Stress-stretch curve for tensile tests on aorta in the circumferential direction. 79

3.10 Fitting constitutive equations to human coronary intima stress-strain data. Data taken from [Holzapfel et al., 2005] 80

3.11 An example of stress-strain data (circumferential porcine ring tests) and a representative curve obtained by taking the average constants of the Mooney-Rivlin curves. 82

3.12 Average curves for each artery and test type using constants shown in Table 3.6. 83

3.13 Collagen content (mean ± standard deviation) of three different artery types as a percentage of dry weight. Statistical difference ($P<0.05$) is indicated with an asterisk (*). 84

3.14 Elastin content (mean ± standard deviation) of three different artery types as a percentage of dry weight. Statistical difference ($P<0.05$) is indicated with an asterisk (*). 85

3.15 Collagen to elastin ratio (C:E) (mean ± standard deviation) of three different artery types. Statistical difference ($P<0.05$) is indicated with an asterisk (*). 86

3.16 Typical histological slides of (a) coronary artery, (b) femoral artery and (c) aorta. 87

3.17 Correlation between alpha and (a) collagen, (b) elastin and (c) C:E, and beta and (d) collagen, (e) elastin and (f) C:E for the femoral artery. 88

3.18 Average curves for femoral and coronary arteries and aortas with collagen to elastin ratios. 89

4.1 Geometry of (a) porcine and (b) human arteries. 101

4.2 Geometry and mesh of MultiLink stent showing (a) complete model of ML Thick stent and one third segments modelled of (b) ML Thick and (C) ML Thin stents. 102

4.3 Geometries and meshes of (a) Palmaz and (b) Cypher stents. 103

4.4 Stress-stretch curves for human arteries and third-order Mooney-Rivlin models fitted to data. 105

4.5 Circumferential stress-stretch data for porcine and human arteries. 105

4.6 (a) Springs attached to stent and node at centre of stent (b) Stiffness-displacement relationship for springs, similar to table input used to describe mechanical behaviour. 107

4.7 Fully expanded ML Thick stent in artery. 109

4.8 Von Mises stresses in human coronary arteries following deployment of (a) Multilink thick and (b) Multilink thin stents. 111

4.9 Stress distributions in (a) human and (b) porcine coronary artery models following expansion of Multilink thick and thin stents. 111

4.10 Stress distributions in (a) human and (b) porcine coronary intima models following recoil of Multilink thick and thin stents. 113

4.11 Von Mises stresses in the intimas of (a) human and (b) porcine coronary arteries following expansion of Palmaz-Schatz (PS), Cypher, and Mulitlink thick (ML) stents. 113

4.12 Contour plots of von Mises stresses in peripheral pig and human peripheral arteries following stent deployment showing individual layers. Shown are (a) the intima, (b) the media and (c) the adventitia. 115

4.13 Stress distributions in pig and human (a) intima, (b) media, and (c) adventitia of peripheral arteries following deployment of Palmaz stent expanded to diameter of 10 mm. 116

4.14 Stresses following nitinol stent deployment in peripheral (a) porcine and (b) human arteries. 117

4.15 Stress-stretch curves for average coronary and femoral porcine arteries and mean coronary -1.96σ and mean femoral +1.96σ. 118

4.16 Stress distributions in the intimas of mean and mean ±1.96σ arteries. 118

5.1 Geometries of (a) stainless steel balloon expanded stent, (b), the expanded geometry of (a), used as the initial configuration for SES1, and (c) the initial configuration of SES2. 128

5.2 Nitinol stent deployment. (a) Stent and artery are coincident, (b) Artery elements are deactivated, (c) Diameter of sheath is reduced to crimp stent, (d)Artery elements are reactivated, (e) Sheath is withdrawn laterally, stent expands and (f) Stent is fully deployed 132

5.3 Stress distributions following BES, SES1 and SES2 placement in (a) coronary intima, (b) coronary media, (c) coronary adventitia, (d) peripheral intima, (e) peripheral media and (f) peripheral adventitia. 135

5.4 Von Mises stress in coronary artery following expansion of BES showing (a) the whole artery and three separate layers, (b) intima, (c) media and (d) adventitia. 136

5.5 Von Mises stress in femoral artery following expansion of SES2 showing (a) the whole artery and three separate layers, (b) intima, (c) media and (d) adventitia. 137

5.6 Contour bands of von Mises stresses in peripheral arteries following expansion of nitinol stents. Stents used in (a), (b) and (c) had diameters of 10 mm and strut thicknesses of 100 μm, 150 μm and 250 μm. 141

5.7 Stress distributions in peripheral arteries showing influence of strut thickness on (a) intima, (b) media and (c) adventitia, and of stent diameter on (d) intima, (b) media and (c) adventitia. 142

6.1 Application of physiological loading to artery. (a) starting configuration. (b) application of blood pressure. (c) application of physiological pre-stretch until the artery face is coincident with the rigid plate. 154

6.2 Application of bending boundary condition by rotating plate showing (a) shape following physiological loading and (b) after bending. 155

6.3 Application of compressive boundary condition by moving plate showing (a) shape following physiological loading and (b) after compression. 156

6.4 Stress distribution in peripheral (a) intima, (b) media and (c) adventitia following bending of a stent at 0° (following recoil), 12°, 18°, 36°, and 54°. 158

6.5 Contour plots of von Mises stresses in peripheral artery following (a) expansion of BES and application of (b)12°, (c) 18°, (d) 36° and (c) 54° of bending. 159

6.6 Factor of safety as a function of the amount of applied bending in a peripheral artery following expansion of a stainless steel stent. 160

6.7 Goodman diagrams for a stainless steel stent in a peripheral artery following (a) 12°, (b) 18°, (c) 36°, and (d) 54° of bending. 161

6.8 Stress distributions in peripheral arteries following deployment of SES with strut thickness of 150 μm. The three layers, (a) intima, (b) media, and (c) adventitia are shown. 163

6.9 Stress distributions in peripheral arteries following deployment of SES with strut thickness of 100 μm. The three layers, (a) intima, (b) media, and (c) adventitia are shown. 164

6.10 Stress distributions in peripheral arteries following deployment of SES with strut thickness of 250 μm. The three layers, (a) intima, (b) media, and (c) adventitia are shown. 165

6.11 A comparison of intimal stresses following bending with three different strut thicknesses (100, 150 and 250 μm) after (a) 36° and (b) 54° of bending. 166

6.12 Strain amplitude as a function of bending in peripheral artery following deployment of stents with strut thicknesses of 100 μm (SES2(a)), 150 μm (SES2) and 250 μm (SES(b)). 167

6.13 Predicted strain amplitude following compression of peripheral artery with implanted nitinol stent for stent strut thicknesses of 100, 150, and 250 μm. 168

6.14 A comparison of strain amplitudes seen in stents with strut thicknesses of 150 μm for compression between 2.5% and 25%. 168

List of Tables

2.1 Classification of injury scores. After Schwartz and Holmes [Schwartz et al., 1994]. 19

2.2 Axial compression of cadaveric lower extremity unstented arteries (Arteries) and 100 mm self expanding nitinol stents when placed in cadaveric lower-extremity arteries (Stents). Adapted from [Nikanorov et al., 2008]. 28

2.3 Bending deformation of 100 mm self expanding nitinol stents when placed in cadaveric lower extremity arteries. Adapted from [Nikanorov et al., 2008]. 29

3.1 Average width and thickness of the artery samples measured for mechanical tests. 75

3.2 Constants fitted to Fung model for human coronary intima, media and adventitia. Error provided is absolute error. 80

3.3 Constants fitted to Gent model for human coronary intima, media and adventitia. Error provided is absolute error. 81

3.4 Constants fitted to Ogden model for human coronary intima, media and adventitia. Error provided is absolute error. 81

3.5 Constants fitted to third-order Mooney-Rivlin model for human coronary intima, media and adventitia. Error provided is absolute error. 81

3.6 Average third-order Mooney-Rivlin constants for porcine aorta and femoral and coronary arteries. 83

3.7 The tissue elements differentiated by the Verhoeff-van Gieson staining. 87

3.8 Collagen content, elastin content and collagen to elastin ratio for coronary and femoral arteries and aorta. The literature data presented is taken from a previous study on canine arteries [Fischer et al., 1966]. 92

4.1 Dimensions of coronary artery models. 102

4.2 Geometric properties of stents used in finite element models. 104

4.3 Third-order Mooney-Rivlin constants fitted to data for human and porcine coronary arteries. 106

4.4 Diameters for ML Thin and Thick stents following expansion and recoil in human and porcine coronary artery models. 110

4.5 Stent diameters following expansion in peripheral artery at diastole and systole 117

5.1 Geometric properties of the BESs and SESs for the coronary and peripheral arteries. 128

5.2 Variations on the SES2 design with variations on strut thickness and diameter. 128

5.3 Material constants for coronary and peripheral arteries. 129

5.4 Material constants taken from Favier et al [Favier et al., 2006] used in nitinol material models. See Chapter 2 for full definitions of terms used. 130

5.5 Loads applied to artery 133

5.6 Lumen gain for different artery and stent types. 'Stages' refers to the degree of stent expansion, and is explained as follows. Stage 1 for BES refers to the stent at the maximum diameter during deployment, after stent recoil. Stages 2 and 3 describe the stent following recoil at the minimum and maximum blood pressure respectively. Stages A and B are used for the SES designs, and refer to the fully deployed stent at the minimum (A) and maximum (B) blood pressures. 138

5.7 Change in diameter and associated maximum strain amplitude (for SES models) caused by change in blood pressure. 139

5.8 Lumen gain, change in diameter and associated strain amplitude with variations in stent design. Note that average lumen is also given relative to the original artery diameter. Definitions of stent designs (SES2(a-d)) are shown in Table 5.2. 143

6.1 Summary of maximum strain amplitudes (and minimum factors of safety) for pulsatile, bending, and compression loading of peripheral arteries after knee/hip flexion of 90°/90°. 169

6.2 Summary of maximum strain amplitudes (and minimum factors of safety) for pulsatile, bending, and compression loading of peripheral arteries after knee/hip flexion of 70°/20°. 170

Contents

Declaration i

Summary ii

Acknowledgements iv

Publications and Presentations v

Nomenclature vii

List of Figures ix

List of Tables xv

Chapter 1 Introduction 1

Stenting in peripheral arteries, a procedure widely and successfully used in coronary arteries, has not proved as effective in other arteries. A background to this problem is provided.

Chapter 2 Literature Review 9

Previous studies appropriate to this work are reviewed. This includes general areas such as cardiovascular disease, injury response, stenting and arterial mechanical properties, as well as details specific to peripheral arterial disease. Clinical cases in coronary and peripheral arteries and using balloon expanded and self-expanding stents are compared. The use of finite element models to study such problems is reviewed.

Chapter 3 Structure-function relations of porcine arteries from different vascular beds 63

Mechanical tests are carried out on porcine coronary and femoral arteries and aorta. Biochemical assays and histology are used to analyse the composition and structure of the arteries, which in turn are compared with the mechanical properties.

Chapter 4 Modelling arteries and the stenting procedure 97

Appropriate means of modelling the deployment of a stent in an artery are investigated. The consequences of using porcine instead of human arteries for pre-clinical trials are presented. The influence of stent design is included.

Chapter 5 Modelling stenting in peripheral arteries 125

Finite element models comparing the deployment of a balloon expanded stent in a coronary artery with a self-expanding stent in a peripheral artery are created. The stresses induced in the artery following stenting are analysed, as well as the fatigue environments. The effect of stent over-sizing and strut thickness are examined.

Chapter 6 Modelling the mechanical environment of peripheral arteries 149

Bending and compression are applied to arteries following stent expansion. The incompatibility of stainless steel stents in peripheral arteries is demonstrated. Nitinol stents were inspected for stresses in the artery and the probability of fatigue related fracture.

Chapter 7 Discussion 177

The findings of the studies presented are summarised and put in context. The limitations of the studies are put forward, and the direction of future work is suggested.

References 187

Appendices 203

1 Introduction

Contents

1.1 Background 2

1.2 Peripheral arterial disease 3

1.3 Finite element modelling 4

1.4 Material properties of arteries 5

1.5 Modelling stenting in the peripheral artery 6

1.6 Aims of the study 7

1.1 Background

Cardiovascular disease (CVD) is the leading cause of death in America, accounting for 35.3% of all deaths in 2005 [Lloyd-Jones *et al.* 2009]. Atherosclerosis is a form of CVD that is characterised by a hardening and thickening of the arteries the results in a reduction in the lumen area. This can lead to heart attacks or strokes, and accounts for up to three quarters of CVD related deaths [Lloyd-Jones *et al.* 2009]. Atherosclerosis is essentially an inflammatory response of the arteries caused by an excess of low-density lipoprotein (LDL), or cholesterol, within the artery wall. These LDLs are ingested by macrophages, which along with T-lymphocytes, form a fatty streak. This, in turn, develops into a plaque [Libby 2002].

Once a plaque is formed, it progresses by remodelling. Although most plaque growth is outwards, if the plaque grows inwards it can narrow the vessel lumen and restrict blood-flow. This remodelling is accompanied by the formation of a fibrous cap over the lipid core. This cap separates the fatty core from the blood flow. If this cap ruptures, a thrombus can be formed, which has the potential to block blood flow, either at the site of the plaque or further downstream. This can lead to a heart attack or a stroke.

Until recently, the most common way of restoring blood flow was to bypass the affected artery by performing Coronary Artery Bypass Grafting (CABG). Although the success rates for CABG are excellent, the recovery time for the patient can be long. More minimally invasive procedures to restore blood flow to the arteries rather than bypass them have become increasingly popular over the past 20 years.

Balloon angioplasty involves the insertion of a PVC or nylon balloon, mounted on a catheter, into the coronary system, usually through the femoral artery. The balloon is guided to the target area by the cardiologist, using guide wires. A pressure is then applied to force saline solution into the balloon, causing it to unfold and expand. This increases the diameter of the artery, restoring blood flow. The balloon is then deflated and removed.

In 2006, over 1.3 million percutaneous coronary interventions (PCI) and 1.1 million cardiac catheterisations were carried out in the United States [Lloyd-Jones *et al.* 2009], making angioplasty the most common therapeutic intervention in the world [Fleisch 1999].

While patency rates for angioplasty are generally satisfactory, in the longer term problems can arise when elastic recoil of the artery causes it to close up, reducing the gain in diameter obtained from balloon angioplasty and restricting the blood flow again. This problem can be overcome with

the use of a stent. Stents are small tubes, cut into wires or struts, which are placed in the artery to prevent elastic recoil. They are usually metallic, with stainless steel the most common material used. These are compressed, or crimped, onto a balloon, which is expanded in the artery using a balloon similar to that used in angioplasty following initial dilation of the artery. When the balloon is deflated and withdrawn, the stent remains *in situ* and resists elastic recoil of the vessel.

Although stents prevent the re-blocking of the artery due to elastic recoil, issues can still arise which can limit the effectiveness of stents. In-stent restenosis (ISR), defined as the narrowing of a vessel wall following angioplasty and stenting, is the most common cause of failure in modern stents. This is caused by the growth of cells within the artery, which can eventually result in a loss of the lumen gain obtained by angioplasty. Like atherosclerosis, restenosis is an inflammatory response. It has been hypothesised that rates of restenosis are related to injury, and hence damage, in the artery following stent deployment [Schwartz 1994]. As such, stents are designed to minimise the damage to the arterial wall, while drug-eluting stents contain anti-inflammatory drugs which suppress the cell growth that leads to ISR following vessel injury.

1.2 Peripheral arterial disease

Peripheral Arterial Disease (PAD) is similar to CAD in that it is characterised by a thickening and hardening of the arterial wall, reducing blood flow. The primary difference is that PAD occurs in peripheral arteries, or those outside the heart. Usually, PAD affects arteries in the legs, and incidence of PAD and CAD are strongly related [Criqui 1992].

Contrasted to the procedure in coronary arteries, where success rates can be over 90%, stenting in peripheral arteries has proved problematic, and is carried out less frequently. The reasons for the differences in outcome between two ostensibly similar procedures are not well documented. It has been suggested that the reason for such complications in peripheral stenting is the extreme mechanical environment experienced by the arteries. For example, flexion of the knee can cause extensive arterial deformation even in healthy subjects [Hoffmann 1997]. These deformations have only recently been quantified [Cheng *et al.* 2006; Nikanorov *et al.* 2008], and the consequences of these have so far only been investigated in terms of stent fracture [Nikanorov *et al.* 2008].

There are a number of other differences between the two procedures, which also have not been studied with regard to stenting. The material properties of the arteries are different; for example

the coronary artery is stiffer than the iliac artery [Schulze-Bauer *et al.* 2003; Holzapfel *et al.* 2005]. This difference is partly due to the variation of material properties with location on the arterial tree, but is amplified by intimal thickening. This phenomenon, which causes the intima to thicken and stiffen with age, is more significant in the coronary arteries compared to the iliac arteries. The geometries are also different, with peripheral arteries generally having a greater diameter and thickness.

The poor success rates seen in early studies using stainless steel stents in peripheral arteries saw the introduction of shape-memory alloy stents. These alloys, which can experience very large (~11%) recoverable strains, are more flexible than stainless steel and are designed to be more flexible for placement in an adverse mechanical environment. While these stents have improved success rates relative to steel stents, the problem of peripheral stenting is so acute that only one stent (LifeStent FlexStar, Bard Peripheral Vascular Inc, AZ) is currently approved by the FDA for use in the femoral and popliteal arteries. Often, biliary stents are used 'off-label', in a procedure for which they are not approved, instead.

The use of nitinol stents in peripheral arteries provides another difference between peripheral and coronary interventions. Nitinol stents, which are compressed to fit inside the artery, attempt to expand to their original diameter when released. As the stent is, by design, larger than the arteries into which it is inserted, the stent does not reach its nominal diameter and so continues to exert an outward radial force on the artery. Steel stents are expanded, experience elastic recoil, and then remain mechanically inert. A further difference between the two stenting procedures is related to the material properties of the stents. The more compliant nitinol stents experience displacement as the artery changes diameter with the change in blood pressure. This leads to a strain-controlled fatigue environment for the stent. In contrast, steel stents, stiffer than the nitinol stents, remain relatively static and undergo very small displacements as a result of the cardiac cycle. The dynamic mechanical environment within peripheral arteries will also have a significant bearing on the fatigue environment of the stent. Stainless steel stents can also straighten the artery into which they are expanded, while nitinol stents will distort to match the shape of the native vessel to a greater extent.

1.3 Finite element modelling

Owing to the diminutive size of many medical devices, traditional techniques for measuring deformation, such as strain gauges, are not suitable for analysis. As a result, finite element

modelling has become a popular tool for evaluating medical devices. It can be used to predict the behaviour of stents when expanded, and measure properties such as foreshortening, opening profile and locations and magnitudes of peak stresses and strains. More recently, it has also been used to model the stent-artery interaction. While finite element analysis is most often used as an element of directive compliance for medical devices, there is enormous potential for design improvement. Aspects of stent expansion such as dog-boning or symmetry of deployment can be optimised, as well as factors associated with the stent-artery interaction such as lumen gain, arterial stresses and tissue prolapse.

Most of the finite element work carried out to date has focussed on coronary arteries, where the majority of stents are placed. A strong case can also be made for the use of finite element models in improving stent design in peripheral arteries. Because both the stent and artery can be investigated using this method, the hypothesised causes of restenosis, stent fracture and elevated arterial stresses, can be evaluated.

1.4 Material properties of arteries

One of the differences between stenting in the coronary and peripheral arteries is the material properties of the target vessels, so it is important to understand these differences. Also, the accuracy of the results obtained from finite element models depends on the suitability of the data used as inputs. There is a need to have a full understanding of the mechanical behaviour of arteries, and to be able to appropriately describe this material behaviour. While mechanical tests of different arteries have been presented [Schulze-Bauer *et al.* 2002; Prendergast *et al.* 2003; Schulze-Bauer *et al.* 2003; van Andel *et al.* 2003; Lally *et al.* 2004; Holzapfel *et al.* 2005; Holzapfel *et al.* 2007], and the biochemical composition of the tissue has been quantified [Fischer *et al.* 1966; Cox 1978; Davidson *et al.* 1985; Zulliger *et al.* 2004; Hu *et al.* 2008], there have been relatively few attempts to link the two for different artery types.

Because of the similarity between their cardiovascular systems, pigs are often used for tests on arteries, for obtaining mechanical properties for finite element modelling and for pre-clinical trials. It is important to understand the differences between arteries, both between species and between arteries from different locations in the arterial tree for the consequences these differences will have on interpretation of animal trials and for improving stent design.

Human and porcine arteries can be compared in terms of mechanical properties. To look at the consequences of the differences in mechanical properties for stenting, finite element modelling can be used. By creating appropriate models, the differences between pre-clinical animal trials and randomised human trials can be highlighted.

1.5 Modelling stenting in the peripheral artery

With the use of suitable material data, stenting in coronary and peripheral arteries can be compared by using finite element modelling. There are two aspects of the differences between the two types of stenting that require attention. The first is the difference in material properties and geometry, both of the stents used and the artery into which they are deployed. These changes, in the geometry and material properties of the artery and stent, as well as the type of stent used, could induce higher stresses in the peripheral arteries, which may in turn result in greater vessel injury and more in-stent restenosis. Furthermore, the pulsatile fatigue cycle, not believed to be as important in stiffer steel stents [Duerig *et al.* 2000], could increase the possibility of stent fatigue fracture.

The second difference between the stenting procedures to be investigated is the mechanical environment. Coronary arteries, attached to the myocardium, undergo large displacements during the cardiac cycle [Ding *et al.* 2002]. However, the arteries do not necessarily experience large strains, and stent fracture is rare in coronary arteries. It has been believed for some time that joint motion induces large deformations in some peripheral arteries, and this is believed to be a cause of stent incompatibility in these arteries [Kroger *et al.* 2004]. More recent angiographic studies, which have quantified these deformations [Cheng *et al.* 2006; Nikanorov *et al.* 2008], enable the mechanical environment to be simulated. One of these studies used the data obtained to create mock-artery models that separately recreated the compression and bending experienced by peripheral arteries [Nikanorov *et al.* 2008]. This allows the stents to be investigated, and the number of fractured stents to be determined. In the same way, use of the angiographic data can be used to create finite element models of the stented peripheral arteries. While the *in vitro* models provide useful information on the likelihood of fatigue, they are limited to the use of mock arteries, and provide little information on stents which do not fail, or the interaction of the stent and artery.

1.6 Aims of the thesis

The objective of this thesis is to determine why rates of restenosis are higher following stenting of peripheral arteries compared to coronary arteries. The underlying hypothesis of the thesis is that the mechanical environment within peripheral arteries is the dominant factor in promoting such high levels of restenosis. Comprehensively addressing this hypothesis requires a number of studies to be undertaken. Firstly, the mechanical properties of arteries from different anatomical locations are to be investigated. Specifically, the coronary and femoral arteries and aorta of young swine are used. These properties are to be compared with the biochemical composition, in this case collagen and elastin content, of the arteries. Appropriate material models will be used to describe the material behaviour of the arteries tested, with the objective of implementing these models into commercial finite element software. It is also intended to relate the composition of the artery, in particularly the proportion of collagen and elastin, to the constants in the material models.

Ideally, human arterial tissue would be used for biomechanical and pre-clinical studies. Realistically, although studies have been carried out on human tissue, in many cases it is unavailable for ethical or other reasons. Even when human arteries are available, tests may be carried out some time post-mortem, and the tissue is often treated with antibiotics to make it safe. In many cases (such as these studies), only animal arteries are available for testing. The pig is the most commonly used pre-clinical animal model for the evaluation of new stent designs. To understand the implications of this for interpreting the results of animal trials, the differences between stenting in human and porcine arteries will be investigated by modelling stent expansion in each of them. The results from tests on porcine arteries will be first compared with similar tests on human arteries from the literature. These in turn can be used as material inputs for stenting models. Finite element models will then be used to investigate why the outcomes of stenting trials in pigs are often different to that observed in man.

Once an appropriate means of modelling stenting has been established, this information will be used to undertake a thorough investigation of the differences between stenting in coronary and peripheral arteries. This study will focus on differences in the arteries (geometry and material properties) and stents (geometry and stent type). Artery stresses and possible stent fatigue from the radial displacement caused by the pulse of blood flow will be investigated.

Differences in material properties and geometry are one of the possible causes of high rates of restenosis. The other one is the mechanical environment. The last objective of this thesis is to

look at the consequences of the bending and compression seen in peripheral arteries following stent deployment.

Ultimately, it is hoped that by appropriate modelling, the reasons for higher rates of restenosis can be better understood. By doing this, a useful tool may be developed which both help to understand the reasons for the high rates of restenosis in peripheral arteries and to provide a method for improving stent design for use in this environment.

2 Literature Review

Contents

2.1 Introduction 11

2.2 Blood Vessels 11

2.2.1 The cardiovascular system 11

2.2.2 Composition and structure 11

2.2.3 Peripheral vessels 14

2.3 Atherosclerosis 15

2.3.1 Peripheral Arterial Disease 16

2.4 Injury Response and Restenosis 17

2.4.1 Role of the Endothelium 19

2.5 Angioplasty and Stenting 20

2.5.1 Coronary stents 21

2.5.2 Stent Design 22

2.5.3 Peripheral stents 23

2.6 Nitinol 29

2.6.1 Phase Transformations 30

2.6.2 Shape-Memory 31

2.6.3 Superelasticity 32

2.6.3.1 Stress-Strain Behaviour 32

2.6.4 Material Models 33

2.6.5 Other Properties 36

2.7 Fatigue 36

2.7.1 Steel 37

2.7.2 Nitinol 38

2.8 Mechanical Properties of Arteries 38
2.8.1.1 Stress-Strain Behaviour 39
2.8.1.2 Incompressibility 41
2.8.1.3 Residual Stresses 41
2.9 Constitutive Modelling 42
2.9.1 Preliminaries 42
2.9.2 Material models for implementation in finite element software 45
2.9.2.1 Fung (2 models) 45
2.9.2.2 Mooney-Rivlin 47
2.9.2.3 Ogden 48
2.9.2.4 Gent 48
2.9.2.5 Holzapfel 49
2.9.2.6 Zulliger 50
2.10 Finite element analysis of stents 52
2.10.1 Expanding stents/balloon-stent interaction 52
2.10.2 Artery material models 58
2.10.3 Stent-artery interaction 59
2.10.4 SMA Stents 60
2.11 Conclusions 62

2.1 Introduction

This chapter gives a review of previous work carried out to investigate the behaviour and properties of stents and arteries. To begin a study on interventional cardiovascular devices, it is essential to have a complete understanding of the environments where they are placed. Therefore, this section begins with an overview of the properties of the cardiovascular system. An emphasis is placed on arteries, including their function, composition and later their mechanical behaviour. The issue of cardiovascular disease, and in particular atherosclerosis, is addressed. Restenosis, the re-closing of opened arteries and the main cause of failure in interventional procedures, is explained. Treatments for this disease, such as angioplasty and stenting, and the associated problems and complications are discussed. This includes discussion on the challenges of treating peripheral arterial disease. Finally, methods for appropriately modelling the stenting procedure are discussed, with sections on constitutive models to describe artery material behaviour, and the implementation of these models in finite element software.

2.2 Blood Vessels

2.2.1 The cardiovascular system

The cardiovascular system consists of a pump (the heart) and of pipes (blood vessels), the purpose of which is to transport a liquid (blood) around the body. Blood is a multi-purpose fluid, and its functions include transportation, regulation, defence and stabilisation. The components of this system are tightly coordinated in order to maintain appropriate blood flow to tissues and organs. For example, the cardiovascular system can respond to changes in blood pressure by regulating the vessel diameter as well as the heart rate.

Blood vessels are divided into efferent vessels, or arteries, which carry blood away from the heart, afferent vessels, or veins, which return blood to the heart, and capillaries, the microscopic vessels which connect the two and allow fluid exchange. Maintaining blood flow through these vessels is critical to the health of the tissues and organs they supply.

2.2.2 Composition and structure

The requirements, and thus anatomy, of blood vessels vary depending on location, local blood pressure, movement of surrounding tissue or muscle, function and species. The basic structure of

arteries and veins are similar, consisting of the intima (tunica intima), the media (tunica media) and the adventitia (tunica externa), see Figure 2.1. Arteries, which carry blood away from the heart, are under high pressure and as such are thick-walled vessels. Veins, which carry blood towards the heart, are under low pressure and are thin walled, with valves to prevent back flow of blood. Arteries usually maintain a relatively round shape, while veins are flatter. This review will focus on the structure of arteries.

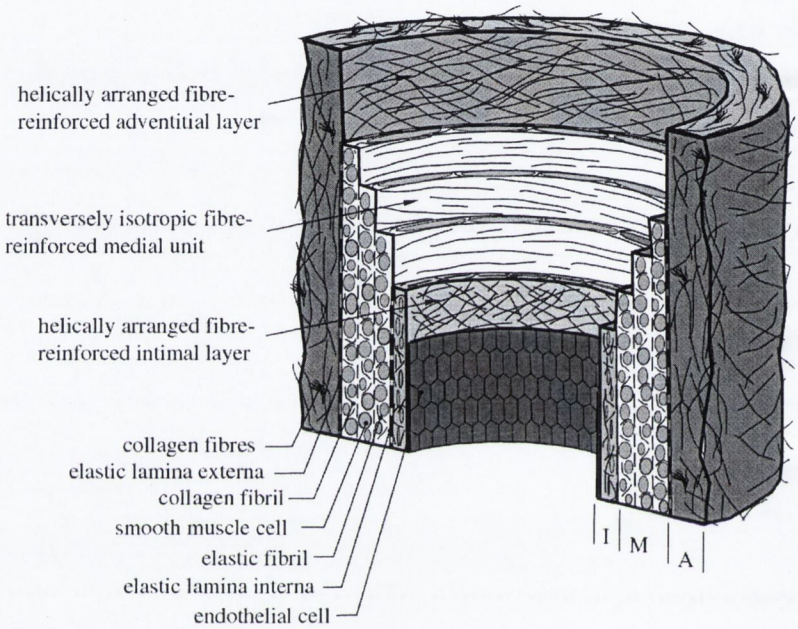


Figure 2.1

Composition of healthy artery showing three distinct layers (intima, media and adventitia) and fiber directions.

[Gasser et al. 2006].

The intima, the innermost layer of blood vessels, consists of an endothelial lining on top of a basil lamina and an internal elastic membrane (sometimes considered part of the media) that separates it from the media. The endothelial lining, over which blood flows, is rippled due to constriction of the vessel. In a straight vessel segment, the endothelial cells are aligned in the direction of the blood flow. These cells are important in regulating both vascular smooth muscle cell migration from the media, and neointimal formation as a response to injury [Kipshidze *et al.* 2004]. The cells communicate with the media using processes that link with the media using processes that extend through the basal lamina and internal elastic lamina [Humphrey 2002]. The basil lamina is made up of elastic fibres and lies between the endothelial lining and internal elastic

membrane, a collection of elastic fibres. In humans, the intima continually thickens with increasing age, even in healthy individuals [Velican *et al.* 1985], eventually becoming the stiffest layer in the artery [Holzapfel *et al.* 2005a].

The media, usually the thickest layer, consists of smooth muscle cells, and elastin and collagen fibres. The muscle tissue lies in discrete concentric layers called musculo-elastic fascicles, which are reinforced by fibres and separated by fenestrated windows of elastin, as shown in Figure 2.2 [Clark *et al.* 1985]. These muscle fibres control the diameter of the artery by contracting and relaxing. The size of the media is determined by the number of these fascicle units through the thickness of the wall, with the thickness of each unit nearly constant [Clark *et al.* 1985]. Collectively, the sheets of smooth muscle, the sheets of elastin and the collagen fibres are oriented in an almost circumferentially aligned helix [Holzapfel *et al.* 2000].

Surrounding the intima and media is the adventitia. Consisting of helically arranged bundles of collagen fibres in a matrix of histological ground substance, the outermost layer has a relatively low stiffness at within the physiological range of pressures. At higher pressures, recruitment of the collagen fibres causes a stiffening of the adventitia, which acts as a sheath to restrain the artery from high distension. The adventitia is connected to the media by the external elastic membrane, a band of elastic fibres.

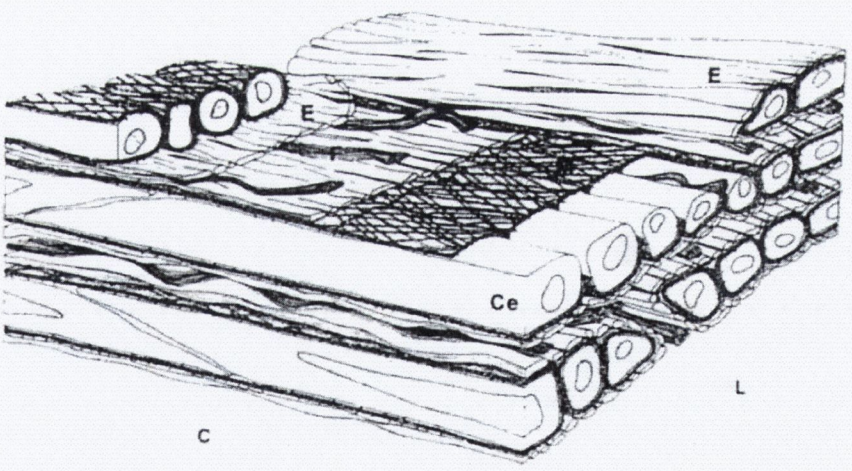


Figure 2.2

The musculo-elastic fascicle, as proposed by Clark and Glagov. A varying number of repeating layers of this unit make up the media in arteries. E = elastin, Ce = smooth muscle cells and F = collagen fiber bundles that exist between the elastin sheets.

[Clark et al. 1985]

2.2.3 Peripheral vessels

As well as the differences between arteries and veins, there are further variations in material properties and geometry in arteries that are functions primarily of the distance from the heart. Conducting, or elastic arteries (Figure 2.3, top), are generally in or near the heart, for example the aorta and pulmonary arteries. These arteries have a lot of elastic fibres, which allow them to function with fluctuations in pressure caused by the heartbeat by damping the pressure peaks. These fluctuations are greater in magnitude closer to the heart, and virtually disappear by the time blood reaches the capillaries. Most arteries in the human body are distribution, or muscular arteries (Figure 2.3, bottom). These arteries have more smooth muscle cells than elastic equivalents. The femoral and popliteal arteries are muscular arteries. While it may be convenient to subdivide arteries into two classes, in reality artery properties change continuously rather than discretely along the arterial tree.

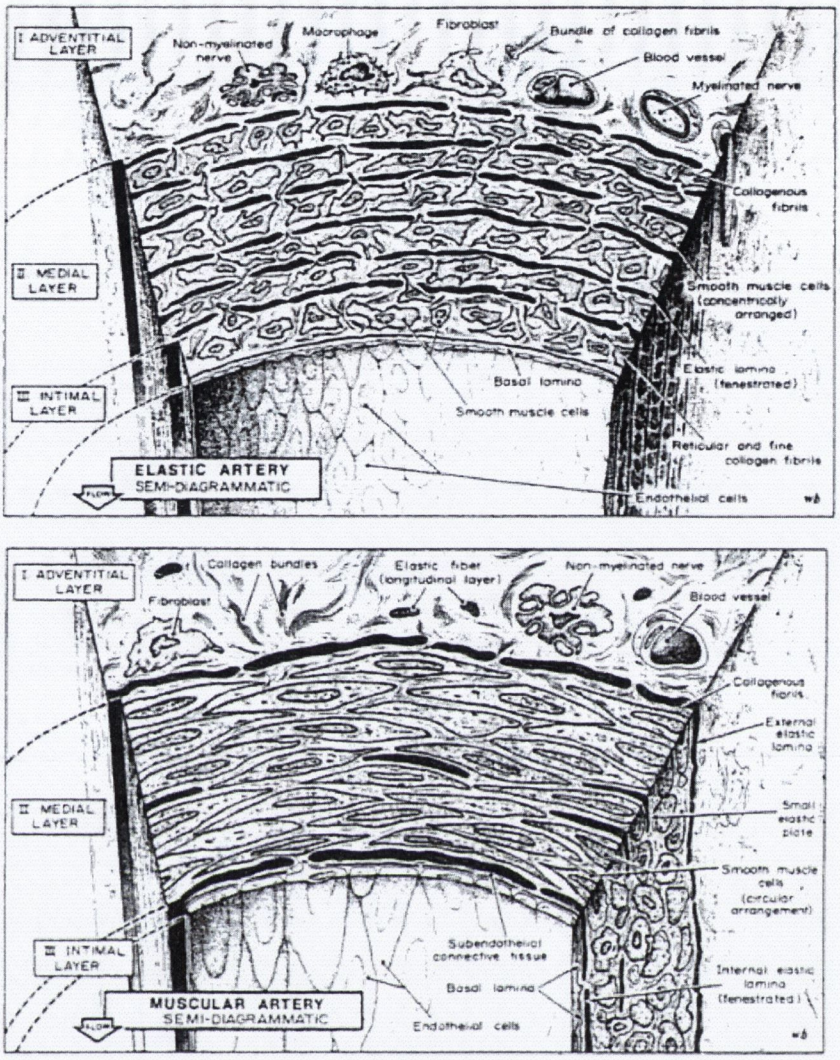


Figure 2.3

Cross sections of typical (top) elastic artery and (bottom) muscular artery.

[Berne et al. 1979].

2.3 Atherosclerosis

Atherosclerosis is a form of arteriosclerosis that is characterised by the formation of a plaque within, rather than on, the media of the artery [Libby 2002]. The disease is caused by excess low-density lipoprotein (LDL) in the blood stream. At normal concentrations, LDLs can pass through the endothelial lining, and move in and out of the intima. However, when the concentration becomes too high, the LDLs begin to accumulate within the intima. Over time, oxidation of the

LDLs causes the endothelial cells to display adhesion molecules, which cause monocytes to attach to the endothelial cells. The monocytes enter the intima, multiply and mature into macrophages. The macrophages then ingest the LDLs until they are packed with fatty droplets. These full macrophages are known as foam cells due to their appearance. These foam cells form a fatty streak, an early form of atherosclerosis. An inflammatory response then occurs to turn the fatty streak into a plaque. The macrophages, as well as endothelial and smooth muscle cells, produce chemicals that encourage smooth muscle cells in the media to migrate towards the outside of the intima, and replicate components of the extracellular matrix. These cells and the matrix combine to form a hard, tough fibrous cap above the foam cells. Once the cap is in place, some of these foam cells die, releasing the lipids which they originally ingested and forming a lipid, or necrotic, core [Libby 2002].

Stenosis occurs when this plaque grows inwards and impedes the blood flow. When extra blood is required in specific tissues, for example during exercise, adequate supply may not be pumped through a stenosed vessel. This can lead to angina or intermittent claudication. However, most of the growth of the plaque is radially outwards, which in itself will not lead to complications such as heart attacks or strokes. The danger is when the cap, weakened and thinned by inflammation, bursts. This allows blood to pass through a space in the cap, where the proteins in the lipid contribute to clot, or thrombus, formation. The plaque also releases chemicals that counter the materials produced by the body to stop clot formation. If the healing process removes the thrombus, the cap will be restored but the plaque will be larger than before rupture. It may take one or multiple clot-repair cycles, but the thrombus may eventually be large enough to completely occlude the flow of blood through the artery. This can lead to a heart attack or stroke [Libby 2002].

2.3.1 Peripheral Arterial Disease

Peripheral arterial disease (PAD) is similar to CVD, in that it is characterised by the occlusion of an artery with fatty plaques, except it occurs in vessels other than coronary and intracranial vessels. Often though, the term PAD is used to describe symptoms affecting arteries in the legs, i.e. the illiac artery and those distal to it. The pathophysiology of PAD is the same as atherogenesis in the coronary arteries [Ouriel 2001], as described above. PAD is diagnosed by measuring the ankle-brachial index (ABI), or the ratio of the blood pressure at the malleolar level by the higher of the two brachial pressures, of less than 0.95 [Ouriel 2001]. Although 18 % of over 65s have PAD [Ouriel 2001], most patients are asymptomatic [Meijer *et al.* 1998]. There is also a strong correlation between PAD and atherosclerosis in other arterial beds. In one study, 90 % of patients undergoing peripheral vascular study also had some degree of coronary atherosclerosis [Hertzer

et al. 1984], while 15.2 % of patients with coronary arterial disease and 7.1 % of patients with cerebrovascular arterial disease also had PAD [1996].

More than half of PAD cases include occlusions in the superficial femoral artery (SFA) [Jaff 2004]. The possible reasons for this include the vessel being one of the longest in the body, the presence of flexion points [Diaz *et al.* 2004], and the lack of collateral vessels to diffuse the disease.

2.4 Injury Response and Restenosis

Both PTA and stent insertion (see Angioplasty and Stenting) cause injury and damage to the arterial wall by inducing stresses and strains beyond normal physiological loading. With PTA, the injury is caused primarily by circumferential stretching of the artery. Stenting causes circumferential stretch too, but also induces injury when stent struts penetrate the artery wall. Depending on the extent of the injury, the artery experiences endothelial damage, fracture of the internal elastic lamina, dissection of the media, and, in severe cases, damage to the adventitia.

The response of the vessel to these injuries is critical in determining the success of the intervention. Restenosis, or the re-narrowing of the vessel wall following PTA or stenting, is the major limitation of both procedures. Although exact definitions vary, often dependant on the method of detection, restenosis is generally taken to mean the loss of lumen gain. Binary restenosis is defined more specifically, with a variety of definitions; an increase of ≥ 30% from the post-angioplasty follow-up, ≥ 70% stenosis of target vessel at follow-up, or stenosis severity ≤ 10% below pre-dilated lesion severity are some of those used. The most common definition is the loss of 50% or greater of the lumen gain. Following PTA, restenosis manifests as tissue growth within the lumen and elastic recoil of the vessel. Stents eliminate vessel recoil, and therefore restenosis following stenting is a result of new tissue formation.

Although the outcomes are similar, restenosis and atherosclerosis are distinct processes. They differ in the histopathology, temporal courses and stimulae [Schwartz *et al.* 1994]. Atherosclerosis is caused by chemical injury to the vessel wall, whereas restenosis is stimulated by the mechanical injury induced by PTA and/or stenting.

"..the pathophysiology of restenosis is a separate process from atherosclerosis. It follows an entirely different time course, has different histopathology, and comes from mechanical rather than biochemical injury in the arterial wall." [Schwartz *et al.* 1994]

The phases of the response to PTA or stenting have been identified as inflammation, proliferation and remodelling [Forrester *et al.* 1991]. An initial thrombus phase has also been included by Edelman and Rogers [Edelman *et al.* 1998]. This is similar to dermal wound healing, the responses of which are also characterised by inflammatory, proliferative and remodelling phases. These phases occur within different time frames and are, to a degree, independent.

Thrombus deposition occurs in the short term (1-3 days) following stent deployment. The amount of thrombus deposition is dependent on the extent of the injury. Although the use of antithrombotic drugs has reduce the incidence of catastrophic thromboses to less than 1%, a degree of thrombus formation is evident following all stent placements. However, reducing thrombosis has no effect on subsequent events [Rogers *et al.* 1993; Rogers *et al.* 1997].

Inflammation occurs at the site of thrombus formation, either at the stent struts or between them. During this phase, surface adherent monocytes (SAMs) are recruited to the injury site. After 3-7 days, these cells migrate to the neointima and are known as tissue-infiltrating monocytes (TIMs) [Edelman *et al.* 1998]. The neo-intima is mostly formed from extracellular matrix and smooth muscle cells.

The intimal cell proliferation phase occurs when inflammatory cells migrate from the artery surface to the neointima about seven days after the procedure. Both smooth muscle cells and monocytes proliferate during this phase. There is a strong linear relationship between the number of monocytes and the intimal cell proliferation [Edelman *et al.* 1998].

The fourth phase, remodelling, consists of elastic recoil and extracellular matrix protein deposition. Elastic recoil is entirely mechanical, and occurs immediately following angioplasty. The use of stents largely eliminates this part of remodelling, though tissue may still recoil through cells in the stent, known as prolapse. During remodelling, elastin is destroyed, and collagen is deposited, altering the collagen to elastin ratio, and thus the mechanical properties.

The magnitude of the response to injury is dependent on the extent of the injury [Schwartz *et al.* 1994]. Using an injury score to describe the extent of the injury to the artery (Table 2.1) shows a good correlation between the injury score and the thickness of neointimal growth, see Figure 2.4 (a) &(b) [Schwartz *et al.* 1994].

Weight of injury	Injury
0	Internal elastic lamina intact; endothelium typically denuded; media may be compressed but not lacerated
1	Internal elastic lamina lacerated; media typically compressed, but not lacerated
2	Internal elastic lacerated; media visibly lacerated. External elastic lamina intact, but may be compressed.
3	External elastic lamina lacerated; typically large lacerations of media extending through the external elastic lamina.

Table 2.1

Classification of injury scores. After Schwartz and Holmes [Schwartz et al. 1994].

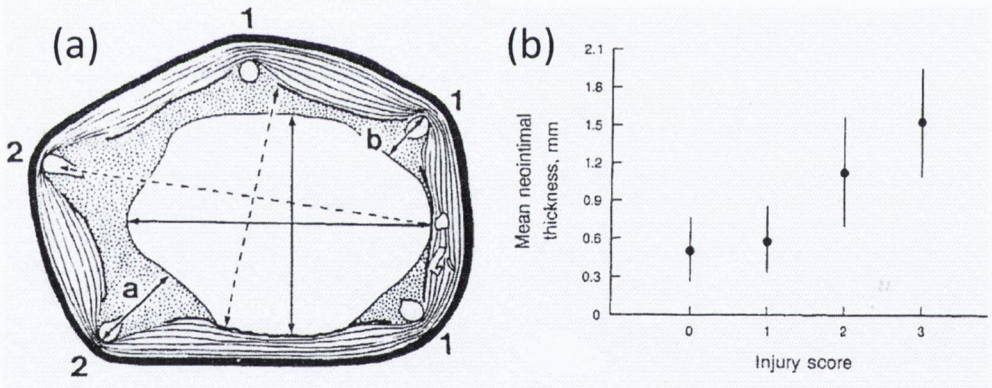


Figure 2.4

(a) Classification of injury scores at different points on cross-section of a stented artery

(b) Correlation between injury score and neointimal growth for stented porcine arteries

[Schwartz et al. 1994]

2.4.1 Role of the Endothelium

The endothelium, the layer of cells that lines the artery wall, is important for regulation of arteries rather than its mechanical properties. Endothelial cells modulate hemostasis and provide a barrier between the smooth muscle cells (SMCs) in the media and growth-promoting factors in the blood stream. Denuding the endothelium, which occurs to various degrees with interventional

procedures, causes neointimal thickening, a cause of restenosis. Re-endothelialisation can occur, the amount of which depends on the extent of the injury [Kipshidze *et al.* 2004]. This can help prevent the migration of SMCs, which appear only in areas where re-endothelialisation has not occurred [Haudenschild *et al.* 1979].

2.5 Angioplasty and Stenting

Blood flow through stenosed arteries can be restored by percutaneous transluminal coronary angioplasty (PTCA). This is an interventional procedure whereby a polymer balloon is inserted to the site of the blockage on the end of a catheter. Pressurised saline is then used to inflate the balloon which, by compressing the plaque against the artery wall and stretching the artery, restores blood flow (see Figure 2.5). The balloon is then deflated and withdrawn from the artery. Over 600,000 such procedures were carried out in the USA in 2006, with roughly the same number again with stents [Lloyd-Jones *et al.* 2009]. While immediate patency is restored in up to 90% of cases [Bredlau *et al.* 1985; Perry *et al.* 1988] and morbidity and mortality rates are very low [Bredlau *et al.* 1985], elastic recoil of the artery and of the plaque can re-occlude the vessel and restrict blood flow again in about 30 % of cases after 6 months in coronary arteries [Leimgruber *et al.* 1986; Gruentzig *et al.* 1987]. This necessitated the use of a better long term solution for keeping vessels open.

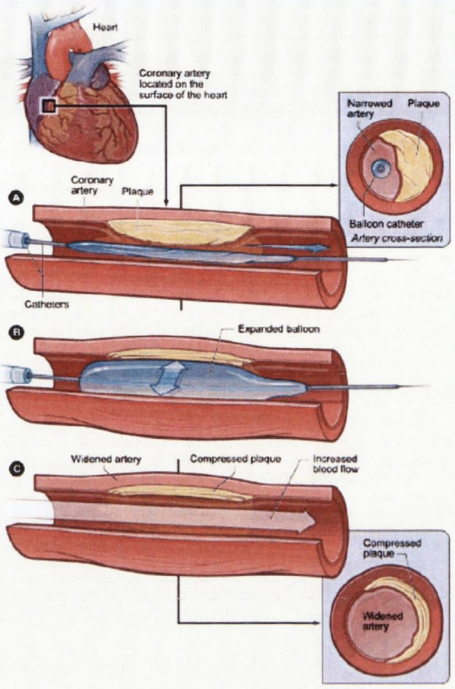


Figure 2.5

Balloon angioplasty.

http://www.nhlbi.nih.gov/health/dci/images/angio_lowres.gif

2.5.1 Coronary stents

Stents are tubular, usually metal structures that are inserted into and expanded in arteries to maintain the lumen gain achieved with PTCA. Balloon expandable stents are crimped onto a polymer balloon to fit inside the artery. It is expanded at the site of the blockage by inflating the balloon. This plastically deforms the stent, which remains when the balloon is withdrawn and acts as a scaffold to prevent elastic recoil of the artery. The success of the stenting procedure is determined by the vessel patency (whether or not blood flows past the blockage), binary restenosis (the loss of 50 % of the lumen gain) and major coronary events (myocardial infarction, stroke, death, etc.). Early trials with a Palmaz-Schatz stent showed improved outcomes compared with angioplasty alone after seven months, though higher risks of vascular complications were also seen [Serruys *et al.* 1994].

Continued optimisation of the design of these stents, as well as the introduction of drug eluting stents (DES) has seen a reduction in restenosis rates from 36 % after 6 months with early bare metal designs [Ellis *et al.* 1992], to 21.3 % and 9.3 % after 1 year for patients with acute

myocardial infarction using bare metal and DE stents respectively [Menichelli *et al.* 2007]. However, problems with late-stent thrombosis, caused by a delayed re-endothelialisation, have been reported with DESs [Pfisterer 2008]. Although rare, such occurrences have high mortality rates.

2.5.2 Stent Design

The first stent was inserted into a human patient by Jacques Puel and Ulrich Sigwart in 1986. Since then, hundreds of stent designs have been patented [Serruys *et al.* 2000; Serruys *et al.* 2005]. One of the most important of these was the Palmaz-Schatz coronary stent (Figure 2.6). This was developed by an Argentinean cardiologist and a retired German rocketeer, and received FDA approval in 1994. The success of this model heralded the beginning of stenting as a viable method of maintaining vessel patency following angioplasty. Subsequent stent designs have attempted to achieve an optimal balance of strength, flexibility, trackability, and low injury to the artery. It has been shown in finite element models [Bedoya *et al.* 2006] and clinical studies [Garasic *et al.* 2000; Kastrati *et al.* 2001] that stent design influences clinical outcome. The influence of some aspects of stent design, such as percentage metal coverage, strut thickness and width, number of struts and strut cross sectional area, are summarised by Morton *et al* [Morton *et al.* 2004].

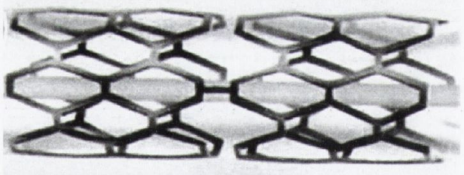


Figure 2.6

Palmaz-Schatz Coronary Stent.

[Bonsignore 2004].

Although there are many stent designs, most are based around the same fundamental principals; expandable ring elements joined by connecting elements, or bridges. Connecting elements are attached to the expandable rings at the peak, valley, or midstrut. Some combinations of this are shown in Figure 2.7. Almost all stent designs are variations on one of these configurations, including stents for use in non-coronary arteries. The notable exception of this is coil stents, which were used early on but lacked sufficient radial strength and scaffolding capability to be successful. Stents can also be defined as open cell or closed cell. Closed cell stents, such as the Palmaz stent (Figure 2.6), have all of the internal inflection points connected peak to peak with a connecting

element. For example, Figure 2.7(a) shows a closed cell design, while Figure 2.7(c), where only every second inflection point is connected, is classified as open cell. Closed cell designs are seldom used anymore because they are inherently inflexible.

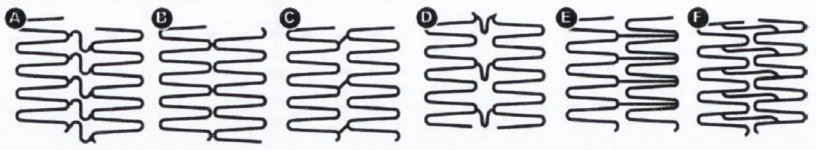


Figure 2.7

Different ways of constructing a stent from expandable rings and connecting elements. (a) closed cell, peak to peak, flex connector. (b) open cell, non-flex connector, peak to peak. (c) open cell, non-flex connector, peak to peak. (d) open cell, flex connector, peak to peak. (e) open cell, non-flex connector, peak to valley. (f) open cell, non-flex connector, midstrut.

[Bonsignore 2004]

2.5.3 Peripheral stents

As PAD is similar to CVD, so peripheral stents are, in many aspects, very similar to coronary stents. The principal of inserting a metal tube to hold the artery open and restore blood flow is the same, and many of the problems and challenges of stenting are associated with both types of vessel. However, despite the similarity of the procedures, the generally successful outcomes of coronary stenting have not been replicated in peripheral arteries. The earliest stents used in peripheral arteries were stainless steel balloon expanded stents, like those used in coronary arteries except with different dimensions. For example, Palmaz stents, one of the earliest designs, were used in femoropopliteal segments and the results compared with PTA alone. Despite greater initial technical success with stenting compared with PTA alone, the improvement diminished with time and the primary angiographic patency rates were identical at 63% and 53% after one and two years respectively [Cejna *et al.* 2001].

The poor results seen with stainless steel balloon expanded stents necessitated a new approach towards lesions in peripheral arteries. This resulted in the development of stents manufactured from more flexible shape memory alloys (SMAs), in particular nitinol (see section 2.6 Nitinol). Nitinol stents, unlike stainless steel models, have shown an improvement in success rates compared with PTA. Early trials showed little improvement in using Wallstents compared with PTA alone after 12 months, but suggested stenting as an option when angioplasty fails [Do *et al.*

1992]. Similar results were presented in another study for the Wallstent, where primary clinical patency was 61% at one year and 49% at two years [Martin *et al.* 1995]. Some improvement was seen with the Smart stent, where primary patency rates were 92%, 76%, 66% and 60% at 6, 12, 18 and 24 months respectively [Mewissen 2004]. A more recent random clinical trial comparing the two procedures found lower rates of restenosis for patients treated with nitinol stents compared to those treated with angioplasty alone [Schillinger *et al.* 2006]. Unlike other lesions, using DESs did not provide a significant improvement compared with bare metal stents [Duda *et al.* 2005; Duda *et al.* 2006].

Peripheral stent designs are, on the whole, very similar to coronary stents (Figure 2.8), and this lack of variation in design philosophy may account for their relative failure in a different environment. A recent stent design, the Bard Lifestent, which organises the connectors in a spiral pattern, has received full FDA approval for use in the SFA. Such designs, specific to peripheral arteries, may lead to future success in stent design.

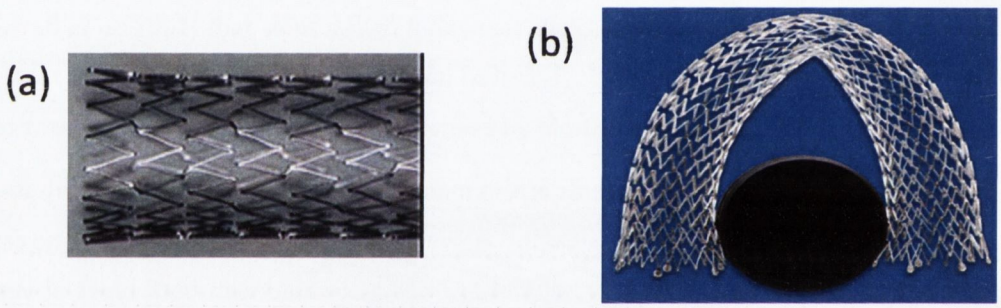


Figure 2.8

(a) Nitinol Smart stent, a typical peripheral stent design.

(b) Smart stent showing high flexibility

www.clevelandclinic.org/heartcenter/images/guide/disease/vascular/stent_smart.jpg

http://www.abbottvascular.com/en_US/content/image/absolute7_lg.jpg

Despite the move to SMA stents, restenosis rates in peripheral arteries, particularly the femoral and popliteal, do not compare favourably with coronary arteries. Although the reasons for this are not fully understood, there are a number of differences between coronary and peripheral arteries that may provide explanations for the results seen in *in vivo* trials. The first difference between the two is size. Peripheral arteries, in general, have larger diameters and thicknesses than coronary arteries. A comparison of sizes in coronary arteries showed higher restenosis rates in smaller arteries [de Feyter *et al.* 1999; Stone *et al.* 2004]. This indicates that, taken independently,

diameter may not adversely affect restenosis rates in arteries, and that the greater diameter of peripheral arteries may not be responsible for higher rates of restenosis. However, the influence of thickness on these studies is not clear. Also, as restenosis is calculated relative to the diameter of the artery, the same neointimal growth provides greater loss of lumen in a small artery than in a large one.

A second difference between the arteries is the composition. Arteries, depending on location on the arterial tree and function, have different ratios of the extracellular components (elastin, collagen and smooth muscle), resulting in different mechanical behaviour [Fung 1993]. Comparison of uniaxial tests on human coronary [Holzapfel *et al.* 2005a] and iliac [Schulze-Bauer *et al.* 2003] arteries shows that these differences include the stress-strain behaviour of all three layers (intima, media and adventitia), the residual stresses, the degree of anisotropy (caused by the fiber orientation), and the relative thickness of the layers. The difference in relative thickness of the layers includes a contribution from the variation in the intimal thickening, which appears to be more significant in the coronary artery [Holzapfel *et al.* 2005a].

The third difference between the artery types is the mechanical environment into which they are implanted. Stents placed in any type of artery experience dynamic environments which vary according to location. Coronary arteries, for example, are attached to the myocardium, and experience motion with each cardiac cycle. The displacements and deformations have been monitored and recorded in a number of studies [Ding *et al.* 2000b; Ding *et al.* 2000a; Ding *et al.* 2002]. This information is generally analysed with respect to the effect on the hemodynamics on the post-stenting environment [Ding *et al.* 2000b; Ding *et al.* 2000a; Weydahl *et al.* 2001; Ding *et al.* 2002; Zeng *et al.* 2003]. The influence of this environment on arterial stresses and the fatigue cycle it imposes on an implanted stent are unknown. However, though coronary stent fracture is potentially serious and may increase rates of restenosis, it is quite rare [Aoki *et al.* 2007; Kim *et al.* 2009].

The mechanical environments experienced by peripheral arteries and stents implanted in them can be broadly divided into pulsatile and flexion driven. The pulsatile environment, common to all arteries, is caused by the pressure change during the cardiac cycle, which causes the artery to increase and decrease in diameter. This induces a high frequency, low amplitude, strain based fatigue cycle. It should be noted that some nitinol stents placed in the SFA are biliary-indicated. They are, therefore, not tested for fatigue suitability for placement in peripheral arteries, and are not cleared by the FDA for such purposes. In fact, only one stent, the Bard Lifestent, has FDA approval for use in the SFA.

Some peripheral arteries are also subject to more complicated loadings, caused by joint flexion. For example, knee flexion has been shown to occlude blood flow in the popliteal arteries, even in patients who do not exhibit PAD [Hoffmann *et al.* 1997]. The mechanical environment was further quantified by Duda *et al*, who identified the presence of 'hinge points' [Duda *et al.* 2002]. This has been defined as 'the first curve in the peripheral artery in an acute angle towards the femur that appeared during knee flexion' by Diaz *et al* [Diaz *et al.* 2004]. The same study expanded on earlier work by specifying the location of hinge points in unstented popliteal arteries of patients with PAD, and relating their formation to knee flexions of up to 100° [Diaz *et al.* 2004]. Accessory flexions, or curves in the artery other than the hinge point, were also classified, as shown in Figure 2.9. A series of articles in 'Endovascular Today', published in 2004, focused on the superficial femoral artery (SFA). One of these studies listed, but did not quantatively measure, the forces acting on the SFA [Jaff 2004]. These forces were (axial) extension and contraction, torsion, compression and flexion. At about the same time, the extreme mechanical environment of the popliteal artery was identified as the cause of biomechanical incompatibility of popliteal stents [Kroger *et al.* 2004]. This study used a number of case studies to show bending, narrowing, compression, shortening, twisting and even destruction of implanted stents. A number of other case studies also showed stent fracture [Babalik *et al.* 2003; Solis *et al.* 2006]. It became clear, therefore, that a more formal quantification of these deformations was required in order to produce stents that are capable of performing in peripheral arteries [Smouse *et al.* 2005].

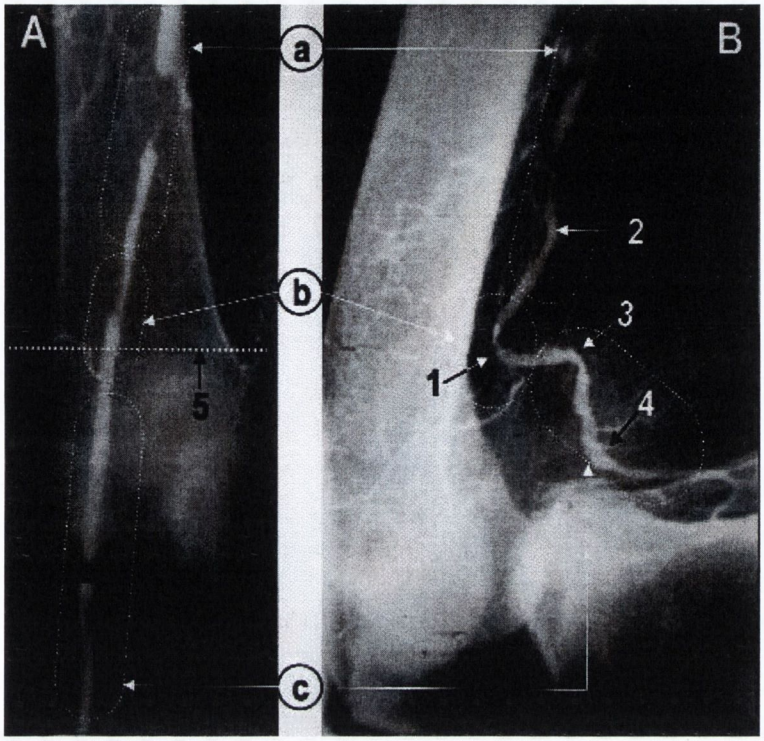


Figure 2.9

Angiographies of (A) knee extension and (B) knee flexion. Point 1 is a hinge point, points 2, 3 and 4 are accessory flexions. The artery is divided into (a) pre-hinge point segment, (b) hinge point zone, and (c) post-hinge point segment.

[Diaz et al. 2004]

A study comparing MR angiographies of unstented SFAs from healthy patients in the supine and fetal positions quantified the twisting and stretch of the artery [Cheng *et al.* 2006]. It showed that the SFA shortened by 13% ± 11% and twisted 2.8 ± 1.7°/cm. A similar study comparing radiographs of stented mid, distal and proximal SFAs and popliteal arteries with knee/hip flexions of 0°/0°, 70°/20° and 90°/90° [Nikanorov *et al.* 2008]. These angles correspond to typical values seen in standing, walking and sitting, as shown in Figure 2.10. The compression of the SFA was found to be comparable to the study by Cheng *et al* [Cheng *et al.* 2006], but lower when a stent was inserted, see Table 2.2. Bending was also measured, with maximums of 33° ± 21° and 54° ± 25° at 70°/20° and 90°/90° respectively found in the popliteal artery, see Table 2.3.

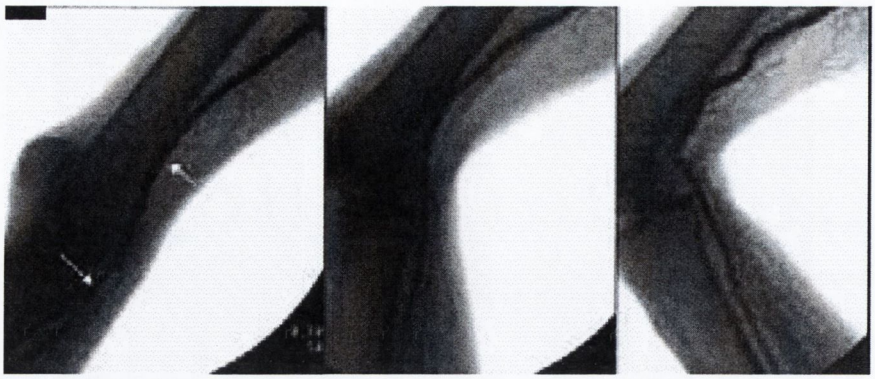


Figure 2.10

Bending of femoropopliteal arterial segment at knee/hip flexion angles of (a) 0°/0°, (b) 70°/20° and (c) 90°/90°.

[Smouse et al. 2005].

Peripheral arteries in the leg are not unique in being subject to external loading which could be problematic for stent placement. Studies on the carotid artery, where plaques often form at or close to the bifurcation, have shown similarities to peripheral arteries in the leg. It has been shown that swallowing, and particularly neck motion cause radial and axial strains as well as crushing [Robertson *et al.* 2008].

Position	Mid-SFA Arteries/Stents	Distal-SFA/Prox-PA Arteries/Stents	Pop Arteries/Stents
Neutral, %	0	0	0
Knee/hip flexion			
70°/20°, %	5% ± 4%/3% ± 4%	14% ± 5%/11% ± 12%	3% ± 4%/33 %± 21%
90°/90°, %	9% ± 5%/4% ± 3%	23% ± 2%/15% ± 14%	14% ± 3%/54% ± 25%

Table 2.2

Axial compression of cadaveric lower extremity unstented arteries (Arteries) and 100 mm self expanding nitinol stents when placed in cadaveric lower-extremity arteries (Stents). Adapted from [Nikanorov et al. 2008].

Position	Mid-SFA	Distal-SFA/Prox-PA	Pop
Knee/hip flexion			
70°/20°	3° ± 4°	11° ± 12°	33° ± 21°
90°/90°	4° ± 3°	15° ± 14°	54° ± 25°

Table 2.3

Bending deformation of 100 mm self expanding nitinol stents when placed in cadaveric lower extremity arteries. Adapted from [Nikanorov et al. 2008].

The response of arteries varies with the type of stent inserted. For the same target diameter, nitinol stents give a lower lumen gain than stainless steel balloon expandable stents [Grenacher *et al.* 2006]. This is due to the higher compliance of nitinol, and also to the fact that balloon expansion allows a greater degree of control over the final diameter achieved by the stent. There are also differences in the endothelial injury caused by PTA, balloon expanded stents and self-expanding stents. Use of PTA and balloon expanded stents causes almost complete endothelial denudation, while up to 50% of the cells may be preserved by using a self-expanding stent [Harnek *et al.* 1999]. This may explain why pre-dilation, where a PTA is carried out prior to insertion of a nitinol stent to achieve a greater lumen diameter, increases the rate of restenosis [Harnek *et al.* 2002].

2.6 Nitinol

Shape memory alloys (SMAs) are highly flexible metal composites that are gaining poplularity for many engineering applications, particularly in bio-medical devices. One of the most commonly used SMAs is nitinol, the name of which derives from the metals that are used to make it (nickel, NI and titanium, TI), and the institute where it was researched (Naval Ordinance Laboratory, NOL). Nitinol is typically composed of nickel and titanium in an approximately 50:50 ratio. This review will focus on Nitinol as an example of an SMA, as it is the material most used in the design of shape-memory peripheral stents.

Shape memory alloys are characterised by their shape memory and super-elasticity, properties that are not found in normal engineering materials. Both of these properties are a result of temperature and stress induced first order phase transformations and are described in further detail below.

2.6.1 Phase Transformations

Nitinol consists of two phases, austentite, the parent phase, and martensite, the daughter phase. The transformation from one phase to another is instantaneous, and occurs when sufficient stress or temperature changes are induced. For example, the martensite phase occurs when the temperature is low enough (the martensite start temperature, M_s) or the stress is high enough to form stress induced martensite (SIM). The temperature and stress transformations are not independent, though. If the temperature is reduced to below the martensite finish temperature (M_f), then raising the stress will not cause phase transformation and the material remains stable. Similarly, if the temperature exceeds the martensite deformation temperature (M_d), then plastic deformation of the austentite will occur at lower energies than SIM. Stress induced phase transformations can only occur between the austentite finish temperature (A_f) and M_d, see Figure 2.11. In some medical devices, the temperature dependant properties of nitinol are important, as they are cooled to fit inside the body, then heat up and resume their designated shape. Such an approach was once used with nitinol stents.

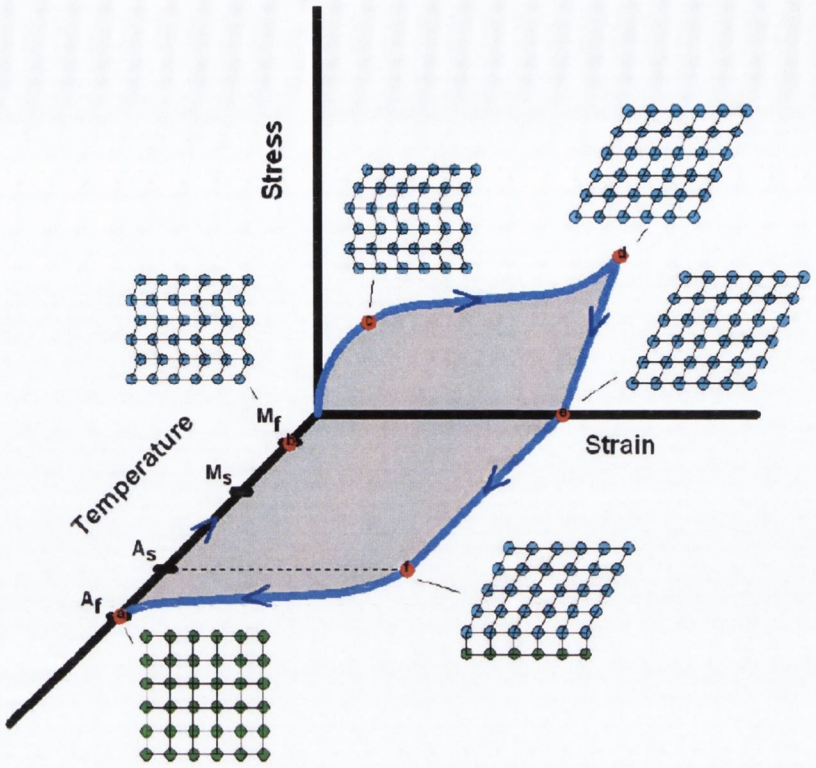


Figure 2.11

Shape memory properties of Nitinol. Above A_f (point a), the material is fully austentite (cubic structure). As the temperature is reduced to below M_f, a phase transformation to twinned martensite (monoclinic B19 structure) occurs. When the material is stressed, detwinning begins (c) until full detwinning (d). When the material is unloaded, elastic recovery begins, but phase transformation is not complete until temperature is raised to A_f again.

[Robertson 2006]

2.6.2 Shape-Memory

Shape memory is the ability of a material to 'remember' a set shape and to return to this configuration following deformation. Shape memory can be useful for biomedical components. Chilling a device prior to implantation means that it can be crimped into a shape more amenable towards placement. When the body heats the device up, the shape memory effect causes it to return to its original shape. An example of this is the Simon vena cava filter, which is cooled to below M_f, collapsed and inserted into position in the heart [Simon *et al.* 1977; Duerig 1990]. Once in place, it is heated to above A_f (usually about 30°) and expands to the initial configuration. Similar principals were once applied to stents to fit them into arteries.

2.6.3 Superelasticity

One of the most useful aspects of nitinol is its superelasticity. This is the ability of the material to experience very large yet recoverable strains. Nitinol can be stretched by up to 11% without experiencing permanent deformation. This is significantly higher than stainless steel, which plastically deforms at strains of 0.3% [Duerig *et al.* 2000].

2.6.3.1 Stress-Strain Behaviour

The stress-strain curve of nitinol demonstrates the superelastic, non-linear and hysteresis properties of the material, see Figure 2.12. It is also influenced by phase transformations during loading and unloading. In the unstressed initial configuration, the material is entirely in the austenite phase. When the material is loaded, a linear response is seen between point A and point B. At point B, the slope changes and a plateau is seen. While the shape of the stress-strain curve is similar to that seen with, for example, steels, this response is not a result of yielding or plastic deformation. Rather, it marks the onset of the phase transformation, and the deformation is fully recoverable. Between point B and point C, the material begins to transform from austenite to martensite. At point C, the material is 100% martensite. As the load is further increased, the material stiffens again, and exhibits linear behaviour again until point D is reached. It should be noted that the slope of C-D is not necessarily the same as A-B, though this may be assumed to be the case to simplify implementation in computer models. When the material is unloaded, hysteresis is seen, i.e. the loading curve is different to the unloading curve. The unloading from point D-C is the same as the loading curve, but a lower stress must be reached before the phase transformation back to austenite begins, at point E. Between E and F, the material transforms back to austenite. At point F, when the transformation is complete, the material unloads back to its original, stress free state.

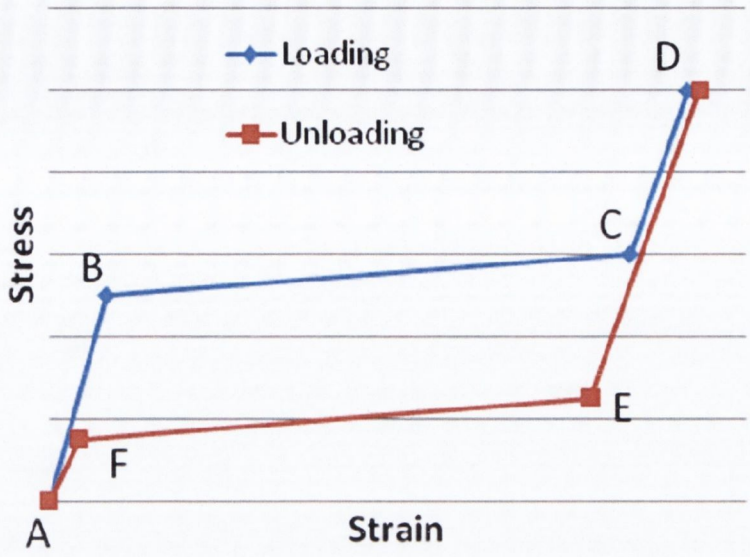


Figure 2.12

Representative stress-strain behaviour of nitinol in loading and unloading under uniaxial tension.

2.6.4 Material Models

Whilst linear materials can be modelled with a comprehensively with only a small number of parameter (Young's modulus, Poisson's ratio and shear modulus), and plastic materials with a further two (yield strength and tangent modulus) in finite element modelling, nitinol material models are by necessity more complicated. They must take account of the non-linear (or multi-linear), elastic nature of the elastic deformation, the phase change that occurs as a result of changes in temperature and/or stress, and the hysteresis between the loading and unloading curves. Some of the methods for modelling nitinol are discussed further in SMA Stents. This section will discuss a material model commonly utilised by commercially available finite element software packages.

The material model used in Marc/Mentat 2007 software (MSC Software Corporation, Santa Ana, California) is based on an algorithm by Auricchio *et al* [Auricchio 2001], and is similar to models used in other finite element packages. The tensile stresses to cause phase transformations are described below;

σ_s^{AS+}= starting tensile stress in austentite to martensite transformation

σ_f^{AS+}= finishing tensile stress in austentite to martensite transformation

σ_s^{SA+} = starting tensile stress in martensite to austentite transformation

σ_f^{SA+} = finishing tensile stress in martensite to austentite transformation

σ_s^{AS-} = starting compressive stress in austentite to martensite transformation

Nitinol behaves differently in tension and compression. This difference is accounted for with a scaling parameter α:

$$\alpha = \sqrt{\frac{2}{3}} \frac{\sigma_s^{AS-} - \sigma_s^{AS+}}{\sigma_s^{AS-} + \sigma_s^{AS+}} \qquad \textbf{(2. 1)}$$

If α is equal to zero, then the responses in tension and compression are the same. The Young's modulus given for the material represents the linear response of the austenitic phase (A-B on Figure 2.12). While a second Young's modulus value may be provided for the linear response of the martensitic phase (C-D on Figure 2.12), the two are usually assumed to be the same. Though not strictly accurate, this simplifies the implementation of the material model. A scalar parameter, ε_l is used to describe the maximum deformation obtainable only by detwinning of the multiple-variant martensite (i.e. the strain reached at the end of the austenite-martensite transformation). This usually has a value between 0 and 0.1. These parameters provide a simplified, but relatively accurate representation of nitinol material behaviour, see Figure 2.13.

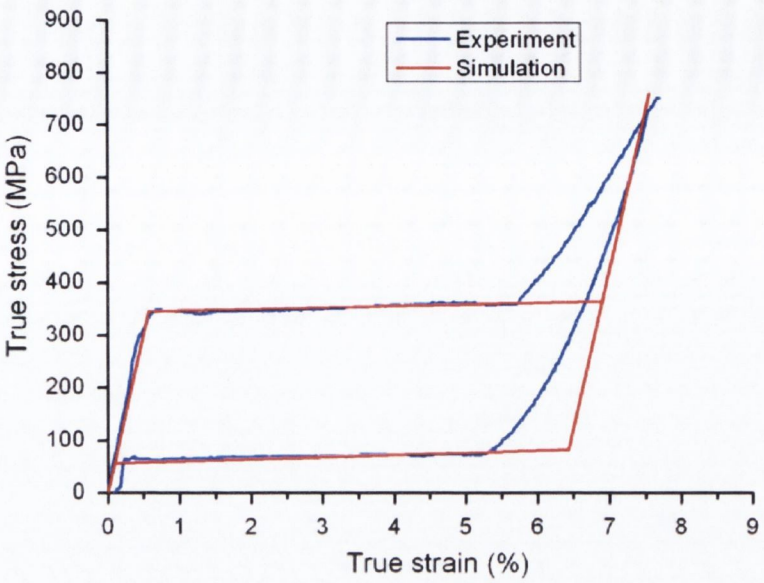


Figure 2.13

Material behaviour of nitinol under uniaxial tension. Blue line shows experimental data on Ti-50.8at%Ni thin wall tubes [Favier et al. 2006], red line shows simulation model used for finite element analysis.

[Wu et al. 2007a]

If a thermo-mechanical model is being used, more parameters are required to fully describe the material behaviour.

$$(\sigma_s^{AS+} = \sigma_0 + R) \quad \textbf{(2. 2)}$$

$$\sigma_0 = \langle \beta \cdot (T - T_0) \rangle \quad \textbf{(2. 3)}$$

σ_0 = mean value of plateaus (hysteresis)

where σ_0 is the mean value of plateaus (hysteresis) β is the slope, T is the current temperature and T_0 is a reference temperature equal to M_f, see Figure 2.14.

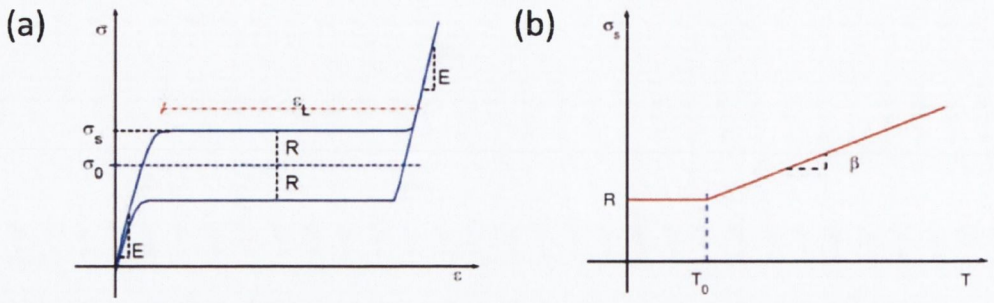


Figure 2.14

Mechanical and thermal behaviour of nitinol showing parameters used to describe constitutive behaviour. (Note:).

[Migliavacca et al. 2004]

2.6.5 Other Properties

As well as being extremely flexible, nitinol is also very biocompatible. It is less thrombogenic in blood than stainless steel [Thierry *et al.* 2002] and despite the high (~50%) nickel content, it releases it at a lesser rate than stainless steel, owing to the high energy bond formed with titanium [Chan *et al.* 1990]. Also, the instantaneous oxidation process that occurs on nitinol forms a similar TiO_2 layer as pure titanium [Bedoya *et al.* 2006]. Furthermore, the MRI compatibility of nitinol is superior to stainless steel, which has more artefacts, while x-ray densities are similar [Duerig *et al.* 2000].

2.7 Fatigue

Fatigue is a process whereby materials fail when subject to repeated loading cycles which induce loads below the ultimate tensile strength (and sometimes below the yield strength). When dealing with fatigue properties, the following terms are defined:

$$\Delta\sigma = \sigma_{max} - \sigma_{min} \quad \textbf{(2. 4)}$$

$$\sigma_m = \frac{\sigma_{max} + \sigma_{min}}{2} \quad \textbf{(2. 5)}$$

$$\sigma_a = \frac{\sigma_{max} - \sigma_{min}}{2} \quad \textbf{(2. 6)}$$

Where σ_{max} and σ_{min} are the maximum and minimum stresses experienced during the fatigue cycle, σ_m is the mean stress and σ_a is the average stress.

The methodology for predicting the fatigue behaviour of a stent depends on the material used, i.e. steel or nitinol.

2.7.1 Steel

For cyclic stresses where the mean stress, σ_m, is greater than zero, Goodman's rule is used to predict fatigue failure. Here, a straight line is drawn between the fatigue endurance strength (S_e) on the y-axis and the ultimate tensile strength (S_{ult}) on the x-axis Figure 2.15. Points above this line are predicted to fail by fatigue, and points below it are predicted to pass. Proximity to this line is used to calculate a factor of safety (FOS) as follows [Marrey *et al.* 2006]:

$$\frac{1}{FOS} = \frac{\sigma_m}{S_{ult}} + \frac{\sigma_a}{S_e} \quad \textbf{(2. 7)}$$

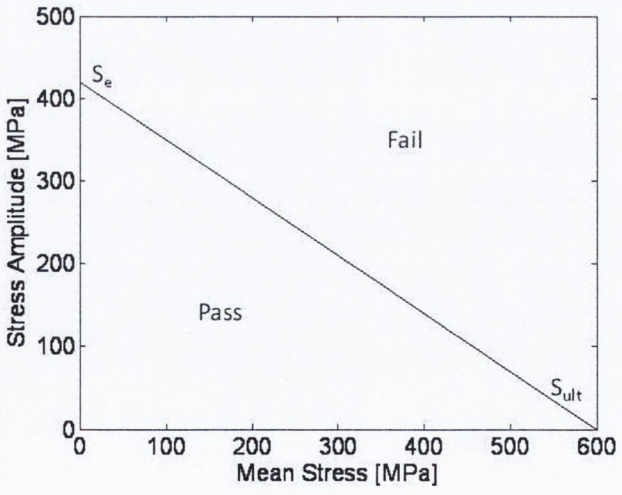


Figure 2.15

Goodman diagram for 316L stainless steel microsamples.

2.7.2 Nitinol

Nitinol exhibits less predictably fatigue behaviour than steel. A previous study, which used a combination of *in vitro* and FE models plotted the fatigue behaviour of nitinol for a range of strain amplitudes and mean strains (note that the fatigue environment is governed by strain rather than stress with this material). The failure of the samples under pulsatile loading was found to depend on the strain amplitude, with the effect of mean strain less clear [Pelton *et al.* 2008]. All samples which failed did so at strain amplitudes of 0.4% or greater. Therefore, a strain amplitude threshold value of 0.4% can be assumed, with samples experiencing lower strain amplitudes predicted not to fail, while samples with higher strain amplitudes may fail (see Figure 2.16). A clear pass/fail line, like that provided by the Goodman curve, cannot be obtained for nitinol, though a FOS can still be provided relative to this threshold value.

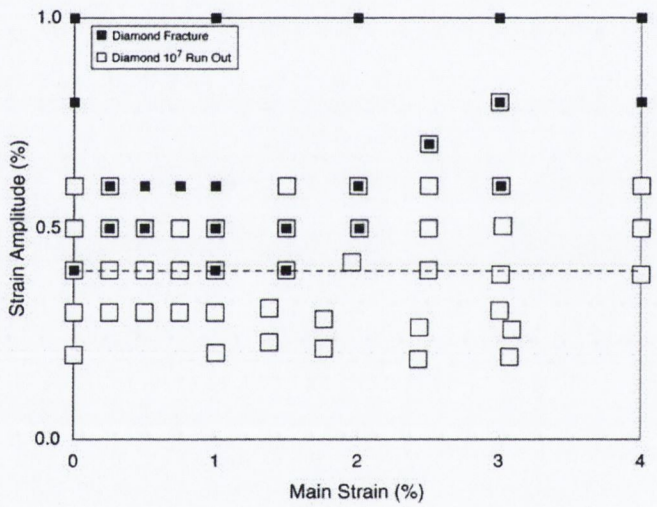


Figure 2.16

Graph showing samples passing (empty squares) and failing (black squares) stent samples at various levels of strain amplitude and mean strain [Pelton et al. 2008]. Dotted line shows strain amplitude value of 0.4%.

[Pelton et al. 2008]

2.8 Mechanical Properties of Arteries

Biomechanics can be simply defined as the "application of mechanics to biology" [Fung 1993], or the "study of the motions experienced by living things in response to applied loads" [Humphrey *et*

al. 2004]. Thus, the fundamental laws of mechanics and thermodynamics apply as much to biological tissues as they do to more traditional engineering materials. It is, therefore, important that the mechanical behaviour of tissues under appropriate loading be understood and adequately described using a suitable mathematical framework.

Idealised engineering materials can be said to exhibit LEHI (linear, elastic, homogenous and isotropic) behaviour [Humphrey *et al.* 2004]. The structure and composition of arteries means that, like most biological soft tissues, they do not behave in this manner.

Broadly speaking, arteries are non-homogeneous, hyperelastic, viscoelastic, anisotropic, nearly incompressible, rubber-like composites. Although research continues in order to better understand the mechanical behaviour of arteries, many of the fundamentals of what we now know were presented in a single paper over 100 years ago. Roy noted thermoelastic behaviour, creep, viscoelasticity, damage prior to evidence of failure, change of properties post-mortem, anisotropy, variation of properties with differences in age, sex and location on the arterial tree, and heterogeneity of the vessel wall [Roy 1881]. Since then, these qualitative observations have been quantified for various conditions, and are discussed in more detail below.

2.8.1.1 Stress-Strain Behaviour

Arteries are highly non-liner in behaviour. At low strains, they are very compliant, but stiffen as the strain is increased. This can be explained by considering the artery to be composed of wavy collagen fibres in a matrix of elastin. Elastin can be considered to be a linear elastic material with a stiffness of between 100 kPa and 1 MPa [Milnor 1989]. The wavy shape of collagen means that it cannot be considered a true linear-elastic material, though once distended it can be approximated as linear elastic with a Young's modulus of 200 MPa [Burton 1954]. At low strains, the elastin bears the load. As the strain is increased, the collagen fibres begin to straighten and recruit in the direction of loading. As these fibres, significantly stiffer than the elastin, begin the bear the load, the response becomes stiffer. The contribution of the individual components to the overall behaviour of the material is well illustrated by experiments which isolate the elastin and collagen by selective digestion [Roach *et al.* 1957]. This allows a comparison between elastin, collagen, and a full artery, as shown in Figure 2.17.

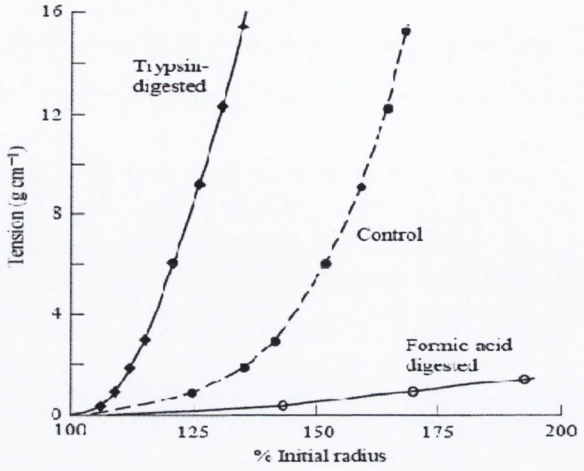


Figure 2.17

Mechanical behaviour of elastin, collagen, and whole artery artery. Elastin is tested on its own by digesting the collagen with formic acid, while collagen is isolated by digesting the artery in trypsin.

[Roach et al. 1957]

True elastic materials return to a stress free configuration following load removal along the same path as the loading, i.e. no energy is dissipated. This is not the case with arteries, where a certain amount of hysteresis is observed. Pseudoelasticity, or the separate consideration of the loading and unloading curves and associated strain energy functions, helps to describe this behaviour [Fung 1993]. Note that pseudoelasticity is not an intrinsic property of a material, but a way of describing its behaviour. The reason for the difference between loading and unloading is not fully understood, but is believed to be viscous dissipation caused by the movement of elastin and collagen in a matrix of proteoglycans and water [Humphrey 2002; Humphrey *et al.* 2004].

Removed from their physiological state, the behaviour of arteries is not, initially, repeatable. Repeated loading and unloading shows a softening of the material, known as the Mullin's effect. If sufficient cycles are carried out, the difference between tests reduces until subsequent curves are coincident. When doing mechanical tests on arteries, preconditioning cycles must be carried out first so that repeatable behaviour is analysed. The number of pre-conditioning cycles required depends on the tissue being tested.

Arteries, being composed of approximately 70 % water [Fischer *et al.* 1966], display viscoelastic properties, i.e. elements of viscous and elastic behaviour. Typically, viscoelastic materials are

strain rate dependant, though the behaviour of soft materials does not depend strongly on this [Fung 1990]. However, arteries do show creep and stress relaxation.

2.8.1.2 Incompressibility

A material is incompressible if its volume does not change during deformation. Carew *et al* [Carew *et al.* 1968] carried out volumetric measurements on arteries subject to internal pressure and longitudinal stretch and found the volumetric change to be very small ($\Delta V/V < 0.00165$). Because of this, it is often assumed that arteries are incompressible, see for example Prendergast *et al* [Prendergast *et al.* 2003]. Others allow for the small amount of compressibility of arteries by assuming them to be nearly incompressible [Lemaitre 2001].

Because the scalar triple product allows a volume to be calculated from three positional vectors, the change in volume can be expressed in terms of det**F**, as shown below.

$$dv = dx^{(1)}.\left(dx^{(2)} \times dx^{(3)}\right) \quad \textbf{(2. 8)}$$

$$= F.dX^{(1)}.\left(F.dX^{(2)} \times F.dX^{(3)}\right) \quad \textbf{(2. 9)}$$

$$= (detF)dX^{(1)}.\left(dX^{(2)} \times dX^{(3)}\right) \quad \textbf{(2. 10)}$$

$$= (detF)dV \quad \textbf{(2. 11)}$$

$$= (detF) = \frac{dv}{dV} \quad \textbf{(2. 12)}$$

This means that for an incompressible material, $detF = 1$. An alternative definition for incompressibility is that the bulk modulus is far greater (≈ 1,000x) than the shear modulus [Humphrey 2002].

2.8.1.3 Residual Stresses

Arteries *in vivo* are not in a stress free state. This can be demonstrated by measuring the length of an arterial segment before and after excision, whereby the length is found to have changed. Similarly, if an artery is cut radially, it will be seen to unfurl. The first published suggestion of a link between this altering of shape and residual stresses appears to be in a Ph.D thisis by Bergel [Bergel 1960]. Furthermore, these residual stresses have been shown to be layer specific in both the circumferential and axial directions. For example, Holzapfel *et al* [Holzapfel *et al.* 2002] show that the intima is compressed axially and circumferentially *in vivo* and extends when separated from the other two layers. This explains the ruffled appearance that the intimal layer has when viewed in cross-section. The media and adventitia are in tension and shrink, both circumferentially and axially. However, Schulze-Bauer *et al* [Schulze-Bauer *et al.* 2002] showed

that the adventitia is in compression circumferentially and in tension axially. Because of these layer-specific residual stresses, an excised artery cut axially cannot be said to be in a stress free state, although this is often assumed. It is believed that the function of the residual stress fields in the artery is to homogenise the stress distribution within the vessel wall. Changes to the homogeneity of the stress fields is hypothesised to cause growth and remodelling in order to restore the vessel to its normal state [Humphrey *et al.* 2004].

2.9 Constitutive Modelling

The stress-strain behaviour of LEHI materials can be described by a single parameter, the Young's modulus. The more complicated behaviour of arteries and other soft biological tissues requires a different approach to suitably describe the material characteristics. Constitutive equations are used to describe the behaviour of a material under certain loading conditions, for example uni-axial or bi-axial tension. The simplest constitutive equation for a solid is the Hookean elastic solid, or a solid which obeys Hooke's law:

$$\sigma = C\varepsilon \qquad \textbf{(2. 13)}$$

However, few materials obey Hooke's law, particularly at large strains. This is especially true for elastomers and soft tissues, where the stress-strain behaviour is determined by long-chain polymeric structure. Unlike linear materials, there is no single solution, or indeed approach, for describing arteries. In this section, a number of constitutive models used to simulate artery behaviour will be reviewed and compared, with an emphasis on their implementation in finite element models.

2.9.1 Preliminaries

The fundamental equations used to describe LEHI materials are based on two assumptions of linear relationships; between the stress and strain and between strain and displacement. These assumptions do not hold true for soft tissue mechanics.

A displacement vector, $\boldsymbol{u}$ is used to describe the difference between the current configuration, (x,y,z), and an original reference configuration, (X,Y,Z).

$$u_x = x(X,Y,Z) - X \quad \textbf{(2. 14)}$$

$$u_y = y(X,Y,Z) - Y \quad \textbf{(2. 15)}$$

$$u_z = z(X,Y,Z) - Z \quad \textbf{(2. 16)}$$

Differentiation gives the displacement gradients;

$$\frac{\partial u_x}{\partial X} = \frac{\partial x}{\partial X} - 1 \quad \textbf{(2. 17)}$$

$$\frac{\partial u_y}{\partial Y} = \frac{\partial y}{\partial Y} - 1 \quad \textbf{(2. 18)}$$

$$\frac{\partial u_z}{\partial Z} = \frac{\partial z}{\partial Z} - 1 \quad \textbf{(2. 19)}$$

In matrix form, this is denoted $[H]$, which can be expressed in terms of the deformation gradient, $[F]$, and the identity matrix $[I]$, using the following equation:

$$[H] = [F] - [I] \leftrightarrow [F] = [I] + [H] \quad \textbf{(2. 20)}$$

where $[F]$ is defined as:

$$[F] = \begin{bmatrix} \frac{\partial x}{\partial X} & \frac{\partial x}{\partial Y} & \frac{\partial x}{\partial Z} \\ \frac{\partial y}{\partial X} & \frac{\partial y}{\partial Y} & \frac{\partial y}{\partial X} \\ \frac{\partial z}{\partial X} & \frac{\partial z}{\partial Y} & \frac{\partial z}{\partial Z} \end{bmatrix} \quad \textbf{(2. 21)}$$

The deformation gradient, F, is an important measure of deformation because it includes both deformation and rigid body motion. It can be related to the Green strain, E, and the linearised strain, ε, using the following equations.

$$[E] = \frac{1}{2}([F]^T[F] - [I]) \quad \textbf{(2. 22)}$$

$$[\varepsilon] = \frac{1}{2}([F] + [F]^T - 2[I]) \quad \textbf{(2. 23)}$$

In materials which experience small strains, calculating the stress relative to the original cross sectional area may provide sufficient accuracy. This is provided by the first Piola-Kirchhoff stress, [Σ]. In materials such as arteries, which can experience very large strains before failure, the current cross-sectional area is required to achieve a true measure of stress. This is given by the Cauchy stress, [σ]. The Cauchy stress, though more accurate, can be difficult to measure. This

means that a way of relating the two stresses is important for experimental work. This is done by using the second Piola-Kirchhoff stress, [S].

$$[\sigma] = \frac{1}{det[F]}[F][S][F]^T \quad \textbf{(2. 24)}$$

$$[\Sigma] = [S][F]^T \quad \textbf{(2. 25)}$$

The second Piola-Kirchhoff stress, [S], which does not have a physical meaning, is useful because it can be related back to the Green strain, [E], as follows:

$$S_{ij} = \frac{\partial W}{\partial E_{ij}} \quad \textbf{(2. 26)}$$

where W is a strain-energy function (SEF), or the area the under stress-strain curve. Most constitutive models which use SEFs are functions of stress invariants, I, which in turn can be expressed in terms of the principal stretches.

$$I_1 = trB \quad \textbf{(2. 27)}$$

$$I_2 = \frac{1}{2}(trB^2 - (trB)^2) \quad \textbf{(2. 28)}$$

$$I_3 = detB \quad \textbf{(2. 29)}$$

Where B is the left Cauchy-Green strain tensor, which is a function of the gradient of the deformation gradient, F.

$$B = FF^T \quad \textbf{(2. 30)}$$

If there are no shear stresses, then the strain invariants are given by

$$I_1 = \lambda_1^2 + \lambda_2^2 + \lambda_3^2 \quad \textbf{(2. 31)}$$

$$I_2 = \lambda_1^2\lambda_2^2 + \lambda_2^2\lambda_3^2 + \lambda_1^2\lambda_3^2 \quad \textbf{(2. 32)}$$

$$I_3 = \lambda_1^2\lambda_2^2\lambda_3^2 \quad \textbf{(2. 33)}$$

Where λ_i is the stretch, defined by

$$\lambda_i = \frac{L_i + \Delta L_i}{L_i} \quad \textbf{(2. 34)}$$

If, as is often the case for arteries, the material is considered incompressible (isochoric), then the final volume is the same as the initial volume, or

$$L_1 L_2 L_3 = \lambda_1 L_1 \lambda_2 L_2 \lambda_3 L_3 \quad \textbf{(2. 35)}$$

$$\lambda_1 \lambda_2 \lambda_3 = 1 \quad \textbf{(2. 36)}$$

$$\lambda_3 = \frac{1}{\lambda_1 \lambda_2} \quad \textbf{(2. 37)}$$

Furthermore, for uniaxial tensile tests where $\lambda_1 = \lambda$ is the stretch in the direction of loading and λ_2 and λ_3 are the stretches in the directions not being loaded, if the material is isotropic then

$$\lambda_2 = \lambda_3 = \frac{1}{\sqrt{\lambda}} \quad \textbf{(2. 38)}$$

The strain invariants then become functions solely of the stretch in the loaded direction.

$$I_1 = \lambda^2 + 2\lambda^{-1} \quad \textbf{(2. 39)}$$

$$I_2 = 2\lambda + \lambda^{-2} \quad \textbf{(2. 40)}$$

$$I_3 = 1 \quad \textbf{(2. 41)}$$

2.9.2 Material models for implementation in finite element software

2.9.2.1 Fung (2 models)

One of the earliest models to describe hyperelastic materials was proposed by Fung. This model is based on a linear relationship between the stiffness $(d\Sigma/d\Lambda)$ and the first Piola-Kirchhoff stress, Σ. Note that this uses the original, not current, cross-sectional area. From a one-dimensional test on strips of mesentery, the linear relationship is given by

$$\frac{d\Sigma}{d\Lambda} = \alpha + \beta\Sigma \quad \textbf{(2. 42)}$$

To find the values of the unknown constants, the solution is of the form

$$\Sigma = c_1 e^{c_2 \Lambda} + c_3 \quad \textbf{(2. 43)}$$

Where α is the y axial intercept and β is the slope. This equation has an exponential solution of the form

$$\frac{d\Sigma}{d\Lambda} = c_1 c_2 e^{c_2 \Lambda} = (\Sigma - c_3) c_2 = c_2 \Sigma - c_3 c_2 \quad \textbf{(2. 44)}$$

Solving gives

$$c_2 = \beta \tag{2.45}$$

$$c_3 = \frac{-\alpha}{\beta} \tag{2.46}$$

Taking the initial condition that the stress is zero when the strain is zero (stretch =1)

$$0 = c_1 e^{\beta} - \frac{\alpha}{\beta} \tag{2.47}$$

This gives a solution for c_1:

$$c_1 = \frac{\alpha}{\beta} e^{-\beta} \tag{2.48}$$

Putting the constants back into the original equation gives

$$\Sigma = \frac{\alpha}{\beta} e^{-\beta} e^{\beta\Lambda} - \frac{\alpha}{\beta} \tag{2.49}$$

$$\Sigma = \frac{\alpha}{\beta}\left(e^{\beta(\Lambda-1)} - 1\right) \tag{2.50}$$

This is a relatively simple material model with just two parameters, but it has been shown to provide a good fit for some soft tissue materials, such as the epicardium [Humphrey 2004]. However, it is strictly a one dimensional relationship, and cannot be applied to three-dimensional behaviour.

A similar model to the one described above was proposed, also by Fung, this time based on a strain-energy function [Fung 1990].

$$W = \frac{1}{2} c(e^{Q} - 1) \tag{2.51}$$

$$\begin{aligned} Q_{orth} = {} & c_1 E_{11}^2 + c_2 E_{22}^2 + c_3 E_{33}^2 + 2c_4 E_{11} E_{22} + 2c_5 E_{22} E_{33} \\ & + 2c_6 E_{33} E_{11} + c_7 (E_{12}^2 + E_{21}^2) \\ & + c_8 (E_{23}^2 + E_{32}^2) + c_9 (E_{31}^2 + E_{13}^2) \end{aligned} \tag{2.52}$$

Where c and c_{1-9} are material constants and E_{11-33} are the nine components of the Green strain. Differentiating this equation gives values for second Piola-Kirchhoff stress, which can be used to determine the Cauchy or first Piola-Kirchhoff stresses.

$$S_{11} = \frac{\partial W}{\partial E_{11}} \tag{2.53}$$

$$= \frac{1}{2} c e^{Q} (2c_1 E_{11} + 2c_4 E_{22} + 2c_6 E_{33}) \tag{2.54}$$

$$= c e^{Q} (c_1 E_{11} + c_4 E_{22} + c_6 E_{33}) \tag{2.55}$$

Although this equation contains ten material parameters, which makes calculations difficult, this is a relatively simple model which incorporates non-linearity and anisotropy. This model can also be simplified in the case of orthotropic or isotropic materials.

2.9.2.2 Mooney-Rivlin

The Mooney-Rivlin hyperelastic constitutive strain energy equation [Mooney 1940] can be used to describe the properties of arteries under uni-axial and bi-axial tension. The form of this equation suitable for incompressible materials is

$$W(I_1, I_2, I_3) = \sum_{i,j,k=0}^{\infty} a_{ijk} (I_1 - 3)^m (I_2 - 3)^n (I_3 - 3)^o \tag{2.56}$$

The 9 parameter version of this equation is

$$\begin{aligned} W = {} & a_{10}(I_1 - 3) + a_{01}(I_2 - 3) + a_{20}(I_2 - 3)^2 \\ & + a_{11}(I_1 - 3)(I_2 - 3) + a_{02}(I_2 - 3)^2 \\ & + a_{30}(I_1 - 3)^3 + a_{21}(I_1 - 3)^2 (I_2 - 3) \\ & + a_{12}(I_1 - 3)(I_2 - 3)^2 + a_{03}(I_2 - 3)^3 \end{aligned} \tag{2.57}$$

Depending on the shape of the curve, it is more usual to use a reduced version of this equation which neglects several of the terms. The more common versions are listed below.

Neo-Hookean

$$W = a_{10}(I_1 - 3) \tag{2.58}$$

Mooney (2)

$$W = a_{10}(I_1 - 3) + a_{01}(I_2 - 3) \tag{2.59}$$

Mooney (3)

$$W = a_{10}(I_1 - 3) + a_{01}(I_2 - 3) + a_{11}(I_1 - 3)(I_2 - 3) \tag{2.60}$$

Signiorini

$$W = a_{10}(I_1 - 3) + a_{01}(I_2 - 3) + a_{20}(I_2 - 3)^2 \quad \textbf{(2. 61)}$$

Second Order Invariant

$$W = a_{10}(I_1 - 3) + a_{01}(I_2 - 3) + a_{20}(I_2 - 3)^2 + a_{11}(I_1 - 3)(I_2 - 3) \quad \textbf{(2. 62)}$$

Third Order Deformation

$$W = a_{10}(I_1 - 3) + a_{01}(I_2 - 3) + a_{20}(I_2 - 3)^2 + a_{11}(I_1 - 3)(I_2 - 3) + a_{30}(I_1 - 3)^3 \quad \textbf{(2. 63)}$$

Yeoh

$$W = a_{10}(I_1 - 3) + a_{20}(I_2 - 3)^2 a_{30}(I_1 - 3)^3 \quad \textbf{(2. 64)}$$

2.9.2.3 Ogden

The Ogden model is described by the following equation [Ogden 1984]:

$$W_{Ogden}(\lambda_1, \lambda_2, \lambda_3) = \sum_{p=1}^{N} \frac{\mu_p}{\alpha_p}\left(\lambda_1^{\alpha_p} + \lambda_2^{\alpha_p} + \lambda_3^{\alpha_p} - 3\right) \quad \textbf{(2. 65)}$$

Where μ_p and α_p are material constants. The two parameter version is

$$W_{Ogden}(\lambda_1, \lambda_2, \lambda_3) = \frac{\mu_1}{\alpha_1}\left(\lambda_1^{\alpha_1} + \lambda_2^{\alpha_1} + \lambda_3^{\alpha_1} - 3\right) + \frac{\mu_2}{\alpha_2}\left(\lambda_1^{\alpha_2} + \lambda_2^{\alpha_2} + \lambda_3^{\alpha_2} - 3\right) \quad \textbf{(2. 66)}$$

2.9.2.4 Gent

Other constitutive models available include the Gent model. One of the advantages of the Gent model, like the Fung stress-strain model, is that it has only two parameters, μ and J_m. In this

model, μ is the shear modulus for infinitesimal deformations and J_m is a constant value which takes account of the limited polymeric chain extensibility [Horgan *et al.* 2002].

$$W_{Gent} = -\frac{\mu}{2} J_m \left(1 - \frac{I_1 - 3}{J_m}\right) \quad \textbf{(2. 67)}$$

2.9.2.5 Holzapfel

One of the most complete constitutive models to describe arterial mechanical behaviour has been proposed by Holzapfel *et al* [Holzapfel *et al.* 2000]. By separating the SEF into isotropic and anisotropic components, this model captures the non-linear hyperelasticity of the artery, as well as the anisotropic nature due to the arrangement of the collagen fibres. The SEF, $\bar{\Psi}$, is expressed as a sum of the isotropic ($\bar{\Psi}_{iso}$) and anisotropic ($\bar{\Psi}_{aniso}$) parts:

$$\bar{\Psi} = \bar{\Psi}_{iso} + \bar{\Psi}_{\text{aniso}} \quad \textbf{(2. 68)}$$

$$\bar{\Psi}_{iso} = \mu(\bar{I}_1 - 3) \quad \textbf{(2. 69)}$$

$$\bar{\Psi}_{aniso} = \frac{k_1}{2k_2} \sum_{i=4,6} (exp(k_2(\bar{I}_i - 1)^2) - 1) \quad \textbf{(2. 70)}$$

where $\bar{I}_1 = tr\bar{C}$ is the first invariant of the modified Cauchy Green tensor $\bar{C} = J^{-2/3}C$ and $\bar{I}_4 = \bar{C}: a_{01} \otimes a_{01}$ and $\bar{I}_6 = \bar{C}: a_{02} \otimes a_{02}$ are stretch invariants of the fibers. The constants μ (or c/2 in some papers) and k_1 have the dimensions of Pa, while k_2 is dimensionless. The directions of the collagen fibers are given by a_{01} and a_{02}, which are direction unit vectors;

$$a_{01} = \begin{bmatrix} 0 \\ cos\beta \\ sin\beta \end{bmatrix} \text{ and } a_{01} = \begin{bmatrix} 0 \\ cos\beta \\ -sin\beta \end{bmatrix}$$

Where β is the angle of the fibres relative to the circumferential direction. Note that this equation defines the fibres in two directions, and they do not have a component normal to the plane of the vessel wall.

This model has been implemented to study stresses in arteries, see for example [Holzapfel *et al.* 2005b; Kiousis *et al.* 2007; Kroon *et al.* 2008]. Note that this model represents a purely isochoric response, and that it can be decoupled further to allow for volumetric changes [Gasser *et al.* 2006].

2.9.2.6 Zulliger

Unlike most models, which are phenomenological, Zulliger *et al* have proposed a model based on the structural arrangement of the artery wall [Zulliger *et al.* 2004]. Like other models, the strain energy function (Ψ) is split into isotropic (Ψ_{iso}) and anisotropic (Ψ_{aniso}) parts. The isotropic part is assumed to consist entirely of elastin, the fraction of which (f_{elast}) can be measured histologically or by assay, and is defined thus:

$$\Psi_{iso} = f_{\text{elast}}\Psi_{\text{elast}} \tag{2.71}$$

where (Ψ_{elast}) is the strain energy function of the elastin, described as a function of an elastic constant, $c_{elast} > 0$.

$$\Psi_{elast} = c_{elast}(I_1 - 3)^{3/2} \tag{2.72}$$

In the same way, the anisotropic SEF is described in terms of the collagen content and a SEF for the collagen.

$$\Psi_{aniso} = f_{\text{coll}}\Psi_{\text{coll}} \tag{2.73}$$

The SEF for the collagen is based on a probability function for the gradual recruitment of the individual collagen fibers, ρ_{fiber}. The SEF for a single collagen fiber is given by

$$\Psi_{fiber}(\varepsilon) = \begin{cases} 0 & for\ \varepsilon \leq \varepsilon_0 \\ c_{col}\big(\varepsilon - log(\varepsilon + 1)\big) & for\ \varepsilon > \varepsilon_0 \end{cases} \tag{2.74}$$

At a given value of ε, the log-logistic distribution is described by

$$\rho_{fiber}(\varepsilon) = \begin{cases} 0 & for\ \varepsilon \leq \varepsilon_0 \\ \dfrac{k(\varepsilon - \varepsilon_0/b)^{k-1}}{b[1 + (\varepsilon - \varepsilon_0/b)^k]^2} & for\ \varepsilon > \varepsilon_0 \end{cases} \tag{2.75}$$

Where b>0 is a scaling parameter and k>0 describes the shape of the distribution. Folding these two equations, see Figure 2.18, gives

$$\Psi_{coll}(\varepsilon) = \Psi_{fiber} * \rho_{fiber} = \int_{-\infty}^{\infty} \Psi_{fiber}(x) \cdot \rho_{fiber}(\varepsilon - x)dx \tag{2.76}$$

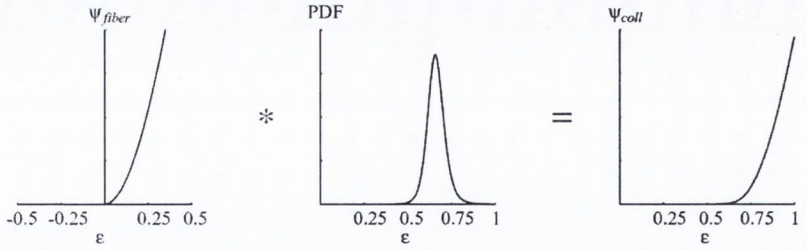


Figure 2.18

The SEF for a single fiber (with ε≥0) folded with a probability distribution function (PDF) gives an overall SEF for the collagen.

[Zulliger et al. 2004]

Assuming that the collagen fibers are aligned at angles α and –α to the circumference, then the corresponding stretch invariants are I_4 and $I_{4'}$.

$$\lambda = \sqrt{I_4} = \sqrt{\lambda_\theta^2 cos^2\alpha + \lambda_z^2 sin^2\alpha} \tag{2.77}$$

This gives the SEF for the anisotropic part of the artery;

$$\Psi_{aniso} = f_{\text{coll}}\left(\frac{1}{2}\Psi_{\text{coll}}\left(\sqrt{I_4} - 1\right) + \frac{1}{2}\Psi_{\text{coll}}\left(\sqrt{I_{4'}} - 1\right)\right) \tag{2.78}$$

Combining the isotropic and anisotropic components gives the overall SEF of the artery;

$$\begin{aligned}\Psi &= f_{\text{elast}} c_{elast}(I_1 - 3)^{3/2} + \Psi_{aniso} \\ &= f_{\text{coll}}\left(\frac{1}{2}\Psi_{\text{coll}}\left(\sqrt{I_4} - 1\right) + \frac{1}{2}\Psi_{\text{coll}}\left(\sqrt{I_{4'}} - 1\right)\right)\end{aligned} \tag{2.79}$$

2.10 Finite element analysis of stents

Finite element analysis has become an accepted and valuable tool in pre-clinical testing of medical devices. The dimensions of devices such as stents (strut dimensions < 1mm) make finite element analysis the most appropriate means of analysing stresses and strains in both a stent and artery.

2.10.1 Expanding stents/balloon-stent interaction

The modelling of an expanding stent is typically undertaken to investigate characteristics such as stress and strain distributions, opening profiles, recoil, foreshortening and radial strength. This enables the design of the stent to be improved before manufacturing. The inflation of catheter-mounted balloons to expand stents is an intricate process to model. The balloon is folded over itself to accommodate a crimped stent. When pressure is applied via saline solution, the balloon expands first by unfolding, and then by an increasing in diameter as it deforms. This results in an initially compliant balloon that stiffens rapidly once the unfolding process is completed. The complex geometries and material non-linearities and anisotropy mean that a complete model incorporating all of the inherent characteristics of the process would be an enormous undertaking. Therefore, depending on the type of results required, different assumptions and simplifications are needed to make the task achievable.

Although almost all stainless steel stents are expanded using a polymer balloon, upon which the stent is crimped, many studies do not explicitly model the balloon. A number of different strategies have been reported in the literature. Stents can be expanded by applying displacement or pressure boundary conditions to simplified balloon models, or directly to the stent. This section gives an overview of the methods used in the literature to simulate the expansion of BESs.

Surprisingly, the first reported finite element study of BESs was published as recently as 2000 [Dumoulin *et al.* 2000]. This modelled the expansion of a single unit of a Palmaz 308 stent by applying a pressure directly to the stent surface (Figure 2.19(a)) and using displacement boundary conditions (Figure 2.19(b)). The use of an elastic-plastic model enabled recoil to be quantified, while foreshortening, resistance to buckling and fatigue properties were also studied. This method of applying a pressure directly to the stent, and not explicitly modelling the balloon, has since been adopted extensively elsewhere in the literature. A similar study looked at the pressure required to expand a stent (similar to the Palmaz) and the likely point of failure of the stent due to stress concentrations [Chua *et al.* 2002]. This method was also used to determine which design factors gave the best performance in terms of pressure to expand, recoil, foreshortening and dog-boning [Migliavacca *et al.* 2002].

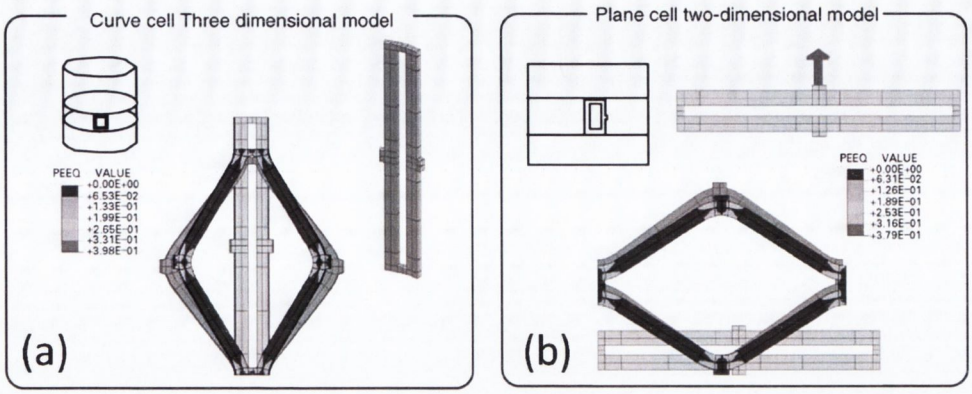


Figure 2.19

Single cell representative of stent expansion. (a) Pressure controlled boundary conditions using 3-d model. (b) Displacement controlled boundary conditions using 2-d model.

[Dumoulin et al. 2000]

It was noted that stents do not expand uniformly using balloon expansion, with the ends of the stent expanding at a greater rate than the centre [Dumoulin *et al.* 2000]. This is followed by a full, uniform expansion of the stent. This can be explained by the fact that although the pressure distribution from the membrane of the balloon is uniform, the direction in which it acts changes as the stent expands. If symmetry is used along the length of the stent, this behaviour is not captured [Dumoulin *et al.* 2000], but if symmetry is only applied in the circumferential direction, this effect is replicated in the finite element model [Chua *et al.* 2002]. A similar effect was noted in another study, which compared a finite element model of a stent expanding under pressure with an *in vitro* model of the same stent model expanded with a balloon, as shown in Figure 2.20 [Migliavacca *et al.* 2005]. This found that the finite element model predicted different rates of expansion for the centre and end of the stent; however, the stent design meant that the finite element model predicted that the ends of the stent expanded less than the centre, while the experiment demonstrated that the reverse was the case. This is because *in vitro*, the balloon dictates the opening profile and final shape of the stent. The same study also found that the pressure-diameter of the stent was not replicated at higher pressures. Nevertheless, it was shown that the stress fields (where plastic deformation occurred) are comparable (Figure 2.21) and that recoil was similar in FE and experimental models at identical diameters.

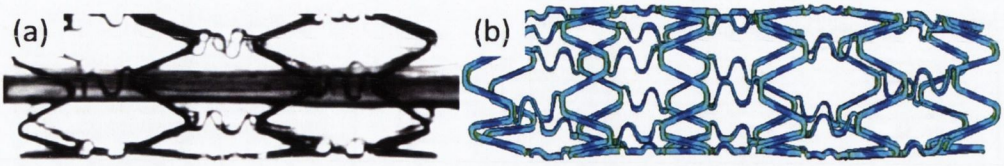


Figure 2.20

Shape of expanded stent at maximum diameter (a) in vitro and (b) using finite element model.

[Migliavacca et al. 2005]

Applying pressure to the inside surfaces of the stent is a simple way of modelling stent expansion without including a balloon. However, in the studies discussed above ([Dumoulin *et al.* 2000; Chua *et al.* 2002; Migliavacca *et al.* 2005]), the initial non-uniformity of the stent expansion was replicated with varying degrees of accuracy, but full, uniform stent expansion did not ensue, see Figure 2.20 (b).

Displacement boundary conditions enable a stent to be expanded accurately to a nominal diameter in a uniform fashion. This is carried out by applying a fixed radial displacement to selected nodes on the stent. This method is mostly used when analysing the interaction of the stent with an artery [Holzapfel *et al.* 2005b; Ballyk 2006; Gijsen *et al.* 2008]. This is because although effects such as recoil and dogboning cannot be simulated, it is the most computationally efficient way of expanding a stent. It has also been used to compare the flexibility of expanded and unexpanded stents [Petrini *et al.* 2004].

A further method involves modelling the expanded geometry of the stent and applying a high pressure to the artery so that it stretches to a diameter greater than that of the stent. The pressure on the artery is then removed (or reduced to the level of blood pressure) so that it wraps around the stent [Prendergast *et al.* 2003; Lally *et al.* 2005; Bedoya *et al.* 2006; Timmins *et al.* 2008].

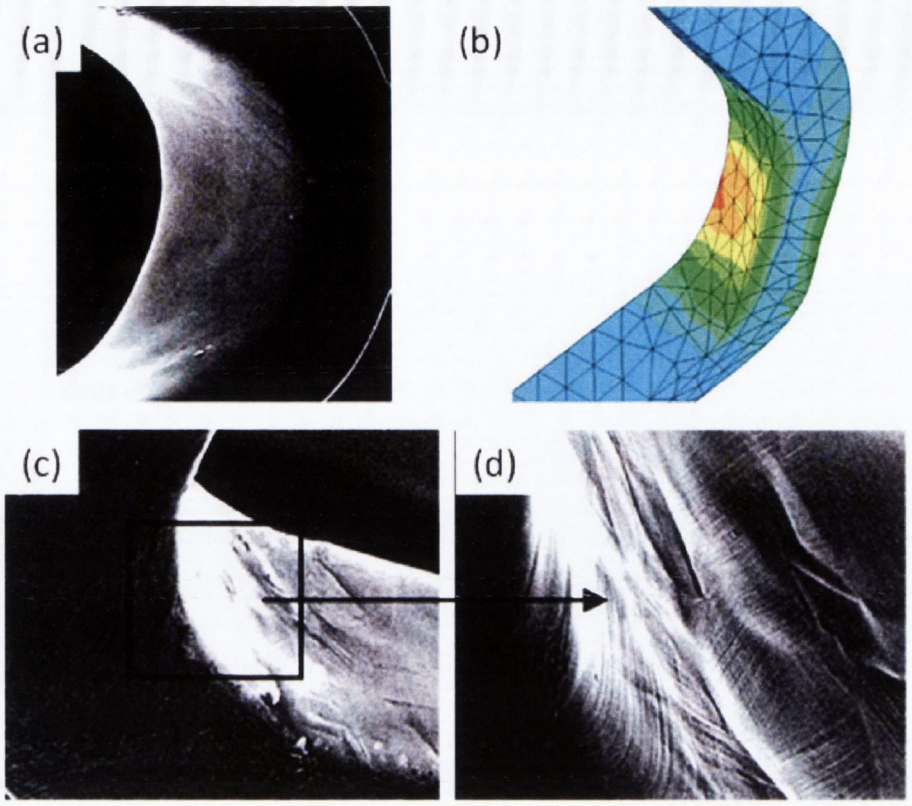


Figure 2.21

Relationship of areas of plastic deformation in (b) finite element model with (c)&(d) Luders lines seen using scanning electron microscope.

[Migliavacca et al. 2005]

Balloon models can be simplified by assuming it to be cylindrical, i.e. without modelling the folding. Pressure [Chua *et al.* 2003; Liang *et al.* 2005; Wang *et al.* 2006] or displacement [Wu *et al.* 2007b] can be applied to the simplified balloon in a similar manner to stents. These methods have the advantage of enabling recoil to be modelled, and are simpler and less time consuming to model than a folded balloon.

Accurately modelling a folded polymer balloon has only recently been undertaken. This method is more complex than those outlined above, but gives the best representation of the stent expansion behaviour. The balloon can be modelled without the folds by applying a negative pressure to a balloon at full diameter, and then re-inflating the balloon to expand a stent, as shown in Figure 2.22(a) [Gervaso *et al.* 2008]. This study used a linear elastic balloon with a Young's modulus of 900 MPa. The results were compared with pressure-diameter relationships provided by a stent manufacturer, as well as with displacement and pressure controlled models,

see Figure 2.23. Although the final shape is similar when using the pressure and displacement control balloons, and foreshortening was similar, the stresses induced in the artery were different. This model was used on a number of stent designs to study prolapsed following expansion in a coronary artery [Capelli *et al.* 2008].

Laroche *et al* modelled the folding of the balloon by imposing a folding algorithm on a cylindrical, tapered balloon (Figure 2.24(a)) [Laroche *et al.* 2006]. A pressure is then applied to the balloon, which opens to expand the stent, as shown in Figure 2.24(b). The balloon is modelled as a hyperelastic material described by the Ogden constitutive equation.

A similar approach is taken by De Beule *et al*, who created a balloon with an initial folded geometry and a Young's modulus of 920 MPa [De Beule *et al.* 2008]. As in the Gervaso *et al* study [Gervaso *et al.* 2008], this paper compared the model of balloon expansion with pressure-diameter data from the manufacturer, as well as with models which were expanded using pressure applied directly to the stent and with a cylindrical balloon with displacement boundary conditions. It was found that modelling the folded balloon gave an accurate description of the stent expansion path, as well as the final shape, see Figure 2.22 (b). Modelling the balloon with displacement boundary conditions gives a good prediction of the final shape of the stent for less computational cost. This model has been used in other studies to investigate the effect of the number of folds, balloon length and symmetry [Mortier *et al.* 2008a] and to study side branch access in bifurcation stenting [Mortier *et al.* 2008b]. A folded balloon model has also been used to investigate stent designs in terms of dogboning and foreshortening [Lim *et al.* 2008]. The non-linear, anisotropic properties of the balloon can be described by a strain energy function for a fiber reinforced composite, as with arteries.

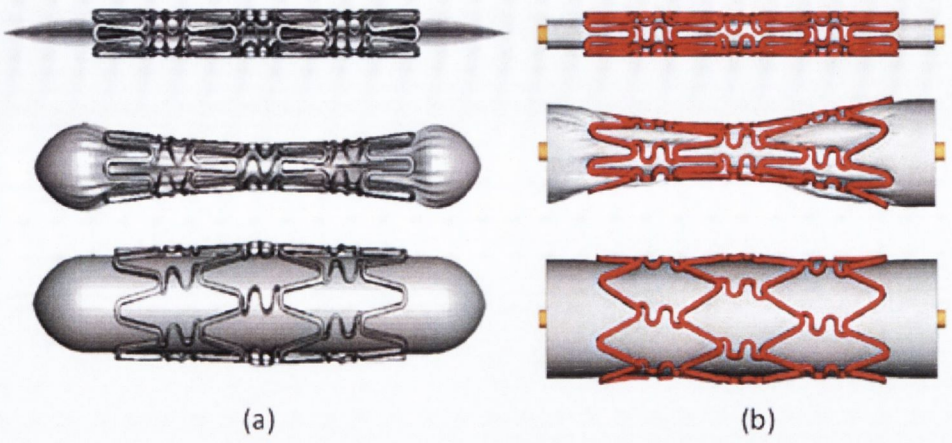


Figure 2.22

A comparison of stent expansion using realistic balloon models. The balloon can be modelled by (a) deflating a cylindrical balloon with a negative pressure and then inflating the balloon or (b) modelling the balloon folding.

[Gervaso et al. 2008] [De Beule et al. 2008]

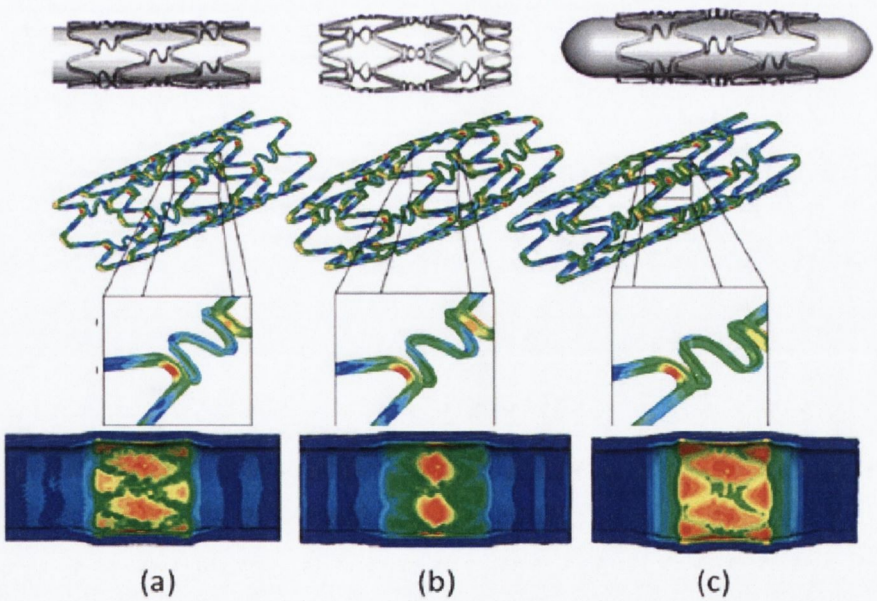


Figure 2.23

Final stent shape, stent von Mises stresses and Artery von Mises stresses for (a) cylindrical balloon expanded with displacement control, (b) pressure applied directly to stent and (c) realistic pressure controlled balloon model.

[Gervaso et al. 2008]

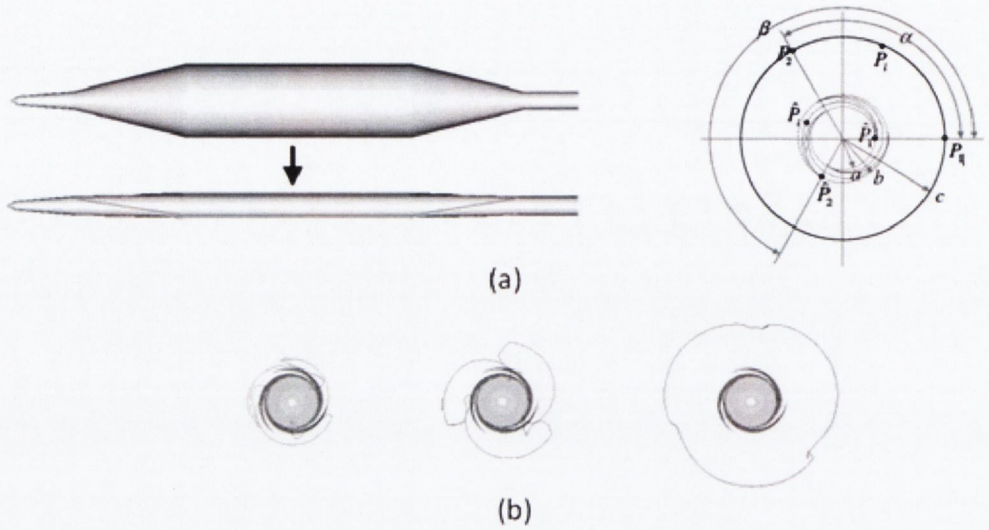


Figure 2.24

Modelling a folded balloon, showing (a) folding the balloon and (b) deployment of the balloon using free expansion.

[Laroche et al. 2006]

Studies by Kiousis *et al* [Kiousis *et al.* 2007; Kiousis *et al.* 2008] used this approach with a cylindrical balloon that did not incorporate the folded geometry of the balloon. Subsequent comparison with experimental results found an excellent correlation with the numerical simulations in the pressure-diameter relationships at the centre and distal end [Kiousis *et al.* 2009]. This captured the dog-boning effect of stent expansion, with the ends opening up before the centre.

2.10.2 Artery material models

An accepted principal of stent design is that stresses in the artery, and thus injury, should be reduced where possible. This necessitates accurate material models in order to determine the stress levels in arteries following stenting, and especially to make comparisons between stent designs. While some early models used linear elastic, isotropic material properties [Chua *et al.* 2004], most use some form of reduced polynomial strain energy density function [Liang *et al.* 2005; Ballyk 2006; Bedoya *et al.* 2006; Wu *et al.* 2007b; Gervaso *et al.* 2008; Gijsen *et al.* 2008; Timmins *et al.* 2008; Pericevic *et al.* 2009]. Others have utilised a Moone-Rivlin SEF [Lally *et al.* 2005; Wu *et al.* 2007b], a Holzapfel model [Holzapfel *et al.* 2005b] and the Ogden model [Zahedmanesh *et al.* 2009].

These SEFs are usually designed to replicate the behaviour of aged human coronary arteries, though such material is not always available for testing. Some models are based on mechanical tests on human femoral arteries [Lally *et al.* 2005], porcine carotid arteries [Bedoya *et al.* 2006], porcine coronary arteries [Pericevic *et al.* 2009]. More recently, Holzapfel *et al* have carried out uniaxial tensile tests in the circumferential and longitudinal directions on the individual layers of aged, disease free, human coronary arteries with intimal thickening [Holzapfel *et al.* 2005a]. This has been implemented by fitting SEFs to the raw data obtained from the circumferential tests to provide a finite element model of a three-layered artery [Capelli *et al.* 2008; Gervaso *et al.* 2008; Zahedmanesh *et al.* 2009].

2.10.3 Stent-artery interaction

As well as determining and improving the mechanical characteristics, finite element models are invaluable for analysing the interaction of an expanded stent with the arterial wall. Models can be created to analyse the effect on fluid flow on the wall shear stresses in a stented artery, whether sufficient lumen gain is achieved, or the stresses induced in the artery. The latter is commonly investigated, as stresses and damage in the arterial wall are believed to be important factors in restenosis. Therefore, understanding the factors which influence these stresses and reducing their magnitude is an important part of medical device analysis and design. However, although it is generally acknowledged that stress-induced injury is the driving factor towards restenosis, the nature of this is not fully understood. It is not known whether, for example, there is a linear or exponential relationship between stress and the rate of neointimal formation, or if there is a threshold value, as there is for other soft tissues [Linder-Ganz *et al.* 2006; Gefen *et al.* 2008]. Therefore, results of finite element analyses tend to be presented in a more generalised form. Stress distributions, or the amount of artery within specified stress ranges, and peak stresses are most commonly presented as measures of injury. The type of stress that causes restenosis is not understood either. Many studies use the von Mises stress, as it describes the overall stress state of the artery [Chua *et al.* 2004; Migliavacca *et al.* 2004; Liang *et al.* 2005; Ballyk 2006; Capelli *et al.* 2008; Gijsen *et al.* 2008; Pericevic *et al.* 2009], while others use the circumferential stress, as it is the most significant [Holzapfel *et al.* 2005b; Bedoya *et al.* 2006; Timmins *et al.* 2008], or the maximum principle stress [Lally *et al.* 2005; Wu *et al.* 2007a; Wu *et al.* 2007b]. A recently proposed model for restenosis following stenting uses a threshold value of the minimum principal (maximum compressive) stress based on cell death in rat muscles under compression [Linder-Ganz *et al.* 2006]. Tissue prolapsed, or lumen loss due to deflection of the artery within the stent, has been shown to alter the fluid flow within the vessel and thus contribute to restenosis [Wentzel *et al.* 2003]. Some finite element studies have quantified the level of prolapsed for

different stent designs [Prendergast *et al.* 2003; Capelli *et al.* 2008] and within a curved vessel [Wu *et al.* 2007b].

2.10.4 SMA Stents

Compared with BESs, there have been fewer published finite element studies investigating the performance of nitinol stents. Interestingly, the first finite element study dealing with stents was in relation to the fatigue life of a nitinol stent. This study looked at the loads experienced by nitinol stents *in vivo* using an elastic-plastic model with Von Mises yield criterion [Whitcher 1997]. Thériault *et al* used a similar material model to simulate the formation of a nitinol stent, and a shape memory alloy material model available in ANSYS to model the deployment of the same stent [Theriault *et al.* 2006]. Auricchio *et al* utilised a phase transformation model to replicate the stress and temperature dependant properties of an SMA [Auricchio *et al.* 2002]. Petrini *et al* [Petrini *et al.* 2005] used a similar model [Auricchio *et al.* 2004] to describe the behaviour of a nitinol vertebrae spacer and a stent under loading.

There are fewer studies again which investigate the interaction between nitinol stents and arteries during and following deployment. The first paper to do this analysed the stresses induced in a coronary artery wall following insertion of a nitinol stent [Migliavacca *et al.* 2004], implementing the material properties described by Auricchio *et al* [Auricchio *et al.* 2002]. Wu *et al* used another model by Auricchio *et al* [Auricchio *et al.* 1997], available in the finite element package ANSYS, to simulate the deployment of a nitinol stent in a stenosed carotid artery [Wu *et al.* 2007a]. SMA stent deployment can be modelled by applying a pressure to the external faces to compress the stent, then removing that pressure to allow the stent to return to its original shape during deployment [Migliavacca *et al.* 2004]. An alternative method is to apply radial displacement to a rigid sheath to compress the stent to fit inside the artery, then reverse the displacement to allow the stent to expand [Wu *et al.* 2007a]. The displacements and stresses of the stent and artery can then be measured, as shown in Figure 2.25.

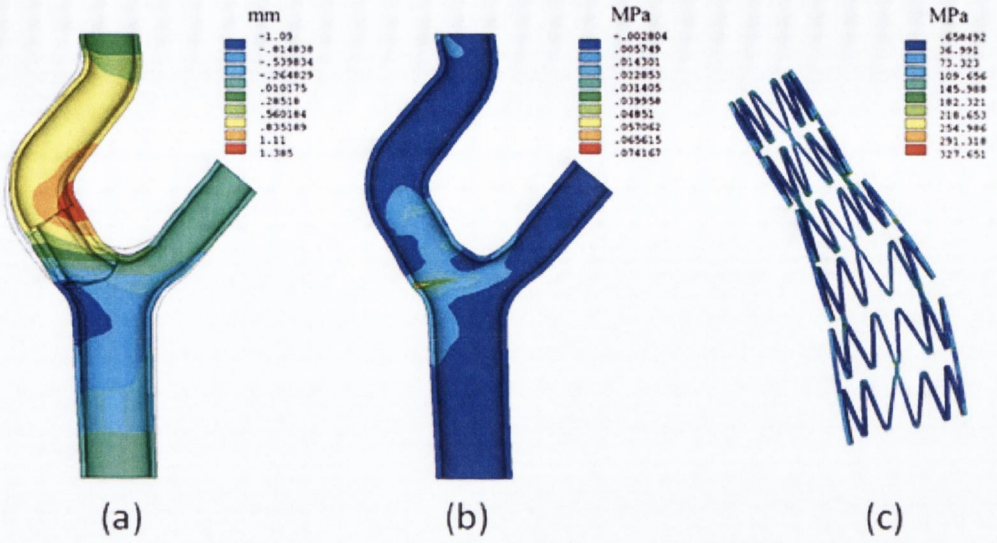


Figure 2.25

Finite element model of stent deployment in carotid artery showing (a) artery displacement, (b) artery stresses and (c) stent stresses following stenting.

[Wu et al. 2007a]

2.11 Conclusions

The papers reviewed in this chapter highlight some of the problems associated with stenting in peripheral arteries. Rates of restenosis and stent fracture are considerably higher than in coronary arteries, even with the use of SMA stents, while DESs have not been as successful as in other arteries. There are many differences between stenting in peripheral arteries compared with coronary arteries. As well as the dimensions and material properties, different types of stents made from different materials are used. These differences have not, to the author's knowledge, been quantified.

The mechanical environment of peripheral arteries appears to be especially problematic. While it is hypothesised that the forces acting on the stent and artery caused by knee flexion cause stent deformation and subsequent fracture, and may raise stresses in the artery, little has been done to measure these effects. However, the work that has been carried out seems promising, and improvements in stent performance are beginning to be reported. It is hoped that greater understanding of stent behaviour within this environment may lead to further improvement in stent design, and subsequently stenting may become a viable option for treatment of PAD.

3 Structure-function relations of porcine arteries from different vascular beds

Contents

3.1 Introduction 65
3.2 Methods 67
3.2.1 Artery extraction 67
3.2.2 Mechanical testing of arteries 67
3.2.2.1 Tensile tests 67
3.2.2.2 Circumferential ring tests 68
3.2.2.3 Radial compressive tests 69
3.2.3 Curve fitting 69
3.2.4 Biochemical analysis 70
3.2.4.1 Elastin Assay 71
3.2.4.2 Collagen Assay (Hydroxyproline) 71
3.2.5 Histology 72
3.2.6 Statistical analysis 73
3.3 Results 74
3.3.1 Mechanical tests 74
3.3.1.1 Geometry 75
3.3.1.2 Coronary arteries 75
3.3.1.3 Femoral arteries 77
3.3.1.4 Aorta 78
3.3.2 Curve Fitting 79
3.3.3 Biochemical analysis 83
3.3.3.1 Collagen content 84
3.3.3.2 Elastin content 84
3.3.3.3 Collagen elastin ratio 85

3.3.4 Histology 86
3.3.5 Relating structure to function 87
3.4 Discussion 90
3.4.1 Mechanical properties 90
3.4.2 Curve fitting 91
3.4.3 Biochemical analysis 92
3.4.4 Histology 92
3.5 Conclusions 95

3.1 Introduction

In order to investigate and predict how stents behave when expanded in arteries, it is important to achieve an appropriate understanding of arterial structure, function and mechanical behaviour. As outlined in Chapter 2, the mechanical properties of human [Schulze-Bauer *et al.* 2003; Holzapfel *et al.* 2005; Holzapfel *et al.* 2007] and porcine [van Andel *et al.* 2003; Lally *et al.* 2004] arteries have been extensively examined. Furthermore, the relative quantities of the constitutive elements of arteries (collagen, elastin, muscle and water) have been quantified [Fischer *et al.* 1966]. While some work has attempted to relate the two [Cox 1978], according to J.D. Humphrey [Humphrey 2002]

"The complementary role of quantitative histology and biomechanics cannot be overemphasized, thus there is a pressing need for continued research along these lines"

Artery mechanical properties can be investigated through a range of mechanical tests, such as uniaxial or biaxial tension, shear, compressive, inflation-extension, etc. For the purpose of this investigation, mechanical tests were limited to uniaxial tension, circumferential ring and compressive tests.

A number of mathematical models are available to describe the behaviour of arteries under the conditions described above. As the material properties of biological soft tissues are more complicated than linear elastic materials, more elaborate mathematical equations are required to depict the stress-strain behaviour. These can directly describe the stress-strain relationship, or the strain-energy of deformation.

Collagen and elastin are the components which dictate the instantaneous behaviour of arteries. The amounts of these ingredients in an artery can be measured using assays, enabling a collagen to elastin ratio to be measured. By carrying out the assays on material used in mechanical tests (half for a collagen assay, half for elastin), it is hoped to compare the composition directly with the mechanical behaviour. This can be done both for every artery type, and to compare different arteries from functionally different beds.

In this chapter, the differences in mechanical behaviour and composition will be investigated for arteries from functionally different beds. While a wide range of mechanical, biochemical, pathological, thermal, biomechanical and other tests are available to create comprehensive sets of data under many conditions, this study is limited to appropriate testing towards understanding the behaviour of arteries under specific conditions. This includes selected mechanical behaviour

of the arteries, their structure and composition, and a comparison of these properties between arteries from functionally different locations on the arterial tree. As human tissue is both difficult to obtain and cannot be tested freshly, porcine arteries were used for the purpose of this investigation. Where possible, the data obtained for the porcine arteries can be compared with similar data for human arteries.

It is hypothesised that the collagen to elastin ratio is the prime determinant of material behaviour, and that by using an appropriate material model arterial behaviour can be predicted from its composition.

3.2 Methods

3.2.1 Artery extraction

Arteries were harvested from female pigs that were approximately 6 months old and weighed 30 – 50 kg. The tissue was harvested using a scalpel within one hour of the pig being put down. Fat and connective tissue were trimmed from the arteries, which were then stored in 0.9% saline solution at 4°. Three artery types were harvested; femoral arteries, right coronary arteries (RCA), and descending aorta.

3.2.2 Mechanical testing of arteries

Three types of mechanical tests were carried out on the extracted tissue. Tensile tests were used for all longitudinal samples. Where the specimens had a sufficiently large diameter for dog-bone shaped samples to be obtained in the circumferential direction, tensile tests were also used for circumferential samples. When this was not possible owing to the small diameters of some of the arteries, ring tests were used instead. Compressive tests were also carried out. Mechanical tests carried out on the arteries took place less than 48 hours post-mortem and were performed at room temperature.

3.2.2.1 Tensile tests

Arteries for use in tensile tests were removed from the saline solution and cut along their length to give flat samples. Samples for the tests were obtained using a dog-bone shaped punch in areas that did not have visible arterial branches. Two punches were used for extracting samples. One of the punches had a central area with a width of 2mm and a length of 7mm, while the other one had a width of 3.5mm and a length of 10mm. Where possible, the larger punch was used, though the presence of arterial branches and the dimensions of some of the samples meant that this was not always possible. As the dimensions of the arteries were different to that of the punch owing to physiological pre-stresses, the width and thickness of the samples was measured at the centre of the dog-bone shaped specimens using a Mitutoyo toolmaker's microscope. The average of three measurements was used for each dimension to obtain the cross-sectional areas.

Specimens were placed in grips in a Zwick tensile testing machine with a 50 N load cell. The grips had sandpaper super-glued to them to minimise slip. A pre-load was applied to remove slack, then the specimen was pre-conditioned for 5 cycles at a load of 0.1 N. The samples were then tested to failure at a strain rate of 60%/min. The Zwick machine measured the load and

displacement at a frequency of 5 Hz, which was converted to stress-strain or stress-stretch graphs.

The stretch, λ, was quantified as

$$\lambda = \frac{l}{l_0} \tag{3. 1}$$

where l is the current length and l_0 is the original length.
As the strains are large, the cross sectional area changes continuously. By assuming the material to be incompressible, this can be taken account of.

$$V = V_0 \tag{3. 2}$$

$$AL = L_0 A_0 \tag{3. 3}$$

$$A = \frac{L_0}{L} A_0 \tag{3. 4}$$

$$A = \frac{A_0}{\lambda} \tag{3. 5}$$

$$\sigma_{cauchy} = \frac{F}{A} = \frac{F\lambda}{A_0} \tag{3. 6}$$

Where V is the current volume (V_0 is original volume), A is the cross sectional area and F is the applied force.

One of the problems associated with tensile tests of soft tissues is slippage of specimens at the grips. Ideally, a visual strain measurement technique should be used, so that slippage of the sample will not alter the results [Holzapfel *et al.* 2005]. The equipment necessary for this type of measurement was not generally available during testing. To determine if sample slip was a significant problem within the range of stretches utilized in this study a small number of tests were undertaken such a visual strain measurement system. The strain was measured using the visual method by placing two marks in the central region of the dog-bone shaped sample and tracking their displacement using a CCTV camera.

3.2.2.2 Circumferential ring tests

Longitudinal tensile tests were not feasible for the femoral or coronary arteries, as suitably large circumferential strips could not be obtained. This was overcome by using ring tests, as described by Cox *et al* [Cox 1982; Cox 1983]. Although they are uniaxial tests, ring tests do not have a finite solution, and the tests are compromised by having stress concentrations caused by bending and residual stresses in the intact ring [Humphrey 2002].

Rings with a height of approximately 1-2mm were cut using a scalpel. The height, thickness and diameter measurements were taken using a Mitutoyo toolmaker's microscope, as described above. The samples were placed in custom-built grips with pins attached and tested to failure. The load-extension data obtained from the tests was converted to stress strain curves using the following formula [Cox 1983].

$$\sigma = \frac{\lambda F}{2tw} \quad \textbf{(3. 7)}$$

$$\lambda = \frac{2d + 2\pi a}{l_0} \quad \textbf{(3. 8)}$$

Where σ is the 1-D Cauchy stress, F is the applied load, t and w are the specimen width and thickness, λ is the stretch, d is the distance between the arms, a is the radius of the arms and l_0 is the initial length. Note that the formula given above is an approximation, and not an exact finite solution determinable from first principals.

3.2.2.3 Radial compressive tests

For the compressive tests, the tissue was cut longitudinally as before. Circular samples were taken of the tissue with a 3mm biopsy punch. Measurements were taken for the diameter and height of the sample using a toolmaker's microscope. A compressive pre-load and pre-conditioning were applied as before, and the samples were tested to the maximum compressive load allowed by the load cell. Two parallel platens were used to apply the compressive load. All samples buckled at sufficiently high loads. While these were, in most cases, far beyond the ranges of stretch studied, samples which buckled at lower values were discarded.

3.2.3 Curve fitting

The stress-strain behaviour of arteries can be described by using appropriate constitutive models. For data from the human coronary and illiac arteries [Schulze-Bauer *et al.* 2003; Holzapfel *et al.* 2005], and for some of the results of the mechanical tests, several constitutive models were fitted to the stress-strain curves. The data from human arteries was included in this part of the study, as describing their behaviour for finite element analysis would be important for future studies (see Chapters 4, 5, and 6). This allowed a direct comparison between the material models, and the selection of an appropriate one for finite element analysis. The models fitted included a simple Fung model, the Gent model, the Ogden model and the third-order Moone-Rivlin model. The form of the equations used are summarised below. More complete details of each model are provided in Chapter 2.

Fung:

$$\Sigma = \frac{\alpha}{\beta}\left(e^{\beta(\lambda-1)} - 1\right) \quad \textbf{(3. 9)}$$

Gent:

$$W_{Gent} = -\frac{\mu}{2} J_m Ln\left(1 - \frac{I_1 - 3}{J_m}\right) \quad \textbf{(3. 10)}$$

Ogden:

$$W_{Ogden} = \frac{\mu_1}{\alpha_1}\left(\lambda_1^{\alpha_1} + \lambda_2^{\alpha_1} + \lambda_3^{\alpha_1}\right) + \frac{\mu_2}{\alpha_2}\left(\lambda_1^{\alpha_2} + \lambda_2^{\alpha_2} + \lambda_3^{\alpha_2}\right) \quad \textbf{(3. 11)}$$

Mooney-Rivlin:

$$W_{MR} = a_{10}(I_1 - 3) + a_{01}(I_2 - 3) + a_{20}(I_1 - 3)^2 + a_{11}(I_1 - 3)(I_2 - 3) + a_{30}(I_1 - 3)^3 \quad \textbf{(3. 12)}$$

The Gent, Ogden and Mooney-Rivlin models were differentiated, and constants fitted to all of the functions to minimise the error between the models and the data using the least squares method. For each artery and test type, the average of the constants was taken to give a representative curve. The stability of the curves given by the constants is important, i.e. the curve should not produce negative stress values for positive strains, and should be monotonically increasing. Furthermore, models were restrained to describing zero stress at a zero strain state.

For the Mooney-Rivlin model, it should also be noted that while imposing positive values is not always necessary for a function to be stable, the average curves, representative of particular tests, were unstable for many of the tests when this restraint was not imposed. Therefore, it was decided to only use positive values to describe the arteries and for implementation in finite element models.

3.2.4 Biochemical analysis

Biochemical analysis was used on tissue samples to determine the relative amounts of collagen and elastin in the arteries. In order to relate the composition of the artery to its mechanical behaviour, the biochemical analysis was undertaken on the tissue that had been tested. Following testing, the specimens were cut in two with a scalpel and the wet weight obtained. The samples were then immediately placed in a freezer at -84°C. For each specimen a mechanical test was

carried out on, one half was analysed for elastin content and the other for elastin content. This enabled a collagen elastin ratio to be obtained for each test.

3.2.4.1 Elastin Assay

A Fastin Elastin Assay (Biocolor, Newtownabbey, Northern Ireland) was used to measure the total elastin content in the arteries. As the samples contained insoluble elastin, it was necessary to convert this to soluble α-elastin. To do this, the samples were placed in screw-top 2ml microtubes with 1.2ml 0.25M oxalic acid in an oven at 100°C. After an hour, the samples were cooled to room temperature and centrifuged. The top 1ml of oxalic acid was extracted and placed in a microtube for analysis. This 1ml of oxalic acid, or the first extraction, was labelled and stored in a fridge at 4°C. A further 1ml of 0.25M oxalic acid was added to the sample which was replaced in the oven. These steps were repeated until the artery was fully dissolved, and the elastin fully solubilised. Depending on sample size and elastin content, this took 4-6 extracts to achieve. When the last extract was completed, 800µl of 0.25M oxalic acid was added to the initial sample. 200µl of each extract was added to a microtube, and this sample was used for analysis. Standards of 12.5, 25, 50 and 100µl α-elastin were prepared, and topped up to 100µl with 0.25M oxalic acid.

The first step of the assay is to add an equal volume of elastin precipitating reagent. After allowing sufficient time for the elastin to precipitate, the tubes are centrifuged and the liquid contents emptied from the tubes. To each tube, 1ml of dye reagent is added. The tubes are then mixed and placed on a rotator for 90 minutes. The tubes are then centrifuged again, and the liquid contents drained. The elastin-dye complex can be seen as reddish deposit at the bottom of the tube. Dye dissociation reagent is then added to the tubes. The appropriate quantity may depend on the concentration of the elastin. Generally, 1ml is added to the tubes. If the samples appear darker than the highest (100µl) standard, then it is further diluted with dye dissociation reagent. The samples are then transferred to a 96 well plate in triplicate, and the absorbance reading at 513nm taken. The readings are converted to elastin measurements using the standards curve. Full details of the assay protocol are provided in Appendix A.

3.2.4.2 Collagen Assay (Hydroxyproline)

As the collagen could not be suitably solubilised for use with a collagen assay, hydroxyproline was used as a measure of collagen content instead. Hydroxyproline is an imino acid, which is believed to occur exclusively with collagen, in a fixed ratio. Therefore, measument of the hydroxyproline content allows calculation of the collagen content. The protocol outlined below is based on a

procedure provided by Kafienah and Sims [Kafienah *et al.* 2004], full details of which are provided in Appendix B.

Samples for analysis were digested in 10mg/ml pepsin (dissolved in 0.5M acetic acid), using a ratio between the wet weight and pepsin of 10:1. The samples were topped up to 500µl with acetic acid. The samples were placed in a rotator in an oven at 60°C for 12 hours. An appropriate aliquot was taken to obtain a reading in the mid-range of the standard curve, in this case 500ng of hydroxyproline. Aliquot sizes of 100µl were used, with 100µl of 38% hydrochloric acid added to each tube. These tubes were mixed, and incubated in an oven at 110°C for 18 hours. Following this, the samples were dried on a heating block at approximately 50°C for 24-48 hours. The samples were then reconstituted with 200µl of ultra-pure water and analysed. Standards of between 0 and 5µl/ml were prepared using hydroxyproline stock solution.

For each sample, 60µl (in triplicate) was added to a clear, 96-well plate. Assay buffer (20µl) and chloromine-T reagent (40µl) were added. The plate was covered in tinfoil and allowed to incubate for 20 minutes at room temperature. Using filtered pipette-tips, 80µl of DMBA reagent was added to each well to give cloudy solutions. These were mixed until the solution turned clear. The plates were then placed in an oven at 60°C for 20 minutes. Following cooling, the plates were placed in a plate reader and readings taken at 570nm. The hydroxyproline content of each sample was then calculated from the standard curve. This was used to work out the total hydroxyproline content in each sample, and thus the amount of collagen.

Individual Hydroxyproline to collagen ratios for each artery in the pig were not available. It has been shown that this ratio varies between species and sites of extraction [Ignat'eva *et al.* 2007]. Previous experiments on the porcine aorta have assumed that the average collagen molecule contains 10% hydroxyproline residues [Davidson *et al.* 1985], and this ratio is assumed for the experiments presented here.

3.2.5 Histology

Histological staining was carried out on artery tissue from the coronary and femoral arteries, as well as the aorta. Specimens were taken from either end of the tissue being used for the mechanical tests and biochemical assays, and ring shapes were taken so that histology could be used to view the cross-sections.

The artery samples are first fixed in paraformaldehyde overnight. They are then dehydrated through progressively stronger alcohol and xylene. After being washed in PBS, they are then

placed in molten paraffin wax. Following cooling, the wax should be re-melted and re-cooled again for better embedding. The samples can then be sliced using a microtome, and mounted on subbed glass slides.

Slides are deparaffinised through xylene and alcohol. The slides are placed in elastin solution for ten minutes, rinsed in deionised water, then differentiated in ferric chloride. The slides are placed in the van Gieson solution for one to three minutes, rinsed in alcohol and dehydrated to xylene.

The stained slides can be examined under a microscope, and photographed. The full set of protocols for histological staining are provided in Appendix C.

3.2.6 Statistical analysis

Results, where appropriate, are expressed as mean ± standard deviation. One way analysis of variance (ANOVA) was used to determine statistical significance, which was set at $P<0.05$. Minitab software version 15.1 (Minitab Inc, PA) was used for all statistical analysis.

3.3 Results

3.3.1 Mechanical tests

Results of the mechanical tests are presented as stress-stretch curves. The Cauchy stress (σ_{11}) is used, as this takes account of the change of cross sectional area with change in load. The geometry of the arteries is also presented. The stress-strain curves were investigated to determine whether the data was suitable for further evaluation – samples that failed at the grips (or which buckled in the case of compressive tests) or at values of less than twice the pre-load, or that showed evidence of slippage were discarded. For the femoral artery, 21 of the 30 samples tested were suitable for analysis, while 9 of the 15 coronary and 10 of the 15 aorta circumferential and longitudinal samples were suitable for tensile tests.

The results of the slip verification tests showed that even by taking measurements to minimise slip, such as gluing sandpaper to the grips, some slip of the specimen did occur, see Figure 3.1. For stretch ratios below two, the amount of slippage was relatively small (less than 8%), and so samples were analysed at values lower than this. Further, the maximum stretches predicted by subsequent finite element models (see Chapters 3, 4, 5 and 6) were less than 1.8. All subsequent plots use stretch measurements based on the gauge length recorded by the materials testing machine.

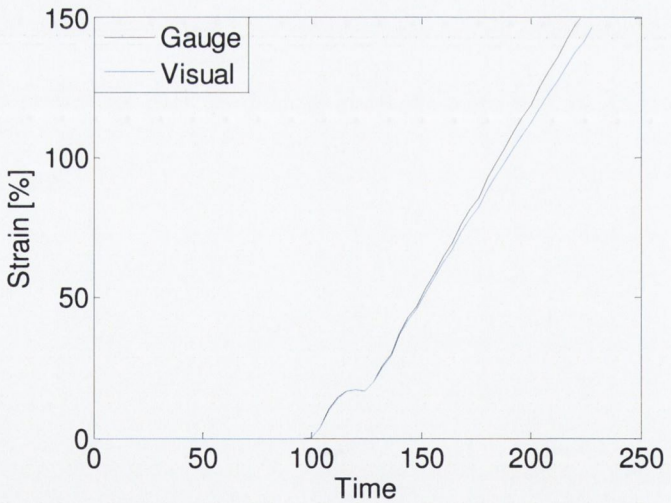


Figure 3.1

Typical slip verification study showing strain measured using gauge length and visual technique.

3.3.1.1 Geometry

Although all of the samples were cut from the same punch, the widths of the dog-bone specimens varied, both between and within artery types, see Table 3.1. This was as a result of residual stresses within the artery, which resulted in significant sample shrinkage following punching. The femoral arteries in the pigs studied had very small inner diameters in the unpressurised state (<1 mm), though they were thicker than the coronary arteries. Statistical difference ($P<0.05$) was found between the thicknesses of all three artery types (Figure 3.2).

	Width	Thickness
Coronary	2.304 ± 0.357	0.429 ± 0.185
Femoral	2.234 ± 0.379	0.770 ± 0.234
Aorta	1.734 ± 0.234	1.794 ± 0.224

Table 3.1

Average width and thickness of the artery samples measured for mechanical tests.

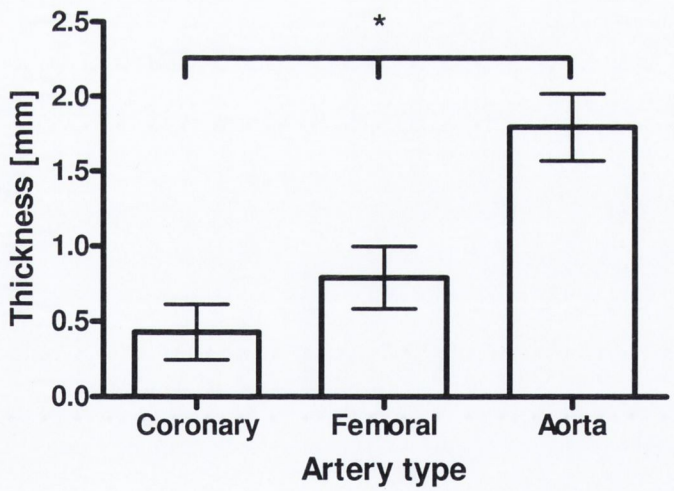


Figure 3.2

Thickness (mean ± standard deviation) of three different artery types. Statistical difference ($P<0.05$) is indicated with an asterisk (*).

3.3.1.2 Coronary arteries

The coronary artery samples tested exhibited behaviour typical of biological soft tissues. The stress stretch data was highly non-linear, see Figure 3.3. The samples, initially highly distensible, stiffen continually as the load is increased. Pre-conditioning the arteries lead to repeatable stress-

strain behaviour within 5 cycles, as demonstrated in Figure 3.3. The arteries show high variability in behaviour, both between samples and between animals. This is seen in the ultimate tensile strength, stiffness, and rate at which the artery stiffens as the collagen fibers are recruited. A comparison of the tests in the longitudinal (tensile, see Figure 3.4) and circumferential (ring tests, Figure 3.5) demonstrates the anisotropy of the material. Note that the stress strain curves show material behaviour after pre-conditioning.

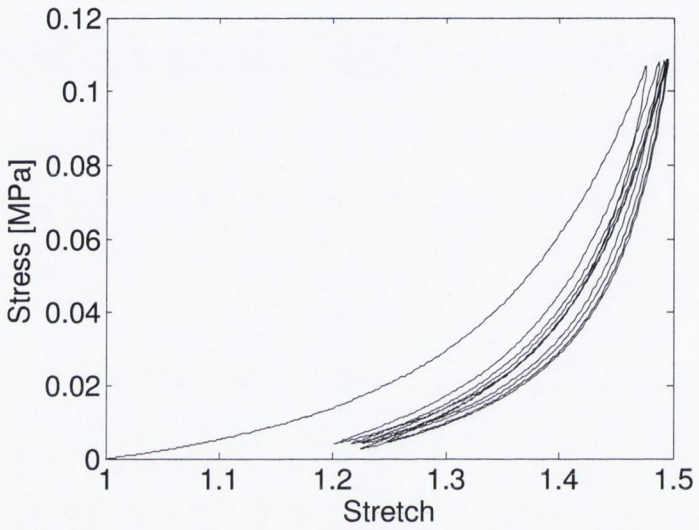


Figure 3.3

Typical pre-conditioning cycles for porcine arteries.

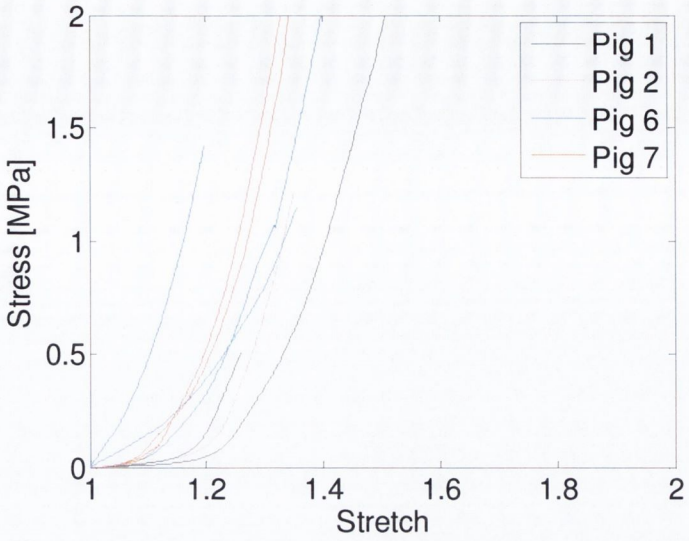


Figure 3.4

Stress-stretch curve for tensile tests on coronary arteries in the longitudinal direction.

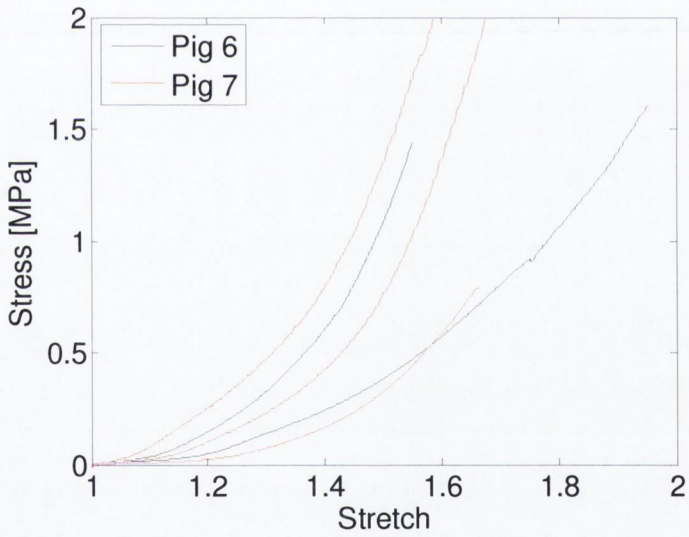


Figure 3.5

Stress-stretch curve for circumferential ring tests on coronary arteries.

3.3.1.3 Femoral arteries

As peripheral arteries were of primary interest for this study, more femoral artery samples were tested than coronary arteries or aortas. This allowed a more comprehensive profile of the

mechanical behaviour of the arteries to be studied. As with the coronary arteries, the femoral arteries show non-linear behaviour (Figure 3.6 and Figure 3.7). As more femoral arteries were tested than coronary arteries, a greater range of material behaviour is seen in the former. Note that for compressive tests, the results are presented as positive stresses and strains by multiplying the values by -1. This enables more direct comparison with the tensile tests.

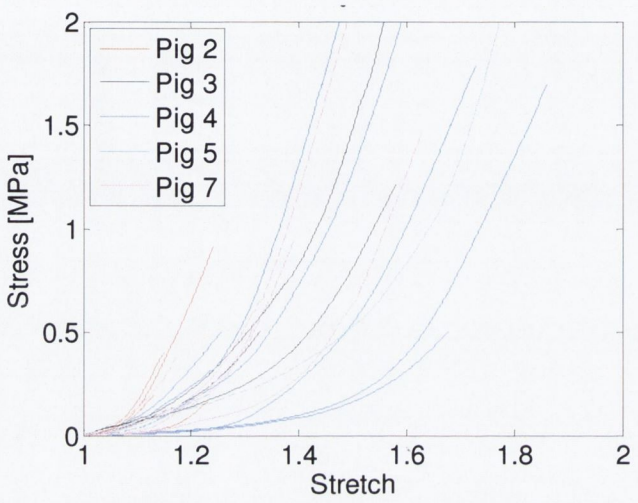


Figure 3.6

Stress-stretch curve for tensile tests on femoral arteries in the longitudinal direction.

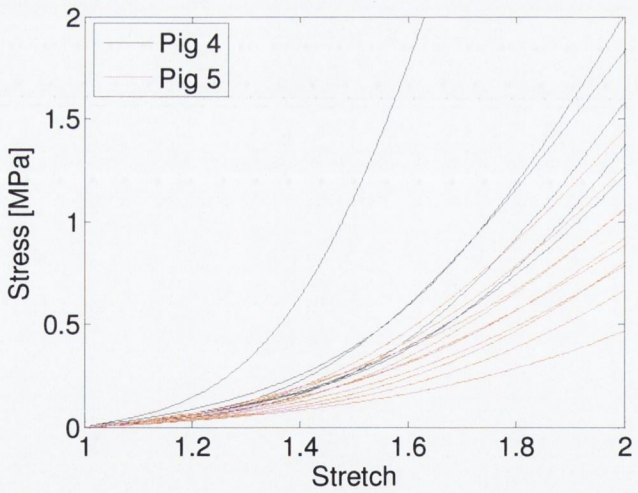


Figure 3.7

Stress-stretch curve for compressive tests on femoral arteries.

3.3.1.4 Aorta

The aorta was the only vessel large enough to allow suitably sized circumferential strips to be tested without the need for ring tests, and so the circumferential and longitudinal properties

could be compared for identical tensile tests. The results show that the aorta is slightly stiffer in the circumferential direction (Figure 3.8 and Figure 3.9). This is different to the coronary artery, where the arteries are stiffer in the longitudinal direction. The longitudinal samples also show less non-linearity, and fail at a lower stress.

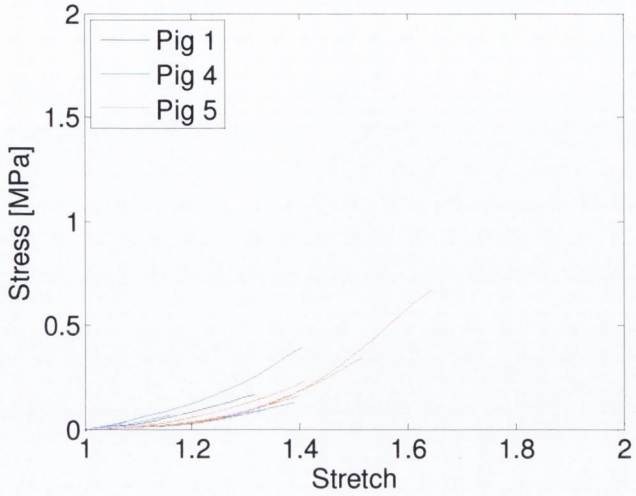


Figure 3.8

Stress-stretch curve for tensile tests on aorta in the longitudinal direction.

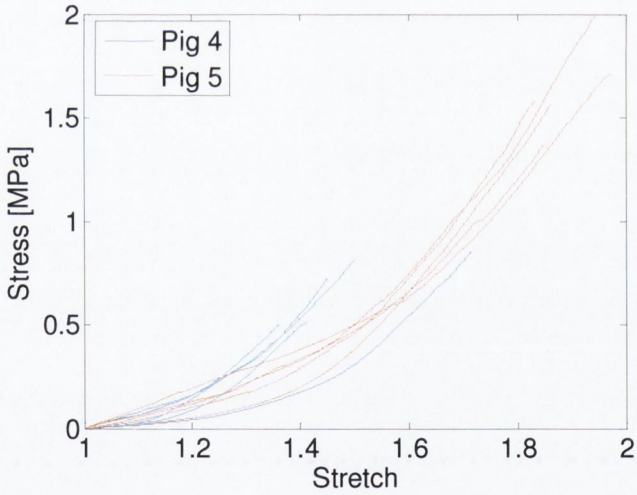


Figure 3.9

Stress-stretch curve for tensile tests on aorta in the circumferential direction.

3.3.2 Curve Fitting

In order to determine an appropriate constitutive material model, several of the commonly used models were compared, as shown in Figure 3.10. The Fung, Gent, Ogden and Mooney-Rivlin models describe the behaviour of hyperelastic arteries to varying degrees of accuracy. Comparisons can be made by looking at the error in the model (the difference between the stress

provided by the constitutive model for a given strain and the data), see Table 3.2, Table 3.3, Table 3.4, and Table 3.5. For a range of arteries, it was found that the Ogden and Third-Order Mooney Rivlin models provided the best fit for the data (the intima of a human coronary artery, [Holzapfel *et al.* 2005]), see Figure 3.10. However, it should be noted that the variation between the different models was small compared with the variation between specimens, even from the same animal.

The Mooney-Rivlin model was selected, as it provided good accuracy, was stable with positive coefficients, and was easily implemented in commercial finite element software.

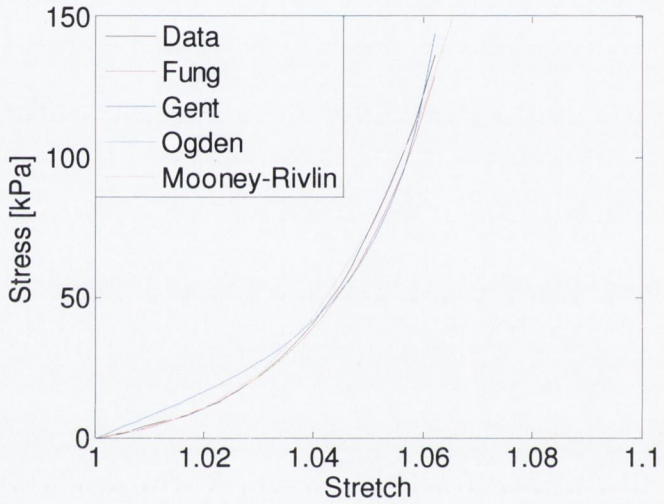


Figure 3.10

Fitting constitutive equations to human coronary intima stress-strain data. Data taken from [Holzapfel et al. 2005]

	Intima	Media	Adventita
α	325.667	3.756	6.298
β	48.257	17.951	25.979
Error	2.902	11.502	11.251

Table 3.2

Constants fitted to Fung model for human coronary intima, media and adventitia. Error provided is absolute error.

	Intima	Media	Adventita
M [kPa]	260.343	21.620	23.875
J_m	0.016	0.328	0.143
Error	25.365	23.220	11.300

Table 3.3

Constants fitted to Gent model for human coronary intima, media and adventitia.Error provided is absolute error.

	Intima	Media	Adventita
μ_1	29727.71	0.047247	0.000469
μ_2	29727.71	0.047247	15.36124
α_1	0.143567	25.56693	60.99805
α_2	0.143567	25.56693	7.78844
Error	36.3707	16.08216	4.771

Table 3.4

Constants fitted to Ogden model for human coronary intima, media and adventitia.Error provided is absolute error.

Constants [Pa]	**Intima**	**Media**	**Adventita**
C_{10}	84237.8	3555.26	7146.48
c_{01}	5057.85	662.391	636.828
C_{20}	765063	18684.4	95792
C_{11}	1.5e6	21548.3	8035.15
C_{30}	42380.6	19774.6	99314.9
Error	7.302	24.457	4.596

Table 3.5

Constants fitted to third-order Mooney-Rivlin model for human coronary intima, media and adventitia. Error provided is absolute error.

The average values for the Mooney-Rivlin constants for each artery and test type were obtained. The strain-energy functions obtained by this method were plotted against the test data. An example of this is seen in Figure 3.11. Each artery type and test then had a set of constants (see Table 3.6), which allowed a plot of the average stress strain curves for each artery, see Figure 3.12. The benefit of having an average curve for each test type is that different artery types can be compared directly, as demonstrated in Figure 3.12. In the longitudinal direction, the coronary artery is the stiffest, the aorta the least stiff, and the femoral artery is between the two (Figure 3.12). The anisotropy of the coronary artery and the aorta can be seen by comparing the behaviour in the longitudinal and circumferential directions. The coronary artery is stiffer in the longitudinal direction than the circumferential direction, whereas the aorta is stiffer in the circumferential direction. Also, a difference in the material response is seen in the femoral artery between tension and compression, where the artery is seen to be significantly less stiff in compression than in tension. Note that the compressive stress-strain curves are presented as positive so that a direct comparison can be made with the tensile counter-parts.

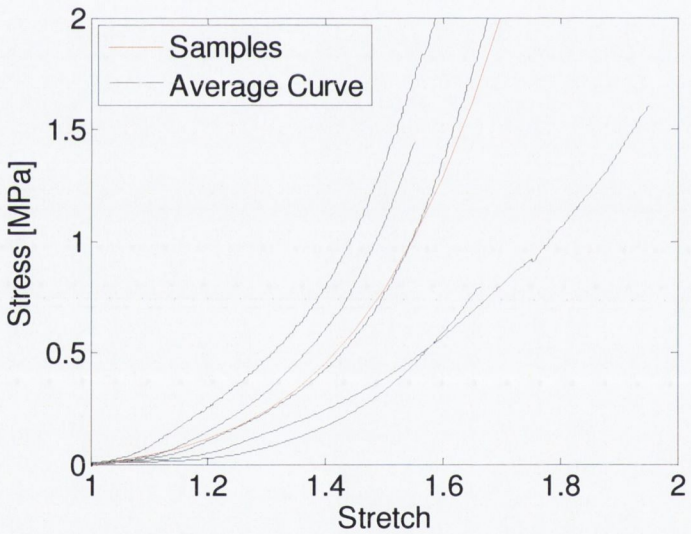


Figure 3.11

An example of stress-strain data (circumferential porcine ring tests) and a representative curve obtained by taking the average constants of the Mooney-Rivlin curves.

	Femoral (long.)	Femoral (comp.)	Coronary (long.)	Coronary (ring)	Aorta (long.)	Aorta (Circ.)
C_{10}	0.044943	0.005352	0.076116	0.021613	0.029342	0.021925
c_{01}	0.026398	0.022095	0.0281	0.054419	0.002369	0.065854
C_{20}	0.391715	0.022939	0.860027	0.140615	0.038586	0.112501
C_{11}	0.524977	0.131445	0.660409	0.078754	0.197393	0.192119
C_{30}	0.397492	0.000391	0.961346	0.083516	0.014235	0.095434

Table 3.6

Average third-order Mooney-Rivlin constants for porcine aorta and femoral and coronary arteries.

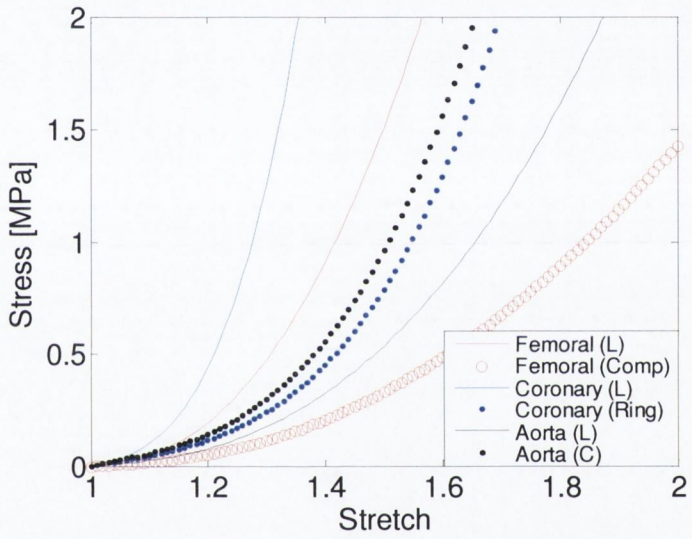


Figure 3.12

Average curves for each artery and test type using constants shown in Table 3.6. *(Note: L = longitudinal, Comp = compressive and C = circumferential).*

3.3.3 Biochemical analysis

Results obtained from the biochemical assays were expressed as a percentage of dry weight. While the elastin content could be ascertained directly from the assay, collagen content was measured indirectly, by measuring hydroxyproline quantities. All assays were measured in triplicate, and samples where the duplicates exceeded ±10% of the mean value were discarded. This was applied to the standards as well as the samples, and only standard curves with R^2 values greater than 0.95 were considered.

3.3.3.1 Collagen content

The coronary arteries analysed had the highest amount of collagen, with 37.37 %, see Figure 3.13 and Table 3.8. The femoral arteries and aortas had averages of 21.79 and 22.09 % collagen respectively. Statistical difference was found between the coronary artery and both the other arteries, but not between the femoral artery and the aorta (Figure 3.13).

3.3.3.2 Elastin content

The aortas were found to have an elastin content of 17.73 ± 5.14 %. This was greater than the coronary (12.22 ± 2.91 %) and femoral (11.71 ±3.27 %) arteries, see Figure 3.14. Statistically significant differences were observed between the aorta and the coronary and femoral arteries, but not between the coronary and femoral arteries, see Figure 3.14.

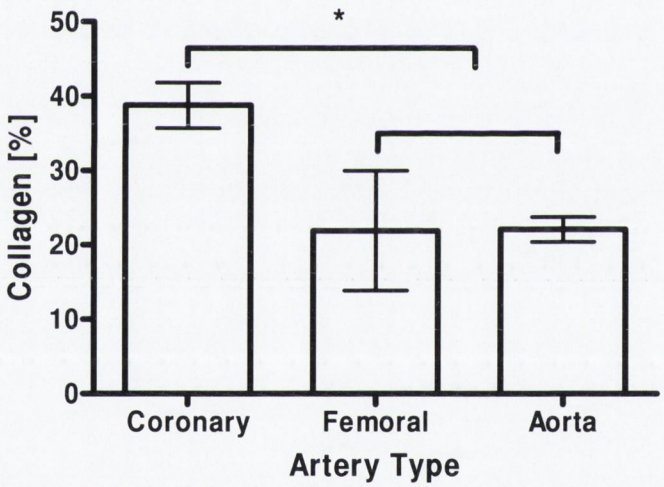


Figure 3.13

Collagen content (mean ± standard deviation) of three different artery types as a percentage of dry weight. Statistical difference ($P<0.05$) is indicated with an asterisk (*).

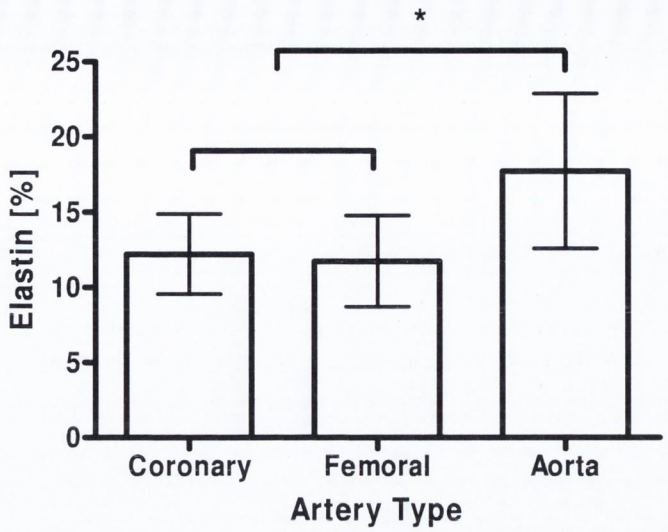


Figure 3.14

Elastin content (mean ± standard deviation) of three different artery types as a percentage of dry weight. Statistical difference (P<0.05) is indicated with an asterisk (*).

3.3.3.3 Collagen elastin ratio

It has been proposed that the ratio of collagen to elastin is related to the distensibility of arteries [Fischer *et al.* 1966]. Therefore, the collagen to elastin ratio (C:E) of the three artery types is presented, see Figure 3.15 and Table 3.8. Statistical differences in C:E were observed between all of the artery types (Figure 3.15).

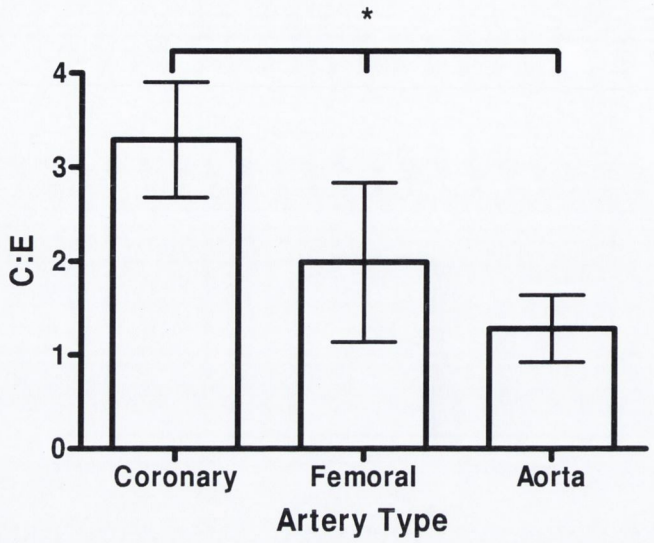


Figure 3.15

Collagen to elastin ratio (C:E) (mean ± standard deviation) of three different artery types. Statistical difference (P<0.05) is indicated with an asterisk (*).

3.3.4 Histology

The histology slides show the distribution of the composite elements within the artery walls. By highlighting the collagen, elastin and smooth muscle tissue in different colours (see Table 3.7 the structure of each artery is highlighted.

In the coronary and femoral arteries, three distinct layers can be seen (Figure 3.16 a & b). The intima appears as a thin, rippled layer. The media is the most significant layer, with muscle fibers (yellow), collagen (red) and elastin (black) all visible. The adventitia of the coronary artery (Figure 3.16 (a)) is thicker, but less dense, than the femoral adventitia (see Figure 3.16 (b)). The intima, media and adventitia of the aorta are less distinguishable. Instead, small, repeating, concentric layers are seen, with little change in the amounts of collagen and elastin between the inside and outside, as shown in Figure 3.16 (c). The elastin (black) is most prominent in the aorta.

Tissue element	Colour
Elastic fibers	Blue black to black
Nuclei	Blue to black
Collagen	Red
Muscle and other	Yellow

Table 3.7

The tissue elements differentiated by the Verhoeff-van Gieson staining.

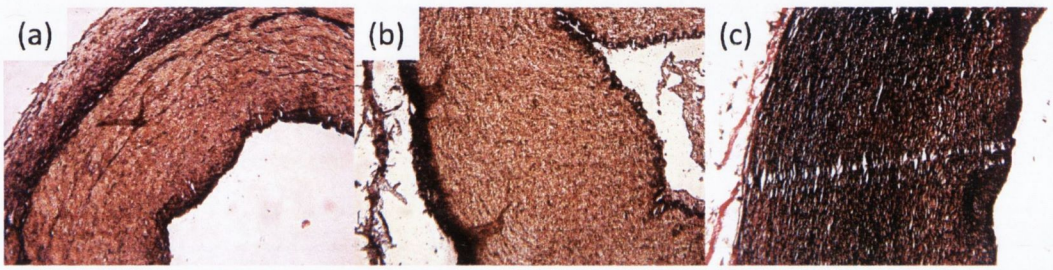


Figure 3.16

Typical histological slides of (a) coronary artery, (b) femoral artery and (c) aorta.

The structure and composition of the arteries can be compared with the average stress-stretch curves. The coronary artery, the stiffest of the three measured, has the most collagen (red) visible. The aorta, the least stiff of the three arteries, has the most elastin (black) visible.

3.3.5 Relating structure to function

One of the objectives of this study was to relate the structure of the artery to its function. In this case, the structure is the collagen to elastin ratio, and the function is the stress-strain behaviour. The Fung constitutive model was used to compare structure and function of the arteries studied, as it only contained two terms and provided a good fit to the data. Plots were made of the two parameters (alpha, α, and beta, β, which do not have a physical meaning) against the collagen content, elastin content and collagen to elastin ratio, see Figure 3.17.

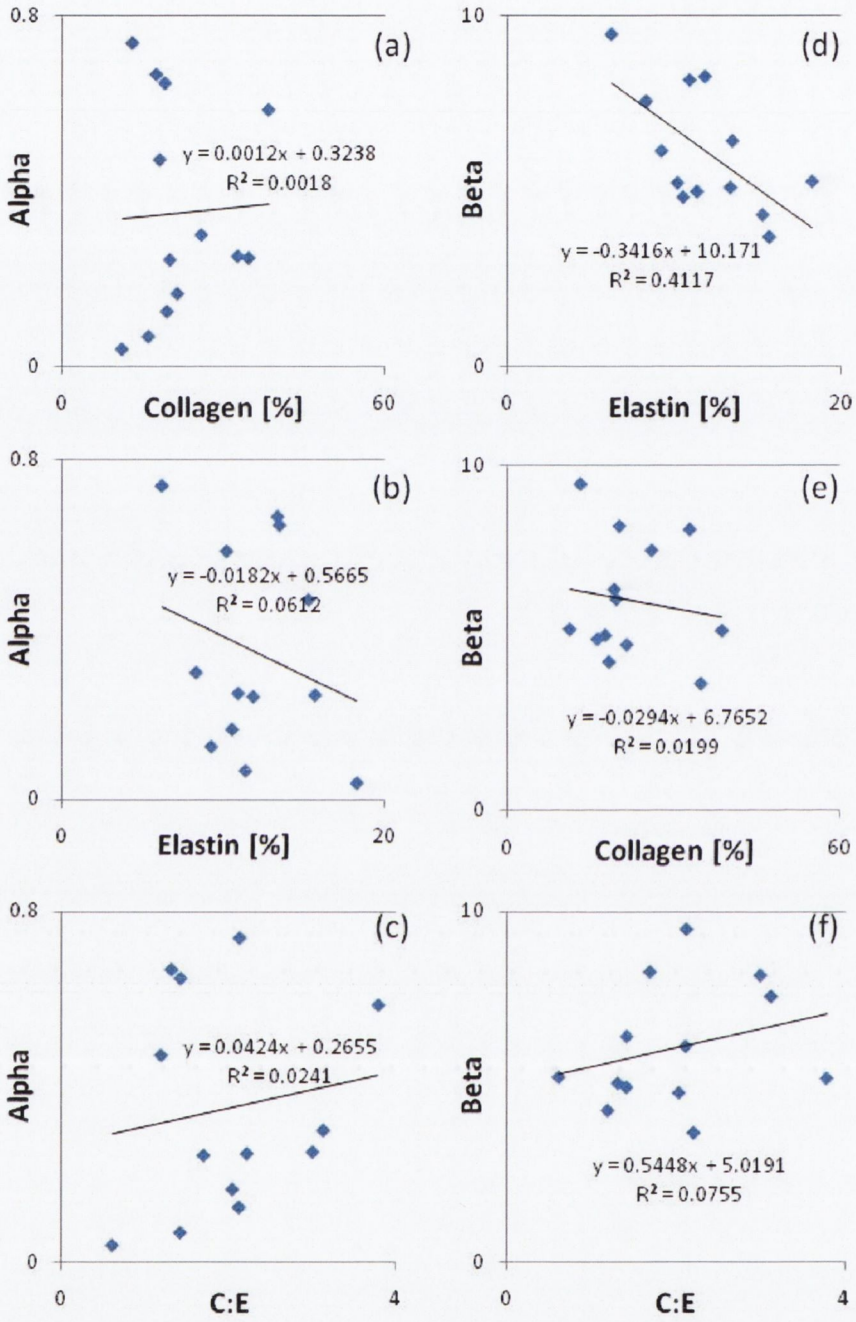


Figure 3.17

Correlation between alpha and (a) collagen, (b) elastin and (c) C:E, and beta and (d) collagen, (e) elastin and (f) C:E for the femoral artery.

Within artery types, there is no relationship between the stiffness of the artery and the collagen to elastin ratio. However, when average curves for each of the artery types are taken, the stiffest

artery (coronary) is shown to have the highest C:E ratio, while the least stiff (aorta) has the lowest C:E ratio Figure 3.18. No correlation is found between either of the two parameters from the Fung constitutive model (and) and the elastin content, collagen content or collagen to elastin ratio. The most notable trend was an inverse relationship between β and the elastin content, with no noticeable correlation between β and the collagen content. Both α and β appeared to increase with increasing C:E ratio.

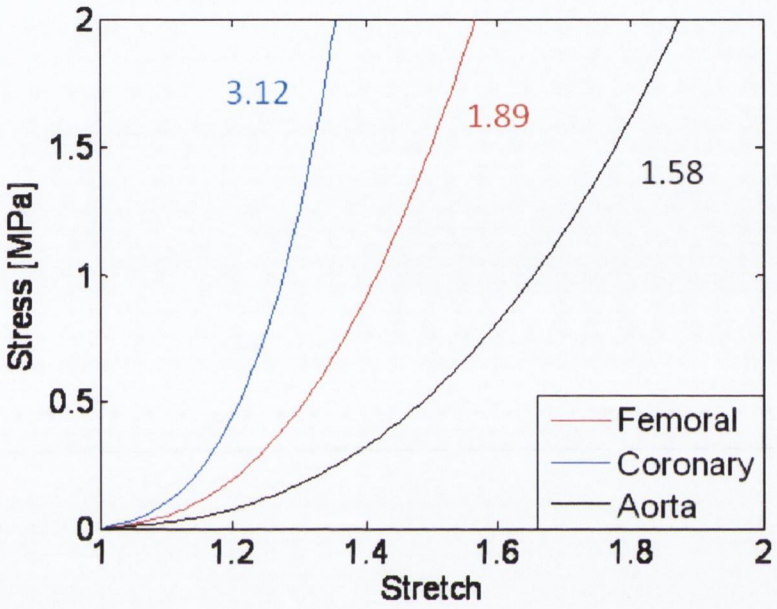


Figure 3.18

Average curves for femoral and coronary arteries and aortas with collagen to elastin ratios.

3.4 Discussion

3.4.1 Mechanical properties

All of the arteries tested exhibited mechanical properties typical of biological soft tissues, and in particular arteries. Large strains and non-linearity were observed before failure. This is to be expected in a material that can be modelled as stiff fibres (collagen) in a ground-matrix (elastin and smooth muscle). The highly distensible matrix, and in particular the elastin, are thought to bear the load at low forces [Roach *et al.* 1957]. As the load is increased, the collagen fibres are recruited in the direction of loading, and so begin to bear the load. As the load is increased, more of these fibres are recruited, and the material continues to stiffen. This behaviour is well documented in the literature [Fung *et al.* 1979; Fung 1981; Humphrey 2002; Humphrey *et al.* 2004]. The alteration of material behaviour with repeated loading, or preconditioning is also shown, where repeatable behaviour is only seen after a number of loading cycles.

Strong anisotropy was also shown for all of the artery types. For the femoral artery, a difference is seen between the compressive and tensile tests. Tests on the coronary artery and aorta produce differences in stiffness according to the direction, longitudinal or circumferential, of loading.

The test show that the femoral artery performs significantly differently in compression than in tension. This could be important for modelling stenting and angioplasty procedures, where accurate prediction of radial compressive forces could be important. Models exist which capture the anisotropy of arteries in tension, but not the difference in behaviour in compression. While data has been published on the tensile and compressive behaviour of plaques [Maher *et al.* 2009], the equivalent results for arteries are not currently available. The data presented herein suggests that further quantification of tension-compression non-linearity in arterial tissue is necessary.

The aorta is the only vessel that allowed a comparison between uniaxial tensile tests in different directions. The longitudinal samples were less stiff than the circumferential ones, and displayed less pronounced non-linearity and had noticeably lower failure strengths. The anisotropy shown suggests the fibres are more aligned in the circumferential direction, as has been seen with human aortic medias and adventitia [Holzapfel *et al.* 2002]. This may explain the less obvious non-linearity and the lower failure strengths. As the dog-bone samples had significantly greater lengths than widths, fibres perpendicular to the load may have been isolated during longitudinal tests. Hypothetically, if the fibres were all aligned perpendicular to the load, then the fibres would not bear load and the structure would demonstrate the mechanical properties of the matrix. More realistically, the fibres would be dispersed, so that a number of them would still be recruited in the direction of loading.

Unlike the aorta, the coronary artery was stiffer in the longitudinal direction, though the test types were not identical. This suggests fibres aligned more towards the longitudinal direction, as has been shown for human coronary artery intima and adventitia [Holzapfel *et al.* 2005].

A number of errors were associated with each test type. When carrying out uniaxial tensile tests, samples will slip from the grips during loading. The slip verification tests showed relatively small amounts of difference (maximum of 8% difference at 100% strain), but were only carried out on three samples. The amount of slip would be expected to depend strongly on the sample being tested. Ideally, all tests should have strain measured using a visual method.

Ring tests are a convenient method of testing smaller samples, where taking circumferential tensile samples is not feasible. This method does not have an exact finite solution, and owing to the necessarily small size of the samples, errors in measurement are proportionally greater. Stress concentrations are also found at the pins. The problem of sample slippage is eliminated with this testing method.

Samples cut for compressive tests showed a radially dependent pre-stretch. The tissue closest to the intima shrunk more than the tissue at the adventitial end, leading to deviations from the cylindrical punch shape; instead of having straight edges, the samples had a conical shape. Average measurements were taken of the diameter at different depths. This effect was more pronounced in the thicker aorta.

3.4.2 Curve fitting

All of the constitutive models investigated showed a good general agreement with the test data, either from experiments or from the literature. Generally, the variation between models was found to be considerably less than the variation between samples, which suggests that capturing the general material behaviour may be more important than predicting exact stress states (except in the case of patient specific studies). The Gent model, which had only two parameters, showed some higher error values at lower strains, and so was considered unsuitable. The Ogden and Mooney-Rivlin models produced very good data fits, and are available in most commercially available finite element software packages. The Mooney-Rivlin model was chosen for future studies, as it provided a good fit to the data, enabled average curves for each artery type to be plotted and was available in MSC Marc finite element software. The Ogden model would also have met these criteria.

3.4.3 Biochemical analysis

Collagen and elastin content in the three artery types studied differed from a similar study on canine arteries [Fischer *et al.* 1966], but the collagen to elastin ratios were very similar, see Table 3.8.

	Collagen	Elastin	C:E	C:E (Literature)
Coronary	37.37	12.22	3.06	3.12
Femoral	21.79	11.71	1.86	1.89
Aorta	22.09	17.73	1.25	1.58

Table 3.8

Collagen content, elastin content and collagen to elastin ratio for coronary and femoral arteries and aorta. The literature data presented is taken from a previous study on canine arteries [Fischer et al. 1966].

Collagen and elastin contents were calculated as a percentage of wet weight, with a water content of 70% assumed to obtain the dry weight percentages [Fischer *et al.* 1966]. This was so that samples could be frozen immediately to prevent tissue degradation. Though a change in water content would alter the relative amounts of collagen and elastin expressed as a percent of the dry weight, the C:E ratio would remain the same.

For all of the biochemical analysis, some error could be expected from pipetting very small quantities of liquid. However, the standard curves all showed very good and consistent fits. The assumption of a collagen to hydroxyproline ratio of 10:1 means that this assay is not as accurate as directly measuring the collagen. This ratio was used because individual ratios were not available for each of the artery types measured.

Because collagen and elastin could not be measured from the same sample, each tested sample was cut in two. The continual variability of artery samples means that each half would not be exactly representative of the whole.

3.4.4 Histology

Histology is useful method for looking at the structure of arteries. Features such as the distinctive layers, the internal and external elastic laminas and the endothelial layer can be discerned, as well

as the repeating units seen in the aorta. It also allows areas of elastin, collagen and other tissue to be discerned.

The stiffest artery, the coronary artery, had large amounts of collagen (red) visible, while the aorta (the least stiff), was predominantly black (elastin). Detailed image analyses were not carried out, but this shows that generalisations about the material properties can be made from investigating the histology, i.e. materials with more collagen visible are stiffer, while less stiff materials would be expected to show more elastin.

These general observations are broadly similar to the results obtained from the biochemical analysis. However, the variability of histological results would bring into question the accuracy of using image analysis for the quantification of biochemical components. Over or under-exposure in the staining process could lead to one of the constitutive elements being over or under-represented. Quantitative histology has been used in previous studies, but with different staining protocols. Collagen and elastin can be stained using porcrosirius red and Verhoeff van Gieson [Hu *et al.* 2008], or hematoxyline and eosin and Miller's elastic stain [Fridez *et al.* 2003]. Based on the results presented here, it is recommended that appropriate assaying is the preferred method of determining the biochemical contents of arteries.

The hypothesis that the structure and composition of arteries, and in particular the collagen to elastin ratio, can be used to predict the behaviour of arteries provided mixed results. Comparing different artery types showed that the stiffest arteries (coronary) had a higher collagen to elastin ratio than the less stiff arteries (aorta), see Figure 3.18. Despite the order being the same, there was no clear relationship between the increase in C:E ratio and the stiffness. For example, there is a greater increase in stiffness between the aorta and femoral artery than between the femoral artery and coronary artery but with a smaller increase in C:E ratio. Also, the demonstrated anisotropy means that even comparing longitudinal tensile properties will incorporate differences in fiber orientation as well as differences in stiffness.

The aorta and the femoral artery have approximately the same collagen content (22.09 and 21.79% respectively), yet exhibit different mechanical behaviour. This reaffirms a suggestion previously proposed that the collagen to elastin ratio "*may be useful in establishing an index of relative distensibility*" [Fischer *et al.* 1966]. In other words, it is the ratio of the two components, rather than the relative amount of either, that is important. It can be speculated that the reason for the difference in behaviour between two materials (femoral artery and aorta) is the amount of elastin, which is higher in the aorta. The amount of elastin, and indeed the amount of smooth

muscle tissue in the matrix in which the collagen fibres are embedded may influence the behaviour of the collagen fibres in tension.

When comparing similar artery and test types, for example longitudinal tests on femoral arteries, no relationship is obtained between the C:E ratio and the stiffness. It was hoped that the C:E ratio could be related to the parameters of the Fung constitutive model, but this proved not to be the case. Although only the femoral longitudinal results are presented here, similar results were found for other tests. Other studies have focussed on the angles of the fibres, and incorporating this into an anisotropic model [Holzapfel *et al.* 2000], as detailed in Chapter 2.

3.5 Conclusions

The arteries tested showed the non-linear, anisotropic qualities expected of biological soft tissues, and were suitable for describing material behaviour for finite element models. Large variations were found between samples, even from the same animals at adjacent sites. Biochemical assays and histology were used to analyse the structure and content of the arteries. Assays gave accurate quantification of the constitutive elements of the arteries, in this case collagen and elastin. This enabled collagen to elastin ratios to be determined for each mechanical test, which in turn allowed the mechanical function of the arteries to be related to the structure. While the large variation of mechanical behaviour within arterial groups meant that a direct correlation between the collagen to elastin ratio and the stiffness could not be determined, between different artery types stiffer arteries were found to have higher collagen to elastin ratios. Ultimately, the composition was found to be a poor indicator of artery function, which suggests that factors such as fiber orientation may be just as important in describing material behaviour.

4 Modelling Arteries and the Stenting Procedure

Contents

4.1 Introduction 98
4.1.1 Background 98
4.2 Methods 101
4.2.1 Finite Element Analysis 101
4.2.1.1 Geometry 101
4.2.1.2 Material Properties 104
4.2.1.3 Boundary conditions 106
4.2.1.4 Parameter study 108
4.3 Results 109
4.3.1 Results analysed 109
4.3.2 Coronary arteries 109
4.3.2.1 Thick versus thin study 110
4.3.2.2 Stent design study 112
4.3.3 Peripheral arteries 113
4.3.3.1 Artery stresses 114
4.3.3.2 Lumen gain 114
4.3.4 Parameter study 117
4.4 Discussion 119
4.4.1 Stent expansion 119
4.4.2 Thick versus thin strut study 119
4.4.3 Influence of stent design on arterial stresses 121
4.4.4 Modelling stent expansion in peripheral artery 122
4.4.5 Parameter study 123
4.5 Conclusions 124

4.1 Introduction

This chapter investigates appropriate methods for modelling the expansion of a stent inside a human artery. As appropriate human tissue is difficult to obtain, porcine arteries are often used, both for pre-clinical trials and for finite element models. Pigs are used for such experiments because of the similarity between the cardiovascular systems of the species. The differences in pathological responses have also been studied extensively. However, few efforts have been made to quantify the differences in mechanical responses between pigs and humans. An understanding of such differences may be important in interpreting the results of pre-clinical trials. Here, the work carried out in Chapter 3 is compared with similar work based on human arteries. The Mooney-Rivlin models obtained in Chapter 3 were used in finite element models, and compared with similar models using human data. The consequences of using animal data were investigated in terms of the stresses induced in arteries using different stent designs.

4.1.1 Background

Pre-clinical testing of medical devices is essential for ensuring their functionality and safety, and is the first step in preparing a device for widespread use in humans. The three broad methods for use in pre-clinical testing are (i) computational modelling, (ii) laboratory bench testing and (iii) animal experimentation. While there are advantages and disadvantages to each of these methods, it is generally seen as desirable to obtain as much information as is possible from (i) and (ii) and less from (iii), owing to cost and ethical reasons. Furthermore, inter-species variations in biological, toxicological and mechanical factors mean that animal models will not always provide a suitable representation of the environment to be experienced by an implant *in vivo*.

Pigs are often used for pre-clincal testing of cardiovascular devices such as stents, angioplasty balloons, heart valves and grafts, owing to the similarity of the cardiovascular systems (see Touchard & Schwartz for refs). Porcine arteries also exhibit similar healing responses to human arteries, including inflammation [Touchard *et al.* 2006] and neo-intimal formation [Schwartz *et al.* 1990]. However, animal models for some medical devices may have little biomechanical relevance [Prendergast *et al.* 2001]. For example, the lower stiffness of porcine arteries has already been identified as potentially problematic, with particular reference to anostomotic connectors [van Andel *et al.* 2003]. This difference is exacerbated by the use of young (~ 6 months) pigs and aged (~ 60 years) patients. Also, the intima of human arteries continually thickens with age, even in the absence of atheriosclerosis [Velican *et al.* 1985]. Layer-specific testing has shown the intima to become mechanically dominant in humans (mean age = 71.5 years) [Holzapfel *et al.* 2005], and has provided useful data for implementation in finite element models [Capelli *et al.* 2008; Gervaso

et al. 2008; Zahedmanesh *et al.* 2009]. Some previous studies had disregarded the intima when modelling arterial behaviour, under the assumption that only the media and adventitia were mechanically relevant in healthy arteries [Holzapfel *et al.* 2000]. The usefulness of constitutive models obtained from animal data for the testing of stents has already been questioned [Holzapfel *et al.* 2005]. This issue has becomes particularly pertinent with the availability of comprehensive human data [Schulze-Bauer *et al.* 2003; Holzapfel *et al.* 2005]. More broadly, questions continue to be asked about the interpretation of results obtained in pre-clinical trials in a clinical setting [Lafont *et al.* 1998; Edelman *et al.* 1999].

Various aspects of stent design have been shown to affect clinical outcome [Grenacher *et al.* 2004; Morton *et al.* 2004]. One such design feature is the thickness of the stent struts. The ISAR-STEREO trial demonstrated that thicker struts induce higher rates of restenosis (25.8 %) than thinner struts (15.0 %) [Kastrati *et al.* 2001]. Finite element models based on this study have shown that the greater recoil seen with the thinner strut models causes lower stresses in the artery wall, which may explain the lower rates of restenosis [Zahedmanesh *et al.* 2009]. In a similar study, but with different stent designs and using rabbit arteries, no difference was found between thick (200 μm) and thin (125 μm) struts in early lumen thrombus or late intimal thickening [Garasic *et al.* 2000]. In an editorial in 'Circulation', a number of trials which compared first generation Palmaz stents with second generation stents were highlighted [Edelman *et al.* 1999]. Three of four trials showed less variability in terms of binary restenosis, percentage restenosis, minimum lumen diameter and late lumen loss between stent types than between the Palmaz trials. In another animal (pig) trial, three stent designs were found to have similar outcomes in terms of injury scores, cellular proliferation idexes, and adventitial areas after 7, 14 and 28 days [Taylor *et al.* 2001]. Randomised clinical trials in humans have shown that stent design is an important factor in determining the outcome [Kastrati *et al.* 2000]. This demonstrates that animal models may not always be a good indicator of the relative success or failure of stents, as the response may be different to that in humans.

The hypothesis of this study is that the failure of certain animal trials to predict long-term stenting outcomes in humans is due to differences in the mechanical properties of arterial tissue between humans and animals. Three studies were carried out to compare particular aspects of the mechanical response in human and porcine arteries. Two studies will be carried out to investigate the influence of stent design on human and porcine coronary arteries. The first of these will look at strut thickness, and will attempt to model the ISAR-STEREO trials [Kastrati *et al.* 2001]. The hypothesis of this study is that the thicker, stiffer intima seen in human arteries may cause greater variation in recoil of stents than porcine arteries according to stent design, which in turn

influences artery stresses and outcome. The second study will look at stent design, and compare the variation seen between stent designs in the two artery types. The intimal thickening seen in human arteries is again hypothesised to differentiate between the two artery types, in this case providing greater variability between stent designs in human arteries. The final study is to investigate the inter-species differences in terms of nitinol stents expanded in peripheral arteries. Here, the lumen gain, and change in lumen diameter during the cardiac cycle is investigated. Most importantly though, the objective of this study is to understand the differences between human and porcine arteries as an environment for stent placement, and to use this information to help interpret the results obtained from pre-clinical animal trials. This study will focus purely on the mechanical response caused by the stent-artery interaction, and will not study the consequences of variation in other factors such as haemodynamics or the pathological response to injury.

4.2 Methods

4.2.1 Finite Element Analysis

Finite element analysis was used to model the expansion of stents in human and porcine arteries. A commercially available finite element analysis software package, Marc/Mentat 2007 (MSC Software Corporation, Santa Ana, California), was used. Finite element models of stents and arteries were created, and the vessel stresses were analysed following stent expansion and following recoil. All models used an implicit single-step Houbolt solver, with friction-free, discrete contact unless otherwise stated. Large strain analysis with an updated Lagrangian procedure was used. Each load-case had fixed times of one second, consisting of 100 steps. Details of mesh-density studies carried out are given with each model presented.

4.2.1.1 Geometry

Models of coronary and peripheral arteries were used for the simulations. Each artery was idealised as a hollow cylinder. These cylinders were subdivided into three concentric hollow cylinders to represent the three layers (intima, media and adventitia) of the artery, as shown in Figure 4.1. The ratios were the same as those obtained from the original studies [Schulze-Bauer *et al.* 2003; Holzapfel *et al.* 2005], see Table 4.1. Symmetry was used where appropriate, depending on the stent type being used in the simulation. Marc type 84, 8-node elements with full and Hermann integration were used to mesh the artery. This element type enabled the use of a hyper-elastic material type. The (full) coronary artery model was discretised by 144,000 elements, with an equal number of elements in each layer.

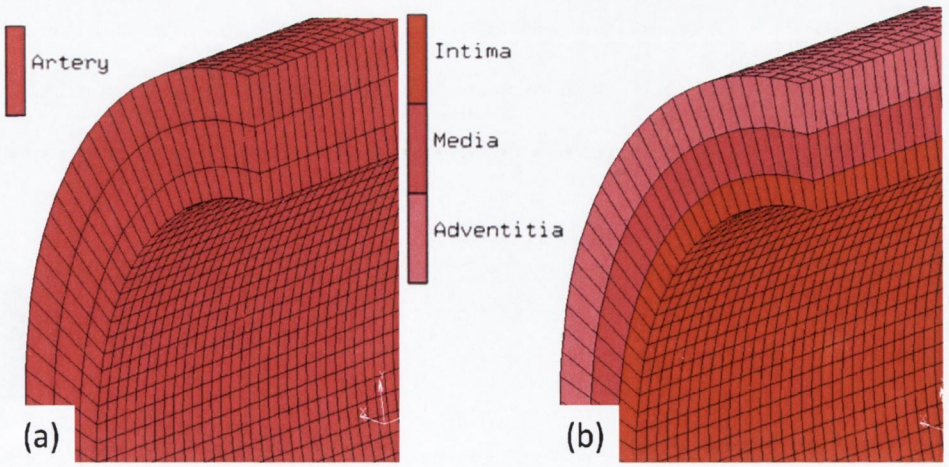


Figure 4.1

Geometry of (a) porcine and (b) human arteries.

	Coronary Artery	Peripheral Artery
Inner Diameter [mm]	3	8
Thickness [mm]	0.5	1
Length [mm]	20	40
Int:med:adv	27:36:40[1]	15:55:32[2]

Table 4.1

Dimensions of coronary artery models. Ratios taken from [1][Holzapfel et al. 2005] and [2][Schulze-Bauer et al. 2003].

To investigate the effect of stent design on arterial stresses, a number of stent designs were modelled for expansion in the arteries described above. To investigate the influence of strut thicknesses on arterial stresses, stent geometries based on the designs used in the ISAR STEREO Trials [Kastrati *et al.* 2001] were used. These were the ACS RX MultiLink (ML Thin) and the ACS MultiLink RX Duet (ML Thick), and were the same geometries as those used by Zahedmanesh *et al* [Zahedmanesh *et al.* 2009]. The two MultiLink designs had the same planar design, but had different strut thicknesses, see Table 4.2 and Figure 4.2. To reduce computational times, symmetry was used where possible. The Multilink models were not symmetrical in the longitudinal direction, but in the circumferential direction the design was repeated every 120°, so one third models could be used.

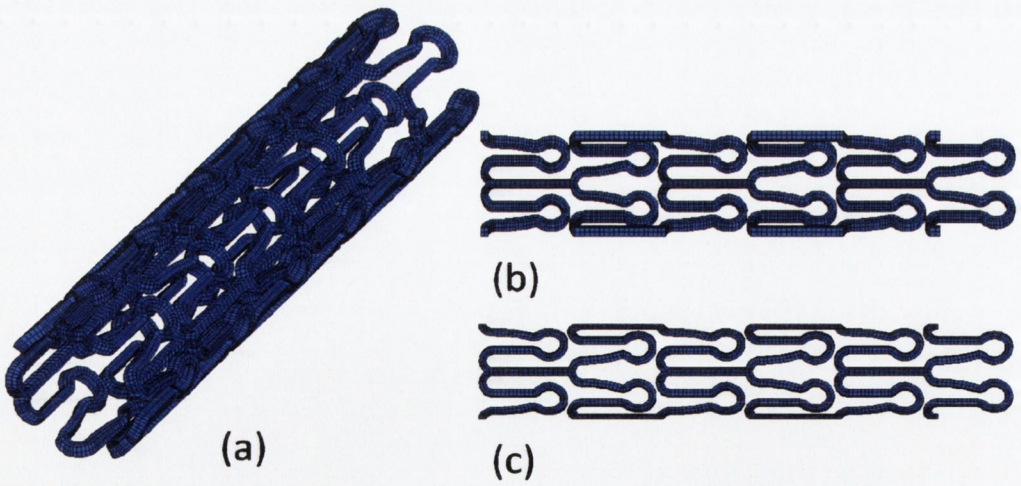


Figure 4.2

Geometry and mesh of MultiLink stent showing (a) complete model of ML Thick stent and one third segments modelled of (b) ML Thick and (C) ML Thin stents.

Two other stent types were modelled. One of these designs was based on the Palmaz stent, as shown in Figure 4.3(a). This was one of the first stents implanted in humans, and is based on a simple slotted tube geometry. The other model was based on the Cypher stent. The geometry for this stent was obtained from the Stent Research Unit at the University of Ghent [Gent], see Figure 4.3(b). All the stent models were meshed with Marc type 7 elements.

A nitinol stent model was also created for expansion in the peripheral artery. This was a generic version of the commercially available nitinol stents. Nitinol stents are initially at their fully expanded diameter, are compressed into sheaths and released in the artery, where they recover their original shape.

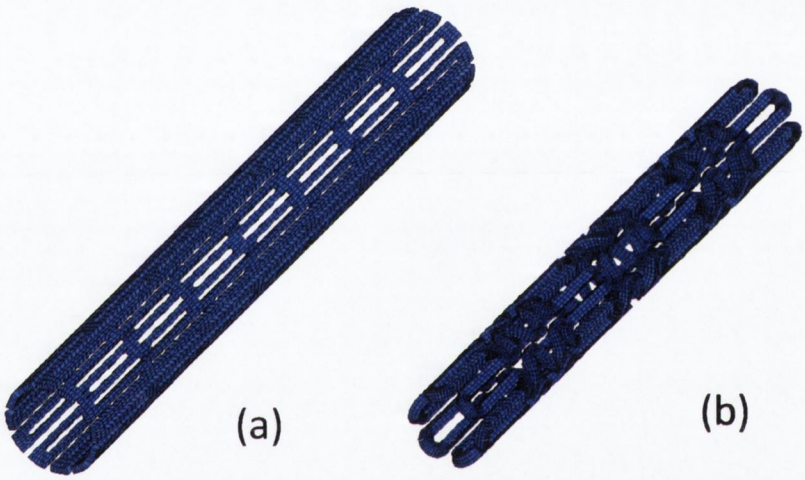


Figure 4.3

Geometries and meshes of (a) Palmaz and (b) Cypher stents.

	Length [mm]	Diameter (outer) [mm]	Strut Thickness [μm]	Repeating units (long x circ)	Symmetry	Target Diameter (inner) [mm]
ML Thin	7.2	1.72	50	3x3	1/3	3.75
ML Thick	7.2	1.54	140	3x3	1/3	3.75
Palmaz	10	1	100	8x12	1/4	3.75
Cypher	8.4	1.15	150	4x6	1/2	3.75

Table 4.2

Geometric properties of stents used in finite element models.

4.2.1.2 Material Properties

The arteries for the simulation were modelled as hyper-elastic by using third-order Mooney-Rivlin models. Data for the porcine artery models was taken from the circumferential ring tests described in Chapter 3. The porcine arteries were assumed to be homogenous. The absence of intimal thickening, the small size of the intima and the small variation in stiffness between the media and adventitia (see Chapter 3) means that this assumption is more valid for porcine arteries. The human arteries were modelled on layer-specific tensile tests carried out on aged (mean age of 71.5 years) human coronary arteries with non-atherosclerotic intimal thickening [Holzapfel *et al.* 2005]. Appropriate constants were fitted to the circumferential data from this study and used to describe the material behaviour in the finite element models (Figure 4.4 and Table 4.3). Note that the data is only available up to stresses of less than 150 kPa (depending on the layer), and that beyond these stresses, interpolation of the curves is assumed.

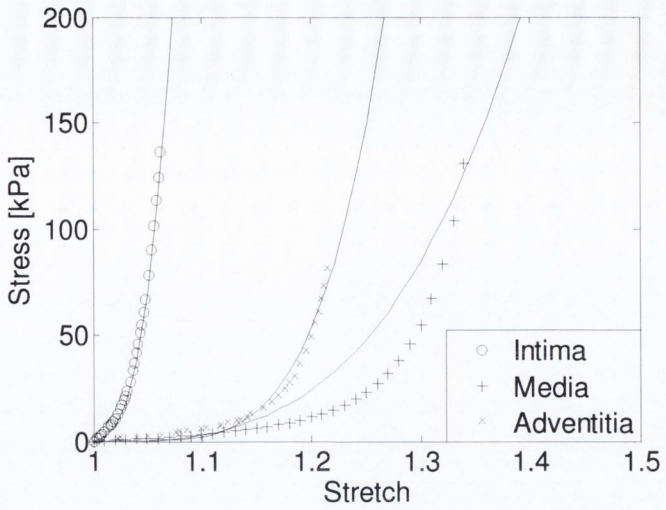


Figure 4.4

Stress-stretch curves for human arteries and third-order Mooney-Rivlin models fitted to data.

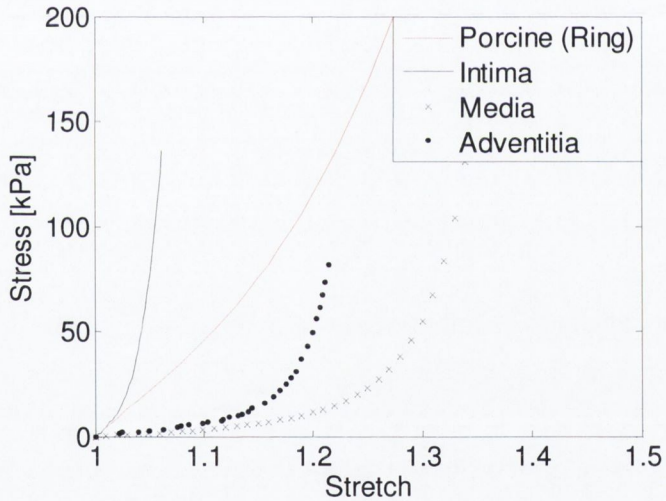


Figure 4.5

Circumferential stress-stretch data for porcine and human arteries.

Constants [Pa]	Intima	Media	Adventitia	Pig
C_{10}	84237.8	3555.26	7146.48	21613
c_{01}	5057.85	662.391	636.828	54419
C_{20}	765063	18684.4	95792	140615
C_{11}	1.5e6	21548.3	8035.15	78754
C_{30}	42380.6	19774.6	99314.9	83516

Table 4.3

Third-order Mooney-Rivlin constants fitted to data for human and porcine coronary arteries.

The material for the stents was 316L stainless steel. This was modelled as a bi-linear, elasto-plastic model based on stress-strain curves obtained from tests on micro-samples [Wiersma *et al.* 2006]. When modelling devices such as stents, it is important to replicate the behaviour of microscopic specimens rather than macroscopic specimens. This is because the dimensions of stent struts are of the same order of magnitude as the grains of the metal. This causes the microscopic specimens to have a lower tensile strength and a higher ductility than macroscopic specimens loaded in the same way [Wiersma *et al.* 2006].

The nitinol model implemented in the MSC Marc software is based on an algorithm developed by Auricchio *et al* [Auricchio *et al.* 2002], which describes the stress induced transformations in a three-dimensional model. The constants were taken from Favier *et al* [Favier *et al.* 2006], and have been used elsewhere in the literature [Wu *et al.* 2007].

4.2.1.3 Boundary conditions

Symmetry was applied where appropriate by applying symmetrical boundary conditions to any nodes that coincided with the planes of symmetry. Physiological boundary conditions were applied to the artery before stent expansion. An average blood pressure of 13.33kPa was applied to the internal faces of the artery, while a pre-stretch of 1.044 [Holzapfel *et al.* 2005] was applied to the ends of the arteries.

The stents were expanded by applying a linearly increasing pressure to the internal faces of the stents. This meant that the balloon was not explicitly modelled. This method was found to produce a non-uniform and/or incomplete stent expansion, depending on the stent design used. For example, the Palmaz stent opened at a greater rate at the ends than at the centre, and did not expand fully, while the Cypher stent expanded at a greater rate at centre than at the ends. This

problem was overcome with the use of spring elements (Figure 4.6(a)). A table input was used to give these springs a variable stiffness that is a function of displacement, see Figure 4.6(b). This means that the springs have a very low stiffness when the stent begins expansion. This stiffness increases once the stent reaches its nominal diameter, and restrains the stent from expanding beyond the specified diameter. The springs are attached at one end to nodes on the stent, and at the other to nodes that run longitudinally along the centre-line of the stent. To allow for longitudinal movement of the stent owing to foreshortening, the centre nodes were tied to nodes on the stent so that the springs remained perpendicular to the stent at all stages of stent expansion. Once the pressure is removed, any inward radial displacement will cause the spring to return to its low stiffness and allow recoil of the stent. This method replicates the restraint that would otherwise be provided by the balloon (stents will not, generally, expand beyond the diameter of the balloon), without the computational cost of modelling the balloon.

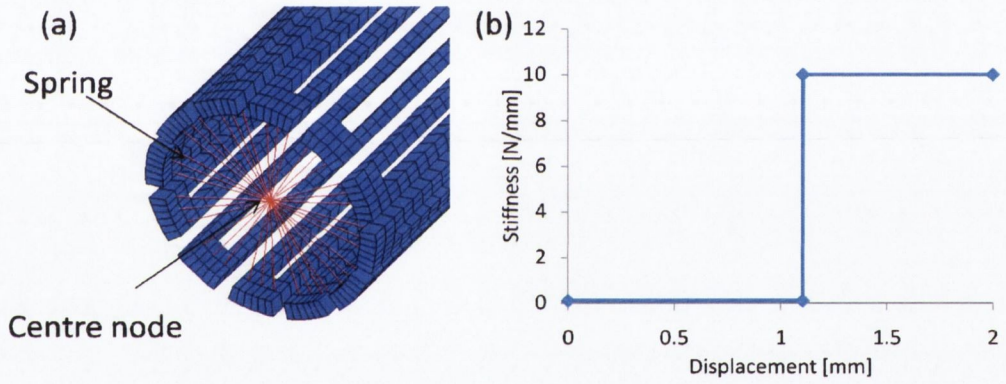


Figure 4.6

(a) Springs attached to stent and node at centre of stent

(b) Stiffness-displacement relationship for springs, similar to table input used to describe mechanical behaviour.

Nitinol stents were deployed by crimping the stents using a rigid sheath until they were of sufficient size to fit inside the artery. The stent was then deployed by withdrawing the sheath laterally and allowing the stent to expand. Full details of this method are detailed in Chapter 5.

It is considered that higher stresses lead to increased injury, and thus to higher rates of restenosis. The injury score suggested in the literature [Schwartz *et al.* 1994] can be related to failure of the tissue. Therefore, it was decided that the von Mises stress would be the most suitable measure of arterial stress. Each element consisted of eight integration points. By taking the average of each of these points, a single value of stress could be obtained for each element.

These values were accumulated, and the total volume of artery, or artery layer, within designated stress ranges was plotted. This gives an overall picture of the stress state of the artery following stent expansion. Contour bands and peak stresses were also measured. These are useful for identifying areas of high stress and therefore likely areas of restenosis. However, these peak stresses can be highly localised, and so results must be interpreted carefully.

To validate the mesh used for the artery, mesh density studies were carried out with the two artery types and the Palmaz stent. The number of elements in the artery was increased from 36,000 (in a one quarter model) to 72,000 and 288,000 elements. The differences in peak stresses were found to be less than 5% between all models, and the amount of arteries within specified stress ranges was less than 2%.

4.2.1.4 Parameter study

Previous and subsequent studies presented here use the average properties taken from mechanical tests. These would be expected to represent results from a population study. However, the data shown thus far has provided a wide spread of values, in geometric, biochemical and mechanical properties. In order to assess the consequences of this, the influence of the distribution of the mechanical properties is investigated. Plotting the expected cumulative frequency of the artery stresses for a given stretch against the observed cumulative frequency produced a curve with a slope of 1.09 and an R^2 value of 0.954. As such, normal distribution was assumed, so it can be said that 95% of data lies within $\pm 1.96\sigma$ of the mean. Therefore, by taking representative curves, more of the data can be represented, rather than just the mean. To investigate this, curves for the longitudinal stress-stretch data of the coronary and femoral porcine arteries were investigated. Using the Mooney-Rivlin constants, curves for the mean plus 1.96 standard deviations and the mean minus 1.96 standard deviations were plotted for the femoral and coronary arteries respectively. These curves represented the stiffest femoral arteries and the least stiff coronary arteries. This represents the worst case scenario in terms of the properties that would be expected to raise stresses in the femoral arteries relative to the coronary arteries.

The consequences of the variations in the data were analysed by expanding a Palmaz-Schatz stent using displacement control in two coronary and two femoral arteries with material properties described by the curves described above. The stresses induced in the arteries following stent expansion were analysed.

4.3 Results

4.3.1 Results analysed

The finite element models were analysed in terms of the recoil of the stent following removal of the inflation pressure, and the stresses induced in the arteries. Recoil was measured by taking the average displacement of the stent nodes following recoil relative to the fully expanded configuration. These values were compared for free expansion and within porcine and human artery models. The nitinol stents in the peripheral arteries were analysed in terms of the lumen gain and the change in diameter associated with the change in pressure between systole and diastole.

4.3.2 Coronary arteries

The mode of stent expansion depended strongly on the stent design. For example, the Palmaz stent showed initial dog-boning (with the ends opening before the centre). The Cypher stent also showed non-uniform expansion characteristics, but the centre opened before the ends. The MultiLink stents showed less regular behaviour, with dog-boning behaviour evident within individual cells rather than on the stent as a whole. However, although the expansion characteristics of each stent were different, all stents showed a uniform final shape at the specified diameter. See, for example, Figure 4.7

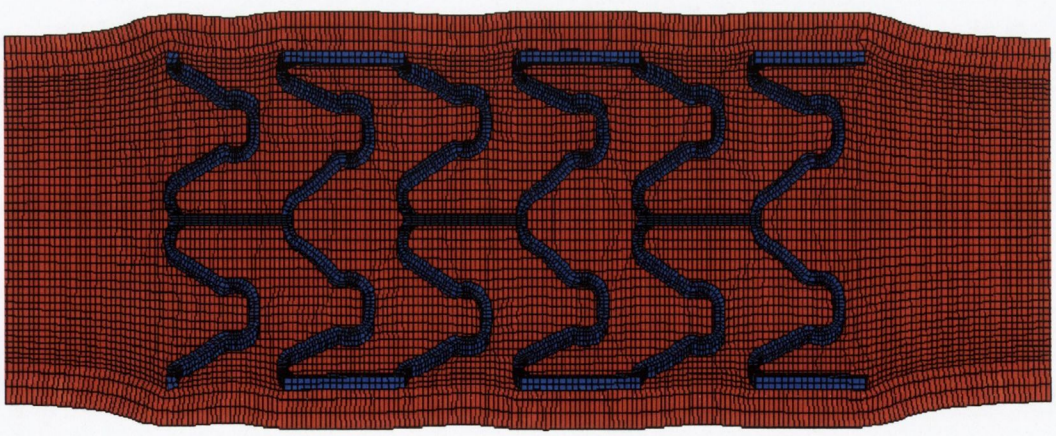


Figure 4.7

Fully expanded ML Thick stent in artery.

The irregular nature of the stent geometries means that even at their fully expanded configuration the stents do not have a single diameter value. Therefore, the average displacement of every node in the stent is used to give a single value of the diameter. While a single value is presented, it should be noted that there are areas of greater and lesser lumen gain within the artery. Values are presented following stent expansion (expansion) and after removal of the applied pressure when the stent has recoiled (recoil).

4.3.2.1 Thick versus thin study

All of the coronary stent models had a target diameter of 3.75 mm. Small variations in the final diameter were predicted, varying according to the stent model (thick or thin) and the artery type (porcine or human), see Table 4.4. Following removal of the pressure, the recoil of the stent was predicted to depend on the stent and artery types (human or porcine). The ML_{Thin} stent in the human artery had the highest recoil, of 7.998%, reduced to 5.151% in the porcine artery. The ML_{Thick} stent had recoils of 5.677% and 4.797% in the human and porcine models.

		Expansion	Recoil	% Change
Human	**Thin**	3.751	3.451	7.998
	Thick	3.752	3.539	5.677
Pig	**Thin**	3.747	3.554	5.151
	Thick	3.752	3.572	4.797

Table 4.4

Diameters for ML Thin and Thick stents following expansion and recoil in human and porcine coronary artery models.

Stresses in the intima of the human and porcine artery models were analysed. In the human artery, this was the stiffest layer, while in the porcine artery all three layers had the same material properties, and the division of the intima was purely geometric.

The fully expanded Multilink thick and thin stents (before recoil) induce similar levels of stress in each of the artery types (Figure 4.8). In the human coronary artery model, there is no greater than 2% difference in each stress range between the thick and thin models, see Figure 4.9(a). Likewise, the differences in stresses between the thick and thin stents following stent expansion are very small (<1% in each stress range) in the porcine artery, see Figure 4.9(b).

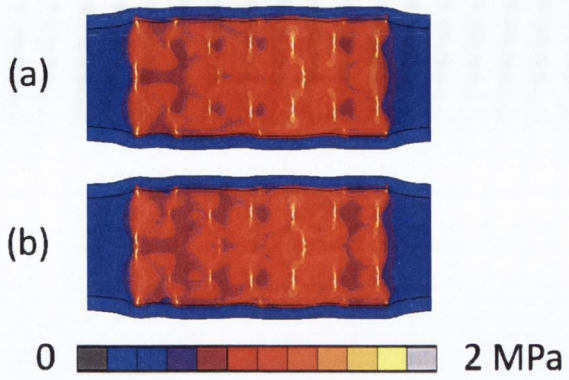


Figure 4.8

Von Mises stresses in human coronary arteries following deployment of (a) Multilink thick and (b) Multilink thin stents.

The human artery intima is predicted to be at higher stresses following stent expansion (ML_{Thick} and ML_{Thin}) than the porcine artery, see Figure 4.9(a) and (b). Less than 1% of the porcine artery is at stresses higher than 750 kPa (with none at stresses higher than 1MPa), compared with 23% for the human artery, with 2.5-3.9 % at 1 MPa or greater using ML_{Thin} and ML_{Thick}. While 62% of the porcine artery is within the lower stress ranges (0-250 kPa), this figure falls to 50% and 52% for ML_{Thin} and ML_{Thick} in the human coronary artery.

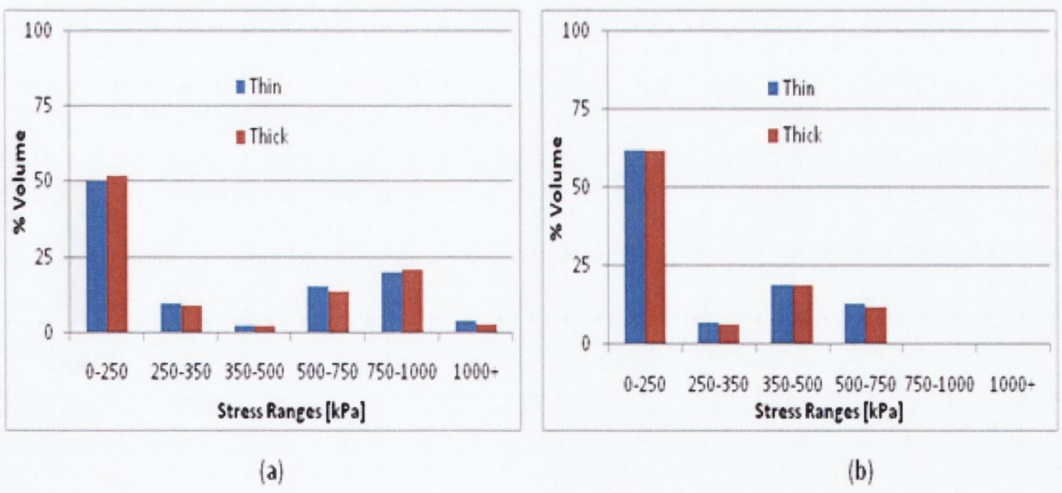


Figure 4.9

Stress distributions in (a) human and (b) porcine coronary artery models following expansion of Multilink thick and thin stents.

Following recoil of the stent, a greater difference was in predicted stress levels was observed between the ML_{Thin} and ML_{Thick} stents than at the maximum stent diameters following stent expansion. The ML_{Thin} stents, which recoiled more than the ML_{Thick} (Table 4.4) induced lower stresses in both artery types following recoil.

In the human intima, the amount of tissue at higher stresses (750-1000 kPa and 1000 kPa or greater) is reduced from 20.6% and 2.6% to 0.9% and 0.3% following recoil with ML_{Thick}, while the amount at mid stress ranges (350-750 kPa) is increased from 15.8% to 37.3%. With the ML_{Thin} model, the corresponding percent of tissue at 750-1000 kPa and 1 MPa or greater is 19.6% and 3.9% after expansion, reducing to 0.36% and 0.12% following recoil. The amount of tissue at stresses between 350 kPa and 750 kPa is increased from 17.1% to 21.8%.

Following recoil, the ML_{Thin} model induces lower stresses in the intima than the ML_{Thick}, with more of the intima in the lower and mid stress ranges (0-500 kPa), and less in the mid to high stress ranges (500 kPa or greater). For example, the ML_{Thin} model has 1.5% of the tissue in the 500-750 kPa range, compared with 25.8% using ML_{Thick}. However, at the higher stress ranges there is less of a difference, with ML_{Thin} placing 0.36% and 0.12% of the intima at stresses of 750-1000 kPa and 1 MPa or greater respectively. These numbers are higher with ML_{Thick}, 0.91% and 0.30% respectively.

In the porcine artery model, like in the human vessel, the ML_{Thin} induces lower stresses in the artery following recoil (Figure 4.10). Using ML_{Thick} places 19.2% and 3.0% of the intima between 250-350 and 350-500 kPa, reduced to 15.3% and 1.5% when using ML_{Thin}. Only small amounts of tissue, less than one percent, are at stresses of 500 kPa or greater in both models.

4.3.2.2 Stent design study

The predicted levels of arterial stresses following stenting depend on the stent design, as shown in Figure 4.11. The Palmaz Schatz (PS), Cypher and Multilink thick (ML) designs all had more tissue at lower stress (<350 kPa) in the porcine artery than in the human artery, while the human vessels have more of the intima at higher stresses (750 kPa or greater). In both the pig and human models it is predicted that the PS stent will induce the highest stresses in the intima, with the Cypher stent producing higher stresses than the ML.

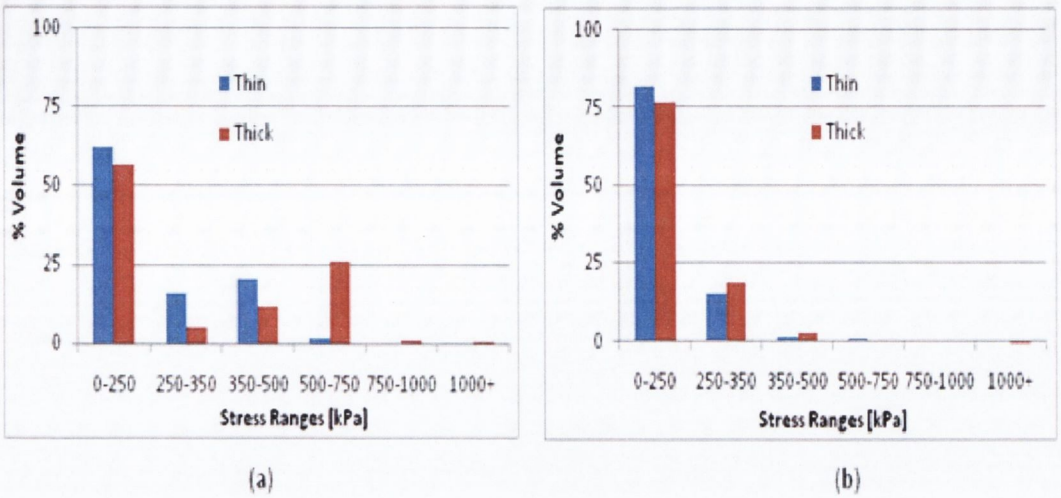


Figure 4.10

Stress distributions in (a) human and (b) porcine coronary intima models following recoil of Multilink thick and thin stents.

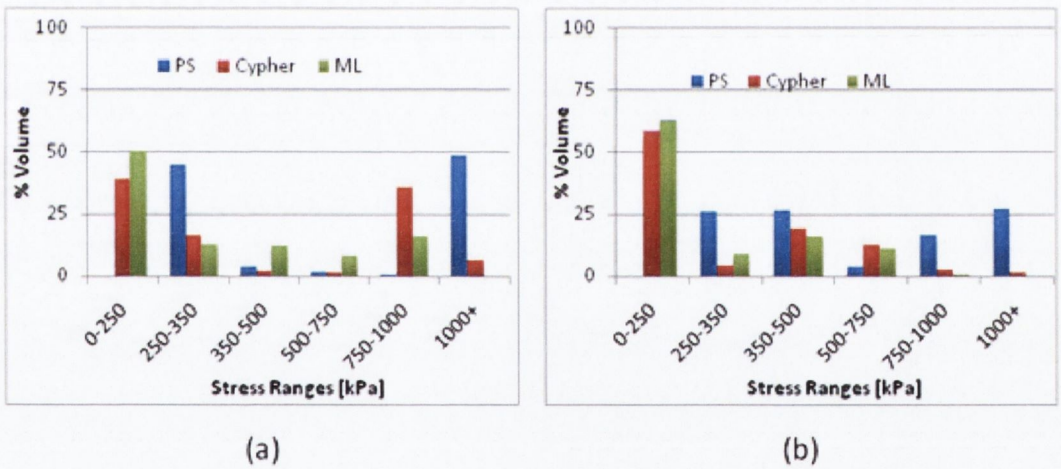


Figure 4.11

Von Mises stresses in the intimas of (a) human and (b) porcine coronary arteries following expansion of Palmaz-Schatz (PS), Cypher, and Mulitlink thick (ML) stents.

4.3.3 Peripheral arteries

The arterial stresses of all three layers were analysed for the expansion of a BES (Palmaz) in porcine and human peripheral arteries, and lumen gain and change in stent diameter was studied for the deployment of a SES in the same artery models. The SES in its stress free, initial configuration had the geometry of the expanded BES.

4.3.3.1 Artery stresses

As with the coronary arteries, the human peripheral artery had higher stresses in the intima than the porcine artery (Figure 4.12 and Figure 4.13). The porcine artery has 56.1% of the intima at stresses less than 300 kPa, compared with 35.1% in the human artery. The human intima also has more of the intima at higher stresses, with 47.9% at stresses of 500 kPa or greater compared with 7.9% for the porcine artery.

Although the intimal stresses are higher in the human artery, the stresses are higher in the media and adventitia of the porcine artery, as shown in Figure 4.12 (b) & (c) and Figure 4.13 (b) & (c). In the human artery, 99.8% of the tissue is at stresses of less than 150 kPa, and 9.6% of the porcine media is at similarly low stresses. All of the human adventitia is at stresses of 100 kPa or less (and 99.7% at less than 50kPa), with 8.7% of the porcine adventitia at such low stresses.

4.3.3.2 Lumen gain

The femoral artery stent diameters were measured in the same way as the coronary artery stents. However, the measurements were taken at systole and diastole, and the percentage change in diameter compared for the two artery types. The porcine peripheral artery model experiences higher lumen gain than the human equivalent at diastole (9.602 compared with 9.580) and systole (9.734 against 9.728), see Table 4.5. The stresses are also higher in the human peripheral artery, as shown in Figure 4.14.

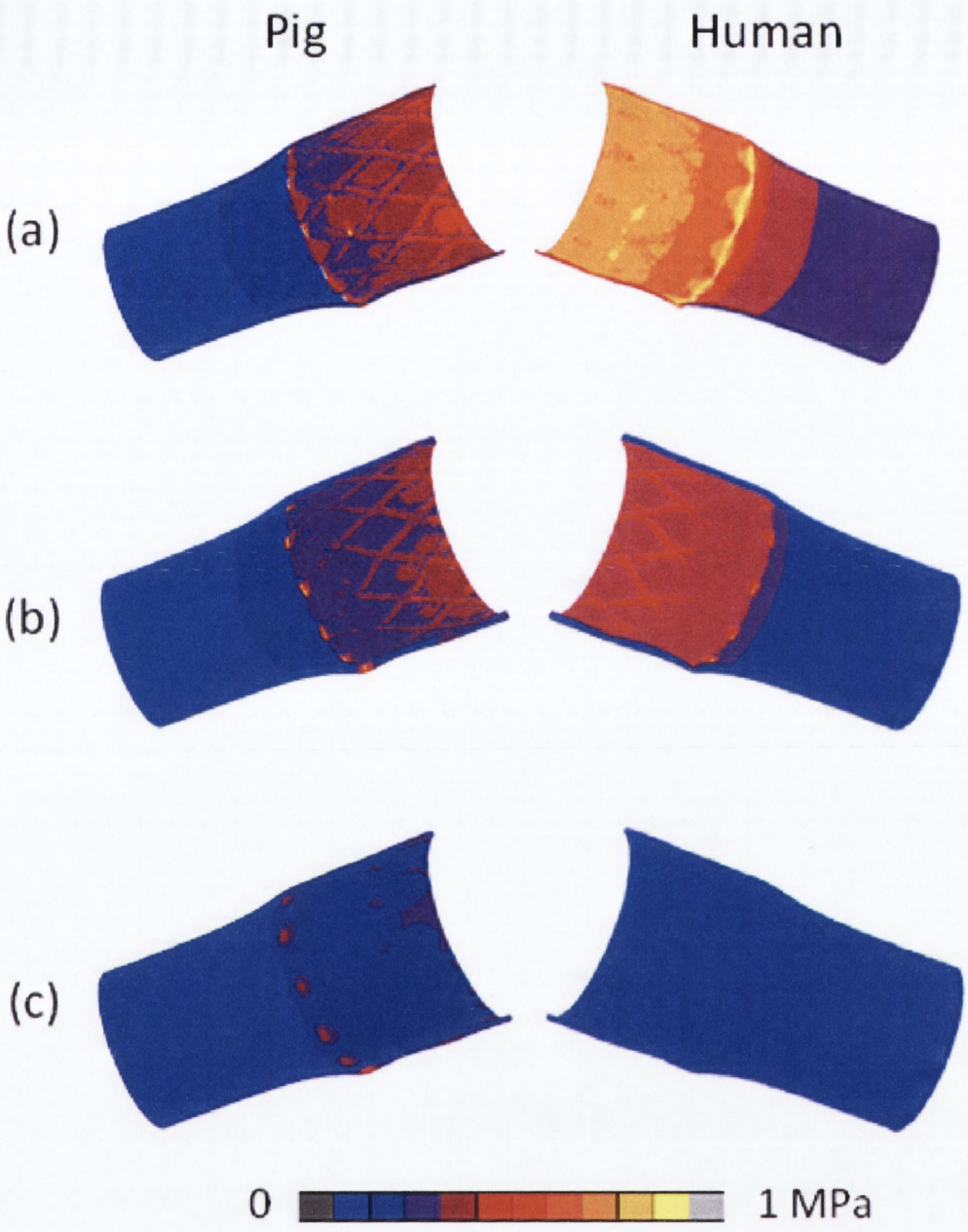


Figure 4.12

Contour plots of von Mises stresses in peripheral pig and human peripheral arteries following stent deployment showing individual layers. Shown are (a) the intima, (b) the media and (c) the adventitia.

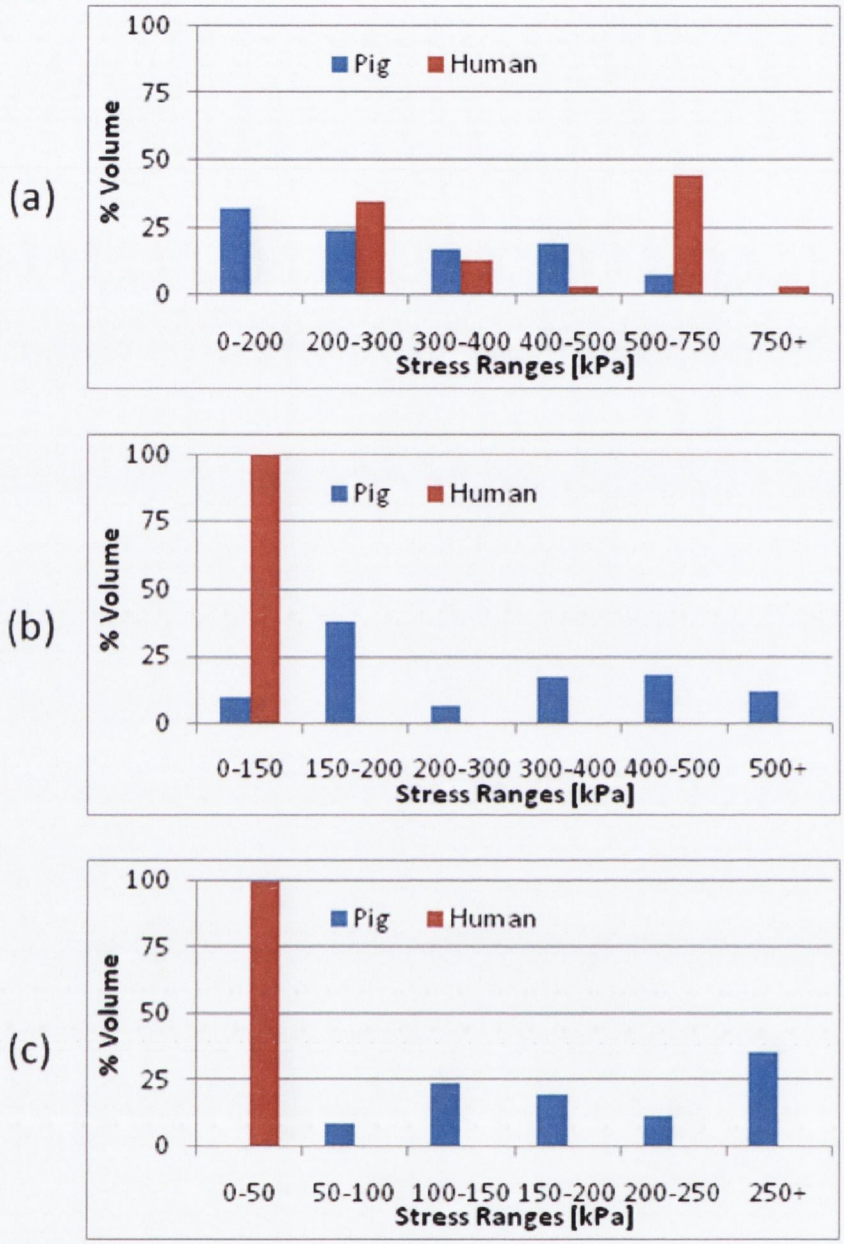


Figure 4.13

Stress distributions in pig and human (a) intima, (b) media, and (c) adventitia of peripheral arteries following deployment of Palmaz stent expanded to diameter of 10 mm.

	Pig	Human
Minimum diameter [mm] (diastole)	9.602	9.580
Maximum diameter [mm] (systole)	9.734	9.728
% Change diameter	1.378	1.545

Table 4.5

Stent diameters following expansion in peripheral artery at diastole and systole.



Figure 4.14

Stresses following nitinol stent deployment in peripheral (a) porcine and (b) human arteries.

4.3.4 Parameter study

The less stiff coronary artery (mean – 1.96σ) showed similar stiffness to the average femoral artery, but the stiffer femoral artery (mean +1.96σ) was stiffer than the average coronary artery, as shown in Figure 4.15.

Analysis of the arterial stresses predicts that the variation in the arterial properties significantly changes the arterial stresses. Comparing a stiffer femoral artery with the average coronary artery shows very similar amounts of the intima within each stress range, with the femoral artery having slightly more (33.8% compared with 27.5%) tissue at stresses of 750 kPa or greater (Figure 4.16). More of a difference is seen between the average femoral artery and the less stiff coronary artery, with 73.9% of the less stiff coronary at stresses of less than 200 kPa, compared with 50% for the average femoral artery. When considering the less stiff coronary artery and the stiffer femoral artery (the parameters which are most likely to predict higher stresses in peripheral arteries), the femoral artery has considerably higher stresses than the coronary artery.

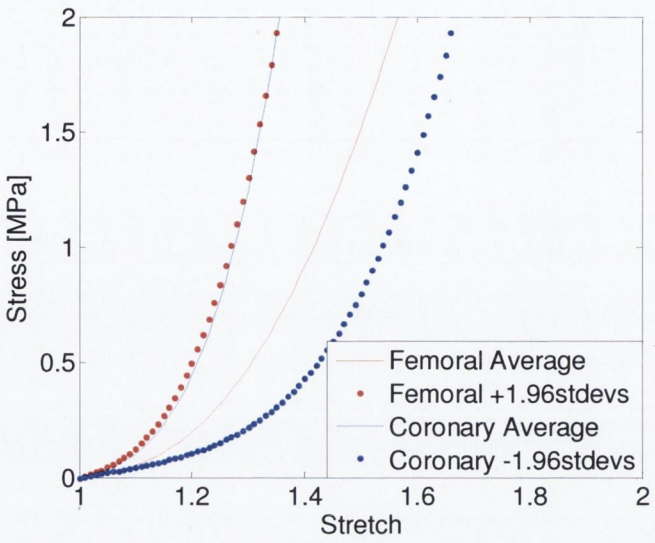


Figure 4.15

Stress-stretch curves for average coronary and femoral porcine arteries and mean coronary -1.96σ and mean femoral +1.96σ.

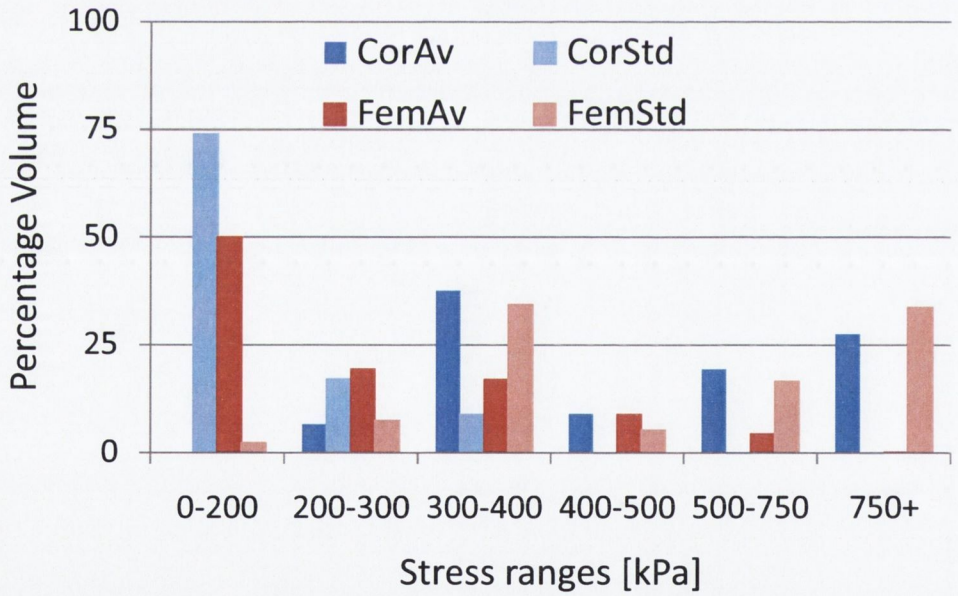


Figure 4.16

Stress distributions in the intimas of mean and mean ±1.96σ arteries.

4.4 Discussion

4.4.1 Stent expansion

The method used to model the expansion of the stents, whereby pressure is applied directly to the stents and springs are used to replicate the restraint of the balloon, provides diverse results, depending on the stent design used. Stents inflated *in vitro* or *in vivo* expand at the ends first, followed by full and, depending on balloon compliance, uniform expansion. Here, the path taken during expansion is markedly different according to the type of stent being modelled. The Palmaz stent opens at the end first, and is the only stent model which replicates the expected behaviour of balloon expanded stents. The Cypher stent opens at the centre first, as has been documented in previous studies [De Beule *et al.* 2008; Gervaso *et al.* 2008]. The two Multilink designs, ML_{Thick} and ML_{Thin}, exhibit more irregular behaviour, where a dog-boning effect is seen within individual cells of the stent rather than in the stent as a whole. In all cases, near uniform, cylindrical expansion results. A previous study has highlighted the importance of fully modelling the balloon-stent-artery procedure in order to accurately predict the arterial stresses following stent expansion [Gervaso *et al.* 2008]. While this spring-constrained model has not been compared to a full balloon-stent-artery model, it is believed that this method provides a good method that satisfactorily captures the arterial stresses with reduced computational time. It also has the advantage, unlike using displacement boundary conditions, of being able to model stent recoil.

Stress-stretch data for the arteries studied is only available for lower stresses (<150 kPa), whereas the stresses seen in the model are considerably higher (>1MPa). Interpolation from the curves is assumed, and this may not reflect the actual material behaviour.

4.4.2 Thick versus thin strut study

The results of this study highlight the mechanical differences between using thick and thin strut stents in arteries. In each artery type (pig and human), there is very little difference in the stress induced in the artery between the two stent types, ML_{Thin} and ML_{Thick} following stent expansion. This is to be expected as, aside from the strut thickness, the stent designs are identical. Therefore, at the same specified diameter, they would be expected to induce the same stresses in the artery. The difference seen between the two could be explained by small variations in the expanding profile of the stents caused by the different thicknesses. A similar study comparing strut thicknesses reported lower stresses using ML_{Thin} following stent expansion [Zahedmanesh *et al.* 2009]. This study used stenosed arteries and had different arterial geometry compared with this

study. These differences may have caused further differences between opening profiles and final deployed shape, which would alter the stresses in the arteries.

Stresses are predicted to be higher in the intima of the human coronary artery than the porcine coronary artery following deployment of the same stent type. This can be explained by the stiffer intima of the human artery experiencing higher stresses at the same strain than the porcine artery. However, stress distribution patterns and the location of peaks stresses are very similar in the two artery types.

Using a stent with thinner struts increases the amount of recoil following removal of the expansion pressure. This increase in recoil, and associated loss of lumen gain, reduces the stresses in the artery. This decrease in tissue at high stresses could explain why the ISAR-STEREO trial showed that using a thin strut stent produced lower rates of restenosis [Kastrati *et al.* 2001], and reaffirms the findings made elsewhere [Zahedmanesh *et al.* 2009].

The type of artery (porcine or human) affects the amount of recoil the stent undergoes, and thus the stresses in the artery following recoil. The stiffer intima of the human coronary artery causes a greater reaction force against the stent following removal of the expansion pressure. As a result of this, although both artery types show lower intimal stresses following recoil when using ML_{Thin}, the difference is more evident in the human artery as a result of greater recoil. This suggests that the porcine arteries are not as sensitive in their mechanical response as human arteries, and may not differentiate between stent types in the same manner as human arteries. This may explain why some pre-clinical trials using animals have failed to differentiate between thick and thin struts [Garasic *et al.* 2000], while human trials have shown lower restenosis rates with thin strut stents [Kastrati *et al.* 2001; Pache *et al.* 2003].

The lower stresses in the artery seen when using ML_{Thin} can be attributed to the lower final diameter rather than a difference in stent design. As the two stent designs induce almost identical stresses at the same diameter, it might be reasonable to assume that if the ML_{Thick} were inflated to a lower diameter, the clinical outcomes might be expected to be the same. However, it has been predicted that the ML_{Thin} causes marginally lower stresses at the same final diameter [Zahedmanesh *et al.* 2009].

Although the difference between the response of the thick and thin strut stents is reduced when using porcine arteries, a difference in response is still predicted. It is not know whether this difference would translate into significantly different rates of restenosis *in vivo*, and so conclusions are somewhat speculative. The models presented here consider only the mechanical

response, and not the pathological reaction to arterial injury. Furthermore damage and permanent deformation of the artery are not considered. This may be very important. The recoil of the stent has been shown, in this study, to depend on the presence of an artery and on the type of artery. One could hypothesise that damage caused to an artery by inserting a stent would cause a stress-softening, altering the amount of recoil of the artery and, by association, the stent. As the amount of recoil is proposed here to be the key difference between the stent types, a model which incorporates these elements of the material behaviour would provide more conclusive evidence for the difference between porcine and human arteries.

4.4.3 Influence of stent design on arterial stresses

As with the study on the influence of strut thickness, this work predicts lower arterial stresses in porcine arteries compared with human arteries following inflation of different stent types. However, the differences between the stresses produced by the three different stent types studied are broadly similar in both artery models. The PS stent is predicted to induce the highest stresses in the human coronary intima, followed by the Cypher stent, with the ML producing the lowest stresses. This order is reflected in the porcine model. The porcine artery shows less of a difference between stent designs than the human arteries. While this may explain why differences in stent design which are evident in randomised trials [Kastrati *et al.* 2000] are not always evident in animal trials [Taylor *et al.* 2001]. However, the differences in response between the human and porcine models presented in this study may not be sufficient to conclusively state that the change in mechanical response between the two species is the reason for the failure of animal trials to differentiate between stent designs in the same way that randomised trials in humans do. It should further be noted that different time points were used in the human and animal trials, and that other factors, such as pathological response, may account for some of the differences.

In this study, the stents were analysed before recoil occurred. This was to isolate the effects of stent design and artery type, rather than the influence of varying recoil between artery types. Here, it may be considered that the models had the same final, rather than initial, diameter.

The material model for the human coronary artery divided the vessel into three layers, each with different material properties. The porcine model was also divided into three layers, but the material properties were not unique to each layer. However, the histological study presented in Chapter 3 confirms that the intima is a thin layer in porcine (coronary and peripheral) arteries, and thus may be considered as a two-layered cylinder. The differences between the media and adventitia are not as pronounced as the differences between these two layers and the intima in

the human artery. Therefore, it may be considered more reasonable to assume homogenous material properties in the porcine artery. This assumption would be invalid in aged human artery models, where the intima is the most significant layer.

Note that as the lengths of the stents relative to the artery were different, so predictions of higher stresses in one model may not indicate a higher likelihood of increased restenosis rates. For example, the PS stent predicts the highest levels of stress, but is also the longest stent studied. In addition, stenosed vessels were not considered for either human or porcine models. All stents were expanded to the same diameter (3.75 mm) irrespective of manufacturer's directions. As such, the results presented here are not suitable for comparison with clinical results, and are useful only in the context presented here.

4.4.4 Modelling stent expansion in peripheral artery

From a mechanical perspective, using porcine arteries underestimates the intimal stresses induced in the peripheral arteries following stent deployment, as is seen in coronary arteries. However, porcine arteries are predicted to have higher stresses in the media and adventitia. The porcine peripheral arteries have a more uniform stress distribution through the three layers. This can be seen in Figure 4.12. This can be explained by the fact that the porcine peripheral artery is modelled as a homogeneous material. In the human artery, the intima is at much higher stresses than the other two layers. As the intima is the stiffest layer, it may act as a buffer between the stent and the other two layers, reducing the stresses.

It is also predicted that lumen gain is increased using porcine arteries. The main reason for this is the presence of intimal thickening in human arteries. The predicted lumen gain provided by shape memory stents in peripheral arteries is very similar in both human and porcine arteries. Although the stent in the human artery is predicted to undergo greater change in diameter with each cardiac cycle, animals would not be used for fatigue testing owing to time constraints.

For the peripheral arteries, the circumferential properties of the human illiac artery were considered. The small size of the porcine artery, as discussed in Chapter 3, meant that only longitudinal material properties could be considered. The small size of the porcine arteries also meant that one geometric model could not be used to represent the two species, as was the case for the coronary artery.

4.4.5 Parameter study

High deviation seen from the mean is seen with biological samples, and in particular with the porcine arteries studied here. While taking average properties is suitable for more general considerations, such as studies representative of populations, an understanding of the influence of this material variation is important. This spread of material properties is also seen in human arteries [Schulze-Bauer *et al.* 2003; Holzapfel *et al.* 2005], and so the results of the study undertaken are appropriate when considering human arteries.

Care should be taken when interpreting these results. If, for example, a similar study was carried out comparing a coronary artery with a coronary artery, (taking curves for the average $\pm 1.96\sigma$), then similar results could be expected. While this would be expected to predict a fuller set of results for these arteries, it could not be concluded that stresses in coronary arteries are significantly different to stresses in coronary arteries; rather, by taking a fuller spectrum of material properties, differences between stiffer and less stiff arteries are highlighted.

In this case, a stiffer femoral artery is predicted to experience higher stresses than a less stiff coronary artery following stent deployment, which indicates greater injury and more restenosis. Therefore, in certain situations, the material properties could be responsible for higher rates of restenosis in femoral arteries. However, the hypothesis that differences in material properties are responsible for higher rates of restenosis can, generally speaking, still be refuted.

4.5 Conclusions

This study shows that while in some aspects porcine and human coronary and peripheral arteries show very similar mechanical behaviour, there are still important differences between the two. The intimal thickening seen in human, and in particular coronary arteries, has a significant effect on the stresses induced in the artery and the mechanical response of both the artery and the stent. While using (young) animal models will not replicate the results seen in humans, they nevertheless provide a valuable predictive tool for pre-clinical testing. By better understanding the differences in mechanical, as well as pathological, responses, the results of pre-clinical animal trials can be better interpreted. This study shows that finite element modelling is an effective tool for understanding such differences, and it is suggested that by using the two together, both methods may provide more useful results in the development of medical devices.

5 Modelling stenting in peripheral arteries

Contents

5.1 Introduction 126

5.2 Materials and methods 126

5.2.1 Geometry 127

5.2.1.1 Artery geometry 127

5.2.1.2 Stent geometry 127

5.2.2 Material models 129

5.2.3 Boundary conditions 130

5.3 Results 134

5.3.1 Influence of stent type on vessel stresses 134

5.3.2 Influence of artery geometry and material properties on vessel stresses 136

5.3.3 Lumen gain 137

5.3.4 Influence of stent design 139

5.4 Discussion 144

5.5 Conclusions 148

5.1 Introduction

Peripheral stenting is, superficially, very similar to coronary stenting. However, the success of stenting in peripheral arteries does not compare favourably with coronary arteries. There are, however, a number of differences between stenting in coronary and peripheral arteries which might explain the discrepancy between restenosis rates. For example, the geometries of the two are different, with peripheral arteries having a greater diameter and thickness. This necessitates the use of larger stents to restore vessel patency. The material properties are also different, with coronary arteries generally being stiffer than peripheral arteries. Intimal thickening, the continuous stiffening and thickening of the intima, appears to be more significant in coronary arteries. Finally, lack of success seen with balloon expandable stents (BESs) made of stainless steel saw a move to nitinol self-expanding stents (SESs) for peripheral arteries. Although these more flexible nitinol stents improved success rates, they still compared unfavourably with coronary stents. Stent fracture is a problem associated with nitinol stents, and a strong correlation has demonstrated between stent fracture and rates of restenosis [Scheinert *et al.* 2005].

While the extreme mechanical environment of the femoral and popliteal arteries has been hypothesised as the cause of higher rates of restenosis in peripheral arteries, the differences outlined above may also contribute to elevated levels of restenosis. It is hypothesised that the differences in geometry, material properties and stent types may cause elevated levels of stress in peripheral arteries, which could lead to higher rates of restenosis. It is also hypothesised that these factors may contribute to a more adverse fatigue environment caused by the high frequency, low magnitude pulsatile nature of blood flow. Stiffer coronary stents are less affected by this environment [Duerig *et al.* 2000].

The hypotheses of this study were tested by creating finite element models of coronary and peripheral arteries and modelling the expansion of BESs and SESs in these arteries. The results were analysed in terms of the stresses induced in the arteries by the stent expansion, and the pulsatile blood pressure induced fatigue environment on the stents.

5.2 Materials and methods

To investigate the hypotheses presented here, finite element models were created of coronary and peripheral arteries (see Figure 4.1) undergoing expansion with both BES and SES. The peripheral artery modelled here has material properties of an illiac artery and is not subject to

external loading. To study the effect of stent type and material properties, a SES with a similar geometry to the BES was analysed, while a second SES model was used to investigate the influence of stent design. The influence of strut thickness and stent over-sizing on peripheral arteries were investigated using the second SES model (SES2) by studying three strut thicknesses and three initial diameters. This meant that one BES design and two SES designs in both coronary and peripheral arteries were studied, with a further four designs in the peripheral artery for a total of ten models. The results were analysed in terms of the von Mises stress induced in the artery following stent implantation and the lumen gain. Also, the change in stent diameter during a cardiac cycle, and the associated stent fatigue stress cycle, were predicted. All finite element analysis was undertaken using Marc/Mentat 2007 software (MSC Software Corporation, Santa Ana, California).

5.2.1 Geometry

5.2.1.1 Artery geometry

Two artery geometries were created, a peripheral artery and a coronary artery. The coronary artery had a thickness of 0.5mm, a diameter of 3mm and a length of 20mm, while the corresponding measurements for the peripheral artery were 1mm, 3mm and 20mm. Both artery types were divided into intimal, medial and adventitial layers according to the ratios described by previous tests [Schulze-Bauer *et al.* 2003; Holzapfel *et al.* 2005]. The artery geometries were the same as those described in Chapter 4, where full details are provided.

5.2.1.2 Stent geometry

Stent geometries of BESs and SESs were created. Slotted tube, closed cell, diamond designs based on the Palmaz stent were used for the BESs, see Figure 5.1(a). These models were designed to be expanded to 1.25 times the inner diameter of the appropriate artery (Table 5.1). The coronary stent models had strut thicknesses of 100 μm, and the peripheral stent models had strut thicknesses of 150 μm.

Two self-expanding stent (SES) designs were created. The first design (SES1) used the expanded geometry of the BES as the initial, zero-stress configuration for the SES, as shown in Figure 5.1(b). This method has been used as a means of eliminating geometry as a variable when comparing the stresses induced in arteries by stent placement [Migliavacca *et al.* 2004]. Design 2 (SES2) was an open cell, 'z' design, a generic version of commercially available nitinol stents, see Figure 5.1(c).

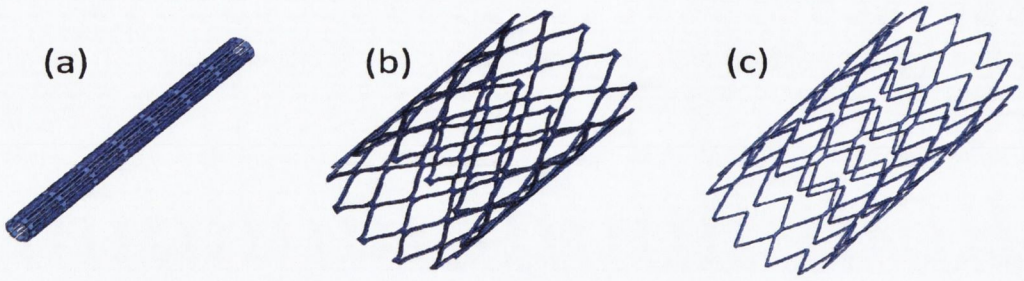


Figure 5.1

Geometries of (a) stainless steel balloon expanded stent, (b), the expanded geometry of (a), used as the initial configuration for SES1, and (c) the initial configuration of SES2.

	Coronary		Femoral	
	BES	**SES1**	**BES**	**SES1**
Length [mm]	10	10	20	20
Thickness [mm]	100	100	200	200
Diameter [mm]	1.125	3.75	3	10
Target diameter [mm]	3.75	3.75	10	10

Table 5.1

Geometric properties of the BESs and SESs for the coronary and peripheral arteries.

Further variations on the design of SES2 were created to investigate the influence of strut thickness and oversizing. The strut thickness was modelled at 100 μm and 250 μm, as well as the original 150 μm design. The initial diameter was also modified to 11 mm and 12 mm.

	Original	Strut thickness		Diameter	
	SES2	**SES2(a)**	**SES2(b)**	**SES2(c)**	**SES2(d)**
Thickness [mm]	150	100	250	150	150
Diameter [mm]	10	10	10	11	12

Table 5.2

Variations on the SES2 design with variations on strut thickness and diameter.

5.2.2 Material models

As described in Chapter 4, separate material models were applied to the coronary and peripheral arteries. Each was modelled as a 3-layered idealised hollow cylinder. Each layer was an isotropic hyperelastic material described by a 3[rd] order Mooney-Rivlin equation;

$$W = a_{10}(I_1 - 3) + a_{01}(I_2 - 3) + a_{20}(I_1 - 3)^2 + a_{11}(I_1 - 3)(I_2 - 3) + a_{30}(I_1 - 3)^3 \quad \textbf{5. 1}$$

The material models for the peripheral and coronary arteries were based on data obtained in two different studies. The coronary artery model was based on data from individual layers of aged (mean age of 71.5 years) human coronary arteries with non-atherosclerotic intimal thickening [Holzapfel *et al.* 2005], while the peripheral artery was based on data from human iliac arteries [Holzapfel 2000]. In each case, the circumferential data was fitted to a third order Mooney-Rivlin hyperelastic strain energy function. The rationale behind this is that the circumferential stress was found to be the most significant in the simulations. The data from which these models are obtained and the constants fitted to them are given in Table 5.3.

	Coronary			Peripheral		
	Intima	**Media**	**Adventitia**	**Intima**	**Media**	**Adventitia**
C_{10}	84237.8	3555.26	7146.48	18846.9	7687.49	0
C_{01}	5057.85	662.391	636.828	193.314	0	5499.99
C_{11}	7650633	18684.4	9579.2	687636	11585.8	0
C_{20}	5.50488e6	8548.3	8035.15	195006	41820.9	0
C_{30}	9.238e7	297746	1.29315e6	53414.1	42623.7	151227

Table 5.3

Material constants for coronary and peripheral arteries.

The material for the BESs was 316L stainless steel. This was modelled as a bi-linear, elasto-plastic model based on stress-strain curves obtained from tests on micro-samples [Wiersma *et al.* 2006] as described in Chapter 4.

The nitinol model implemented in the MSC Marc software is based on an algorithm developed by Auricchio *et al* [Auricchio *et al.* 2002], which describes the stress induced transformations in a three-dimensional model. The constants (Table 5.4) were taken from Favier *et al* [Favier *et al.*

2006], and have been used elsewhere in the literature [Wu *et al.* 2007]. Note that nitinol material properties are sensitive to changes in material properties dependent on the manufacturing process [Favier *et al.* 2006]. Here, average properties which do not take account of this variation are used.

Property	Value
E	60GPa
v	0.3
σ^{s}_{AS}	346MPa
σ^{f}_{AS}	365MPa
σ^{s}_{SA}	83MPa
σ^{f}_{SA}	57MPa
α	0.09
ε	0.063

Table 5.4

Material constants taken from Favier et al *[Favier et al. 2006] used in nitinol material models. See Chapter 2 for full definitions of terms used.*

5.2.3 Boundary conditions

Symmetrical boundary conditions were applied to all nodes that coincided with the symmetrical planes. The expansion of the BES was modelled by applying a pressure directly to the internal faces of the stent, without directly modelling the balloon. This method was found to produce a non-uniform and incomplete stent expansion when applied. Further details of this method are reported in Chapter 4.

The SESs were compressed from their fully expanded diameter using a sheath modelled as a rigid cylinder with a diameter greater than that of the stent. The sheath is used to compress the stent by applying displacement boundary conditions to reduce its diameter so that it can fit into the artery without contacting the wall. As the artery and stent are coincident in places at the start of the model (Figure 5.2(a)), the artery elements are first deactivated (Figure 5.2 (b)). When the stent is compressed (Figure 5.2(c)), the artery elements are reactivated (Figure 5.2(d)). The sheath is then withdrawn laterally (Figure 5.2(e)). As the restraint of the sheath is removed, the super-elastic stent begins to return to its original shape (Figure 5.2(f)).

At the moment the sheath leaves contact with the end of the stent as it is withdrawn, the stent undergoes a relatively large motion during a single increment of the simulation. The problems this

causes with convergence can be overcome by applying a small pressure to the end of the stent to replace the restraint of the sheath when it is withdrawn. This pressure is then removed over a number of steps to allow full expansion of the stent. Although the time taken to expand the stent is now increased, the shape of the stent during expansion is not affected. As the model contains no time-dependent properties, such as strain-hardening in the metal or viscoelasticity in the artery, the stresses in the artery are not affected.

While the geometry of the SES models, like the BES models, is symmetric about three axes, the method of deployment, where the stent expands from the distal to the proximal end, is not symmetric in the longitudinal direction. To fully model this, a model twice the size of the BES models, where symmetry about the longitudinal plane was not considered, was required. This led to very high computational cost. In order to reduce this cost, this larger half model was compared with a quarter model to investigate the effect, if any, the lack of symmetry caused any changes in the stress state of the artery following stent deployment. It was found that although the opening profile of the stent was slightly altered, only very small changes in stress were observed when using a half model. Therefore, the one quarter symmetrical model was used for subsequent simulations described below.

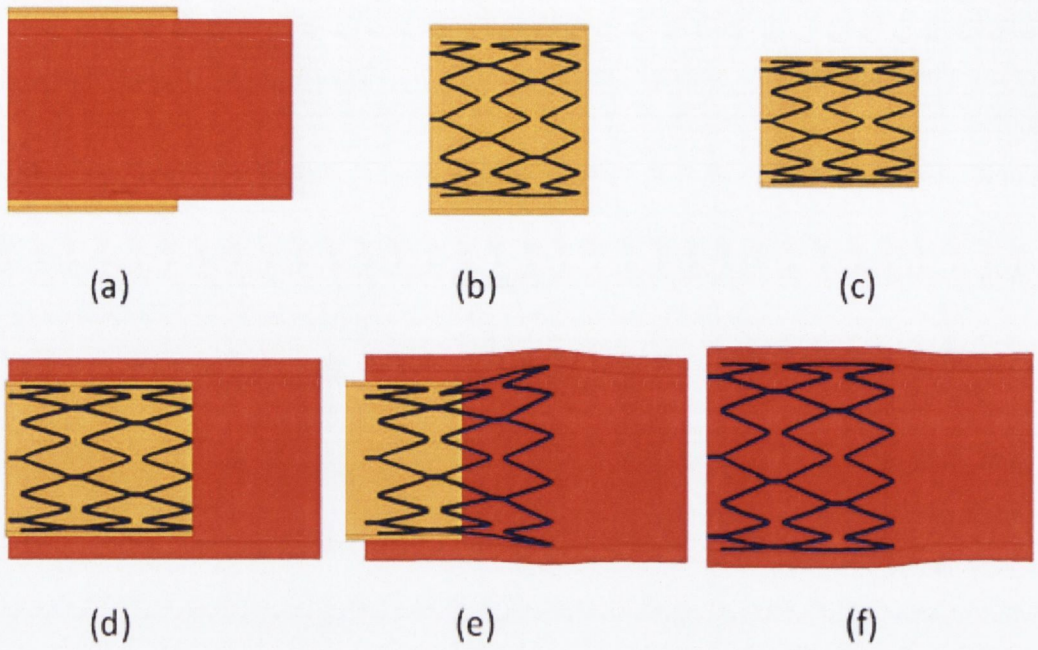


Figure 5.2

Nitinol stent deployment

- *(a) Stent and artery are coincident*
- *(b) Artery elements are deactivated*
- *(c) Diameter of sheath is reduced to crimp stent*
- *(d) Artery elements are reactivated*
- *(e) Sheath is withdrawn laterally, stent expands*
- *(f) Stent is fully deployed*

Two types of physiological loading were applied to the arteries (Table 5.5). The axial pre strain, assumed to be constant during the cardiac [Schulze-Bauer *et al.* 2003], was applied to the artery prior to expansion of the stent. For BES models, the strain was applied at the start of the simulation, whilst for the SES models the strain was added once the artery elements had been reactivated after the crimping of the stent. Blood pressure was applied to the inner faces of the arteries and stents. The minimum blood pressure seen during the cardiac cycle was applied at the same time as the axial stretch. This was increased to the maximum level once the stent had been expanded.

	Coronary	Femoral
Axial stretch	1.044[1]	1.07[2]
Minimum blood pressure[3] [kPa]	10.666	8
Maximum blood pressure[3] [kPa]	16	13.332

Table 5.5

Loads applied to artery

(1) *[Holzapfel et al. 2005]*

(2) *[Schulze-Bauer et al. 2003]*

(3) *[Mills et al. 1970]*

To investigate the influence of (1) the stent type, (2) the stent design and (3) the artery properties, each model was assessed in terms of the stresses induced in the artery and the lumen gain. To analyse the stresses, each element in each layer was assigned a single stress value by taking the average stress of the integration points within the element. The volume of elements within specified stress ranges were then accumulated and graphed. The peak stresses in the artery were also analysed. The lumen gain was expressed as a ratio of the average outer diameter of the stent following expansion to the initial diameter of the artery. As a result of the change of blood pressure, representing the cardiac cycle, the artery and stent changed diameter. The effect of this was measured by quantifying the percentage change in diameter of the artery, and by measuring the strain amplitude induced in the stent by this cycle.

5.3 Results

Generally, BESs are used in coronary arteries and SESs in peripheral arteries. By comparing these two procedures directly, the effects of differences in stent and artery can be summarised. The models predict that more of the coronary artery was in higher stress ranges following BES expansion than the peripheral artery following SES placement (Figure 5.3). The peak stresses were also higher in a coronary artery are significantly higher than in a peripheral artery, (see Figure 5.4 and Figure 5.5), with the highest stresses predicted in the intima of both models. However, by modelling both BES and SES stenting in both artery types, the influence of stent type and artery geometry and material properties can be isolated. The consequences of altering the stent design (strut thickness and diameter) are also presented.

5.3.1 Influence of stent type on vessel stresses

In the coronary artery, the BES is predicted to cause significantly higher peak stresses than either of the SES designs, see Figure 5.3. Half the intima of the coronary artery experiences stresses of 750 kPa or greater due to implantation of a BES (Figure 5.3(a)). Neither of the SES designs cause stresses above this level, while most of the intima, 53% and 87% for SES designs 1 and 2 respectively, are at stresses of 300 kPa or less (Figure 5.3(d)). The BES also causes higher peak stresses in the media and adventitia of the coronary artery, where both the SES designs place greater than 90% of these layers in low (0-10kPa) stress ranges. Note that the range of stresses is much higher for the intima (0-750 kPa) (Figure 5.3(a) and (d)) than for the media (0-25 kPa) (Figure 5.3(b) and (e)) or adventitia (0-30 kPa) (Figure 5.3(c) and (f)). The difference between stent types is less significant in the peripheral artery, though it is shown that the BES still induces higher stresses than either of the SES designs. The BES places 3% of the intima in the highest (750 kPa +) range, compared with none for the SES designs, and has slightly more tissue in the 500-750 kPa range.

There is a greater difference between the BES and SES designs than there is between the two SES stent designs. Generally, SES2 induces lower stresses than SES1. This is best demonstrated in the intima of the coronary artery, where 31% of the layer is at a stress of 350 kPa or greater using SES1. This figure is reduced to less than 1% using SES2. The difference between the two is less in the media and adventitia of the coronary artery and in all three layers of the peripheral artery.

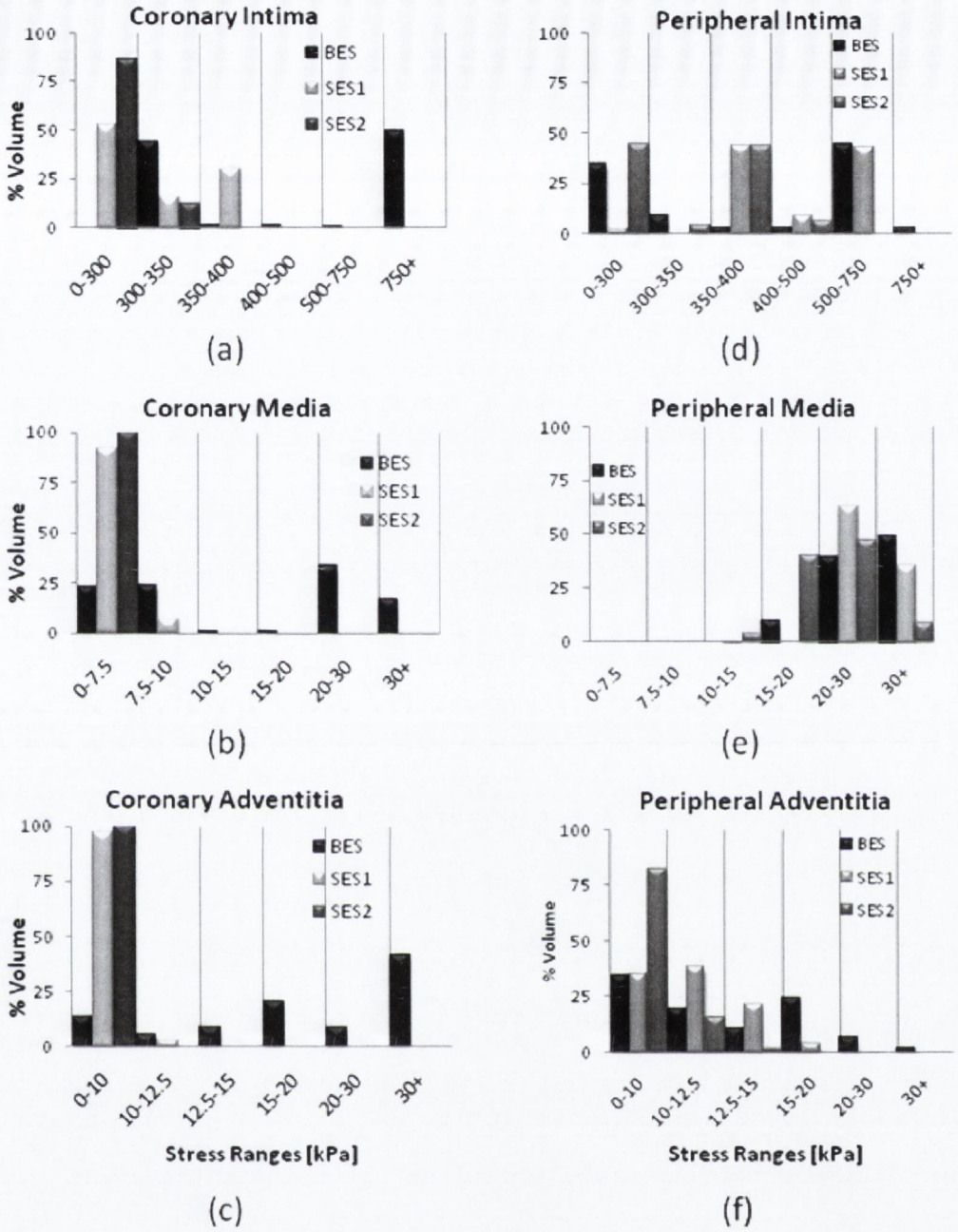


Figure 5.3

Stress distributions following BES, SES1 and SES2 placement in (a) coronary intima, (b) coronary media, (c) coronary adventitia, (d) peripheral intima, (e) peripheral media and (f) peripheral adventitia.

5.3.2 Influence of artery geometry and material properties on vessel stresses

Implanting a BES is predicted to produce higher stresses in the intima and adventitia of a coronary artery than a peripheral artery, see Figure 5.3. Generally, more of the peripheral artery is within the mid stress ranges, and more of the coronary artery is at the higher, but also the lower stresses. 50% of the intima is at a stress of 750 kPa or higher in the coronary artery, while the peripheral artery has 3% in the same stress ranges. The adventitia is subject to relatively low stresses in all cases, though considerably more of the layer is at higher stresses in the coronary artery. In the media, unlike the intima and adventitia, the peripheral artery has more tissue at higher stresses. Both SES designs are predicted to produce higher stresses in the peripheral than coronary artery. In the intima for example, SES1 and SES2 place 53% and 6.84% respectively of the layer at stresses of 400 kPa or greater in the peripheral artery, compared with 1% and 0% in the coronary artery.

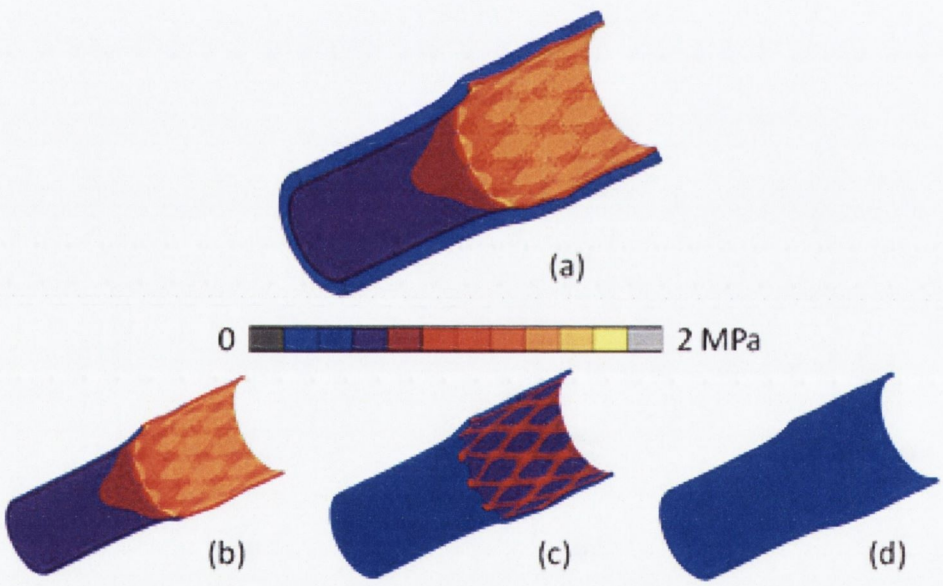


Figure 5.4

Von Mises stress in coronary artery following expansion of BES showing (a) the whole artery and three separate layers, (b) intima, (c) media and (d) adventitia.

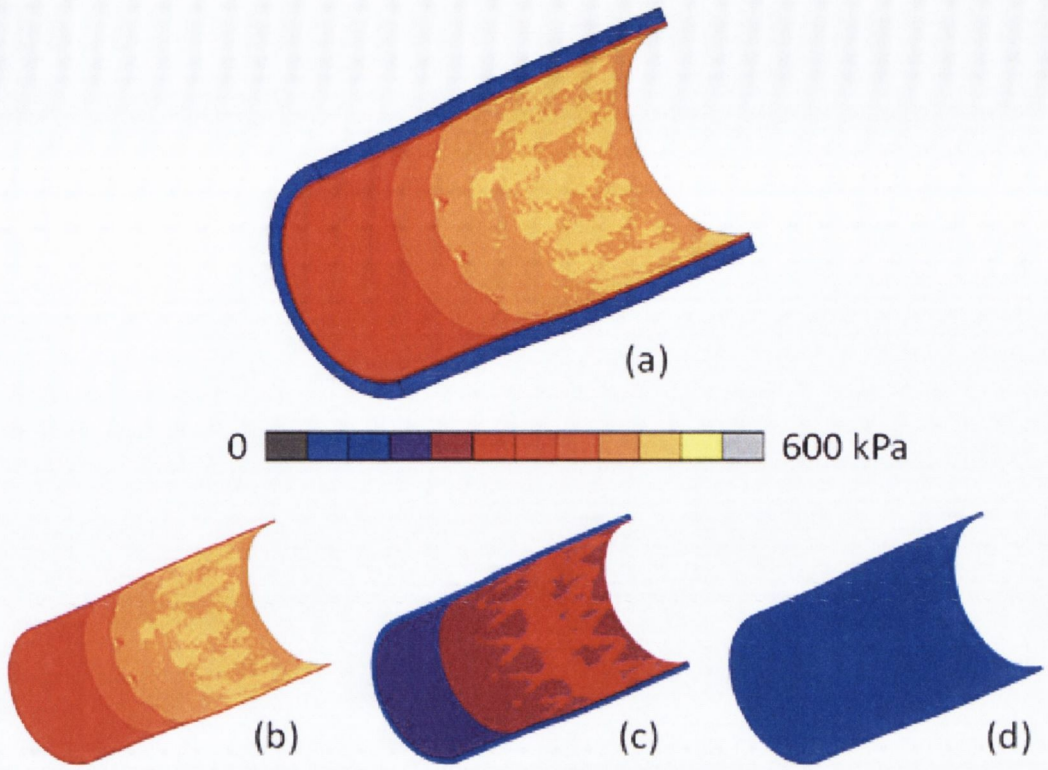


Figure 5.5

Von Mises stress in femoral artery following expansion of SES1 showing (a) the whole artery and three separate layers, (b) intima, (c) media and (d) adventitia.

5.3.3 Lumen gain

The lumen gain is presented as a percentage of the original diameter. In all models, the target diameter is 1.25 times the original diameter. To make a valid comparison in terms of lumen gain, the lumen diameter of the deployed stent at the minimum blood pressure (diastole) is taken. Different stages of deployment are defined for each stent type. For BESs, Stage 1 is follows the full expansion of the stent at minimum blood pressure. Stage 2 is after recoil of the stent has occurred, and Stage 3 is where the blood pressure has been raised to the maximum value. Two stages are defined for the SESs; Stage A and Stage B. Stage A is when the stent is deployed at diastole, while Stage B is at systole. In the coronary artery, use of a BES gives greatest lumen gain, with the inner diameter of the artery increasing from 3 mm to 3.733 and 3.505 mm following stent expansion and recoil respectively (**Error! Reference source not found.**). This minimum value of 3.505 (at diastole) represents a ratio between post-stenting and pre-stenting diameter of 1.168, compared with a target ratio of 1.25. Using a SES reduces the lumen gain to a ratio of 1.096 and 1.108 for SES 1 and 1.108 and 1.076 for SES 2. The peripheral artery also experiences greater

lumen gain with use of a BES than SES. A ratio of 1.248, the highest of any model, is obtained using a BES in a peripheral artery. Like the coronary artery, SES1 provides greater gain than SES2, giving a lumen gain of 1.225 and 1.244 against 1.198 and 1.216. For all three stent designs, the peripheral artery experiences greater gain than the coronary counterpart.

Artery	Stent	Stage	Diameter	Lumen Gain
Coronary	BES	1	3.733	1.244
		2	3.505	1.168
		3	3.513	1.171
	SES1	A	3.288	1.096
		B	3.324	1.108
	SES2	A	3.183	1.061
		B	3.229	1.076
Peripheral	BES	1	9.984	1.248
		2	9.882	1.237
		3	9.900	1.238
	SES1	A	9.799	1.225
		B	9.948	1.244
	SES2	A	9.580	1.198
		B	9.728	1.216

Table 5.6

Lumen gain for different artery and stent types. 'Stages' refers to the degree of stent expansion, and is explained as follows. Stage 1 for BES refers to the stent at the maximum diameter during deployment, after stent recoil. Stages 2 and 3 describe the stent following recoil at the minimum and maximum blood pressure respectively. Stages A and B are used for the SES designs, and refer to the fully deployed stent at the minimum (A) and maximum (B) blood pressures.

The change in diameter of the stents between diastole and systole represents the strain controlled fatigue environment experienced by the stent over its lifetime in an *in vivo* environment. In the coronary artery, the BES experiences a 0.23% change in diameter during each cardiac cycle, while SES1 and SES2 change by 1.09% and 1.45% respectively (Table 5.7). In the peripheral artery, the BES changes by 0.18% per cycle, with SES1 changing by 1.52% and SES2 by 1.54%.

Previous work has determined a threshold value for strain amplitude of 0.4% below which failure is not predicted to occur in nitinol stents [Pelton *et al.* 2008]. The maximum predicted strain amplitudes due to the cardiac cycle are provided in Table 5.7. None of the stents modelled are predicted to exceed the strain amplitude threshold value of 0.4%, and the lowest factor of safety seen is 5.8.

Artery type	Stent type	% Change in Diameter	Maximum Strain Amplitude	Factor of Safety
Coronary	BES	0.23		
	SES 1	1.09	0.069 %	5.80
	SES 2	1.45	0.055 %	7.27
Peripheral	BES	0.18		
	SES 1	1.52	0.038 %	10.53
	SES 2	1.54	0.045 %	8.89

Table 5.7

Change in diameter and associated maximum strain amplitude (for SES models) caused by change in blood pressure.

5.3.4 Influence of stent design

The original SES2 design, with a strut thickness of 150 μ and an initial diameter of 10 mm was modified. These new stent designs had geometric parameters as outlined in Table 5.2. The effect of these design alterations was quantified in terms of the stresses induced in the arteries, the lumen gain and the strain amplitude.

Analysis showed that increased strut thickness led to increased stresses in the artery (Figure 5.6). This is particularly evident in the intima, where the amount of tissue at higher stresses of 400 kPa or greater increases from 0 % with a strut thickness of 100 μ to 6.84 % at 150 μm and 49.58 % at 250 μm (Figure 5.7). A similar trend is seen in the media, where the amount of tissue at 20 kPa or greater increases from 45.20 % to 55.91 % and 73.37 %, and the adventitia, where the amount of tissue at low stresses (< 7.5 kPa) diminishes with increasing strut thickness.

The nominal diameter of the stents also influences the magnitude of the arterial stresses, with higher stresses predicted when a larger stent is used. In the intima, the amount of tissue at low

stresses (less than 300 kPa) decreases from 44.76 % to 33.13 % and 21.81 % as the stent diameter is increased from 10 mm to 11 m and 12 mm. While the 10 mm stent places none of the intima at stresses of 500 kPa or more, the 11 mm stent has 49.72 % of the intima in this stress range, increasing to 55.83 % with the 12 mm stent. In the media, the amount of tissue increase at 30 kPa or higher increases from 8.51 % to 47.79 % and 56.47 % with the larger 11 mm and 12 mm stents, as shown in Figure 5.7.

Changing the stent design also alters the behaviour of the stent in the fatigue environment. Although no direct correlation is predicted between the increase in strut thickness and the percentage change in diameter, it can be seen that increased strut thickness leads to higher lumen gain (Table 5.8). Increasing the strut thickness also leads to reduced maximum strain amplitudes, and thus higher factors of safety.

Similarly, increasing the nominal stent diameter increases the average lumen gain, from 9.654 mm with a 10 mm stent to 9.736 mm with an 11 mm stent and 10.586 mm with a 12 mm stent. However, the increased lumen gain is in this case associated with increased strain amplitude, see Table 5.8. The factor of safety of 1.739 for the 12 mm stent would be considered low for a medical device.

While this study was not replicated for coronary arteries and stents, similar results could be expected for all artery types when varying the strut thickness and diameter of the nitinol stents.

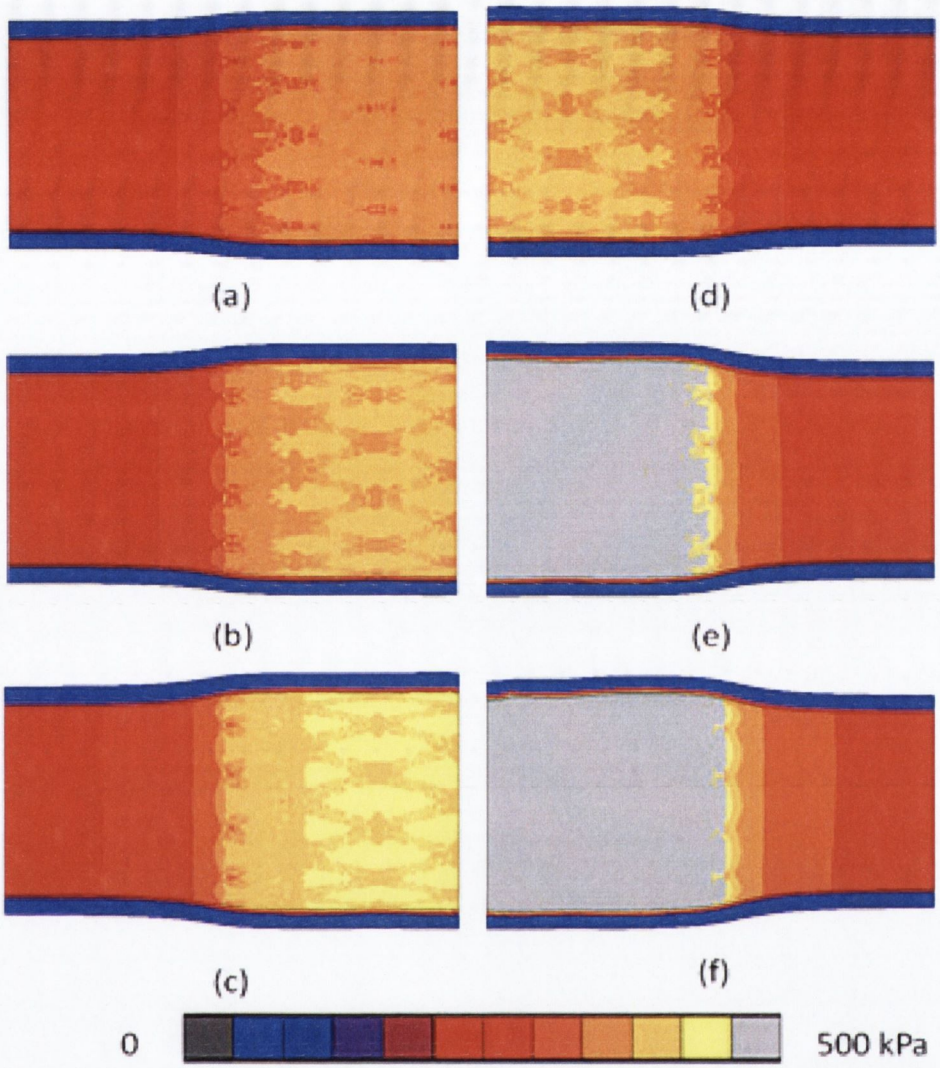


Figure 5.6

Contour bands of von Mises stresses in peripheral arteries following expansion of nitinol stents. Stents used in (a), (b) and (c) had diameters of 10 mm and strut thicknesses of 100 μm, 150 μm and 250 μm respectively. Stents used in (d), (e) and (f) had strut thicknesses of 150 μm and nominal diameters of 10 mm, 11 mm and 12 mm respectively.

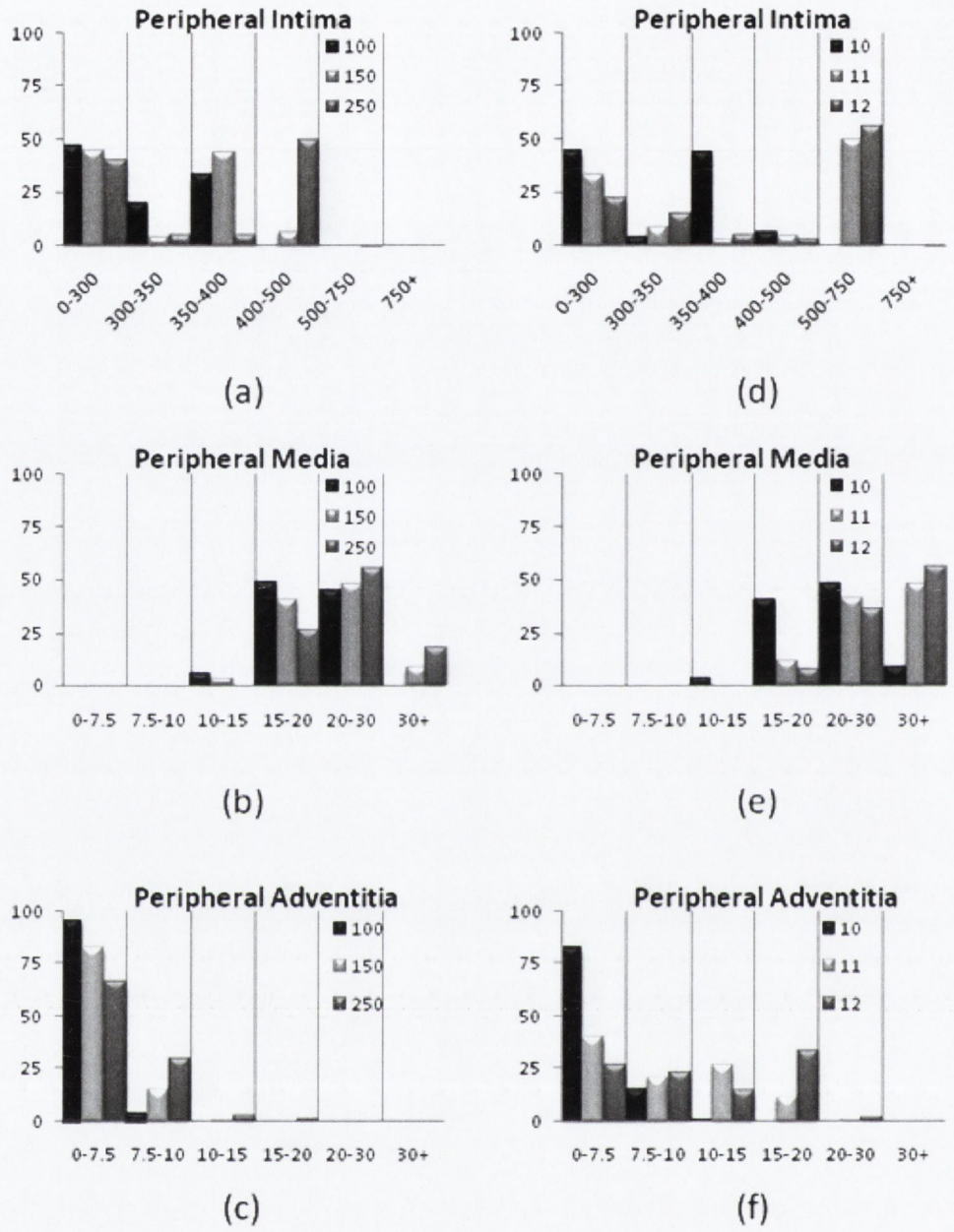


Figure 5.7

Stress distributions in peripheral arteries showing influence of strut thickness on (a) intima, (b) media and (c) adventitia, and of stent diameter on (d) intima, (b) media and (c) adventitia.

		Min Lumen	Max Lumen	Average Lumen	% Change	Max strain amplitude
Strut Thickness	**SES2(a)**	8.824	9.032	8.928 (1.116)	2.357	0.057
	SES2	9.580	9.728	9.654 (1.207)	1.545	0.045
	SES2(b)	9.683	9.856	9.770 (1.221)	1.787	0.035
Stent Diameter	**SES2**	9.580	9.728	9.654 (1.207)	1.545	0.045
	SES2(c)	9.669	9.802	9.736 (1.217)	1.158	0.1
	SES(d)	10.489	10.683	10.586 (1.323)	1.850	0.23

Table 5.8

Lumen gain, change in diameter and associated strain amplitude with variations in stent design. Note that average lumen is also given relative to the original artery diameter. Definitions of stent designs (SES2(a-d)) are shown in Table 5.2.

5.4 Discussion

It is well established that the injury caused to the vessel wall due to the implantation of a stent is a key contributor to in-stent restenosis [Schwartz *et al.* 1994]. Arterial stresses predicted using computational techniques such as the finite element method provide an indirect measure of the degree of injury following stenting. However, a full understanding of the relationship between stress, injury and restenosis has not been established. Therefore, the results presented here are useful only in a comparative sense. The highest stresses in the artery following stent expansion are, in all models, predicted to be in the intima. This can be explained by the fact that the intima experiences the highest level of strain, and is the stiffest layer in both the coronary and peripheral arteries. The high levels of stress seen in the intima compared with the media and adventitia is significant, as the endothelium that lines this layer of tissue is believed to be important in regulating vascular smooth muscle cell proliferation and migration and neointimal formation [Kipshidze *et al.* 2004].

The predictions of arterial stresses for the two different artery types depend strongly on the type of stent used. Using a BES is predicted to induce higher stresses in the coronary than the peripheral artery. One of the reasons for this is that the coronary artery is on average stiffer than the peripheral. Arterial stresses will also be influenced by the thickness to diameter ratio, which is greater in the coronary (0.167) than the peripheral artery (0.125). Conversely, when using a SES, the stresses are higher in the peripheral artery in the intima and media than in the coronary artery. The difference can be explained by comparing the lumen gain of the two types of artery. SESs do not expand to their full diameter due to the constraint of the artery. The coronary artery, which is slightly stiffer and has a greater thickness compared with its diameter, provides a greater resistance to stent expansion than the peripheral artery. This leads to less lumen gain in the coronary artery, and also lower levels of vessel stress. This prediction is obviously limited to the specific mechanical properties for human coronary and peripheral inputted into the finite element model, and may change with disease progression where the properties of the plaque itself will influence lumen gain. Differences in medial stresses were also predicted. While increased damage in the media will promote additional neointimal formation [Fingerle *et al.* 1990; Kipshidze *et al.* 2004], it is often considered less significant than intimal injury, and unlikely to occur independently. Also, the lower ranges of stresses seen in the media compared with, for example, the intima, may indicate a lower likelihood of injury in the media.

This study also suggests that the type of stent used (i.e. BES or SES) is a more important factor in determining the peak stresses in the artery than the stent design (i.e. SES1 or SES2). It is predicted

that using a BES induces higher levels of peak stress than a SES in all three layers of the artery. This is most evident in the coronary artery, and to a lesser extent in the peripheral artery. The elevated stress ranges in the coronary artery may suggest higher levels of arterial injury compared with, for example, the iliac artery due to implantation of a BES. This may partially explain the results of animal model studies, where per cent stenosis rates of 53.52% for coronary arteries and 46.12% for peripheral arteries were found following implantation of balloon expandable stents [Krueger *et al.* 2006], although the predictions of the finite element simulations are based on human material properties and geometries.

There are two methods for increasing the lumen gain obtained by using a SES. The first is to increase the strut thickness of the stents, and the second is to increase the diameter of the stent. Both methods give greater lumen gain, but also increase the arterial stresses. Similarly, reducing the stent thickness reduces the lumen gain. The fatigue environment is affected in different ways using each of these methods. Increasing the strut thickness decreases the strain amplitude, improving the performance in the pulsatile fatigue environment. However, increasing the nominal stent diameter causes large increases in stresses, and also increases the probability of fatigue failure. For this reason, SES over-sizing should be avoided as a means of increasing lumen gain. Rather, it is suggested that increasing stent strut thickness is the more desirable method of increasing lumen gain with shape-memory stents.

In general, however, BES are used in coronary arteries and SES are used in peripheral arteries. Based on the predictions of peak intimal stresses, there is no evidence that implanting SES in peripheral arteries will induce higher levels of injury than implanting BES in coronary arteries. In fact, the lower injury to the intima due to the expansion of a SES compared to a BES may, even in the absence of the benefits of greater flexibility to accommodate external loading [Cheng *et al.* 2006; Nikanorov *et al.* 2008], partially explain the better clinical results of SES compared to BES in peripheral arteries [Sabeti *et al.* 2004]. Therefore a number of alternative explanations must be considered for the higher rates of restenosis observed clinically following stent implantation in the femoral and popliteal arteries compared to the coronary arteries.

This first is that it is the external mechanical environment within certain peripheral arteries, either flexional [Nikanorov *et al.* 2008], pulsatile or torsional [Cheng *et al.* 2006], or a combination of these, may be responsible for the high levels of vessel injury and hence restenosis observed in peripheral arteries following stenting. We have previously demonstrated using finite element modelling that vessel stresses in arteries implanted with stainless steel BES are significantly greater during physiological levels of joint flexion than during balloon expansion. What remains to be elucidated is whether similar levels of arterial stresses are developed due to implantation of

more flexible nitinol stents. A second possible explanation is that peak stresses are a poor indicator of the likelihood of intimal injury following stenting. It may be that a lower stress (or strain) threshold value exists, above which endothelial damage occurs. For example, greater volumes of the intima in the peripheral artery are subjected to stresses greater than 350kPa following implantation of a SES compared to the coronary artery following implantation of a BES, even through peak stresses are significantly greater in the coronary artery. While we are not proposing any particular injury threshold value in this study, there is reason to believe that such limits exist for soft tissues [Linder-Ganz *et al.* 2006; Gefen *et al.* 2008], and accurately determining such parameters for arteries would greatly enhance the predictive abilities of computational methods in stent design.

A third possible explanation is that the pulsatile environment generated by the cardiac cycle is more likely to lead to stent fatigue in the peripheral arteries than the coronary arteries, and hence higher levels of restenosis [Scheinert *et al.* 2005]. BES demonstrate smaller changes in diameter during the cardiac cycle than the SES. This is reported in the literature, where BES are said to be inert, stiff tubes which deform little between diastole and systole, whereas SES are more dynamic, and move with the artery [Duerig *et al.* 2000]. The changes in diameter in arteries with BES of 0.23% and 0.18% seem to agree well with experimental values of <0.25% [Duerig *et al.* 2000]. The model's predictions of maximum strain amplitudes in both the coronary and peripheral arteries suggest that stent fatigue does not occur due to the cardiac pulsatile cycle, with agrees with *in vitro* experiments that demonstrate that the strain amplitudes caused by this pulsatile environment are too low to cause fatigue failure in the stent [Pelton *et al.* 2004; Pelton *et al.* 2008]

However, these results should be interpreted with caution, as failure is predicted under conditions which exceed those seen physiologically. Furthermore, a high factor of safety is required for medical devices, and factors such as irregular, realistic artery geometries, high levels of stenosis, hard or calcified plaque, eccentric stenoses or incorrect sizing of a stent could lower this value sufficiently to cause concern. For example, stents in carotid arteries are 7.7 times more likely to fracture if calcification is present [Ling *et al.* 2008]. This study also shows that stent oversizing may contribute both to reduced performance in fatigue, and to higher stresses leading to greater restenosis rates. This is supported by a stent oversizing study which shows a correlation between the stent to artery ratio and the percent stenosis and injury score [Zhao *et al.* 2009]. It is reported that severe oversizing (stent to artery ratio of 1.4 or greater) produces exuberant neointimal proliferation.

Regardless, it would appear that the pulsatile environment created by the cardiac cycle is not, in normal cases, the primary cause of stent fatigue failure. While it cannot be ignored as a potential cause of fracture as the frequency of this loading is very high, it needs to be considered as acting synergistically with the loading acting on stented arteries due to muscle contractions and joint movement.

There are a number of limitations with the model presented in this study. The use of an isotropic model is a simplification in the analyses presented here. There is considerable anisotropy evident in some of the data that these models are based on [Holzapfel 2000; Holzapfel *et al.* 2005]. Although the use of a cylindrical arterial geometry is a simplification, and differences in vessel morphology exist along the vascular tree, it gives more generally applicable results when comparing stent designs than using patient specific geometry. As previously eluded to, this study has only considered a single set of averaged material properties and geometries for the coronary and peripheral arteries, whereas in reality there will be considerable patient and disease specific variation in these properties. Future studies will attempt to incorporate such variability into the models in order to confirm some of the general conclusions drawn from the results of this study on the differences between the two artery types. The decision not to model a stenosed vessel is also more practical for comparing stent designs and types. Lumen gain in peripheral arteries can be increased by post-dilating with a balloon. This would be expected to increase the lumen gain, but also the injury levels. SES cannot be considered static like BES, as they continue to expand once deployed. Remodelling can also allow the stents to migrate through the vessel wall [Duerig *et al.* 2000]. These effects are not incorporated into this or, to the authors' knowledge, any current computational model. The arteries in this study are modelled as hyperelastic, another major limitation as in reality significant stress softening and permanent deformation will occur following stenting. Accounting for micro-damage to the tissue at high stress levels would also lead to more accurate model predictions.

5.5 Conclusions

Using SES rather than BES in a peripheral artery is predicted to lead to lower stresses being induced in the artery, but with the consequence of lower lumen gain. Stent fatigue in the peripheral arteries would not appear to be due to the pulsatile mechanical environment provided by the cardiac cycle. This study also provides no evidence for the hypothesis that differences in geometry and material properties between the coronary and peripheral arteries is responsible for the higher levels of injury in peripheral arteries following stenting. Future studies should therefore focus on the flexion [Nikanorov *et al.* 2008] or torsional [Cheng *et al.* 2006] driven environments in the femoral and popliteal arteries as the more likely cause of higher injury and restenosis.

6 Modelling the mechanical environment of peripheral arteries

Contents

6.1 Introduction 150

6.2 Methods 152

6.2.1 Overview 152

6.2.2 Geometry 152

6.2.3 Material properties 152

6.2.4 Boundary conditions 153

6.2.4.1 Mechanical environment 153

6.3 Results 157

6.3.1 Bending 157

6.3.1.1 Balloon expanded stents 157

6.3.1.2 Self-expanding stents 161

6.3.2 Compression 167

6.3.3 Influence of factors in peripheral arteries 168

6.4 Discussion 171

6.4.1 Artery bending 171

6.4.2 Artery compression 173

6.5 Conclusions 175

6.1 Introduction

Stent fracture and in stent restenosis (ISR) continue to hinder the use of stents in peripheral arteries [Lampmann, 1999; Kroger *et al.*, 2004; Mewissen, 2005; Scheinert *et al.*, 2005]. For some time, there has been a consensus that the mechanical environment, caused by flexion of the knee and/or hip joints, was contributing to these problems. The femoral and popliteal arteries, in particular, are subject to large motions and resultant external forces. These motions can, for example, occlude the popliteal artery even in healthy subjects [Hoffmann *et al.*, 1997]. It was also suggested that the presence of 'hinge points', about which the arteries bend or kink could be problematic for stenting [Diaz *et al.*, 2004], while the viability of stenting as a solution to PAD has been questioned [Lampmann, 1999], with the biomechanical environment being identified as the source of stent incompatibility in the popliteal artery [Kroger *et al.*, 2004].

More recently, attempts have been made to quantify the deformations of peripheral arteries, in order to understand better the mechanical environment into which stents are placed. Axial extension/contraction, torsion, compression and flexion have been identified as the forces acting on the SFA [Jaff, 2004]. Radiographic studies have been used to measure the deformation of stented and unstented arteries. These found axial compression and bending deformation of the SFA, the femoropopliteal segment and the popliteal artery [Nikanorov *et al.*, 2008], as well as axial compression and extension and twisting of the SFA [Cheng *et al.*, 2006]. For example, walking (knee/hip flexion of 70°/20°) causes an average compression of up to 14% and average bending of 33°. Sitting (knee/hip flexion of 90°/90°) increases average compression to a maximum of 23% and bending to 54° [Nikanorov *et al.*, 2008]. The amount of compression and bending depends on location.

The study by Nikanorov *et al* [Nikanorov *et al.*, 2008] allowed *in vitro* experiments to be set up that replicated the conditions observed *in vivo* using angiograms. The numbers of fractures for six different stent designs were reported for bending and axial deformation.

The objective of this study is to use the finite element method to investigate how the mechanical environment of peripheral arteries will influence the outcome of stenting. Finite element models of the deployment of stainless steel and nitinol stents in peripheral arteries were created. To these models, bending and compressive boundary conditions were applied. This allowed arterial stresses to be measured, as well as the stress amplitude and mean stress (for stainless steel stents), and strain amplitude (for nitinol stents) of the stents, which dictate the likelihoods of fatigue failure in stainless steel and nitinol stents.

The hypothesis under investigation is that the mechanical environment induced by joint flexion in peripheral arteries creates conditions that could cause elevated stresses in the artery, leading to amplified vessel injury and hence ISR, while also placing the stent in an environment that could increase the possibility of stent fracture due to fatigue. As the consequences of the pulsatile mechanical environment have already been studied in Chapter 5, this study further investigates the separate effects of the bending and compression induced in the artery by joint flexion. By doing this, the contribution of the pulsatile, bending and compressive environments can be investigated both in terms of arterial stresses and likelihood of fatigue related fracture of the stent.

6.2 Methods

6.2.1 Overview

The methods outlined here were used to create finite element models that replicate the mechanical environment of the femoral and popliteal arteries. The model boundary conditions to simulate the mechanical environment of femoral and popliteal arteries are based on data obtained from radiographic studies on those arteries [Cheng *et al.*, 2006; Nikanorov *et al.*, 2008].

6.2.2 Geometry

A finite element model was created of a peripheral artery. Although the conditions of the segment between and including the femoral and popliteal artery are being studied, a single artery was created. As described in Chapters 4 and 5, the artery had a length of 40 mm, an inner diameter of 8 mm, and a thickness of 1 mm and was modelled as a cylinder consisting of three concentric layers.

Two stent types were considered, a stainless steel balloon expanded stent (BES), and a nitinol self-expanding stent (SES). The BES was based on the Palmaz stent, as described in Chapters 4 and 5 and had a length of 20 mm and strut thickness of 150 μm. The SES used for the simulations was the same model (SES2) as described in Chapter 5. The stent was based on commercially available nitinol stents and had a strut thickness of 150 μm. It also had a diameter of 10 mm, designed to give a lumen gain of 1.25 times the inner diameter of the artery. Further models were created as variations on the SES2 design, with strut thickness of 100 μm (SES2(a)) and 250 μm (SES2(b)), with full details given in Chapter 5.

Symmetry was used to reduce the models to one quarter of their original size. A mesh density study was carried out on the nitinol stents by comparing the principal strains after crimping the stent from the initial diameter (10mm) to 5mm. The number of elements used to mesh the stent was increased until no appreciable difference was seen in the predicted strain values. Higher mesh densities were required at the crowns of the stent to achieve this.

6.2.3 Material properties

As before, the BES material model was based on 316L stainless steel and had bi-linear elastic-plastic behaviour. The SES was described by a Nitinol material model, and the artery layers had third-order Mooney-Rivlin constants fitted to data for aged human illiac arteries [Schulze-Bauer *et al.*, 2003].

6.2.4 Boundary conditions

The BES expansion was modelled as before, with a pressure applied and removed as a ramp load on the internal faces of the stent. Springs, with an initial low stiffness that increased at a specified stent diameter, were used to give the constraint of the balloon. The SES models were also deployed in the manner presented in Chapter 5, whereby a rigid sheath was compressed to fit the stent into the artery, then removed laterally to allow the stent to expand within the artery.

6.2.4.1 Mechanical environment

While the stent expansion was modelled as before, the more complex loadings being modelled here necessitated a slightly different approach towards the boundary conditions on the artery. Symmetrical boundary conditions were first applied to all nodes coinciding with planes of symmetry. The artery was then fixed from longitudinal movement at both ends, see Figure 6.1(a). Blood pressure was applied to the internal faces of the artery as a ramp load (Figure 6.1(b). A fixed displacement was then applied to one end of the stent to give it an axial pre-stretch, as shown in Figure 6.1(c). The stent was then deployed as appropriate, depending on whether a BES or SES was being modelled.

Following deployment of the stent, a rigid plate is used to apply the bending and compressive boundary conditions. This plate is a surface, larger than the artery, which is coincident with the face of the artery following application of the pre-strain. When the stent is deployed, a glue contact condition is applied between the plate and the artery. The pre-load displacement can then be removed, and compression or bending can be applied by moving the plate, see Figure 6.2. This method of applying a displacement to the plate instead of directly to the artery was used because it eliminated stress concentrations that were found to occur at the points of application of the boundary conditions when applied directly to nodes on the artery. This method does not alter the stresses in the artery as a result of physiological loading.

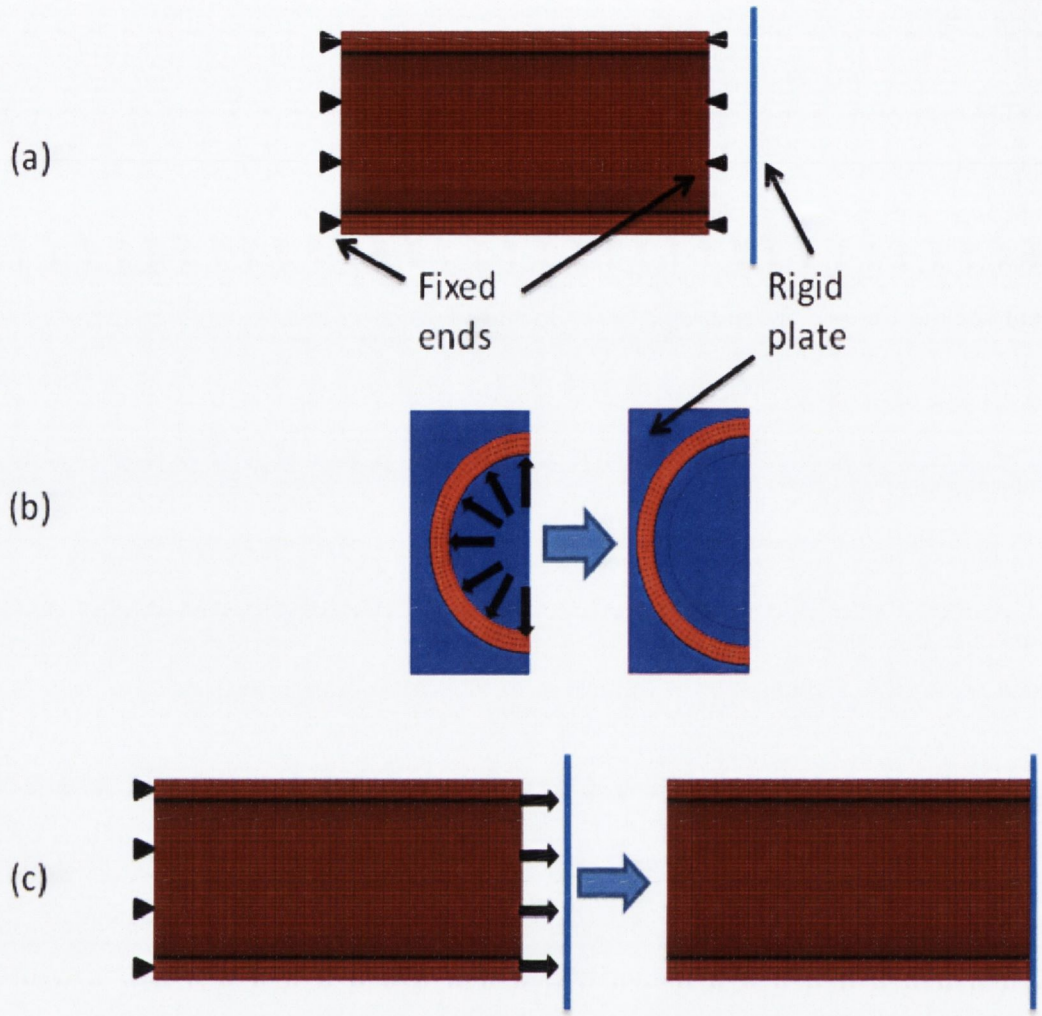


Figure 6.1

Application of physiological loading to artery. (a) starting configuration. (b) application of blood pressure. (c) application of physiological pre-stretch until the artery face is coincident with the rigid plate.

6.2.4.1.1 Bending

The bending boundary condition was applied by rotating the plate about the axis of symmetry. As the maximum bending was recorded in the popliteal artery and was 54° ± 25° [Nikanorov *et al.*, 2008], the plate was rotated through 60° and the model analysis undertaken for every 6° of rotation. Note that friction-free contact is assumed between all surfaces during stent deployment. During bending, a 'glue' contact is used between the artery and the stent to allow for the growth of tissue which occurs following implantation.

6.2.4.1.2 Compression

Compression was applied by moving the plate through 25% compressive stretch, representing the maximum stretch seen in the distal SFA/proximal popliteal artery of 23 ± 2 % [Nikanorov *et al.*, 2008]. Note that the value of 25% is calculated relative to the length of the artery following the application of the physiological axial strain. Two situations were considered; for the first, a friction free environment, representing a newly implanted stent. Secondly, a glue contact condition between the stent and the artery following stent expansion was modelled, representing the situation where neo-intimal tissue formation over the stent limits relative motion between the implant and the artery. As tissue growth occurs within days of stent implantation, the second scenario would be expected to be most representative of a stent *in vivo* for a long-term fatigue environment.

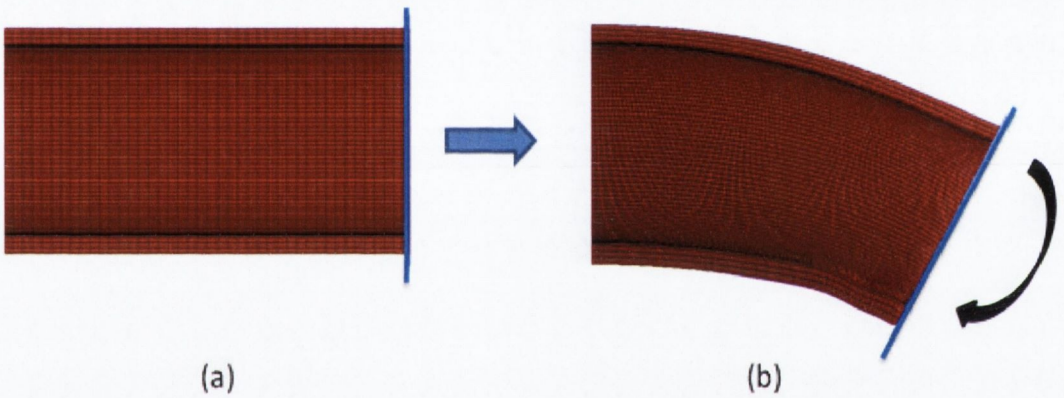


Figure 6.2

Application of bending boundary condition by rotating plate showing (a) shape following physiological loading and (b) after bending.

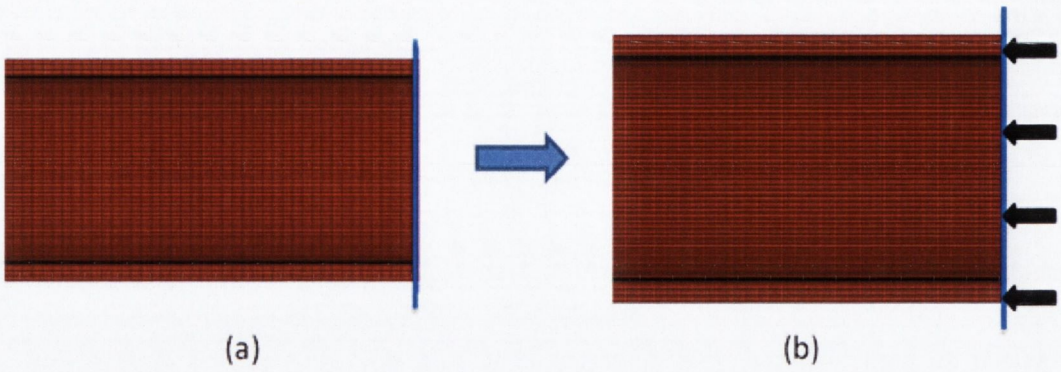


Figure 6.3

Application of compressive boundary condition by moving plate showing (a) shape following physiological loading and (b) after compression.

6.3 Results

As with the previous studies (see Chapters 4 and 5), elevated vessel injury is hypothesised to lead to higher rates of restenosis [Schwartz *et al.*, 1994]. Because of this, von Mises stresses are measured in the artery. It is proposed that increased von Mises stresses, a failure criterion, lead to a higher probability of tissue fissuring and increased injury score. The stresses in the artery are measured for each element. By taking the average stress at each element, a single value of stress can be assigned, and the accumulated volume of tissue within specified ranges predicted.

6.3.1 Bending

Arterial stresses following bending were analysed at 0° (following recoil), 12°, 18°, 36°, and 54°. The values of 12° and 18° represent close to average bending values of the distal SFA/ proximal popliteal artery at knee/hip flexions of 70°/20° and 90°/90° of 11° ± 12° and 15° ± 14°. Similarly, the values of 36° and 54° represent the popliteal artery at knee/hip flexions of 70°/20° and 90°/90° of 33° ± 21° and 54° ± 25°.

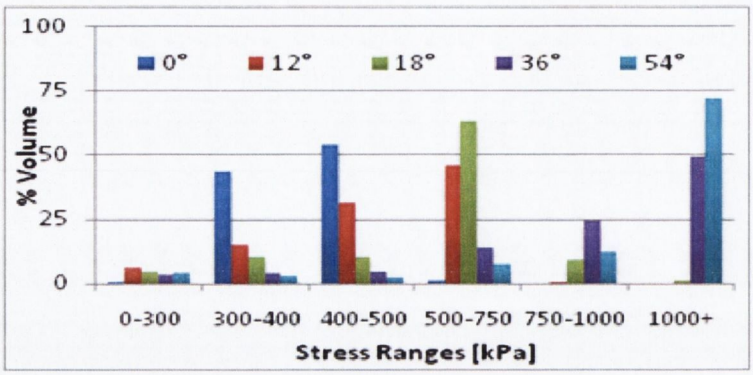
6.3.1.1 Balloon expanded stents

6.3.1.1.1 Artery Stresses

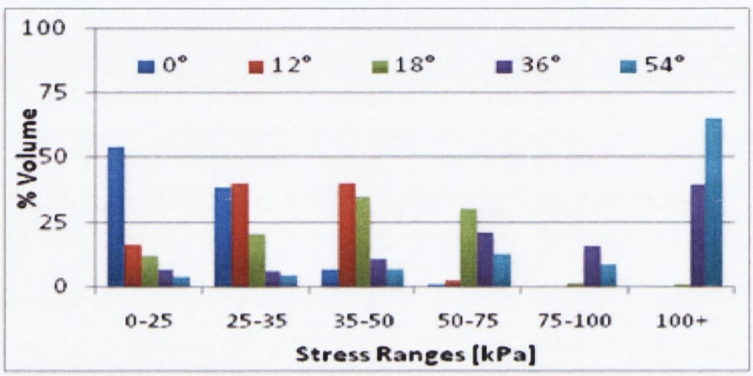
Each increment of bending applied to the artery is predicted to increase the stresses in each layer of the vessel wall, see Figure 6.4 and Figure 6.5. Applying 12° of bending decreases the amount of the intima at stresses of 500 kPa or lower from 98.3% to 52.8%, and places 46.1% of the intima at stresses between 500-750 kPa. As the amount of bending is increased, the amount of tissue in the higher stress ranges (assumed, in this case, to be 500 kPa or greater) increases. At 18°, 74.3% of the intima is at 500 kPa or more, with 10.8 % at more than 750 kPa. After 36° of bending, the amounts of tissue at 750-1000 kPa and 1000 kPa or more are 24.2% and 49.1% respectively. This increases to 11.9% and 71.45% when the bending is increased to 54°.

Higher stresses with increased bending are also predicted in the media and adventitia. In the media, the amount of tissue at 100 kPa or greater increases from less than 1% for 12° and 18° to 39.6% and 65.4% for 36° and 54°. Likewise, the amount of the adventitia at 100 kPa or more increases from 0% after stent expansion and less than 1% at 12° and 18° to 23.3% and 59.0% after 36° and 54° of bending.

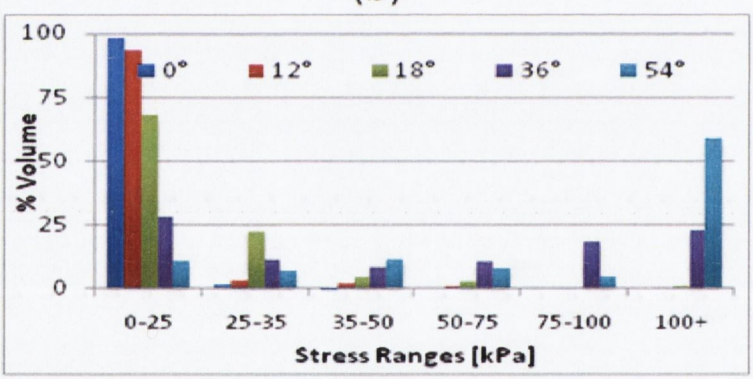
The peak stresses are located at the end of the stent, where the artery is in tension. As the bending is increased, high stresses are also seen distally/proximally to the stent, though the location of the peak stresses is the same, see Figure 6.5.



(a)



(b)



(c)

Figure 6.4

Stress distribution in peripheral (a) intima, (b) media and (c) adventitia following bending of a stent at 0° (following recoil), 12°, 18°, 36°, and 54°.

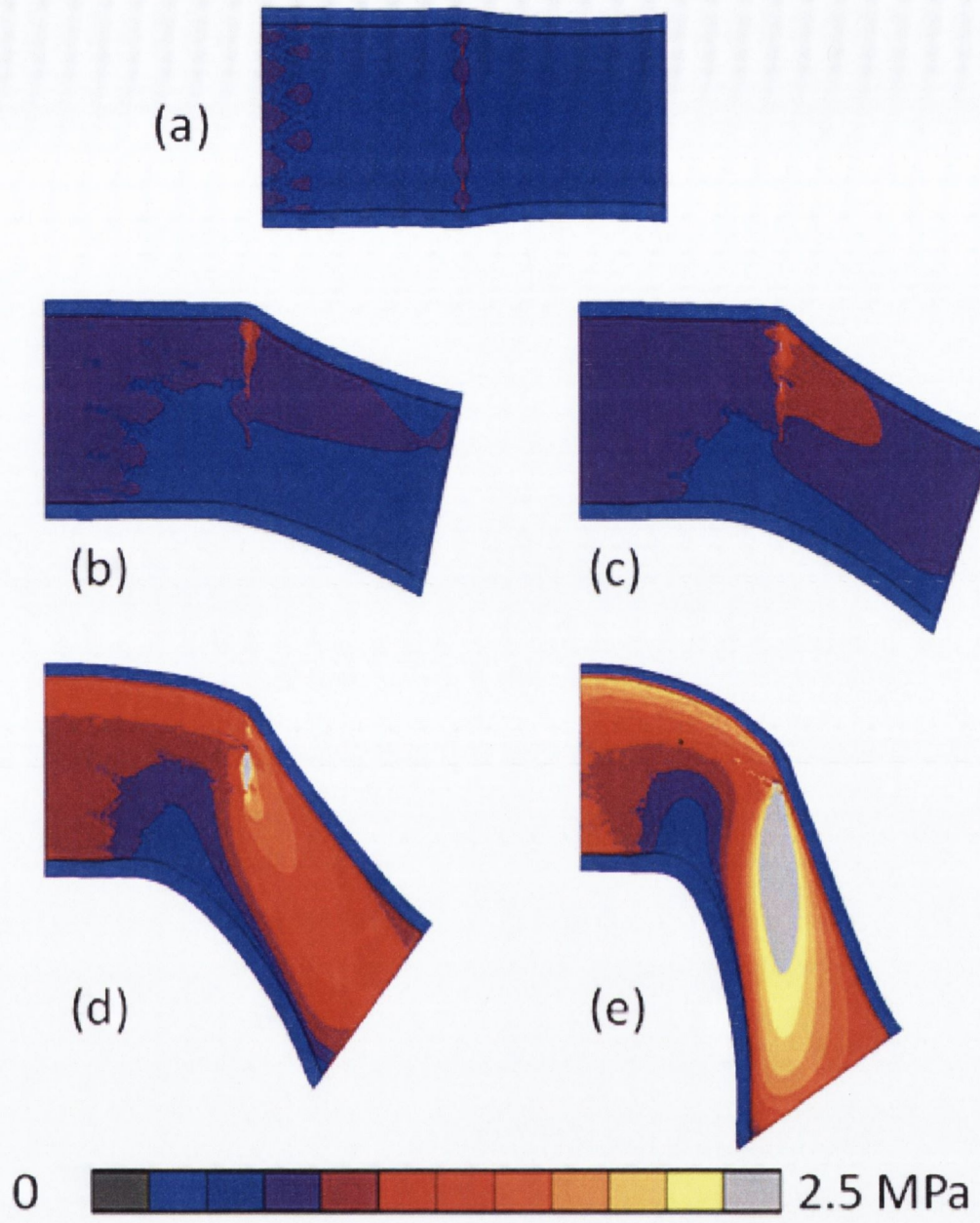


Figure 6.5

Contour plots of von Mises stresses in peripheral artery following (a) expansion of BES and application of (b)12°, (c) 18°, (d) 36° and (c) 54° of bending.

6.3.1.1.2 Stent fatigue

As stent fracture has been related to restenosis, the possibility of stent fatigue fracture was investigated. For stainless steel, the stress amplitude (σ_a) and the mean stress (σ_m) were plotted on a Goodman curve for each integration point of the stent elements. Using a fatigue endurance

limit (S_e) of 420 MPa and an ultimate tensile strength (S_{ult}) of 600 MPa [Wiersma *et al.*, 2006], a factor of safety could be determined for each integration point and represented graphically. The factor of safety (FOS) was calculated from

$$\frac{1}{FOS} = \frac{\sigma_m}{S_{ult}} + \frac{\sigma_a}{S_e} \qquad \textbf{(6. 1)}$$

For nitinol SES, the strain amplitude was measured. A threshold value of 0.4% [Pelton *et al.*, 2008] was taken, with strain amplitude values over 0.4% more likely to cause fatigue failure.

Increasing the amount of bending in the artery following insertion of a BES lowers the minimum factor of safety in the stent from 1.43 at 6° to 1.14 at 60°, see Figure 6.6. Plotting each integration point on a Goodman curve shows that as well as the factor of safety decreasing with increasing bending, the amount of points close to the line (FOS = 1) increases substantially (Figure 6.7).

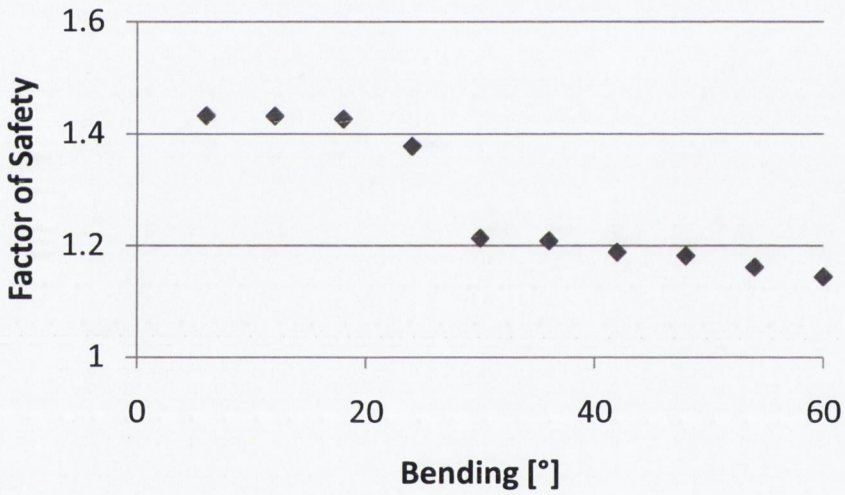


Figure 6.6

Factor of safety as a function of the amount of applied bending in a peripheral artery following expansion of a stainless steel stent.

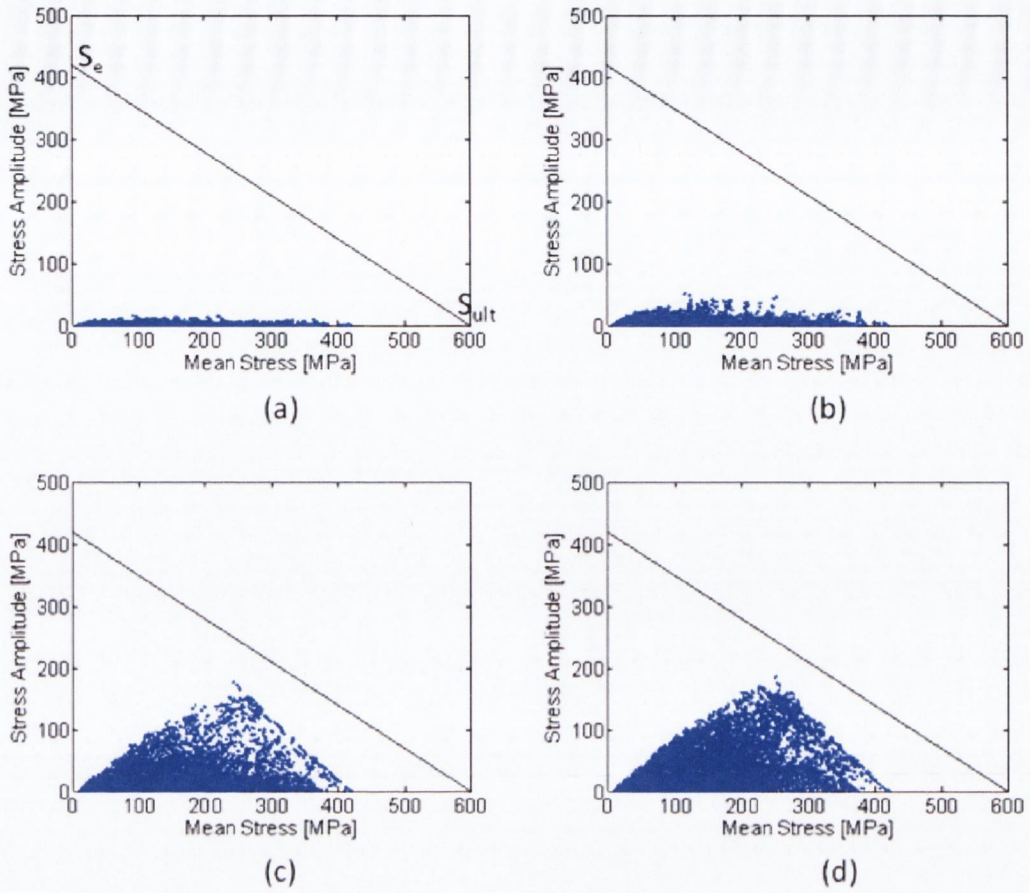


Figure 6.7

Goodman diagrams for a stainless steel stent in a peripheral artery following (a) 12°, (b) 18°, (c) 36°, and (d) 54° of bending.

6.3.1.2 Self-expanding stents

6.3.1.2.1 Artery stresses

As with the BES, bending an artery following implantation of an SES is predicted to increase the stresses in all the intima, media and adventitia of the peripheral artery, as shown in Figure 6.8. In all three layers, bending of 12° and 18° causes only minor changes in the arterial stress states. In the intima, the amount of tissue at lower (0-250 kPa) stresses is increased from none before bending is applied to between 12.9 and 18.3%, depending on the amount of bending. A greater effect is seen when the bending is increased to 36° and 54°. In the intima, 2.6% of the tissue is at stresses between 500-750 kPa, with less than 1% at stresses greater than this. After 54° of bending, 20.8% of the intima is at stresses between 500-750 kPa, with a further 6.9 and 4.3% at stresses of 750-1,000 kPa and 1MPa or greater. Similar trends are seen in the media and

adventitia, where bending of 12° and 18° made small changes to the stress distributions, while bending of 36° and 54° placed more of the tissue at higher stress ranges.

Altering the strut thickness causes variation in the stresses in each arterial layer at the various degrees of bending, as shown in Figure 6.9, Figure 6.10 and Figure 6.11. The trends are similar for each strut thickness, more significant changes in the stress states predicted after bending of 36° and 54°. Using a thinner strut (SES(a)) reduces the amount of intimal tissue at higher stresses. After 54° of bending, the amount of the intima between 500-750 kPa is reduced from 22.3% for SES2(b) (250 μm thick struts) to 20.8% for SES2 (150 μm thick struts) and 15.5% for SES2(a) (100 μm thick struts). Likewise, the amount of tissue at 750 kPa or greater is reduced from 13.7% with SES2(b) to 11.3% and 8.7% with SES and SES2(a).

In the media and adventitia, the same trends are observed, where implanting a stent with thicker struts is predicted to increase the amount of tissue at higher stresses.

For all values of bending, each of the SES models produces lower arterial stresses than the BES model. For example, the amount of tissue at the highest stress ranges (1,000 kPa or greater for the intima, 100 kPa or greater for media and adventitia) following 54° of bending is greater than 50% in all of the BES model, but does not exceed 16.1% in any of the SES models.

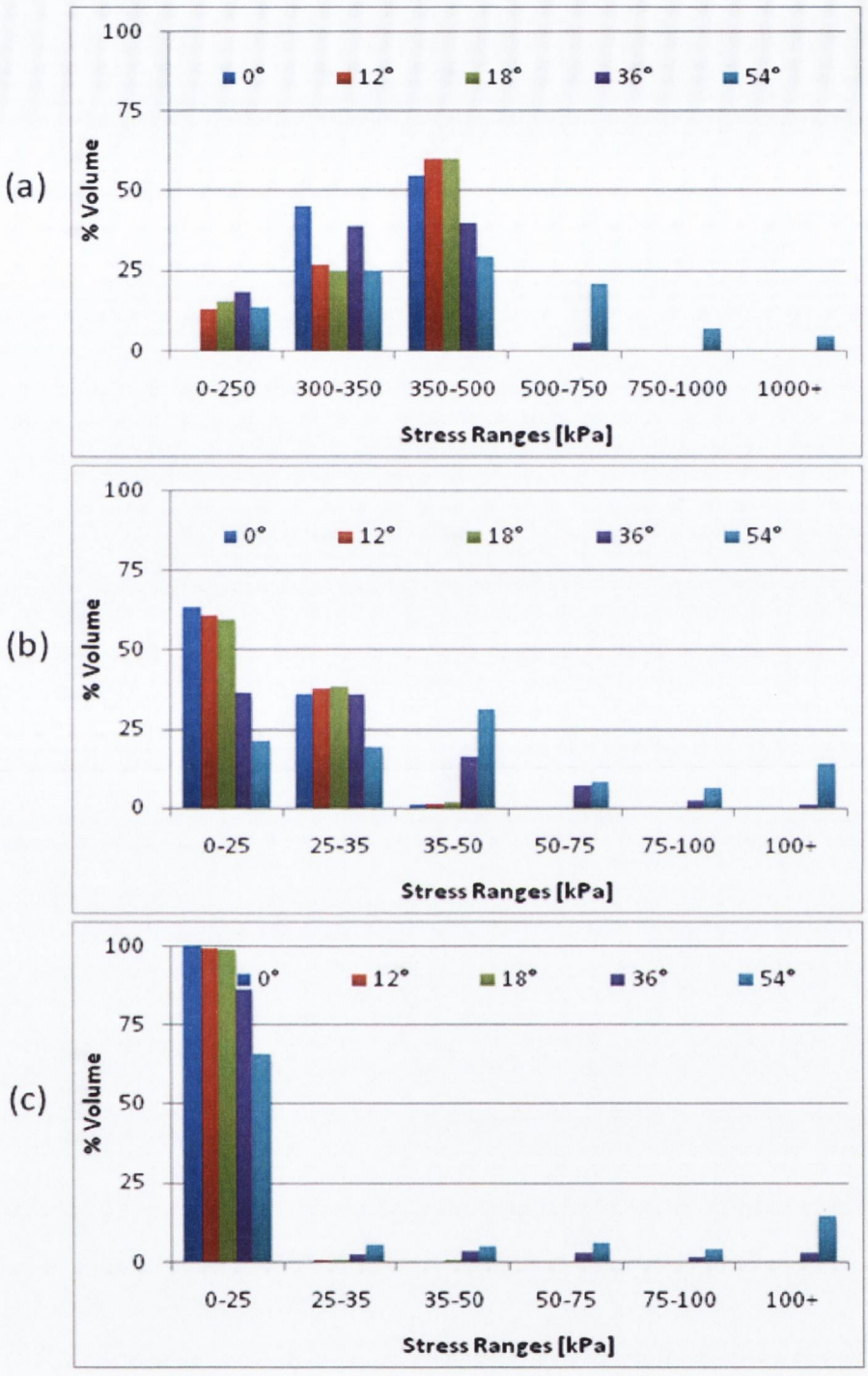


Figure 6.8

Stress distributions in peripheral arteries following deployment of SES with strut thickness of 150 μm. The three layers, (a) intima, (b) media, and (c) adventitia are shown.

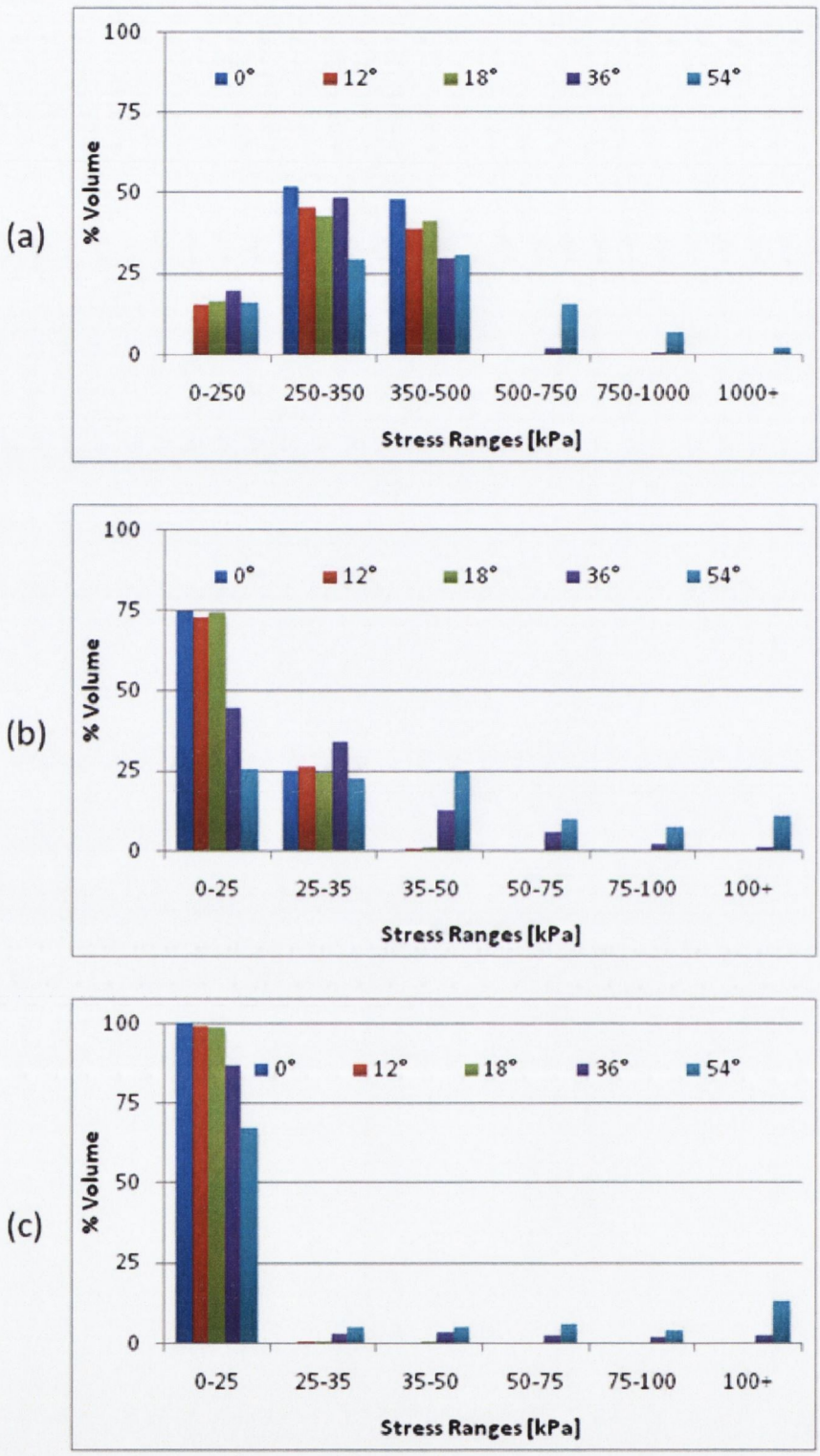


Figure 6.9

Stress distributions in peripheral arteries following deployment of SES with strut thickness of 100 μm. The three layers, (a) intima, (b) media, and (c) adventitia are shown.

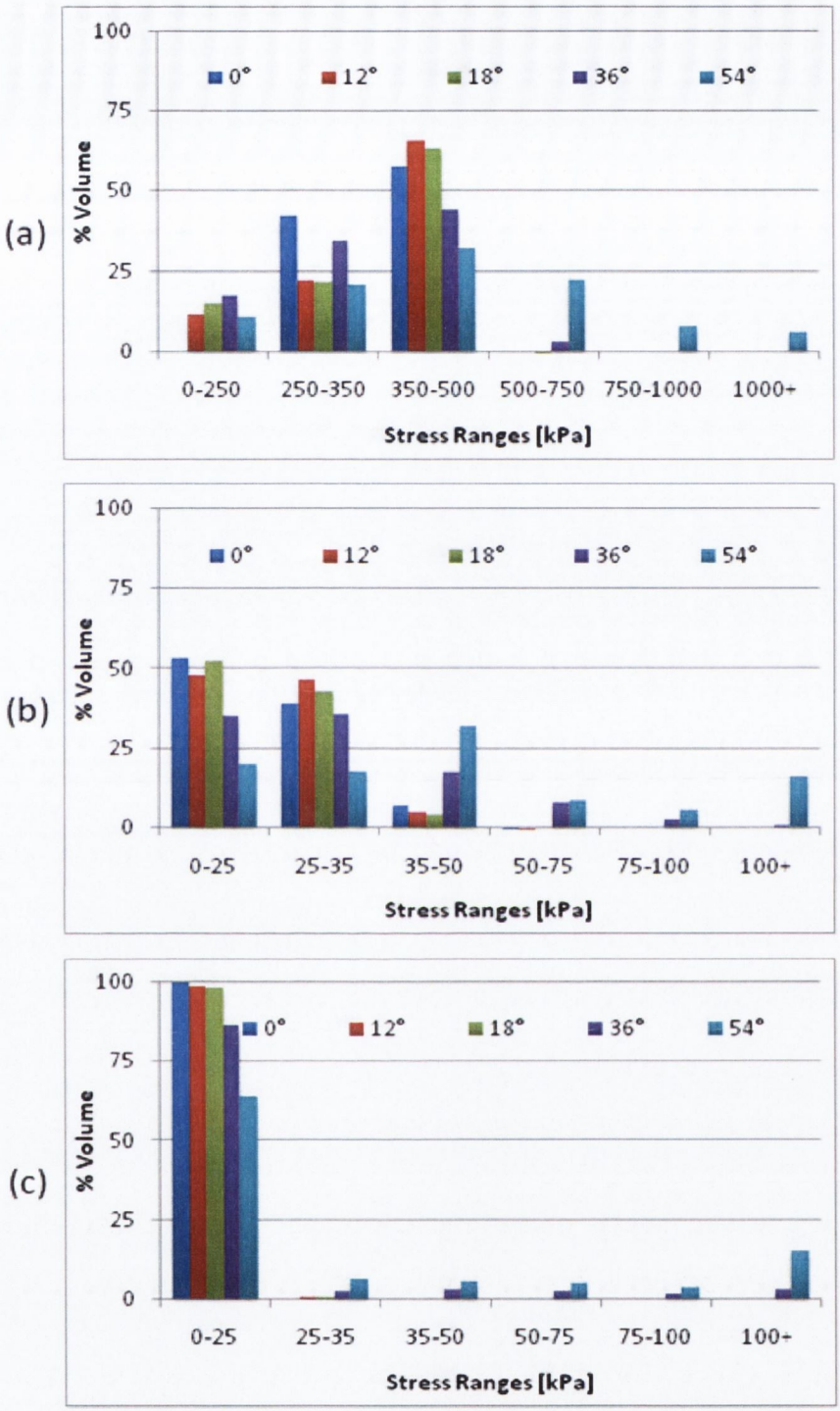
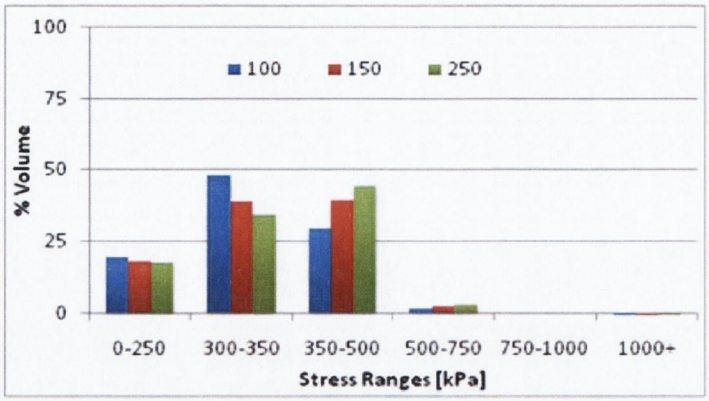


Figure 6.10

Stress distributions in peripheral arteries following deployment of SES with strut thickness of 250 μm. The three layers, (a) intima, (b) media, and (c) adventitia are shown.

(a)



(b)

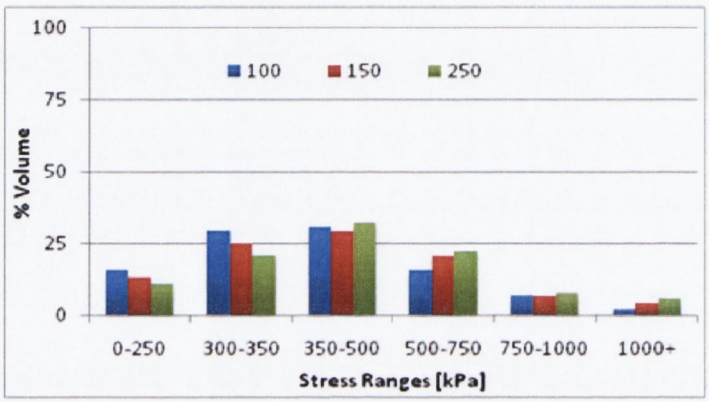


Figure 6.11

A comparison of intimal stresses following bending with three different strut thicknesses (100, 150 and 250 μm) after (a) 36° and (b) 54° of bending.

6.3.1.2.2 Stent fatigue

The maximum strain amplitude experienced by the stent during arterial bending was measured for every 6° and plotted. The strain amplitude was predicted to rise as bending was increased for all stent models. SES2(a), with a strut thickness of 100 μm, exceeded the strain amplitude threshold value of 0.4% with bending of between 24° and 30°, reaching a maximum value of 0.66% after 60° of bending (Figure 6.12). When the strut thickness is increased to 150 μm (SES2), the strain amplitude threshold value is not reached until bending of between 54° and 60°. Furthermore, the 250 μm strut thickness stent is predicted to reache a maximum strain amplitude of 0.39% at bending of 60°. This is below the strain threshold value of 0.4%, so the model is not predicting the stent failure due to bending. Also, the maximum strains predicted during bending are less than 3%. As the nitinol material modelled can experience recoverable strains of 6.3% (see Chapter 5), the stent will not permanently deform.

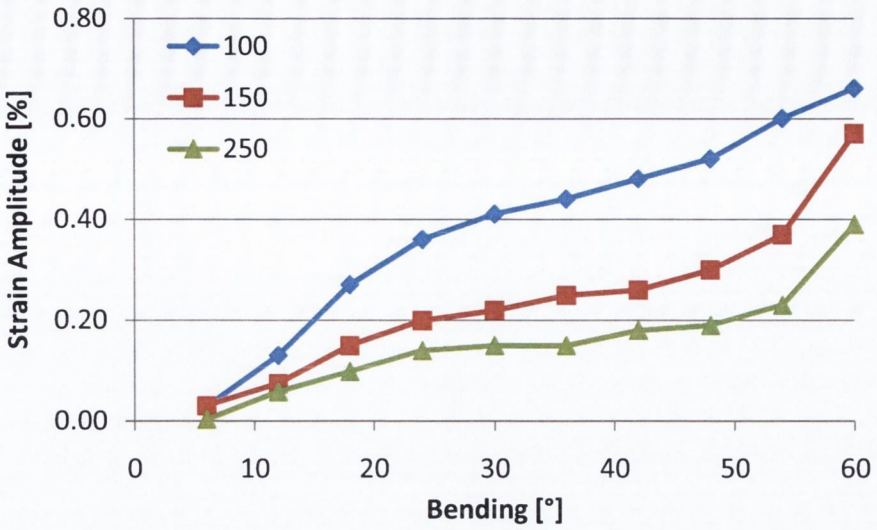


Figure 6.12

Strain amplitude as a function of bending in peripheral artery following deployment of stents with strut thicknesses of 100 μm (SES2(a)), 150 μm (SES2) and 250 μm (SES(b)).

6.3.2 Compression

As with bending, the strain amplitude of the stent is predicted to increase as artery compression is increased. Also, the strain amplitude experienced by the stent depends on the strut thickness, see Figure 6.13. All of the stent models predict a sharp increase in strain amplitude at low compression values, followed by a near plateau, with the strain amplitude increasing again at higher compression values. The compressive value at which the strain amplitude starts to increase again depends on the strut thickness. At all levels of compression, SES2(b) has the lowest strain amplitude. In this model, the strain amplitude increases from 0.2% at 12.5% compression, to 0.37% at 25%. SES2 has a lower strain amplitude than SES2(b) at compressive values of 15% or lower. Compressing the artery by more than 17.5% induces a higher strain amplitude in SES2.

The consequence of modelling the stent-artery interaction as glued contact was investigated by comparing the model with an equivalent frictionless (μ=0) model. The effect of friction depends on the degree of compression, see Figure 6.14. The frictionless model predicts a greater increase in strain amplitude at low levels of compression, which levels off as the compression is increased.

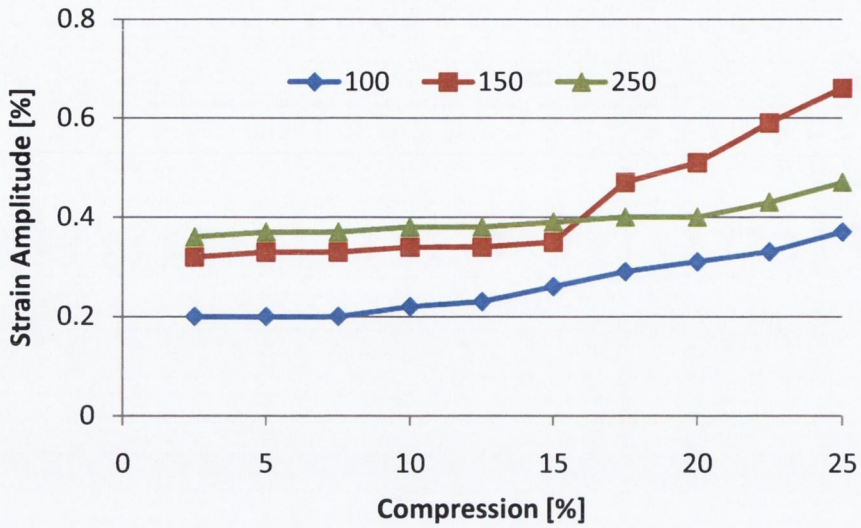


Figure 6.13

Predicted strain amplitude following compression of peripheral artery with implanted nitinol stent for stent strut thicknesses of 100, 150, and 250 μm.

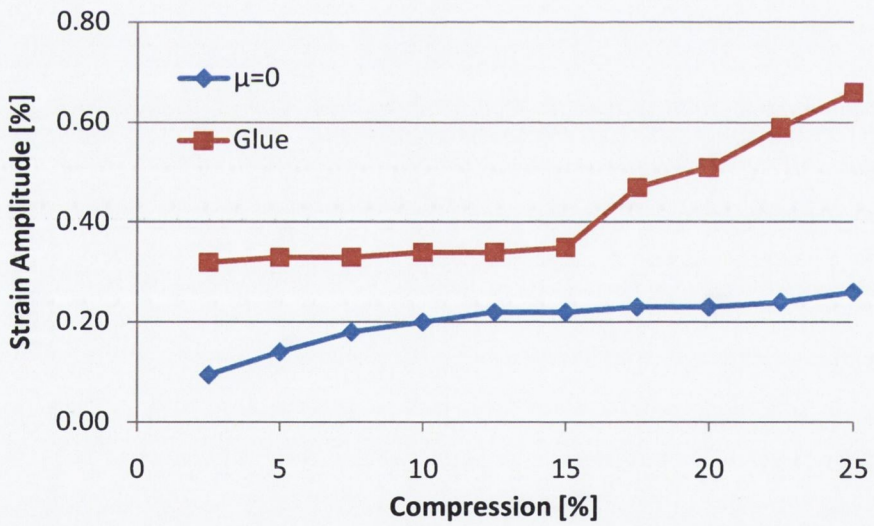


Figure 6.14

A comparison of strain amplitudes seen in stents with strut thicknesses of 150 μm for compression between 2.5% and 25%.

6.3.3 Influence of factors in peripheral arteries

The dominant mechanical force acting on the stents in relation to the fatigue environment is a function of location, see Table 6.1

and Table 6.2

. The iliac artery, for which bending and compressive loading has not been documented, has the highest factor of safety as the stent is only loaded by the pulsatile blood flow. In the femoral and femoro-popliteal segment, compression is the factor most likely to lead to stent fatigue failure, both under walking (knee/hip flexion of 70°/20°, see Table 6.1) and sitting (knee/hip flexion of 90°/90°, see Table 6.2) loading. The popliteal artery has the lowest factors of safety under bending.

	Bending/ Compression Values	Pulsatile SA (FOS)	Bending SA (FOS)	Compression SA (FOS)	Lowest FOS
Iliac	-	0.045 (8.89)	-	-	8.89 (Pulsatile)
Femoral	3°/5%	0.045 (8.89)	0.015 (26.67)	0.165 (2.42)	2.42 (Compression)
Femoro-popliteal	11°/14%	0.045 (8.89)	0.072 (5.56)	0.173 (2.31)	2.31 (Compression)
Popliteal	33°/9%	0.045 (8.89)	0.235 (1.70)	0.166 (2.38)	1.70 (Bending)

Table 6.1

Summary of maximum strain amplitudes (and minimum factors of safety) for pulsatile, bending, and compression loading of peripheral arteries after knee/hip flexion of 70°/20°.

	Bending/ Compression Values	Pulsatile SA (FOS)	Bending SA (FOS)	Compression SA (FOS)	Lowest FOS
Illiac	-	0.045 (8.89)	-	-	8.89 (Pulsatile)
Femoral	4°/9%	0.045 (8.89)	0.02 (20)	0.168 (2.38)	2.38 (Compression)
Femoro-popliteal	15°/23%	0.045 (8.89)	0.115 (3.48)	0.302 (1.32)	1.32 (Compression)
Popliteal	54°/14%	0.045 (8.89)	0.37 (1.08)	0.173 (2.31)	1.08 (Bending)

Table 6.2

Summary of maximum strain amplitudes (and minimum factors of safety) for pulsatile, bending, and compression loading of peripheral arteries after knee/hip flexion of 90°/90°.

6.4 Discussion

6.4.1 Artery bending

The results presented here demonstrate the incompatibility of simple stainless steel stents in arteries subject to bending. These stents, far stiffer than the arteries into which they are implanted, cause significant increases in stress in all three layers of the artery. The high peak stresses observed in the artery model and the volume of high tissue within high stress ranges are likely to lead to extensive tissue damage, and subsequent neo-intimal hyperplasia. Furthermore, bending the artery causes permanent deformation of the stent. This increases the probability of fatigue related fracture, and may affect the haeomodynamics of the vessel.

The magnitude and location of the high stresses in the artery would explain the lack of improvement of this type of stenting relative to PTA alone in femoral arteries [Cejna *et al.*, 2001]. Although the bending cycle modelled here is not predicted to cause fatigue failure of the stent (factor of safety greater than one for all integration points), this is for an idealised artery and a relatively short stent. A calcified or eccentric plaque, a longer lesion (and stent) or an eccentric plaque would be amongst the factors that could reduce the factor of safety and lead to stent fracture. Furthermore, the Goodman diagrams presented do not account for residual stresses which may be inherent in the stent following manufacturing and/or crimping.

Nitinol stents, though closer in compliance to arteries than steel stents, are still stiffer than the arteries into which they are inserted. The higher flexibility offered by these shape-memory alloy stents reduces the arterial stresses following bending. This suggests that damage to the arterial tissue is reduced, and restenosis rates would be expected to be lower in arteries where a SES is used compared with a BES. Clinical studies have shown that, unlike steel stents, the use of nitinol stents in the femoral artery improves rates of restenosis compared with balloon angioplasty alone [Schillinger *et al.*, 2006].

The fracture of nitinol stents continues to hinder their use in peripheral arteries. Therefore, a fatigue analysis of the stents is essential for full assessment of their performance. Unlike single-phase metals like steel, however, calculating a factor of safety for nitinol is not straightforward. Studies on nitinol stents have shown that although a threshold value for strain amplitude exists below which the material will not fail, the effect of the mean strain is less clear [Pelton *et al.*, 2004; Pelton *et al.*, 2008]. Therefore, the only suitable means of measuring the factor of safety for a nitinol stent is the strain amplitude threshold value of 0.4%. It should be noted that this value is obtained in experiments designed to model the high frequency, low amplitude strain controlled environment of the cardiac cycle pulse [Pelton *et al.*, 2008]. However, as 10 million bending cycles

caused by walking could be expected over a ten year period, this value can still be used for the lower frequency, higher amplitude bending fatigue cycle. The FE methodology presented in this chapter can therefore be adapted to predict the likelihood of fatigue failure of any given stent design.

Strut thickness is again shown to be an important factor in stent performance when considering the bending environment of peripheral arteries. Increasing the strut thickness causes an increase in arterial stresses following stent deployment and following arterial bending relative to thinner strut models. However, this increase in stress is small in all layers of the artery. Stents with thicker struts also produce lower strain amplitudes, decreasing the likelihood of fatigue failure. There is, therefore, a trade-off between reducing stresses in the artery and improving performance in the fatigue environment. In the case of bending, it can be argued that the increase in arterial stresses associated with stents with thicker struts is small relative to the benefit of improved fatigue behaviour. For example, SES2(b) is predicted not to fail in fatigue with a maximum strain amplitude below 0.4%, and produces a relatively small increase in arterial stress.

Two of the SES designs analysed predict strain amplitudes of above 0.4% after sufficient bending. However, this threshold value merely suggests the possibility of fatigue – there is no clear pass/fail line as there is with steel on a Goodman diagram. Therefore, it cannot be said with any great certainty that the stainless steel stent studied would perform better in fatigue than SES and SES(a). Instead, the nitinol stents should only be compared with other nitinol stent designs.

The maximum bending of 60° applied to the arteries is in the upper end of that predicted in patients [Nikanorov *et al.*, 2008]. The value used for testing for binary fracture was 48°, while the average for walking (70°/20° knee hip flexion) was 33° in the popliteal artery. The maximum flexion of 90°/90° for the knee and hip would be expected to occur less frequently, for example when sitting. Therefore, applying bending of 60° may over-estimate the bending experienced *in vivo*. However, by measuring values at every 6°, a more complete picture has been built up. The short length of the stents modelled may influence the results. Ideally, a longer segment of artery would be modelled, but this greatly increases computational cost. For example, the high stresses seen distal to the stent in the artery may be an artefact of the length of artery analysed and the boundary conditions. Nonetheless, this method is similar to *in vitro* bending tests and is still valid for the comparative results presented here.

6.4.2 Artery compression

The fatigue-related behaviour of nitinol stents in a compressive environment is strongly dependant on the strut thickness (Figure 6.13). As the artery is compressed, the diameter of the stent increases, inducing a fatigue environment similar to that caused by pulsatile blood flow on the stent. As the artery and stent are glued for the compression step of the simulation, the stented segment of the artery is stiffer than the non-stented segment, and so deforms less. The behaviour of the stents can be divided into two stages. Initially the stent, with the artery, is subject to an increase in diameter. At a high enough deflection, the compressive forces on the stent become significant. For example, when using SES (strut thickness of 150 μm), the change in diameter is the driving force behind the fatigue environment at compression of 15% or less. After this, the stent begins to be compressed more, and this drives the increase in strain amplitude.

At high values of compression, the strain amplitude of the nitinol stents may become significant. However, at average values of 9% and 14% for the mid SFA, femoral-popliteal segment and popliteal artery respectively [Nikanorov *et al.*, 2008], or 13% for the SFA [Cheng *et al.*, 2006], the strain amplitudes for all of the stent designs are below the value of 0.4% required for fatigue failure. Only in the femoro-popliteal segment, where the average axial compression of the artery is 23% is fatigue failure likely. All of the values obtained are, however, considerably higher than the strain amplitudes predicted in stents subject to a pulsatile fatigue environment. As compression occurs with joint flexion, this is a lower frequency event than the change in diameter associated with blood pressure. Nevertheless, as with bending, over a long enough period sufficient cycles may be accumulated to cause fatigue.

In an experimental study based on angiographic results, fracture was found in a total of 9 of 58 stents tested with 5% compression, and 20 of 58 tested with 48° of bending [Nikanorov *et al.*, 2008]. Although no fracture is predicted under a compressive cycle in this study, differences in artery properties, stent length and stent over-sizing could be sufficient to raise the strain amplitude predicted in the models presented here. However, the hypothesis of bending as the primary instigator of stent fracture is corroborated. Furthermore, stents which did not fracture in compression showed 100% fracture rates in bending, while the stent which did not fracture in bending had a 50% fracture rate in compression. Only one stent, the Absolute (Abbott Vascular, Santa Clara, CA) showed similar behaviour in compression and bending, with a 3% fracture rate in both tests [Nikanorov *et al.*, 2008]. This highlights the importance of stent design, and shows that compression and bending affect the fatigue properties of the stent in different ways. This is consistent with the findings here, which suggest that a given stent design (in this case with thicker struts) which is predicted to perform better in bending, may not perform as well in compression.

Likewise, while another stent design (with thinner struts) will perform better in compression, it may be more likely to experience fatigue failure in bending.

The behaviour of non-stented segment of the artery in compression is like that of a buckling column. It is, therefore, and artefact of the length of the unstented artery segment, which is essentially arbitrary. While this is believed to be a sufficient model for measuring stent fatigue, this limitation makes the model unsuitable for measuring arterial stresses without verification of the full behaviour of the artery in compression.

The prevalence of one mechanical factor (i.e, pulsatile, bending or compression) over the others depends on the location of the artery. The popliteal artery, which experiences the greatest amount of bending, is most likely to induce stent fatigue failure.

6.5 Conclusions

The results presented here show the contribution of artery bending towards increased stress in stented arteries, and the deformation and fatigue of the stents. The contribution of fatigue in compression is also demonstrated. Thus, the hypothesis of the study, that the mechanical environment produced by joint flexion raises arterial stresses and causes stent fatigue, is corroborated. It is predicted that compression contributes to fatigue failure, but due to normal activity, bending is the major contributor towards fatigue failure. Bending is also likely to cause stresses of sufficient magnitude and in appropriate areas to increase rates of ISR. This is likely to depend strongly on the extent of bending and the frequency at which this occurs. This would be specific towards each patient, and depend upon the degree of bending imposed by walking and sitting down, and the frequency of these activities.

A simple change in design (strut thickness) has been shown to affect the performance of the stents, both in terms of arterial stresses and stent fatigue. Further optimisation, therefore, could be expected to improve stent performance. The method tested here would be a suitable tool for such design modifications, while physical testing like that performed elsewhere would be suitable for validation [Nikanorov *et al.*, 2008]. In one of the few lesion sites that drug elution has not significantly improved results [Duda *et al.*, 2005], improving the mechanical design and behaviour of the stent is essential towards making stenting a viable treatment for PAD.

7 Discussion

Contents

7.1 Overview 178

7.2 Structure function relations of porcine arteries 178

7.3 Modelling the stenting procedure 179

7.1.3 Artery models 179

7.2.3 Stent deployment 181

7.4 Stenting in peripheral arteries 182

7.1.4 Differences between coronary and peripheral stenting 182

7.2.4 The mechanical environment of peripheral arteries 182

7.5 Stent design 183

7.6 Future work 184

7.1 Overview

The main objective at the beginning of this thesis was to investigate the reasons for the higher rates of restenosis seen in peripheral arteries compared with coronary arteries. To do this, a number of studies to obtain preliminary data were needed, followed by studies investigating factors which could explain these outcomes. Firstly, a comprehensive investigation of the mechanical and structural properties of the arteries from functionally different vascular sites was carried out for porcine arteries. The next study looked at the consequences of using these porcine arteries both for pre-clinical tests and for computational modelling. These two studies provided the basis for a full investigation into the differences in stenting procedures between the two artery types. One study focussed on the differences in geometry, material properties and stent types used in the procedures, while the next one was based on the mechanical environment of peripheral arteries.

7.2 Structure function relations of porcine arteries

The porcine arteries tested for this study behaved, in many ways, the same as human arteries. Non-linear, hyperelastic stress-strain responses with large recoverable strains were demonstrated. Anisotropy was also shown between the circumferential and longitudinal directions. A difference in response was also exhibited between tension and compression. Collagen fibres can be said to only bear loads in tension. When a sample is compressed, much less of the artery is in tension, so the response shows less stiffness. The order of stiffness is also the same as human arteries, with the coronary artery being the stiffest and the aorta the least stiff.

The main difference presented between porcine and human arteries here is that human arteries are stiffer (see, for example, Figure 4.5). It should be noted though, that this may owe as much to differences in ages as to inter-species variability. The porcine arteries tested here were from pigs less than 6 months old, as is often the case for such studies. The human tissue it is being compared to, and which is most valid for in terms of angioplasty and stent modelling, is usually older. Human arteries stiffen with age, and intimal thickening occurs in all arteries. This is not observed in animals, and accounts for much of the observed difference in behaviour. The hypothesis that the function of arteries is determined by composition is affirmed between different artery types, but not within artery types.

The hypothesis that the collagen to elastin ratio is the prime determinant of material behaviour is refuted. The complex structure of the materials being studied means that factors such as the fiber orientations are important descriptors of material behaviour, and a single variable, such as the ratio of the constituents, is insufficient to predict mechanical behaviour.

7.3 Modelling the stenting procedure

7.1.3 Artery models

While the presented similarities of human and porcine tissues indicate the appropriateness of using pigs in pre-clinical animal trials, it is also important that the differences between the two are understood so that data obtained from these trials can be better understood. The work presented here (see Chapter 4) shows that the two artery types differ in mechanical response when comparing different aspects of stent design. In particular, differences are seen in arterial stresses and in the recoil of the stent.

Changes in strut thickness, for otherwise identical stent designs, have been shown to influence rates of restenosis [Kastrati *et al.*, 2001]. The reason for this can be attributed to the amount of recoil undergone by the stent. The amount of recoil is dependent on the material properties of the stent, the degree of inflation, and aspects of stent design. However, it is also dependent on the external reaction forces acting on the stent. For free expansion, these forces are zero. When expanded in an artery, the elastic recoil of the artery will increase the amount of recoil. The influence of the artery can again be related to a number of factors, including arterial geometry and material properties, and in humans the degree of stenosis. The results presented in this study predict a variation in recoil according to the material properties of the artery, which in turn affects the stresses in the respective arteries.

Another study presented shows that differences in mechanical responses according to stent design may be less pronounced in porcine than in human arteries. This is consistent with some animal trials which do not differentiate between stent designs [Taylor *et al.*, 2001], while stent design has been demonstrated as a factor which influences the outcome of stenting procedures in humans [Kastrati *et al.*, 2000]. However, the difference in response presented here is relatively minor, and the order of the stents in terms of the stresses induced in the artery remain the same. Other factors, such as the time frame (pre-clinical trials are often a month or less in duration, compared with six months to two years for many randomised human trials), and the interspecies

variation in pathological response [Schwartz *et al.*, 1994] and the lack of stenotic plaque would also account for the differences between animal and human trials.

This work has highlighted one of the aspects of the differences between responses in the arteries of two species. By complementing this work with such an understanding of other areas of variance of stent behaviour between pre-clinical and clinical settings, it may be possible to both reduce the number of animal trials and increase the relevancy of data obtained from them. Suitable use of finite element models may also provide a more pertinent method of comparing stent designs.

One difficulty highlighted is the variation of mechanical properties of arteries. This sort of variation can be expected in the geometry as well. Accurately representing this kind of widely differing environment can be difficult. It is suggested that taking an average stress-stretch curve to represent the mechanical properties and using a cylindrical artery for the geometry is the most suitable method of capturing the behaviour of a population. This may not be sufficiently accurate in a patient-specific approach, but such a study is not necessitated here. However, the consequences of the change in material properties has been highlighted.

It is desirable to use human arterial properties for mechanical testing and for finite element models. The drawback to using this tissue is the availability of fresh human tissue. Ethical and safety reasons mean that human arterial tissue is difficult to obtain. Even when the tissue is obtained, it may be several days post-mortem, and may have been treated with antibiotics to make it safe to handle. Understanding the drawbacks of using more readily available porcine arteries for mechanical testing would make the interpretation of results more relevant.

High peak stresses are predicted to be experienced by the artery in many of the models presented here. The stresses in some cases (particularly following bending) exceed those documented in the stress-stretch curves on which the material models are based. As such, the material may alter beyond the stress/strain described by the source curves. Further, the tissue may fail at sufficiently high stress/strain. It may be suggested that even if an accurate stress states cannot be established, areas of high stress where restenosis could occur can still be identified.

As hypothesised, the difference in mechanical response between human and porcine arteries, both in terms of recoil and in arterial stresses, may be a contributor to the failure of some animal trials to differentiate between stent designs in the same way as randomised trials in humans.

7.2.3 Stent deployment

Accurate modelling the expansion of a stent has been shown to be necessary to precisely capture both the stresses and final shape of the stent and the interaction with the artery [De Beule *et al.*, 2008; Gervaso *et al.*, 2008]. However, fully modelling the balloon-stent interaction, as well as the stent-artery and balloon-artery interactions is an intricate problem. The method used, whereby multi-stiffness springs are used to restrain the stent, provides a method of deploying a stent which allows for a uniform expansion and recoil with reduced computational costs. While this model would not predict the realistic expansion profiles attained by fully modelling the balloon-stent interaction, it is suitable for the purposes of these studies.

The modelling of the nitinol stent deployment does not require the use of a balloon, and so in that sense is simpler to model. Other aspects of this procedure present other complications when modelling this procedure. The method of deployment modelled, where the stent is crimped in a sheath and released in the artery by removing this sheath, has not been verified, and is designed to allow deployment of the stent within the artery rather than replicate the delivery process. For example, the stent is not crimped as much as would be necessary *in vivo* to negotiate the stent into position, but merely enough to fit inside the artery. It does capture the expansion behaviour shown by these stents, with one end expanding followed by full expansion. This is similar to the dog-boning seen using balloon expanded stainless-steel stents.

There are a number of limitations of the material model which would compromise the results. By using an isotropic model, the stresses will not fully reflect those of an anisotropic material. This has been shown to affect the accuracy of calculations for stresses in the artery [Holzapfel *et al.*, 2002]. The lack of permanent deformation in the artery material model also limits the results, particularly when measuring recoil. Pseudoelasticity (separate modelling of loading and unloading curves) of the arteries is not incorporated either. Together, these two material properties would be expected to soften the unloading curves, which could be important when measuring recoil, which has been demonstrated to be an important factor in determining arterial stresses. It would also be expected to be important when modelling the fatigue environment of peripheral arteries.

Modelling the behaviour of nitinol stents presents additional problems to the ones outlined above. One of the visco-elastic properties of arteries is creep, where a constant force leads to an increase in displacement over time. Once deployed, nitinol stents continue to exert a chronic outward force on the artery. The viscoelasticity of the arteries results in continued expansion of the stent over a period of 180 days [Zhao *et al.*, 2009]. This would alter the lumen gain, the

arterial stresses, and the pulsatile driven fatigue environment in ways that cannot be captured in this model.

Throughout the studies undertaken, von Mises stress is assumed to be the stimulus for restenosis. This is hypothesised to correlate with levels of injury, which have been correlated with amount of neo-intimal formation [Schwartz *et al.*, 1994]. This injury is scored based on stent penetration into the artery (see Chapter 2 for further details). Therefore, it seems reasonable to assume that a failure criterion which takes account of the overall stress state of the artery is appropriate as the driver of restenosis. However, compelling cases can also be made for other criteria. On one hand, it can be argued that the tissue fails in tension, and so the first principal stress may be a better measure of injury. On the other hand, a compressive (minimum principal stress) threshold has been established for muscle tissue [Linder-Ganz *et al.*, 2006]. In work ongoing in the Trinity Centre for Bioengineering, this has been proposed as the stimulus for a multi-scale model to predict restenosis [Boyle *et al.*, 2008]. There are credible arguments to be made that the stimulus is strain rather than stress based. The relationship between the stimulus and injury is also not fully understood. It has been shown that increased injury score increases neo-intimal growth, but the relationship between the stimulus (for example, von Mises stresses) could be linear, exponential or a threshold value, amongst others. In this regard, restenosis is a poorly understood process.

7.4 Stenting in peripheral arteries

7.1.4 Differences between coronary and peripheral stenting

The hypothesis that differences in geometry, material properties and stent type between peripheral and coronary arteries is responsible for the higher rates of restenosis seen in the former can be rejected. The higher stiffness of the target bed and the stent in the coronary arteries result in higher stresses than those predicted in peripheral arteries. This leads to a more adverse fatigue environment in the peripheral arteries, but this is unlikely, on its own, to cause stent fracture.

7.2.4 The mechanical environment of peripheral arteries

Bending and compression of peripheral arteries are predicted to be the main causes of high rates of restenosis. The high stresses in the artery and permanent deformation of a stainless steel stent after artery bending show the incompatibility with this therapy for PAD. The number of

integration points with low factors of safety is also raised, suggesting that in a less idealised model the stent could experience fracture from fatigue.

Using a nitinol stent gives significantly lower stresses in the artery following stent deployment and following bending. Interestingly, the stresses are lower in a peripheral artery with a nitinol stent following bending than in a coronary artery following expansion of a stainless steel stent. This does not necessarily indicate lower rates of restenosis. The pathological responses of the two artery types are different. Also, the stent and artery segment modelled are small compared with some of the long lesions that can be seen in, for example, the femoral artery. Such lesions are treated with either long or multiple stents. The latter case introduces a new factor that could influence artery stresses and the fatigue life of the stents; the stent-stent interaction. The limiting factor restricting the modelling of such lesions, and associated longer and/or multiple stents, is computational power. Such a model would require multiples of the number of elements used here, possibly more if it were not possible to assume symmetry.

Compression and/or bending of a nitinol stent are still predicted to raise the probability of fatigue failure, even for the relatively short stents modelled. Combined with the high peak stresses seen in the arteries following bending, this confirms the main hypothesis of the thesis, i.e. that the mechanical environment is the primary factor for the higher rates of restenosis seen in peripheral arteries compared with coronary arteries.

7.5 Stent design

Stent design has been shown, in clinical studies, to affect the outcome of stenting procedures. This is reflected by a number of findings in this study. Stent design is shown to influence both the amount of stent recoil, and the arterial stresses in pig and human arteries following stenting.

For nitinol stents, two design factors which could increase lumen gain, strut thickness and diameter, were investigated. Increasing the initial stent diameter, or oversizing, gave an increase in lumen gain, but also large increases in stress and diminished behaviour in fatigue. This has been shown to raise levels of intimal hyperplasia [Zhao *et al.*, 2009], and it is recommended that this practise be avoided. Increasing strut thickness, which also predicts greater lumen gain, improves the performance of the stent in fatigue. This is true of the pulsatile fatigue environment, but also the bending environment.

Finite element modelling of peripheral arteries may, in some cases, be limited by the number of elements needed to create a full model. Smaller models such as the ones here represent a valuable design tool to optimise stent performance. It is suggested that by combining the models presented here to improve stent design with the types of tests outlined previously [Nikanorov *et al.*, 2008], a stent design which would not cause excessive arterial stresses when subject the loading associated with peripheral arteries and which would not fail by fatigue could be found.

7.6 Future work

The work presented here is a first analysis of the performance of stents in peripheral arteries. There is scope for improvement within the models presented here, and for supplementary studies.

The material models presented here could be improved to more accurately model the arterial response. By including anisotropy, viscoelasticity and plasticity, the behaviour of the arteries could be more accurately predicted. To implement such a material model, more data may be needed. Layer specific biaxial data, such as that available for the human iliac artery [Schulze-Bauer *et al.*, 2003] would be necessary. Viscoelastic and plasticity data for the appropriate arteries, and perhaps layers, would also be required.

More accurate assessments of stent designs could be made if the fatigue predictions were confirmed with mechanical tests, as described previously [Nikanorov *et al.*, 2008]. Only basic design features (stent diameter and strut thickness) were investigated. A more rigorous investigation could be undertaken with these two methods, with the longer term goal of bringing ISR rates in peripheral arteries in line with coronary arteries.

Peripheral arteries in this study has referred to arteries in the leg, the iliac, femoral and popliteal arteries. These are not the only arteries in the body which experience loading due to joint motion. The carotid artery in particular experiences large deformations in relation to head turning and swallowing [Robertson *et al.*, 2008]. This can lead to axial and radial deformations, as well as stent crushing. Nitinol stent deployment has been modelled in carotid arteries [Wu *et al.*, 2007]. The methods used here for simulating the mechanical environment of peripheral arteries could be used in a similar fashion on carotid arteries. The shorter lesion and stent lengths of this artery make it suitable for modelling for the purposes of investigating stent fatigue. The presence of a bifurcation may make the hemodynamics a critical factor when analysing the artery for likely

areas of restenosis. Stent fractures do occur in other sites, but are not believed to be as prevalent. A study has been carried out where the deformations of a renal artery are used to model the loading experienced by a cobalt-chromium stent [Hsiao *et al.*, 2007]. Although fatigue failure is not predicted, it is found that artery bending and using over-lapping stents lowers the factor of safety. This study does not look at the stent-artery interaction.

Ultimately, the use of finite element modelling has been shown to be a useful tool for pre-clinical testing of stents. It can be used to compare stent designs in all artery types, and for modelling the deployment and interaction of stents in peripheral arteries.

References

Aoki, J., G. Nakazawa, et al. (2007). "Incidence and clinical impact of coronary stent fracture after sirolimus-eluting stent implantation." Catheter Cardiovasc Interv **69**(3): 380-6.

Auricchio, F. (2001). "A robust integration-algorithm for a finite-strain shape-memory-alloy superelastic model." International Journal of Plasticity **17**(7): 971-990.

Auricchio, F. and L. Petrini (2002). "Improvements and algorithmical considerations on a recent three-dimensional model describing stress-induced solid phase transformations." International Journal for Numerical Methods in Engineering **55**(11): 1255-1284.

Auricchio, F. and R. L. Taylor (1997). "Shape-memory alloys: Modelling and numerical simulations of the finite-strain superelastic behavior." Computer Methods in Applied Mechanics and Engineering **143**(1-2): 175-194.

Babalik, E., M. Gulbaran, et al. (2003). "Fracture of popliteal artery stents." Circ J **67**(7): 643-5.

Ballyk, P. D. (2006). "Intramural stress increases exponentially with stent diameter: a stress threshold for neointimal hyperplasia." J Vasc Interv Radiol **17**(7): 1139-45.

Bedoya, J., C. A. Meyer, et al. (2006). "Effects of stent design parameters on normal artery wall mechanics." J Biomech Eng **128**(5): 757-65.

Bergel, D. H. (1960). The visco-elastic properties of the arterial wall. London, University of London. **Ph.D.**

Berne, R. M. and American Physiological Society. (1979). Handbook of physiology : a critical, comprehensive presentation of physiological knowledge and concepts. Bethesda (Md.), American Physiological Society.

Bonsignore, C. (2004). "A decade of evolution in stent design." SMST-2003: Proceedings of the International Conference on Shape Memory and Superelastic Technologies: 519-528.

Bredlau, C. E., G. S. Roubin, et al. (1985). "In-hospital morbidity and mortality in patients undergoing elective coronary angioplasty." Circulation **72**(5): 1044-52.

Burton, A. C. (1954). "Relation of structure to function of the tissues of the wall of blood vessels." Physiol Rev **34**(4): 619-42.

Capelli, C., F. Gervaso, et al. (2009). "Assessment of tissue prolapse after balloon-expandable stenting: influence of stent cell geometry." Med Eng Phys **31**(4): 441-7.

Carew, T. E., R. N. Vaishnav, et al. (1968). "Compressibility of the arterial wall." Circ Res **23**(1): 61-8.

Cejna, M., S. Thurnher, et al. (2001). "PTA versus Palmaz stent placement in femoropopliteal artery obstructions: a multicenter prospective randomized study." J Vasc Interv Radiol **12**(1): 23-31.

Chan, C. M., S. Trigwell, et al. (1990). "Oxidation of an Niti Alloy." Surface and Interface Analysis **15**(6): 349-354.

Cheng, C. P., N. M. Wilson, et al. (2006). "In vivo MR angiographic quantification of axial and twisting deformations of the superficial femoral artery resulting from maximum hip and knee flexion." J Vasc Interv Radiol **17**(6): 979-87.

Chua, S. N. D., B. J. Mac Donald, et al. (2002). "Finite-element simulation of stent expansion." Journal of Materials Processing Technology **120**(1-3): 335-340.

Chua, S. N. D., B. J. Mac Donald, et al. (2003). "Finite element simulation of stent and balloon interaction." Journal of Materials Processing Technology **143**: 591-597.

Chua, S. N. D., B. J. MacDonald, et al. (2004a). "Effects of varying slotted tube (stent) geometry on its expansion behaviour using finite element method." Journal of Materials Processing Technology **155-56**: 1764-1771.

Chua, S. N. D., B. J. MacDonald, et al. (2004b). "Finite element simulation of slotted tube (stent) with the presence of plaque and artery by balloon expansion." Journal of Materials Processing Technology **155-56**: 1772-1779.

Clark, J. M. and S. Glagov (1985). "Transmural organization of the arterial media. The lamellar unit revisited." Arteriosclerosis **5**(1): 19-34.

Cox, R. H. (1978). "Passive mechanics and connective tissue composition of canine arteries." Am J Physiol **234**(5): H533-41.

Cox, R. H. (1982). "Comparison of mechanical and chemical properties of extra- and intralobar canine pulmonary arteries." Am J Physiol **242**(2): H245-53.

Cox, R. H. (1983). "Comparison of arterial wall mechanics using ring and cylindrical segments." Am J Physiol **244**(2): H298-303.

Davidson, J. M., K. E. Hill, et al. (1985). "Longitudinal gradients of collagen and elastin gene expression in the porcine aorta." J Biol Chem **260**(3): 1901-8.

De Beule, M., P. Mortier, et al. (2008). "Realistic finite element-based stent design: the impact of balloon folding." J Biomech **41**(2): 383-9.

de Feyter, P. J., P. Kay, et al. (1999). "Reference chart derived from post-stent-implantation intravascular ultrasound predictors of 6-month expected restenosis on quantitative coronary angiography." Circulation **100**(17): 1777-83.

Diaz, J. A., M. Villegas, et al. (2004). "Flexions of the popliteal artery: dynamic angiography." J Invasive Cardiol **16**(12): 712-5.

Ding, Z. and M. H. Friedman (2000a). "Dynamics of human coronary arterial motion and its potential role in coronary atherogenesis." J Biomech Eng **122**(5): 488-92.

Ding, Z. and M. H. Friedman (2000b). "Quantification of 3-D coronary arterial motion using clinical biplane cineangiograms." Int J Card Imaging **16**(5): 331-46.

Ding, Z., H. Zhu, et al. (2002). "Coronary artery dynamics in vivo." Ann Biomed Eng **30**(4): 419-29.

Do, D. D., J. Triller, et al. (1992). "A Comparison Study of Self-Expandable Stents Vs Balloon Angioplasty Alone in Femoropopliteal Artery Occlusions." Cardiovascular and Interventional Radiology **15**(5): 306-312.

Duda, S. H., M. Bosiers, et al. (2006). "Drug-eluting and bare nitinol stents for the treatment of atherosclerotic lesions in the superficial femoral artery: long-term results from the SIROCCO trial." J Endovasc Ther **13**(6): 701-10.

Duda, S. H., M. Bosiers, et al. (2005). "Sirolimus-eluting versus bare nitinol Stent for obstructive superficial femoral artery disease: The SIROCCO II trial." Journal of Vascular and Interventional Radiology **16**(3): 331-338.

Duda, S. H., B. Pusich, et al. (2002). "Sirolimus-eluting stents for the treatment of obstructive superficial femoral artery disease: six-month results." Circulation **106**(12): 1505-9.

Duerig, T. W. (1990). Engineering aspects of shape memory alloys. London ; Boston, Butterworth-Heinemann.

Duerig, T. W., D. E. Tolomeo, et al. (2000). "An overview of superelastic stent design." Minimally Invasive Therapy & Allied Technologies **9**(3-4): 235-246.

Dumoulin, C. and B. Cochelin (2000). "Mechanical behaviour modelling of balloon-expandable stents." J Biomech **33**(11): 1461-70.

Edelman, E. R. and C. Rogers (1998). "Pathobiologic responses to stenting." Am J Cardiol **81**(7A): 4E-6E.

Edelman, E. R. and C. Rogers (1999). "Stent-versus-stent equivalency trials : are some stents more equal than others?" Circulation **100**(9): 896-8.

Ellis, S. G., M. Savage, et al. (1992). "Restenosis after placement of Palmaz-Schatz stents in native coronary arteries. Initial results of a multicenter experience." Circulation **86**(6): 1836-44.

Favier, D., Y. Liu, et al. (2006). "Influence of thermomechanical processing on the superelastic properties of a Ni-rich Nitinol shape memory alloy." Materials Science and Engineering a-Structural Materials Properties Microstructure and Processing **429**(1-2): 130-136.

Fingerle, J., Y. P. Au, et al. (1990). "Intimal lesion formation in rat carotid arteries after endothelial denudation in absence of medial injury." Arteriosclerosis **10**(6): 1082-7.

Fischer, G. M. and J. G. Llaurado (1966). "Collagen and elastin content in canine arteries selected from functionally different vascular beds." Circ Res **19**(2): 394-9.

Fleisch, M., Meier, B. (1999). "Management and outcome of stents in 1998: long-term outcome." Cardiology In Review **7**(4): 215-218.

Forrester, J. S., M. Fishbein, et al. (1991). "A paradigm for restenosis based on cell biology: clues for the development of new preventive therapies." J Am Coll Cardiol **17**(3): 758-69.

Fridez, P., M. Zulliger, et al. (2003). "Geometrical, functional, and histomorphometric adaptation of rat carotid artery in induced hypertension." J Biomech **36**(5): 671-80.

Fung, Y. C. (1981). Biomechanics : mechanical properties of living tissues / Y.C. Fung. New York

Fung, Y. C. (1990). Biomechanics : motion, flow, stress, and growth. New York ; London, Springer-Verlag.

Fung, Y. C. (1993). Biomechanics : mechanical properties of living tissues. New York ; London, Springer-Verlag.

Fung, Y. C., K. Fronek, et al. (1979). "Pseudoelasticity of arteries and the choice of its mathematical expression." Am J Physiol **237**(5): H620-31.

Garasic, J. M., E. R. Edelman, et al. (2000). "Stent and artery geometry determine intimal thickening independent of arterial injury." Circulation **101**(7): 812-8.

Gasser, T. C., R. W. Ogden, et al. (2006). "Hyperelastic modelling of arterial layers with distributed collagen fibre orientations." Journal of the Royal Society Interface **3**(6): 15-35.

Gefen, A., B. van Nierop, et al. (2008). "Strain-time cell-death threshold for skeletal muscle in a tissue-engineered model system for deep tissue injury." J Biomech **41**(9): 2003-12.

Gervaso, F., C. Capelli, et al. (2008). "On the effects of different strategies in modelling balloon-expandable stenting by means of finite element method." J Biomech **41**(6): 1206-12.

Gijsen, F. J., F. Migliavacca, et al. (2008). "Simulation of stent deployment in a realistic human coronary artery." Biomed Eng Online **7**: 23.

Grenacher, L., E. Ganger, et al. (2004). "Experimental functional analysis of self-expanding stents using a new developed ex vivo model." Invest Radiol **39**(6): 374-83.

Grenacher, L., S. Rohde, et al. (2006). "In vitro comparison of self-expanding versus balloon-expandable stents in a human ex vivo model." Cardiovasc Intervent Radiol **29**(2): 249-54.

Gruentzig, A. R., S. B. King, 3rd, et al. (1987). "Long-term follow-up after percutaneous transluminal coronary angioplasty. The early Zurich experience." N Engl J Med **316**(18): 1127-32.

Harnek, J., E. Zoucas, et al. (1999). "Differences in endothelial injury after balloon angioplasty, insertion of balloon-expanded stents or release of self-expanding stents: An electron microscopic experimental study." Cardiovasc Intervent Radiol **22**(1): 56-61.

Harnek, J., E. Zoucas, et al. (2002). "Insertion of self-expandable nitinol stents without previous balloon angioplasty reduces restenosis compared with PTA prior to stenting." Cardiovasc Intervent Radiol **25**(5): 430-6.

Haudenschild, C. C. and S. M. Schwartz (1979). "Endothelial regeneration. II. Restitution of endothelial continuity." Lab Invest **41**(5): 407-18.

Hertzer, N. R., E. G. Beven, et al. (1984). "Coronary artery disease in peripheral vascular patients. A classification of 1000 coronary angiograms and results of surgical management." Ann Surg **199**(2): 223-33.

Hoffmann, U., Vetter, J., Rainoni, L., Leu, A.J., Bollinger, A. (1997). "Popliteal artery compression and force of active plantar flexion in young healthy volunteers." Journal of Vascular Surgery: 281-287.

Holzapfel, G. A., T. C. Gasser, et al. (2000). "A new constitutive framework for arterial wall mechanics and a comparative study of material models." Journal of Elasticity **61**(1-3): 1-48.

Holzapfel, G. A., T. C. Gasser, et al. (2002a). "A structural model for the viscoelastic behavior of arterial walls: Continuum formulation and finite element analysis." European Journal of Mechanics a-Solids **21**(3): 441-463.

Holzapfel, G. A., G. Sommer, et al. (2007). "Layer-specific 3D residual deformations of human aortas with non-atherosclerotic intimal thickening." Annals of Biomedical Engineering **35**(4): 530-545.

Holzapfel, G. A., G. Sommer, et al. (2005a). "Determination of layer-specific mechanical properties of human coronary arteries with nonatherosclerotic intimal thickening and related constitutive modeling." Am J Physiol Heart Circ Physiol **289**(5): H2048-58.

Holzapfel, G. A., M. Stadler, et al. (2005b). "Changes in the mechanical environment of stenotic arteries during interaction with stents: computational assessment of parametric stent designs." J Biomech Eng **127**(1): 166-80.

Holzapfel, G. A., M. Stadler, et al. (2002b). "A layer-specific three-dimensional model for the simulation of balloon angioplasty using magnetic resonance imaging and mechanical testing." Annals of Biomedical Engineering **30**(6): 753-767.

Horgan, C. O. and G. Saccomandi (2002). "A molecular-statistical basis for the gent constitutive model of rubber elasticity." Journal of Elasticity **68**(1-3): 167-176.

Hsiao, H. M., A. Nikanorov, et al. (2007). "Simulation of renal stent in respiration." Proceedings of the Frontiers in Biomedical Devices Conference: 25-26.

Hu, J. J., A. Ambrus, et al. (2008). "Time courses of growth and remodeling of porcine aortic media during hypertension: a quantitative immunohistochemical examination." J Histochem Cytochem **56**(4): 359-70.

Humphrey, J. D. (2002). Cardiovascular solid mechanics : cells, tissues,and organs. New York, Springer.

Humphrey, J. D. and S. L. Delange (2004). An introduction to biomechanics : solids and fluids, analysis and design. New York, Springer.

Ignat'eva, N. Y., N. A. Danilov, et al. (2007). "Determination of hydroxyproline in tissues and the evaluation of the collagen content of the tissues." Journal of Analytical Chemistry **62**(1): 51-57.

Jaff, M. (2004). "The nature of SFA disease." Endovascular Today **4**: 13-15.

Kafienah, W. and T. J. Sims (2004). "Biochemical methods for the analysis of tissue-engineered cartilage." Methods Mol Biol **238**: 217-30.

Kastrati, A., J. Mehilli, et al. (2001). "Intracoronary stenting and angiographic results: strut thickness effect on restenosis outcome (ISAR-STEREO) trial." Circulation **103**(23): 2816-21.

Kim, H. S., Y. H. Kim, et al. (2009). "Incidence and predictors of drug-eluting stent fractures in long coronary disease." Int J Cardiol **133**(3): 354-8.

Kiousis, D. E., T. C. Gasser, et al. (2007). "A numerical model to study the interaction of vascular stents with human atherosclerotic lesions." Ann Biomed Eng **35**(11): 1857-69.

Kiousis, D. E., T. C. Gasser, et al. (2008). "Smooth contact strategies with emphasis on the modeling of balloon angioplasty with stenting." International Journal for Numerical Methods in Engineering **75**(7): 826-855.

Kiousis, D. E., A. R. Wulff, et al. (2009). "Experimental studies and numerical analysis of the inflation and interaction of vascular balloon catheter-stent systems." Ann Biomed Eng **37**(2): 315-30.

Kipshidze, N., G. Dangas, et al. (2004). "Role of the endothelium in modulating neointimal formation: vasculoprotective approaches to attenuate restenosis after percutaneous coronary interventions." J Am Coll Cardiol **44**(4): 733-9.

Kroger, K., F. Santosa, et al. (2004). "Biomechanical incompatibility of popliteal stent placement." J Endovasc Ther **11**(6): 686-94.

Kroon, M. and G. A. Holzapfel (2008). "A new constitutive model for multi-layered collagenous tissues." J Biomech **41**(12): 2766-71.

Krueger, K. D., A. K. Mitra, et al. (2006). "A comparison of stent-induced stenosis in coronary and peripheral arteries." J Clin Pathol **59**(6): 575-9.

Lafont, A. and D. Faxon (1998). "Why do animal models of post-angioplasty restenosis sometimes poorly predict the outcome of clinical trials?" Cardiovasc Res **39**(1): 50-9.

Lally, C., F. Dolan, et al. (2005). "Cardiovascular stent design and vessel stresses: a finite element analysis." J Biomech **38**(8): 1574-81.

Lally, C., A. J. Reid, et al. (2004). "Elastic behavior of porcine coronary artery tissue under uniaxial and equibiaxial tension." Ann Biomed Eng **32**(10): 1355-64.

Lampmann, L. E. (1999). "Stenting in the femoral superficial artery: an overview." Eur J Radiol **29**(3): 276-9.

Laroche, D., S. Delorme, et al. (2006). "Computer prediction of friction in balloon angioplasty and stent implantation." Biomedical Simulation, Proceedings **4072**: 1-8.

Leimgruber, P. P., G. S. Roubin, et al. (1986). "Restenosis after successful coronary angioplasty in patients with single-vessel disease." Circulation **73**(4): 710-7.

Lemaitre, J. (2001). Handbook of materials behavior models. San Diego, Calif. ; London, Academic.

Liang, D. K., D. Z. Yang, et al. (2005). "Finite element analysis of the implantation of a balloon-expandable stent in a stenosed artery." Int J Cardiol **104**(3): 314-8.

Libby, P. (2002). "Atherosclerosis: the new view." Sci Am **286**(5): 46-55.

Lim, D., S. K. Cho, et al. (2008). "Suggestion of potential stent design parameters to reduce restenosis risk driven by foreshortening or dogboning due to non-uniform balloon-stent expansion." Ann Biomed Eng **36**(7): 1118-29.

Linder-Ganz, E., S. Engelberg, et al. (2006). "Pressure-time cell death threshold for albino rat skeletal muscles as related to pressure sore biomechanics." J Biomech **39**(14): 2725-32.

Ling, A. J., P. Mwipatayi, et al. (2008). "Stenting for carotid artery stenosis: fractures, proposed etiology and the need for surveillance." J Vasc Surg **47**(6): 1220-6; discussion 1226.

Maher, E., A. Creane, et al. (2009). "Tensile and compressive properties of fresh human carotid atherosclerotic plaques." J Biomech.

Marrey, R. V., R. Burgermeister, et al. (2006). "Fatigue and life prediction for cobalt-chromium stents: A fracture mechanics analysis." Biomaterials **27**(9): 1988-2000.

Martin, E. C., B. T. Katzen, et al. (1995). "Multicenter trial of the wallstent in the iliac and femoral arteries." J Vasc Interv Radiol **6**(6): 843-9.

Meijer, W. T., A. W. Hoes, et al. (1998). "Peripheral arterial disease in the elderly: The Rotterdam Study." Arterioscler Thromb Vasc Biol **18**(2): 185-92.

Menichelli, M., A. Parma, et al. (2007). "Randomized trial of Sirolimus-Eluting Stent Versus Bare-Metal Stent in Acute Myocardial Infarction (SESAMI)." J Am Coll Cardiol **49**(19): 1924-30.

Mewissen, M. W. (2004). "Self-expanding nitinol stents in the femoropopliteal segment: technique and mid-term results." Tech Vasc Interv Radiol **7**(1): 2-5.

Mewissen, M. W. (2005). "Stenting in the femoropopliteal arterial segment." Tech Vasc Interv Radiol **8**(4): 146-9.

Migliavacca, F., L. Petrini, et al. (2002). "Mechanical behavior of coronary stents investigated through the finite element method." J Biomech **35**(6): 803-11.

Migliavacca, F., L. Petrini, et al. (2004). "Stainless and shape memory alloy coronary stents: a computational study on the interaction with the vascular wall." Biomech Model Mechanobiol **2**(4): 205-17.

Migliavacca, F., L. Petrini, et al. (2005). "A predictive study of the mechanical behaviour of coronary stents by computer modelling." Med Eng Phys **27**(1): 13-8.

Mills, C. J., I. T. Gabe, et al. (1970). "Pressure-flow relationships and vascular impedance in man." Cardiovasc Res **4**(4): 405-17.

Milnor, W. R. (1989). Hemodynamics. Baltimore, Williams & Wilkins.

Mooney, M. (1940). "A Theory of Large Elastic Deformation." Journal of Applied Physics **11**(9): 582-592.

Mortier, P., M. De Beule, et al. (2008a). "Numerical study of the uniformity of balloon-expandable stent deployment." J Biomech Eng **130**(2): 021018.

Mortier, P., M. De Beule, et al. (2008b). "Finite element analysis of side branch access during bifurcation stenting." Med Eng Phys.

Morton, A. C., D. Crossman, et al. (2004). "The influence of physical stent parameters upon restenosis." Pathol Biol (Paris) **52**(4): 196-205.

Nikanorov, A., H. B. Smouse, et al. (2008). "Fracture of self-expanding nitinol stents stressed in vitro under simulated intravascular conditions." J Vasc Surg **48**(2): 435-40.

Ogden, R. W. (1984). Nonlinear elastic deformations. New York, John Wiley & Sons.

Ouriel, K. (2001). "Peripheral arterial disease." Lancet **358**(9289): 1257-64.

Pache, J., A. Kastrati, et al. (2003). "Intracoronary stenting and angiographic results: strut thickness effect on restenosis outcome (ISAR-STEREO-2) trial." J Am Coll Cardiol **41**(8): 1283-8.

Pelton, A. R., X. Y. Gong, et al. (2004). "Fatigue testing of diamond-shaped specimens." SMST-2003: Proceedings of the International Conference on Shape Memory and Superelastic Technologies: 293-302.

Pelton, A. R., V. Schroeder, et al. (2008). "Fatigue and durability of Nitinol stents." Journal of the Mechanical Behavior of Biomedical Materials **1**(2): 153-164.

Pericevic, I., C. Lally, et al. (2009). "The influence of plaque composition on underlying arterial wall stress during stent expansion: The case for lesion-specific stents." Med Eng Phys.

Perry, R. A., A. Seth, et al. (1988). "Success and complication rates of coronary angioplasty in patients with and without previous myocardial infarction." Eur Heart J **9**(1): 37-42.

Petrini, L., F. Migliavacca, et al. (2004). "Numerical investigation of the intravascular coronary stent flexibility." J Biomech **37**(4): 495-501.

Petrini, L., F. Migliavacca, et al. (2005). "Computational studies of shape memory alloy behavior in biomedical applications." J Biomech Eng **127**(4): 716-25.

Pfisterer, M. E. (2008). "Late stent thrombosis after drug-eluting stent implantation for acute myocardial infarction: a new red flag is raised." Circulation **118**(11): 1117-9.

Prendergast, P. J., C. Lally, et al. (2003). "Analysis of prolapse in cardiovascular stents: a constitutive equation for vascular tissue and finite-element modelling." J Biomech Eng **125**(5): 692-9.

Prendergast, P. J. and S. A. Maher (2001). "Issues in pre-clinical testing of implants." Journal of Materials Processing Technology **118**(1-3): 337-342.

Roach, M. R. and A. C. Burton (1957). "The reason for the shape of the distensibility curves of arteries." Can J Biochem Physiol **35**(8): 681-90.

Robertson, S. W. (2006). On the mechanical properties and microstructures of nitinol for biomedical stent applications. Materials Science and Engineering. Berkeley, University of California. **PhD:** 108.

Robertson, S. W., C. P. Cheng, et al. (2008). "Biomechanical response of stented carotid arteries to swallowing and neck motion." J Endovasc Ther **15**(6): 663-71.

Rogers, C., M. J. Karnovsky, et al. (1993). "Inhibition of experimental neointimal hyperplasia and thrombosis depends on the type of vascular injury and the site of drug administration." Circulation **88**(3): 1215-21.

Rogers, C., M. A. Kjelsberg, et al. (1997). "Heparin-coated stents eliminate mural thrombus deposition for days without affecting restenosis." Circulation **96**(8): 3983-3983.

Roy, C. S. (1881). "The Elastic Properties of the Arterial Wall." J Physiol **3**(2): 125-59.

Scheinert, D., S. Scheinert, et al. (2005). "Prevalence and clinical impact of stent fractures after femoropopliteal stenting." Journal of the American College of Cardiology **45**(2): 312-315.

Schillinger, M., S. Sabeti, et al. (2006). "Balloon angioplasty versus implantation of nitinol stents in the superficial femoral artery." N Engl J Med **354**(18): 1879-88.

Schulze-Bauer, C. A., C. Morth, et al. (2003). "Passive biaxial mechanical response of aged human iliac arteries." J Biomech Eng **125**(3): 395-406.

Schulze-Bauer, C. A. J., P. Regitnig, et al. (2002). "Mechanics of the human femoral adventitia including the high-pressure response." American Journal of Physiology-Heart and Circulatory Physiology **282**(6): H2427-H2440.

Schwartz, R. S. and D. R. Holmes (1994). "Pigs, Dogs, Baboons, and Man: Lessons for Stenting from Animal Studies." Journal of Interventional Cardiology **7**(4): 355-368.

Schwartz, R. S., J. G. Murphy, et al. (1990). "Restenosis after balloon angioplasty. A practical proliferative model in porcine coronary arteries." Circulation **82**(6): 2190-200.

Serruys, P. W., P. de Jaegere, et al. (1994). "A comparison of balloon-expandable-stent implantation with balloon angioplasty in patients with coronary artery disease. Benestent Study Group." N Engl J Med **331**(8): 489-95.

Serruys, P. W. and A. H. Gershlick (2005). Handbook of drug-eluting stents. London, Taylor & Francis.

Serruys, P. W. and M. J. B. Kutryk (2000). Handbook of coronary stents. London, Martin Dunitz.

Simon, M., R. Kaplow, et al. (1977). "A vena cava filter using thermal shape memory alloy. Experimental aspects." Radiology **125**(1): 87-94.

Smouse, H. B., A. Nikanorov, et al. (2005). "Biomechanical forces in the femoropopliteal arterial segment." Endovasc. Today **4**: 60-66.

Solis, J., S. Allaqaband, et al. (2006). "A case of popliteal stent fracture with pseudoaneurysm formation." Catheter Cardiovasc Interv **67**(2): 319-22.

Stone, G. W., S. G. Ellis, et al. (2004). "A polymer-based, paclitaxel-eluting stent in patients with coronary artery disease." N Engl J Med **350**(3): 221-31.

Taylor, A. J., P. D. Gorman, et al. (2001). "A comparison of four stent designs on arterial injury, cellular proliferation, neointima formation, and arterial dimensions in an experimental porcine model." Catheter Cardiovasc Interv **53**(3): 420-5.

Theriault, P., P. Terriault, et al. (2006). "Finite element modeling of a progressively expanding shape memory stent." J Biomech **39**(15): 2837-44.

Thierry, B., Y. Merhi, et al. (2002). "Nitinol versus stainless steel stents: acute thrombogenicity study in an ex vivo porcine model." Biomaterials **23**(14): 2997-3005.

Timmins, L. H., C. A. Meyer, et al. (2008). "Mechanical modeling of stents deployed in tapered arteries." Ann Biomed Eng **36**(12): 2042-50.

Touchard, A. G. and R. S. Schwartz (2006). "Preclinical restenosis models: challenges and successes." Toxicol Pathol **34**(1): 11-8.

van Andel, C. J., P. V. Pistecky, et al. (2003). "Mechanical properties of porcine and human arteries: implications for coronary anastomotic connectors." Ann Thorac Surg **76**(1): 58-64; discussion 64-5.

Velican, C. and D. Velican (1985). "Study of coronary intimal thickening." Atherosclerosis **56**(3): 331-44.

Wang, W. Q., D. K. Liang, et al. (2006). "Analysis of the transient expansion behavior and design optimization of coronary stents by finite element method." J Biomech **39**(1): 21-32.

Wentzel, J. J., F. J. Gijsen, et al. (2003). "Shear stress, vascular remodeling and neointimal formation." J Biomech **36**(5): 681-8.

Weydahl, E. S. and J. E. Moore (2001). "Dynamic curvature strongly affects wall shear rates in a coronary artery bifurcation model." J Biomech **34**(9): 1189-96.

Whitcher, F. D. (1997). "Simulation of in vivo loading conditions of nitinol vascular stent structures." Computers & Structures **64**(5-6): 1005-1011.

Wiersma, S., F. Dolan, et al. (2006). "Fatigue and fracture in materials used for micro-scale biomedical components." Biomed Mater Eng **16**(2): 137-46.

Wu, W., M. Qi, et al. (2007a). "Delivery and release of nitinol stent in carotid artery and their interactions: a finite element analysis." J Biomech **40**(13): 3034-40.

Wu, W., W. Q. Wang, et al. (2007b). "Stent expansion in curved vessel and their interactions: a finite element analysis." J Biomech **40**(11): 2580-5.

Zahedmanesh, H. and C. Lally (2009). "Determination of the influence of stent strut thickness using the finite element method: implications for vascular injury and in-stent restenosis." Med Biol Eng Comput.

Zeng, D., Z. Ding, et al. (2003). "Effects of cardiac motion on right coronary artery hemodynamics." Ann Biomed Eng **31**(4): 420-9.

Zhao, H. Q., A. Nikanorov, et al. (2009). "Late stent expansion and neointimal proliferation of oversized Nitinol stents in peripheral arteries." Cardiovasc Intervent Radiol **32**(4): 720-6.

Zulliger, M. A., P. Fridez, et al. (2004). "A strain energy function for arteries accounting for wall composition and structure." J Biomech **37**(7): 989-1000.

Appendix A

Protocol for elastin assay

Introduction

The following is the protocol followed for calculating the elastin content in porcine arteries. Note that the arteries contained insoluble elastin, which must be converted to soluble α-elastin for measurement. This protocol is based on that provided by the elastin assay kit manufacturers (Biocolor, Newtownabbey, Northern Ireland).

Prepare standards and digest samples

1. Prepare standards of 0, 12.5, 25, 50 and 100µl in 1.5/2ml micro-tubes using α-elastin standard stock. Top up to 100µl using 0.5M oxalic acid.
2. Digest samples in 1.2ml of 0.5M oxalic acid. Micro-tubes with screw tops and O-rings should be used to avoid evaporation. Place samples in oven at 100°C for one hour.
3. After one hour, remove the samples from the oven, centrifuge at >10,000g for 10 minutes and allow to cool.
4. Extract the top 1ml of the sample and place in a numbered micro-tube.
5. Add 1ml of 0.5M oxalic acid to the sample and replace in the oven for a further hour.
6. Repeat Steps 3-5 until the sample is fully dissolved. This usually takes 4-5 extracts. Add 800µl of 0.5M oxalic acid to the sample following the final extraction.
7. Take 100µl from each of the extracts and the initial micro-tube with the digested sample and add to a labelled micro-tube.
8. Add an equal volume of elastin precipitating reagent to each of the samples.
9. Mix the contents of the tubes using a vortex mixer and leave for 10 minutes to allow complete precipitation of the elastin.
10. Centrifuge tubes at >10,000g for 10 minutes.
11. Drain the liquid contents of the micro-tubes into a beaker. Remove remaining fluid by tapping inverted tubes lightly onto a paper towel.

Formation of elastin-dye complex

1. Add 1ml of dye reagent to all tubes. Mix using a vortex mixer.
2. Place tubes on rotator and leave for 90 minutes to allow the dye-elastin reaction to occur.
3. Centrifuge the tubes at > 10,000g for 10 minutes.

Recovery of elastin-dye complex

1. Drain the tubes of unbound dye by emptying the liquid contents into a beaker. Remove remaining fluid by tapping the inverted tube firmly onto a paper towel. Fluid droplets should be removed from the rim of the tube using a Q-tip. The elastin-dye complex is observed as a sludge, varying in colour from pink to dark red/brown, depending on the quantity of elastin.

Release and recovery of elastin bound dye

1. Add 1ml of dye dissociation reagent to each tube.
2. Mix using a vortex mixer, allow to stand for 10 minutes, then mix again.
3. Inspect the colour of the tubes by comparing them with the elastin standards. If the sample appears darker than the highest standard, dilute the sample by taking a fraction of it and adding an appropriate amount of dye dissociation reagent. For example, very dark samples are diluted by taking 250µl of the sample and 750µl of dye dissociation reagent.

Elastin measurement

1. Transfer 200µl of each sample (in triplicate) to a clear 96-well plate.
2. Take absorbance readings at a wavelength of 513nm. The three readings for each sample should not exceed ±10% of the mean.
3. Use the (average) absorbance readings and the standards curve to calculate the elastin content of each measured sample.
4. Calculate the total elastin content per sample.

Appendix B

Protocol for determination of total collagen content via hydroxyproline assay

Introduction

The following is the protocol followed for calculating the collagen content in porcine arteries. This was carried out indirectly by measuring the hydroxyproline content and using a fixed ratio to determine the quantity of collagen. The protocol outlined below is based on a procedure provided by Kafienah and Sims [Kafienah *et al.* 2004].

Digestion

1. Prepare 10mg/ml pepsin by dissolving in 0.5M acetic acid.
2. Place samples in screw-top micro-tubes with O-rings. Add pepsin solution at a ratio between the wet weight of the collagen to the pepsin solution of 10:1. Top up to 500µl with 0.5M acetic acid.
3. Place samples in rotator in oven at 60°C for approximately 12 hours, or until all the samples are digested.
4. Take aliquot sizes so that each one contains approximately 500ng Hydroxyproline, or 150ng per well (in the middle of the standard curve). If the required volumes are very small (i.e. 1µl or less), it may be necessary to dilute the samples in acetic acid over two steps. Top up to 100µl with acetic acid.

Hydrolyzation and neutralisation procedure

1. Add 100µl of 38% HCL to each tube.
2. Mix tube contents using a vortex mixer.
3. Incubate in an oven at 110°C for 18 hours.
4. Centrifuge the tubes at >5,000g for 5 minutes.
5. Dry the samples by placing on a heating block
6. Add 200µl of ultra-pure water to each sample to dissolve.
7. Use a vortex mixer to re-suspend the tube contents.

Material preparation

Hydroxyproline stock solution

1. Add 40mg of trans-4-Hydroxy-L-proline to 40ml of ultra-pure water to create a 1mg/ml stock solution.
2. Store at 4°C and use within 3 months.

Citrate stock buffer

Add the following to a glass jar to create 100ml of solution:

1. 80ml ultra-pure water
2. 5.04g citric acid monohydrate
3. 11.98g sodium acetate trihydrate
4. 7.22g anhydrous sodium acetate
5. 3.4g sodium hydroxide
6. 1.26ml glacial acetic acid
7. Add ultra-pure water to bring total volume to 100ml
8. Filter with whatman paper
9. Store at 4°C

Assay buffer

Add the following to a 15ml falcon tube. Note that this solution must be prepared freshly before assay.

1. 1.5ml n-propanol
2. 1ml ultra-pure water
3. 5ml citrate stock buffer

Chloramine-T reagent

Add the following to a 15ml falcon tube. Note that this solution must be prepared freshly before assay.

1. 141mg chloramine T
2. 0.5ml ultra-pure water
3. Place in an oven at 60°C for 10 minutes to dissolve
4. 0.5ml n-propanol
5. 4ml citrate stock buffer
6. Wrap the tube in tinfoil until use

DMBA Reagent

Add the following to a 15ml falcon tube. Note that this solution must be prepared freshly before assay.

1. 6ml n-propanol
2. 3ml 70% perchloric acid
3. 4.5g 4-(Dimethylamino)benzaldehyde
4. Wrap the tube in tinfoil until use

Hydroxyproline standards

1. Create a 50µg/ml Hydroxyproline solution from the 1mg/ml stock solution (see above).
    a. Take 50µl Hydroxyproline stock solution (1mg/ml)
    b. Add 950µl 0.5M acetic acid
2. Mix the solution and briefly spin on a desktop centrifuge.
3. Prepare standards in 1.5/2ml micro-tubes as outlined in Table B.1.
4. Mix standards in vortex mixer.

Standard ID	Standard (µg/ml)	Volume of 50µg/ml HYP (µl)	Volume of acetic acid to make 1ml	Ng HYP/well
Blank	0	0	1000	0
STD 1	0.1	2	998	6
STD 2	0.25	5	995	15
STD 3	0.5	10	990	30
STD 4	1	20	980	60
STD 5	2	40	960	120
STD 6	3.5	70	930	210
STD 7	5	100	900	300

Table B.1

Volumes for preparing HYP standards.

Assay procedure

1. Add 60µl (in triplicate) of standards and samples to a clear 96-well plate.
2. To each well add
    a. 20µl of assay buffer
    b. 40µl of chloramine-T reagent
3. Cover the plate with tinfoil and incubate for 20 minutes at room temperature.
4. Add 80µl of DMBA reagent. Use filter tipped pipette tips, as this solution can stain pipettes.
5. Cover the 96-well plate with a SealPlate (a clear, adhesive cover).
6. Incubate in an oven for 20 minutes.
7. Allow the plate to cool for 10 minutes.
8. Read the samples in a plate reader at a wavelength of 570nm to obtain Hydroxyproline concentrations in each sample.
9. Use the standard curve and collagen:Hydroxyproline ratio to calculate the collagen contents.

Appendix C

Histology protocols

Paraformaldehyde (PFA) fixative

The 4% PFA fixative is prepared as follows.

1. Place 180ml of ultra-pure water in an autoclave bottle. Heat to 60°C using a hot plate with stirring. Wrap the bottle in tinfoil.
2. While stirring, add 8g of paraformaldehyde powder to the heated water. Cover and maintain at 60°C.
3. Add 2 drops of 4M NaOH. The solution should clear within a couple of minutes, though there may be some fine particles that do not go away. Do not heat above 70°C.
4. Remove from heat and add 20ml of 10X PBS. Adjust pH to 7.2 using HCL. Final volume will be 200 ml.
5. Cool the solution by placing on ice and cover with foil to protect from the light.
6. Sterile filter solution and aliquot solution in 15ml falcon tubes, with 10ml in each tube.
7. Store aliquots at -20°C.

Wax embedding

Fixation

Place the sample in a 1.5ml micro-tube. Add 1ml of 4% PFA fixative solution and incubate overnight. Wash three times in PBS (for 5 minutes) and store in fresh PBS at 4°C until ready to use.

Dehydration

Artery samples are dehydrated by placing in gradually increasing strengths of alcohol (EtOH), see Table C.1. The samples are placed in 24-well plates. Note that when using xylene, the samples must be placed in micro-tubes, as xylene will dissolve the 24-well plates. The samples should be placed in wells in the 24-well plates at room temperature with contents and for the time described by

Solution	Time
Distilled water	30 minutes
70% EtOH	1 hour
80% EtOH	1 hour
90% EtOH	1 hour
100% EtOH	1 hour
100% EtOH	1 hour
Xylene	1 hour

Table C.1

Dehydration to xylene procedure for artery samples.

Wax embedding

1. Paraffin wax beads are placed in moulds and put in an oven at 65°C until they are fully melted. The samples are placed in the moulds and aligned as desired.
2. The moulds are covered in tinfoil and placed on a hot plate at 65° for 3 hours, then allowed to cool.
3. The following day, heat the moulds to re-melt the wax. Move the specimens gently and ensure they are in the correct position and orientation.
4. Place mounting plugs into the molten wax and allow to cool again.

Slicing and mounting

1. Mount the plugs in a microtome.
2. Cut slices at 5-10μm.
3. Place slices (3-4 together) in water bath at ~50°C.
4. Push subbed slide down onto slice at slight angle and remove from the water bath. Slices should adhere to slide.
5. Allow to dry overnight.

Verhoeff-van Gieson staining

Working elastic stain solution

Add the following to a Coplin jar and mix well.

1. 20 ml hematoxylin solution, alcoholic.
2. 3 ml ferric chloride solution.
3. 8 ml weigert's iodine solution.
4. 5 ml deionised water .

Working ferric chloride solution

Add the following to a Coplin jar and mix well.

1. 3 ml ferric chloride solution.
2. 37 ml deionized water.

Deparaffinise slides

Slides must be deparaffinised to make them suitable for staining. Slides are placed in racks and dipped in the solutions as described by (Table C.2). Following staining, the slides are dehydrated again by following the procedure described by (Table C.3).

Solution	Time
Xylene	5 minutes
Absolute alcohol	30 seconds
Absolute alcohol	30 seconds
100% EtOH	30 seconds
70% EtOH	30 seconds
Xylene	30 seconds

Table C.2

Deparaffinisation procedure before staining.

Solution	Time
Deionised water	30 seconds
Deionised water	30 seconds
70% EtOH	30 seconds
70% EtOH	30 seconds
Xylene	30 seconds

Table C.3

Dehydration procedure following staining.

Staining

The working elastic stain solution, working ferric chloride solution and the van Gieson solution are poured into recpticles that allow the slides to be covered in the solution. The steps for placing the slides in the solutions are described below. This protocol is taken from the instructions provided with the Accustain elastic stain kit (Sigma-Aldrich, St. Louis, MO).

1. Deparaffinise slides to deionised water (see above).
2. Place slides in working elastic stain solution for 10 minutes.
3. Rinse in deionised water.
4. Differentiate in working ferric chloride solution.
5. Rinse in tap water.
6. Check microscopically. If over differentiated, return to working elastic stain solution.
7. Rinse in 95% alcohol to remove iodine.
8. Rinse in deionised water.
9. Stain in Van Gieson solution for 1-3 minutes.
10. Rinse in 95% alcohol.
11. Dehydrate to xylene and mount (see above).

Subbing glass slides

Glass slides are prepared for use in histology by using the following procedures.

Preparing subbing solution

The solution for subbing the slides is prepared as follows:

1. Heat 500ml of deionised water to 60°C. Use a thermometer to ensure the temperature does not exceed 60°C.
2. Add 2.5g of gelatine and dissolve.
3. Add 0.25g of chromium potassium sulphate and allow to dissolve.
4. Filter solution using standard filter paper.
5. Store at 4°C for a maximum of 6 months.

Subbing procedure

The solution is applied to the slides as follows.

1. Load slides into slide staining racks.
2. Dip racks into 95% ethanol.
3. Remove racks and place into clean and well rinsed dish pan.
4. Rinse slides in deionised water for 20 minutes.
5. Remove the racks of slides and dip into fresh deionised water for 20 seconds, then into the warm gelatine-chrom-alum (subbing) solution for 20 seconds.
6. Lift the slides out and drain as much as possible.
7. Place slides (in holders) onto tissue paper.
8. Ensuring slides are not in contact with each other, cover with tissue paper and leave to dry overnight.